

**From mechanically milled powders to Mg-SiC  
nanocomposites: relationships between processing,  
microstructure and mechanical properties**

vorgelegt von

Dipl.-Ing.

Daniela Stefanie Hübler

ORCID: 0000-0002-0272-9343

an der Fakultät III – Prozesswissenschaften  
der Technischen Universität Berlin  
zur Erlangung des akademischen Grades

Doktorin der Ingenieurwissenschaften  
- Dr.-Ing. -

genehmigte Dissertation

Promotionsausschuss:

Vorsitzender: PD Dr.-Ing. Sören Müller  
Gutachterin: Prof. Dr.-Ing. Claudia Fleck  
Gutachter: Prof. Dr. Aleksander Gurlo  
Gutachter: Prof. Dr. Dr. h. c. Ralf Riedel

Tag der wissenschaftlichen Aussprache: 28. Oktober 2021

Berlin 2022



*... to my present and future family  
and the ones who passed away*

*Enjoy each step,*

FOR IN EVERY MOMENT

THERE IS SOMETHING TO LEARN

- John P. Strelecky -



## **Abstract**

---

Magnesium nanocomposites are promising for use as lightweight components in the automotive and aviation industries, since reinforcing pure magnesium with ceramic nanoparticles not only increases strength, but also improves ductility. SiC nanoparticles are particularly suitable as a reinforcement phase due to their high specific fracture toughness and their stable behaviour towards magnesium. However, the production of magnesium nanocomposites has some challenges, such as the achievement of a homogenous distribution of the nanoparticles and an ultra-fine structure in the completely dense material. These requirements were met via a new powder metallurgical production route, which includes mechanical milling, cold isostatic pressing, sintering and indirect hot extrusion. Initially, powder composites with a uniform SiC distribution and a nano- to sub-microcrystalline structure were produced by mechanical milling. The composite powder was then pressed into green compacts by cold isostatic pressing followed by sintering. The density increased up to 93 %, but hot extrusion was required to completely densify the magnesium nanocomposites. By achieving a sub-microcrystalline microstructure by hot extrusion, all challenges were overcome by the new processing route. However, extrusion also leads to a textured material, which is the reason why hot isostatic pressing was carried out as alternative last consolidation step. The achieved microstructure did not meet the requirements. Therefore, the mechanical properties were only investigated on the extruded Mg-SiC nanocomposites. An increase in hardness was observed with an increasing reinforcement content. Compression and tensile tests of the extruded nanocomposites showed a compression up to 41.5 %, however, the influence of the texture on the tensile elongation behaviour resulted in only minimal elongation of at most 2.5 %. Fatigue tests on macro and nano scale suggest that conclusions on plastic deformability of pure Mg can be drawn from nano fatigue to macro fatigue. Furthermore, nanocomposites showed less plastic strain than pure Mg produced in the same way. Using the new powder metallurgical production route, significantly higher fatigue endurance limits were achieved for milled Mg and its nanocomposites than for non-milled Mg.

### **Keywords**

Mg-SiC nanocomposite, powder metallurgy, mechanical properties, fatigue behaviour, nanoindentation



## Kurzfassung

---

Der Einsatz von Magnesium-Nanokompositen als Leichtbaukomponenten ist in der Automobil- und Flugindustrie vielversprechend, da aufgrund der Verstärkung des reinen Magnesiums nicht nur die Festigkeit erhöht, sondern auch die Duktilität verbessert werden kann. SiC-Nanopartikel sind relativ inert gegenüber Magnesium und eignen sich als Verstärkungsphase besonders aufgrund ihrer hohen spezifischen Bruchzähigkeit. Die Herstellung der Magnesium-Nanokomposite birgt allerdings einige Herausforderungen, wie zum Beispiel die gleichmäßige Verteilung der Nanopartikel und ein ultrafeines Gefüge im vollständig dichten Material. Über eine neue pulvermetallurgische Herstellungsrouten konnten diese Anforderungen durch hochenergetisches Kugelmahlen, kalt-isostatisches Pressen, Sintern und indirektes Warm-Strangpressen erfüllt werden. Zunächst konnten Pulverkomposite mit gleichmäßiger SiC-Verteilung und nano- bis submikrokristallinem Gefüge hergestellt werden. Das Kompositpulver wurde über kalt-isostatisches Pressen zu Grünlingen gepresst und anschließend gesintert, wodurch die Dichte auf 93% erhöht werden konnte. Um die Nanokomposite vollständig zu verdichten, wurde indirektes Warm-Strangpressen genutzt. Da Strangpressen allerdings auch zu einem texturiertem Material führt, wurden die Nanokomposite zudem über einen alternativen Verfahrensschritt, dem heiß-isostatischen Pressen, verdichtet. Allerdings entsprach die Mikrostruktur nicht den oben genannten Anforderungen, sodass die mechanischen Eigenschaften nur an den stranggepressten Mg-SiC-Nanokompositen untersucht wurden. Mittels Nanoindentation konnte zusätzlich die Härte der Kompositpulverpartikel nach dem Kugelmahlen ermittelt werden, die mit steigendem SiC-Gehalt stieg. In den Druck- und Zugversuchen konnten die stranggepressten Nanokomposite Stauchungen von bis zu 41.5 %, jedoch nur geringe Dehnungen von maximal 2.5 % erreichen, was auf den Einfluss der Textur zurückzuführen ist. Die Ermüdungsversuche legen nahe, dass Rückschlüsse zur plastischen Verformbarkeit von der Nano- zur Makroermüdung gezogen werden können. Unter Verwendung des neuen pulvermetallurgischen Produktionsweges wurden für Mg und seine Nanokomposite signifikant höhere Ermüdungsfestigkeiten erreicht als für reines, nicht kugelmahlenes Mg.

### **Schlüsselwörter**

Mg-SiC-Nanokomposit, Pulvermetallurgie, mechanische Eigenschaften, Ermüdungsverhalten, Nanoindentation

## **Eidesstattliche Erklärung**

---

Hiermit versichere ich gegenüber der Fakultät III der Technischen Universität Berlin an Eides statt, dass ich die vorliegende Dissertation selbstständig und nur unter Zuhilfenahme der im Literaturverzeichnis genannten Quellen und Hilfsmittel angefertigt habe. selbstständig und nur unter Zuhilfenahme der im Literaturverzeichnis genannten Quellen und Hilfsmittel angefertigt Weiter erkläre ich, dass ich zu keinem Zeitpunkt anderweitig eine Promotionsabsicht angemeldet noch ein Promotionseröffnungsverfahren beantragt habe. In Fällen von Co-Autorschaft sind die Eigenanteile gemäß §5 einzeln für die jeweilige Veröffentlichung aufgeführt.

Berlin, den

Daniela Stefanie Hübler



## Acknowledgements

---

This dissertation is the result of my work as doctoral student and research assistant within the project “Processing, microstructure evolution and mechanical properties (under quasi-static and cyclic loading) of Mg-SiC nanocomposites” at the Chair of Materials Science and Engineering at the Technische Universität Berlin in collaboration with the Dispersive Solids group at the Technische Universität Darmstadt. Without the support of several persons, the dissertation would not have been possible.

I am grateful to Prof. Dr.-Ing. Claudia Fleck and to Dr.-Ing. Sepideh Kamrani for giving me the opportunity to work on this project, for their guidance, scientific advice, the discussions and the opportunity to develop myself further. My special thanks go to Claudia Fleck for her supervision of the thesis and her continuous encouragement.

I would like to thank Prof. Dr. Dr. h. c. Ralf Riedel and the colleagues in Darmstadt for the warm welcome and their support and for giving me a great time even during long working hours.

Special thanks to Prof. Dr. Aleksander Gurlo for his willingness to evaluate this thesis and his flexibility in terms of time.

I acknowledge Dr.-Ing. Anke Märten for her academic guidance, encouragement and support throughout the course of this work. Huge and special thanks go to all of my colleagues for the great time together and for not only scientific discussions. I also would like to thank my student assistants for the great support during the sample preparation and data analysis.

I acknowledge the financial support of the German Research Foundation, without which I would not be able to conduct this research.

Special gratitude goes to my beloved husband Tom, who always has my back, and for his unconditional love, even in difficult times. Many thanks to my parents-in-law for their advice and the gentle push towards the finish line.

Last but not least, the greatest thanks and appreciation go to my parents and my sister for turning me into the person I am today and always supporting me, no matter what happens.

## List of publications

---

This doctoral thesis is primarily based on the manuscripts I, III, IV and V, which have been published in the following peer reviewed journals. Manuscript II was mainly included because of the nanoindentation analysis of the nanocomposite powders.

- I. D. Penther, C. Fleck, A. Ghasemi, R. Riedel, S. Kamrani, Development and characterization of Mg-SiC nanocomposite powders synthesized by mechanical milling, *Key Engineering Materials*, 742 (2017) 165–172, <https://doi.org/10.4028/www.scientific.net/KEM.742.165>  
Postprint, chapter 4
- II. A. Ghasemi, D. Penther, S. Kamrani, Microstructure and nanoindentation analysis of Mg-SiC nanocomposite powders synthesized by mechanical milling, *Materials Characterization*, 142 (2018) 137–143, <https://doi.org/10.1016/j.matchar.2018.05.023>  
Postprint, chapter 5
- III. D. Penther, A. Ghasemi, R. Riedel, C. Fleck, S. Kamrani, Effect of SiC nanoparticles on manufacturing process, microstructure and hardness of Mg-SiC nanocomposites produced by mechanical milling and hot extrusion, *Materials Science and Engineering: A*, 738 (2018) 264–272, <https://doi.org/10.1016/j.msea.2018.09.106>  
Postprint, chapter 6
- IV. D. Hübler, A. Ghasemi, R. Riedel, C. Fleck, S. Kamrani, Effect of hot isostatic pressing on densification, microstructure and nanoindentation behaviour of Mg-SiC nanocomposites, *Journal of Materials Science*, 55 (2020) 10582-10592, <https://doi.org/10.1007/s10853-020-04758-5>  
Postprint, chapter 8
- V. D. Hübler, K. Winkler, R. Riedel, S. Kamrani, C. Fleck, Cyclic deformation behaviour of Mg-SiC nanocomposites on the macro and nano scale, *Fatigue & Fracture of Engineering Materials & Structure*, (2021) 1-14, <https://doi.org/10.1111/ffe.13600>  
Postprint, chapter 10



# Content

<b>1. INTRODUCTION.....</b>	<b>1</b>
<b>2. STATE OF THE ART .....</b>	<b>3</b>
<b>2.1. MAGNESIUM.....</b>	<b>3</b>
2.1.1. DEFORMATION MECHANISMS .....	4
2.1.2. DEVELOPMENT OF TEXTURE .....	6
<b>2.2. METAL MATRIX COMPOSITES (MMCs) .....</b>	<b>8</b>
2.2.1. THE EFFECT OF REINFORCEMENTS .....	8
2.2.2. SiC AS PARTICLE REINFORCEMENT .....	11
<b>2.3. PROCESSING ROUTES .....</b>	<b>12</b>
2.3.1. POWDER METALLURGY .....	13
2.3.2. MECHANICAL MILLING .....	14
2.3.3. COLD-ISOSTATIC PRESSING (CIP) .....	15
2.3.4. SINTERING .....	17
2.3.5. HOT ISOSTATIC PRESSING (HIP).....	18
2.3.6. INDIRECT HOT EXTRUSION.....	19
<b>2.4. MECHANICAL PROPERTIES OF Mg-SiC NANOCOMPOSITES .....</b>	<b>21</b>
2.4.1. QUASISTATIC LOADING.....	21
2.4.2. CYCLIC LOADING .....	25
<b>3. OUTLINE OF THE THESIS AND OVERVIEW OF THE PUBLICATIONS .....</b>	<b>30</b>
<b>4. MANUSCRIPT I .....</b>	<b>32</b>
4.1. ABSTRACT .....	33
4.2. INTRODUCTION .....	33
4.3. EXPERIMENTAL PROCEDURES .....	34
4.4. RESULTS AND DISCUSSION .....	35
4.5. SUMMARISING CONCLUSIONS.....	40
4.6. ACKNOWLEDGEMENT .....	40
4.7. REFERENCES.....	40
<b>5. MANUSCRIPT II .....</b>	<b>42</b>
5.1. ABSTRACT .....	43
5.2. INTRODUCTION .....	43
5.3. EXPERIMENTAL .....	44
5.4. RESULTS.....	47
5.5. DISCUSSION .....	53
5.6. CONCLUSION .....	55
5.7. ACKNOWLEDGEMENTS.....	56
5.8. REFERENCES.....	56
<b>6. MANUSCRIPT III .....</b>	<b>59</b>
6.1. ABSTRACT .....	60
6.2. INTRODUCTION .....	60
6.3. MATERIALS AND METHODS .....	62
6.4. RESULTS.....	63

6.5.	DISCUSSION .....	71
6.6.	CONCLUSIONS .....	73
6.7.	ACKNOWLEDGEMENT .....	74
6.8.	REFERENCES.....	74
7.	ADDITIONAL RESULTS ON MANUFACTURING PROCESSES .....	77
7.1.	SINTERING BEHAVIOUR .....	77
7.2.	EXTRUSION BEHAVIOUR .....	78
8.	MANUSCRIPT IV .....	79
8.1.	ABSTRACT .....	80
8.2.	INTRODUCTION .....	80
8.3.	EXPERIMENTAL PROCEDURE .....	82
8.4.	RESULTS.....	83
8.5.	DISCUSSION .....	88
8.6.	CONCLUSIONS .....	92
8.7.	ACKNOWLEDGEMENT .....	92
8.8.	REFERENCES.....	93
9.	ADDITIONAL RESULTS ON MECHANICAL PROPERTIES .....	95
9.1.	COMPRESSION TEST .....	95
9.2.	TENSILE TEST .....	96
10.	MANUSCRIPT V .....	98
10.1.	ABSTRACT .....	99
10.2.	INTRODUCTION .....	99
10.3.	MATERIALS AND METHODS .....	101
10.4.	RESULTS.....	104
10.5.	DISCUSSION .....	111
10.6.	CONCLUSIONS .....	117
10.7.	ACKNOWLEDGEMENTS.....	117
10.8.	REFERENCES.....	119
11.	OVERALL DISCUSSION .....	123
11.1.	MANUFACTURING PROCESS .....	123
11.2.	MECHANICAL PROPERTIES .....	125
11.2.1.	COMPRESSION BEHAVIOUR.....	125
11.2.2.	TENSILE BEHAVIOUR .....	127
11.2.3.	FATIGUE BEHAVIOUR .....	129
12.	CONCLUSION AND OUTLOOK.....	131
13.	LIST OF SYMBOLS AND ABBREVIATIONS.....	133
14.	REFERENCES.....	135



# 1. Introduction

Magnesium (Mg) and its alloys are a widespread choice for different applications in the automobile, aerospace and electronics industries. In addition to the good stiffness-to-weight ratio [1], high dimensional stability and superior damping characteristics, Mg is the lightest structural metal with a density of two-thirds that of aluminium [2,3]. Due to its hexagonal close-packed (hcp) crystal structure with limited slip systems, Mg is more brittle and has a low ductility, low elastic modulus and low strength compared to other metals like aluminium. In order to improve the light weight construction potential of Mg and achieve a material with low density and yet excellent specific mechanical properties, such as strength, stiffness and creep resistance, significant efforts have been made to develop Mg matrix composites [4–6].

Mg-SiC nanocomposites are particularly attractive because of the low reactivity of SiC with the Mg matrix. The SiC nanoparticles remain incoherent to the matrix and can thus prevent grain growth during the manufacturing process, which increases the strength. Another advantage of nanoparticles is their high specific surface area. A good wettability between Mg matrix and SiC nanoparticles leads to a continuous interface and ensures their load bearing capacity. Recent work showed the potential of nanoparticles as reinforcements enhancing both strength and ductility of Mg composites compared to micro-sized particles [7]. In addition, nano-sized reinforcements can withstand deformation much better without fracturing and therefore have a higher ultimate strength [5,8–11]. By reinforcing Mg with SiC nanoparticles, the strength increases compared to pure Mg, while the ductility can be maintained or even improved [7,12]. It is known that the production of nanocomposites with low scattered mechanical properties is challenging. Homogeneously distributed nanoparticles, a nano- to sub-microcrystalline microstructure and a completely dense material are the key factors [5,13,14].

The functionality of nanoparticles strongly depends on their uniform distribution in the matrix. However, due to their small particle size and large specific surface area, nanoparticles tend to agglomerate. This makes nanoparticles extremely difficult to incorporate, distribute and disperse uniformly in the Mg matrix. To overcome agglomeration, mechanical milling as a powder metallurgy technique is promising to achieve an acceptable distribution of the reinforcing particles. Moreover, milling is one of the most effective methods for the mechanical reduction of grain size and the production of nanocrystalline powders. In Al- and Ti-based composites, this was attributed to the plastic deformation and thus strain hardening of the powder, which is enhanced by the hard reinforcing particles [15–17]. Overall, powder metallurgy techniques offer further

advantages over casting techniques, which often lead to segregation and thus agglomeration of nanoparticles at the grain boundaries during solidification [8].

The consolidation of the nanocomposite powder and the further densification of the bulk material is usually done by pressing and sintering [18], and/or by extrusion [19]. However, effective compaction to achieve full density and a nanocrystalline structure is challenging. Regarding the last consolidation step, extrusion leads to a preferred crystallographic orientation (texture) of the grains in the material. This means that the mechanical properties depend on the grain orientation and are therefore anisotropic. In contrast, hot isostatic pressing results in a random grain orientation and isotropic properties, which are beneficial for many applications.

This thesis presents a new powder metallurgical manufacturing route for Mg-SiC nanocomposites. The aim was to achieve a uniform distribution of the nanoparticles, and at the same time, to produce a sub-microcrystalline microstructure through mechanical milling, cold-isostatic pressing, sintering, and hot extrusion. Additionally, the effect of extrusion on the microstructure and hardness was compared to hot isostatic pressing. Through nanoindentation measurements, not only the hardness but also the elastic modulus of the nanocomposite powder was compared with that of the bulk nanocomposite. Mechanical properties regarding tensile, compression, and fatigue behaviour were investigated and are discussed considering the structure-property relationship.

## 2. State of the art

The following literature review shows the current state of research regarding magnesium (Mg) and its composites, in particular Mg-SiC nanocomposites. Typical processes to produce Mg nanocomposites are presented with their advantages and disadvantages. For the present thesis, the powder metallurgical processing route is highlighted. Special methods to investigate mechanical properties and characterize the Mg-SiC nanocomposites are presented.

### 2.1. Magnesium

Magnesium (Mg) is the lightest engineering lightweight structural metal with a density of  $1.74 \text{ g/cm}^3$ . Its good stiffness-to-weight ratio [1], high dimensional stability and excellent damping characteristics, compared to aluminium [2,3], make Mg a widespread choice for different applications, especially in the automotive, aerospace and electronics sectors. However, its poor creep resistance and poor ductility limit the applications of Mg. General properties of Mg are briefly summarized in Table 1, together with properties crucial for industrial use. Advantages and drawbacks in relation to the use as crash material [1] are listed in the right part of the table.

Table 1. General properties of magnesium on the left-hand side and properties crucial for industrial use on the right-hand side.

Properties		Advantages	Drawbacks
Crystal structure	Hexagonal close-packed (hcp)	High specific mechanical properties	Poor creep resistance
Density (RT)	$1.738 \text{ g/cm}^3$	High dimensional stability	Poor ductility
Elastic modulus	45 GPa	High thermal conductivity	Low elastic modulus
Linear thermal expansion coefficient (RT)	$26 \cdot 10^{-6} \text{ 1/K}$	Excellent damping properties	Fast loss of strength with increasing operating temperature
Yield strength	80-180 MPa	Good workability	Difficult deformability
Fracture strain	1-12%	Recyclability	
Melting point	$650 \pm 0,5^\circ\text{C}$		
Boiling point	$1090^\circ\text{C}$		

### 2.1.1. Deformation mechanisms

Magnesium has a hexagonal close packed (hcp) crystal structure with a nearly ideal ratio of the length of the  $c$ - to  $a$ -axis ( $c/a$  ratio) of 1.624 [20], which leads to the largest possible packing density. Thereby,  $a$  is the interatomic distance within the (0001) basal plane in each of the densest packed directions, and  $c$  is the height of the unit cell [21]. Figure 1 shows the hcp unit cell and the three-dimensional close packing of atoms in the ABA stacking order. In face-centred cubic (fcc) crystal structures, the high packing density is related to the good workability, which makes them able to deform more easily. The hcp crystal structure, however, is brittle at room temperature (RT).

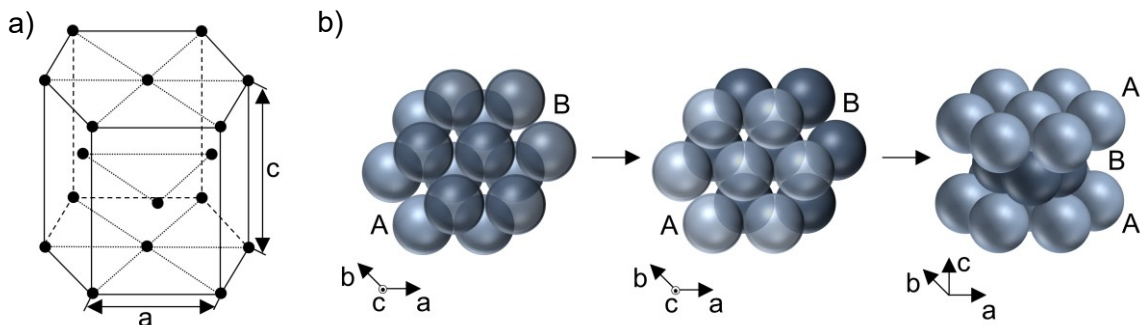


Figure 1. Illustration of a) the hexagonal close packed (hcp) unit cell; b) the 3D close packing of atoms in the stacking order ABA.

Plastic deformation occurs through two mechanisms at the same time [21], namely slip and deformation twinning, which are shown in Figure 2. During slip, multiple atomic planes slide over one another. Atoms move along a close packed plane (slip plane) in a certain slip direction, thereby generating dislocations that lead to an irreversible change of shape. The magnitude and direction of the lattice distortion, in which the atoms move, is described by the Burgers vector  $b$ . During deformation twinning, twins are formed through a group of atoms rotating as a primitive cell in its collectivity along a preferred plane [22]. In contrast to slip, twinning is reversible in most of the cases.

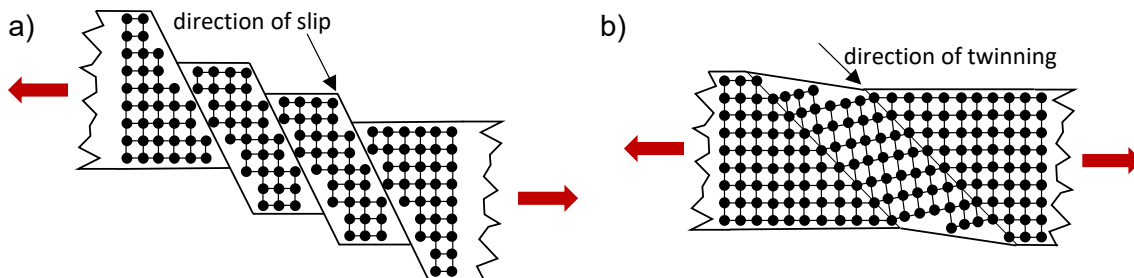


Figure 2. Schematic illustration of the plastic deformation mechanisms a) slip and b) deformation twinning.

According to the von Mises criterion, at least five independent slip systems are required for a crystal structure to flow plastically and thus behave ductile [23]. Due to its hcp structure, Mg has only two independent slip systems with three symmetrical slip

directions of the type  $\langle 11\bar{2}0 \rangle$  in the basal plane (0001), which explains its brittle behaviour at room temperature [24]. A schematic illustration of the major slip planes and directions, namely basal, prismatic and pyramidal, are shown in Figure 3.

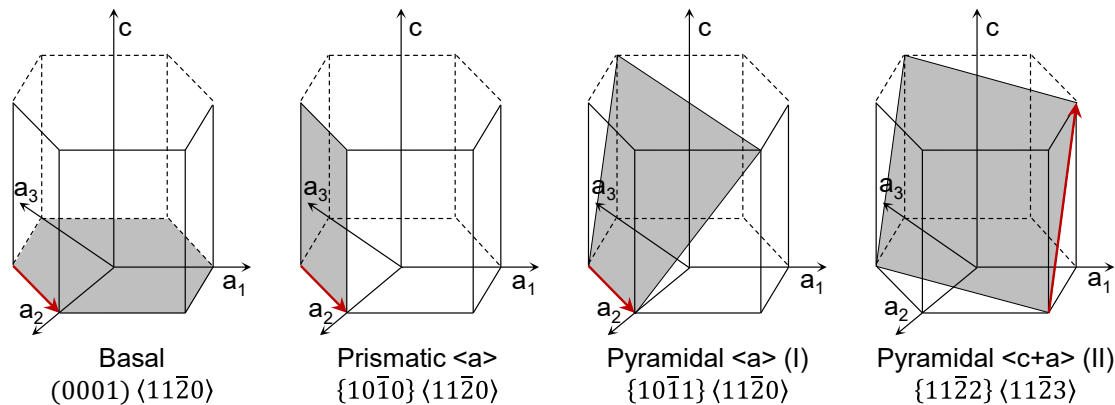


Figure 3. Schematic illustration of major slip systems of magnesium. Adapted from [25].

To initiate slip and, thus, dislocation movement, a critical shear stress (CRSS) value is necessary. The resolved shear stress describes the shear component along a slip plane that is neither perpendicular nor parallel to the stress axis and is related to the applied stress by the Schmid factor [26]. Additional slip systems, such as prismatic slip and the dislocation movement on the first order pyramidal planes, are more difficult to activate. These slip systems have a higher CRSS at room temperature and allow deformation only in  $\langle a \rangle$  direction. Figure 4a shows the CRSS of the mentioned slip systems in pure Mg.

At room temperature, dislocation slip occurs along basal planes in  $\langle a \rangle$  direction, more precisely the basal plane (0001) in  $\langle 11\bar{2}0 \rangle$  direction, and exhibits by far the lowest CRSS of all deformation mechanisms [27,28]. Therefore, it is the dominant deformation mechanism at room temperature. The second order pyramidal slip additionally allows deformation in  $\langle c \rangle$  direction; this is the reason why this type is referred to as  $\langle c+a \rangle$  pyramidal slip. Biswas et al. estimated by simulation that the CRSS for prismatic and  $\langle a \rangle$  pyramidal slip is 12 times and  $\langle c+a \rangle$  pyramidal slip I and II is 10 times larger than basal slip [29]. Therefore, regions of high stress concentration, such as grain boundary triple points or dislocation pile-ups, are necessary to activate these slip systems [30].

A temperature increase is another way to activate additional slip systems due to a decrease in CRSS. Therefore, ductile deformation of pure magnesium is only possible above 225 °C [31]. Figure 4b summarizes different deformation behaviours and occurring microstructural effects as a function of temperature and strain. Additionally, Agnew and Dyugulu confirm that a temperature rise of 100 °C can increase the total elongation by a factor of two to three [32].

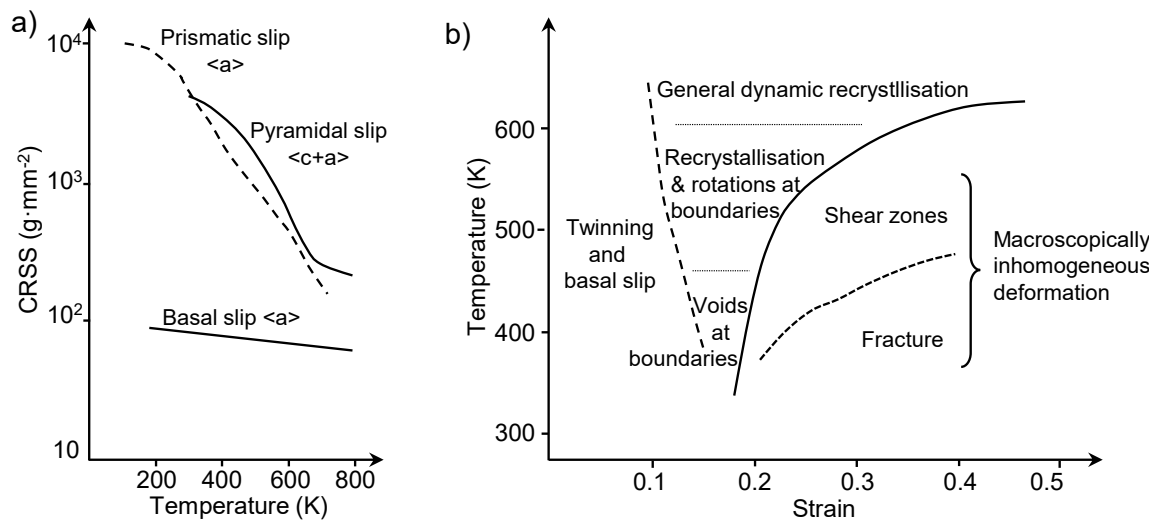


Figure 4. a) Critical resolved shear stress (CRSS) for various slip systems in pure Mg. b) Deformation behaviour of pure Mg as a function of temperature and strain. Adapted from [28].

Besides slip, another important deformation mechanism of Mg is twinning. The extent of the shear and thus the twinning depends on the  $c/a$  ratio. Due to the lower  $c/a$  ratio of 1.624 compared to the ideal ratio of 1.633, the crystal elongates in  $[0001]$ -direction perpendicular to the basal plane during twin formation, while shortening in the other directions [24]. In case of compression twinning, the twin reorients nearly parallel to the compression axis [30]. At the same time, dislocation structures, basal loops and stacking faults are formed due to twinning, which are responsible for hardening [33]. Grain boundary sliding sets even at low macroscopic strains [34].

In contrast to compression, tension cannot trigger twinning in the same way. The twins are mainly formed on twin planes of type  $\{10\bar{1}2\}$  and result from the atom rotation parallel to the plane of type  $\{1\bar{2}10\}$  in the shift direction of  $\langle 10\bar{1}1 \rangle$  [21,24], while compressive stress leads to an atom rotation perpendicular to the  $c$ -axis [35].

### 2.1.2. Development of texture

In a polycrystalline material, the distribution of the crystallographic orientations of grains describes its texture. The grain orientation can be changed by activating slip and twinning depending on compression or tensile stress [36–38]. A strong texture is observed when most of the grains are oriented anisotropically, whereas in a weak texture the grains are isotropically oriented.

Since Mg exhibits an almost ideal  $c/a$  ratio, it is often assumed, that it develops an ideal basal texture. However, it was shown that a slight tilt of the  $c$ -axis (off-basal texture) by  $\pm 20^\circ$  is typical, which can be attributed to the activation of non-basal slip modes [30].

There are differences in the alignment between compression and tension as well as in slip and twinning modes. In compression, the normal of the active slip plane rotates towards the compression axis and the grains orient along the c-axis [39], whereas the basal plane aligns perpendicularly to the deformation direction creating the (0001) basal texture as shown in Figure 5 [21]. In contrast in tension, the active slip direction aligns parallel to the applied stress [39].

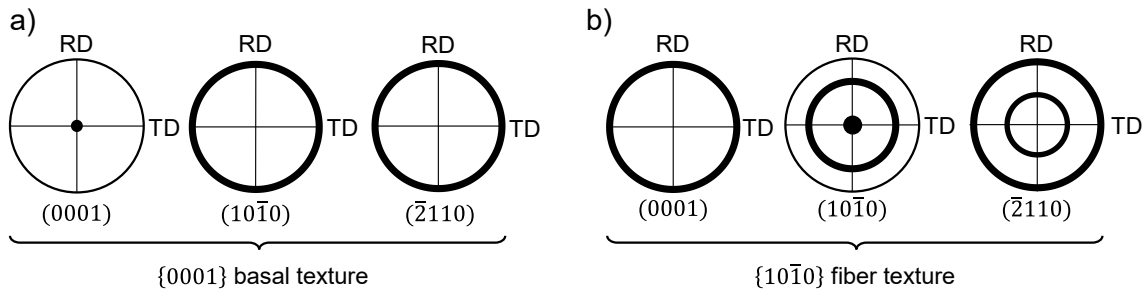


Figure 5. Ideal pole figures of a) the {0001} basal and b) {10 $\bar{1}$ 0} fiber texture of Mg. Adapted from [40].

The texture is also highly affected by processes such as rolling and extrusion, where the fibre texture is typically created by the aligning of (10 $\bar{1}$ 0) prismatic planes parallel to the process direction [41]. However, the resulting strong tensile-compression asymmetry significantly influences the application of pure Mg.

The tensile-compression asymmetry can be weakened by weakening the texture using precipitates and reinforcements. This keeps ductility and strength at a high level. Figure 6a shows the resolved shear stress (RSS) as a function of the grain orientation. The c-axis of the hexagonal crystal structure is aligned parallel to the normal direction, resulting in a low RSS and a strong texture. By tilting the grains out of the c-axis and thus weakening the texture, a higher RSS is necessary to activate slip, which favours prismatic and pyramidal slip leading to an increase in ductility, as visualized in Figure 6b. Therefore, the production of metal matrix composites (MMC), or in this case magnesium matrix composites with a refined grain and thus random grain orientation leads to improved strength and ductility.

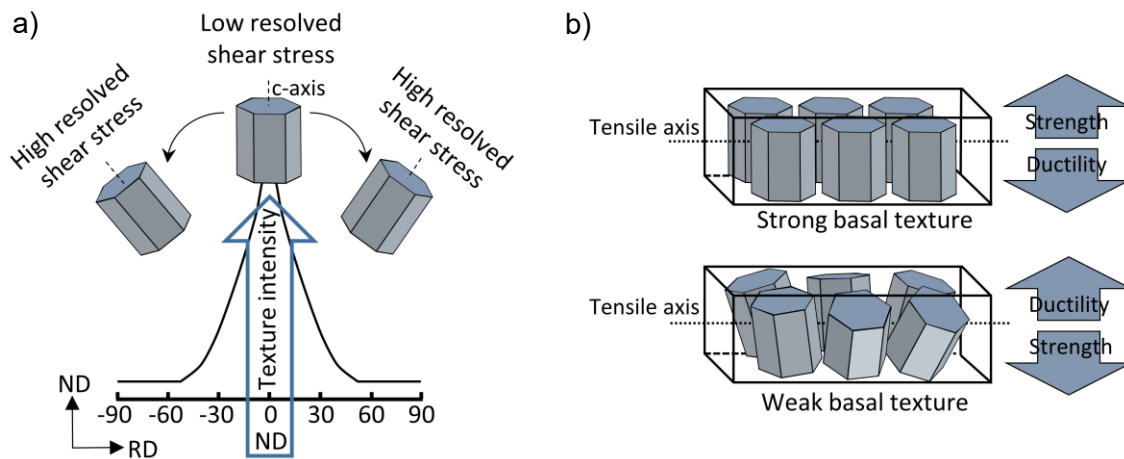


Figure 6. a) Resolved shear stress as a function of the grain orientation. An alignment of the c-axis in normal direction (ND) favours basal slip (RD: rolling direction); b) a strong basal texture increases strength but decreases ductility, and vice versa for a weak basal texture. Adapted from [42].

## 2.2. Metal matrix composites (MMCs)

Metal matrix composites (MMCs) consist of a metallic matrix phase and a reinforcing phase. Among others, MMCs are used in aviation and automotive industry [11]. The aim of an MMC is to combine the favourable properties of the metal matrix and the reinforcing phase. Aluminium, titanium and steel are the most commonly used matrix materials, while Mg is still seldom employed due to its brittle behaviour at room temperature. However, through reinforcing Mg, different glide systems are activated, as explained above, leading to a significant improvement in mechanical properties.

### 2.2.1. The effect of reinforcements

In general, metals, polymers and ceramics are typical reinforcements that can exist in different morphologies such as particles, fibres and whiskers. In case of metal matrices, particles are best suited as reinforcement phase, since the production of particle-reinforced composites is easier and more cost efficient compared to fibre- and whisker-reinforced-composites. In terms of the reinforcement material, polymers and ceramics have a low density, which is advantageous for lightweight constructions. Additionally, it has been proven that the strength of the composite itself can be changed significantly when using ceramic particles, due to their higher strength. The functionality of the reinforcements is affected by their size, shape, volume fraction, and their distribution within the metal matrix [43–46]. The fracture strength is inversely proportional to the square of the particles size [47]. In case of ceramic reinforcements with a high elastic modulus, elastic modulus and hardness increase linearly in MMCs with increasing reinforcement content [48]. Yield strength and ultimate tensile strength increases as well [7], while ductility often decreases [49]. However, a homogeneous distribution of

reinforcement particles is important to achieve these improvements. The homogeneous distribution is especially difficult when using nanoparticles, which tend to cluster due to their high specific surface area and the interacting van der Waals forces [50]. The higher the cluster formation, the lower the stress at which the composite breaks due to micro crack initiation on particles clusters [51]. A homogeneous distribution of nanoparticles may achieve the same improvements as micron particles even with a lower reinforcement content [52]. Because nanoparticles have a higher relative surface energy compared to microparticles, nanoparticles tend to adhere better, which is the reason why fewer defects occur. Another reason is the higher fracture toughness compared to microparticles, which highly decreases particle fracture and interface cracking during processing [14].

Good adhesion of the reinforcing particles to the Mg matrix leads to excellent stress transfer and is described by the so-called "load-bearing effect". The effect is associated with an increase in strength, microhardness and elastic modulus of the composite [53,54]. The load-bearing effect further improves with decreasing grain size, which is the reason why nanoparticles often have the best load-bearing capacity compared to micron particles [55].

Since the increase in strength is related to a hindered movement of dislocations, different strengthening mechanisms are claimed to be responsible for the increased strength in particulate reinforced composites, due to grain refinement and particle size of the reinforcements:

- i) Orowan mechanism [55–57]:  $\tau_{OR} \approx \frac{G \cdot b \cdot \sqrt{f}}{r}$ ;
- ii) Dislocation density strengthening [14,58];
- iii) Hall-Petch strengthening [35,59]:  $\sigma_y = \sigma_0 + \frac{K_y}{\sqrt{d}}$ ;
- iv) Mismatch in coefficient of thermal expansion (CTE) [60,61].

In nanocomposites, these mechanisms interact and influence each other. Figure 9 shows a schematic illustration of the three stages of the Orowan bypassing mechanisms, which is a particle-induced strengthening mechanism and especially significant in nanocomposites with homogeneously distributed nanoparticles smaller than 100 nm. When approaching the particles, the dislocation line bends and bypasses the particles if the stress is high enough, leaving a dislocation ring around the bypassed particles. This pinning effect can be described by the shear stress  $\tau_{OR}$ , which depends on the shear modulus  $G$ , the Burgers vector  $b$  and the distance between the impenetrable particles, depending on the volume fraction  $f$  and the radius  $r$  of the particles. However, the Orowan strengthening increases with decreasing particle size until it reaches a critical value  $r = 1.7$  nm below which it drops abruptly [55].

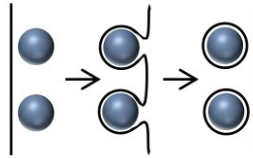


Figure 7. Schematic illustration of Orowan strengthening.

With decreasing particle size, the dislocation density increases [33,35]. Furthermore, a closely spaced position of nanoparticles within the MMC increases the resistance to passing dislocations, which results in dislocation pile-up. The resulting dislocation density strengthening is schematically illustrated in Figure 8. Round particles are located in grains and at grain boundaries, where dislocation, represented by black lines, have accumulated. Dislocation density strengthening is characterized by the accumulation of dislocations, which often move on different slip planes and act as barriers, thus preventing each other from moving further through the grain. Consequently, a higher stress is needed to activate other slip planes in order for the dislocations to move further.

Since small particles must be bypassed by the dislocations, they act as additional barriers for them. Additionally, local plastic deformation and thus dislocations occur around the nanoparticles in the Mg matrix, which are ascribable to the significant difference between the elastic modulus of the nanoparticles and the matrix. The rest of the matrix deforms elastically up to a certain stress [61].

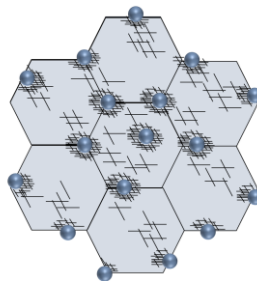


Figure 8. Schematic illustration of the dislocation density strengthening.

Figure 9 shows a scheme of the Hall-Petch strengthening, also called grain boundary strengthening. This mechanism is based on the misorientation of neighbouring grains. Dislocations can no longer slide on their slip planes, due to the defects and the altered shear stress required to overcome the grain boundaries, which is the reason why they accumulate at them. Furthermore, the accumulate dislocations create a stress field, which hinders the following dislocations from gliding. The larger the misorientation, the greater the inability to move. In large grains, more dislocations can accumulate, resulting in a greater driving force to initiate dislocation movement in the neighbouring grain due to the higher path length, the higher amount of accumulated dislocations and thus the higher stress concentration. As a result, a small grain size hampers dislocation

movement more effectively. Yet, a larger amount of grains increases the possibility that favourably oriented neighbouring grains exist, so that dislocations can continue to move. In contrast to the other strengthening mechanisms, which cause a decrease in ductility, grain refinement result in an increase in ductility [62].

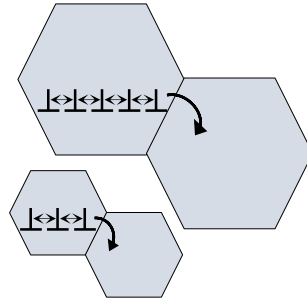


Figure 9. Schematic illustration of the Hall-Petch strengthening (grain boundary strengthening).

According to the Hall-Petch relationship, yield stress  $\sigma_y$  is inversely proportional to the square of the grain size  $d$  and depends on the strengthening coefficient  $K_y$  and on the starting stress for dislocation movement  $\sigma_0$  [35,59]. A high plastic deformation can lead to the formation of subgrains and afterwards to a reduction of grain size. Furthermore, because of their incoherence with the Mg matrix, nanoparticles effectively pin grain boundaries and hinder grain growth during processing, leading to an increase in ductility [63]. In addition to the fact that fatigue strength can also be improved, the greatest advantage of nanocomposites lies in the simultaneous increase in strength and ductility, while the density remains almost the same [33,61].

Depending on the crystal structure and CTE of both matrix and reinforcement, a mismatch at the interface can also lead to an increase in strain hardening, due to dislocation formation [60,61]. However, Redsten et al. [64] investigated alumina-dispersion-strengthened aluminium and suggested that the mismatch of the linear CTE too small to have a significant effect when a critical particle size  $d^*$  is reached. The critical particle size is described by the equation:  $d^* = b/(\Delta\alpha \cdot \Delta T)$ , where  $b$  is Burgers vector,  $\Delta\alpha$  the difference of the linear expansion coefficients and  $\Delta T$  the difference in temperatures at which the slip begins, but the diffusion has not begun yet. In case of Mg-SiC, all values are known ( $b=0.32$  nm [65],  $\Delta\alpha=22 \cdot 10^{-6}$  K $^{-1}$ , and  $\Delta T=165$  K [66]) and the critical particle size  $d^*$  is approximately 88 nm.

### 2.2.2. SiC as particle reinforcement

To produce a Mg nanocomposite, silicon carbide (SiC) as a stiff and strong material with a low density of 3.2 g/cm $^3$  is a good choice. SiC occurs as  $\alpha$ -SiC in a hcp structure [67] and as  $\beta$ -SiC in a face-centred cubic (fcc) structure [68]. In contrast to Al $_2$ O $_3$  and Y $_2$ O $_3$ ,

only one study conjectured that SiC could react with the Mg matrix to form  $Mg_2Si$ , but this could not be proven [69]. The thermally stable behaviour is a further advantage of SiC, since it prevents reactions with the Mg matrix and consequently the formation of secondary phases. With a high elastic modulus (460 MPa) and a relatively low CTE of  $3.2 - 5.1 \cdot 10^{-6} \text{ 1/K}$  (298-1273 K) [70], SiC is suitable to increase the strength in the MMC and ensure a good adhesion to the Mg matrix [51]. The average CTE of the nanocomposite is then reduced with increasing volume fraction of SiC nanoparticles, which is due to the constraining effect of the expansion by the nanoparticles [51]. The strengthening effect occurs, however, only above a critical volume fraction of nanoparticles, which was observed by Friend in aluminium composites [71]. Below the critical value, composites have lower strength compared to the unreinforced metal matrix. Subramanian et al. investigated Mg-SiC nanocomposites and determined a minimum volume fraction of 0.27% SiC nanoparticles, which is required to increase compressive and tensile strength [58]. In addition, nanoparticles increase the wear rate up to two orders of magnitude in comparison to pure Mg [72].

### 2.3. Processing routes

Metal-matrix composites can be produced by various processing techniques, which can be classified into liquid phase and solid phase processes. Typical processing routes with their sub-processes for Mg matrix composites are shown in Figure 10, whereby stir casting and squeeze casting are considered as liquid phase processes and powder metallurgy as solid phase process.

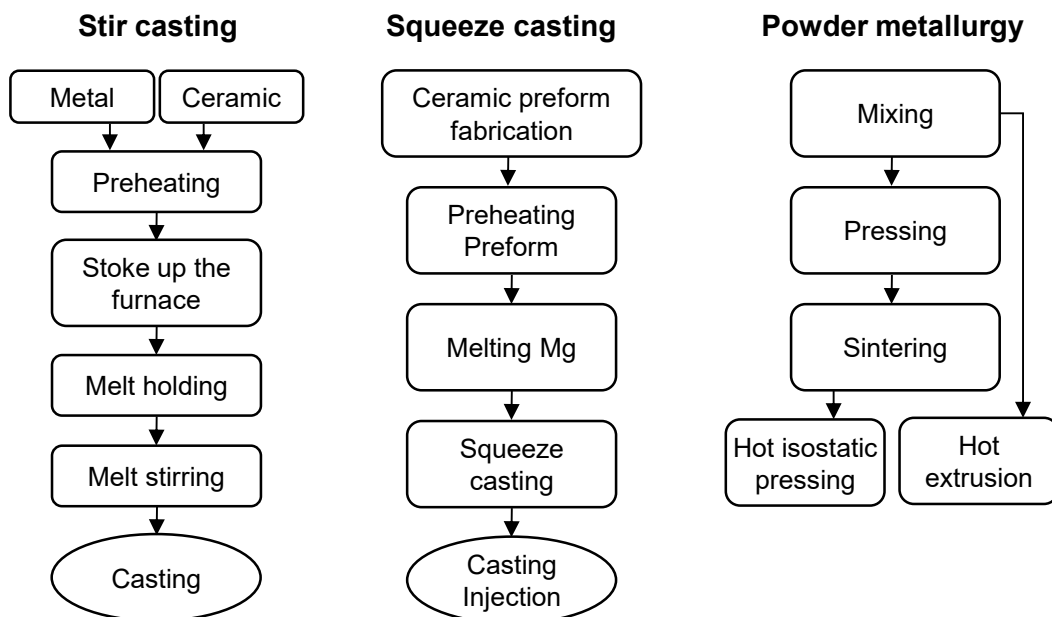


Figure 10. Typical processing routes for Mg matrix composites. Adapted from [2,53].

In the case of liquid phase processes, the reinforcing phase is given into the molten metal matrix and the mixture is usually processed through a casting process, including melt infiltration and melt oxidation processes [61], stir casting [73], squeeze casting [74]. The advantage of these methods is the production of complex near-net-shape composites. A major concern is the segregation of reinforcing particles at grain boundaries especially during solidification and the entrapment of gases and unwanted inclusions during the process. Also, second phases are likely to be formed [75,76]. Yet, these technologies are not cost effective enough to produce a large volume of nanocomposites. Furthermore, the reproducibility of the microstructure and thus the properties of the composites are difficult to achieve by liquid phase processes [61].

The production of the composite by solid phase processes, such as powder metallurgy (PM) [7,69], spray deposition [43], and injection moulding [77], is more complicated but offers several advantages. Powder metallurgical production offers a reliable stable reproducibility, due to the multitude of adjustable parameters. It is also more cost-effective and the material loss as well as the post-processing of the produced parts are lower compared to liquid phase processes. When manufacturing nanocomposites, a homogeneous distribution of SiC nanoparticles within the metal matrix is important. Therefore, the powder metallurgy (PM) technique seems to be most appropriate.

### **2.3.1. Powder metallurgy**

The powder metallurgy (PM) route can handle almost any type of material and large volumes of nanoparticles that can be integrated into the matrix. Using the PM route, the grain size distribution can be better controlled through various parameters. In addition, interfacial reactions between particles and matrix are reduced compared to casting processes, due to the lower temperatures during the powder metallurgical process. In the production of nanocomposites, PM offers a broader range of sub-processes, with which nanoparticle clusters can be broken up. These sub-processes can be combined according to the requirements. The main sub-processes are presented in Figure 10. Mixing includes mechanical milling of the powder in order to reduce particle size and distribute nanoparticles homogeneously. Pressing includes uniaxial and cold-isostatic pressing (CIP). If defined component edges are required, the powder is first pressed uniaxial followed by CIP. Otherwise, the powder is directly pressed in a rubber mould using CIP. Sintering includes various methods such as gas pressure sintering and spark plasma sintering, whereby additional pressure is applied to the samples. In addition to pressureless liquid phase sintering, however, conventional solid phase sintering is carried out in most cases. Further densification is achieved by hot isostatic pressing, where a relatively high pressure is applied compared to the other sintering methods. Hot

extrusion is usually carried out with powder as starting material, but can also be used in the compacted state. In addition to a deformation of the material, which leads to a texture, hot extrusion is usually accompanied by an increase in density.

### 2.3.2. Mechanical milling

The principle of a planetary ball mill, which is employed for high-energy mechanical milling, is shown in Figure 11a. The milling containers fulfil two superimposed-movements: the self-rotation and the rotation around the centre. Milling balls are used to process the powder in the milling container. Thereby, milling balls rotate in the container and deform the powder between them and between the container wall (Figure 11b). Ceramic milling balls provide the highest strength and wear resistance to prevent mixing of abrasive particles from the balls with the powder. The higher the ball-to-powder ratio (BPR), the more effective the milling process, as the number of collisions per time unit increases [78].

Depending on the material composition, a BPR between 10 and 40 was employed in several studies, while Abdellahi et al. have determined through simulations a BPR of 26:1 as the optimal value [79]. Often, a process control agent is utilised to prevent excessive cold welding. According to the BPR, Abdellahi et al. determined a weight percentage of 1.64 as the optimum value of the process control agent. Further, initial differences in particle size of the different powders can be compensated through a longer milling time [50].

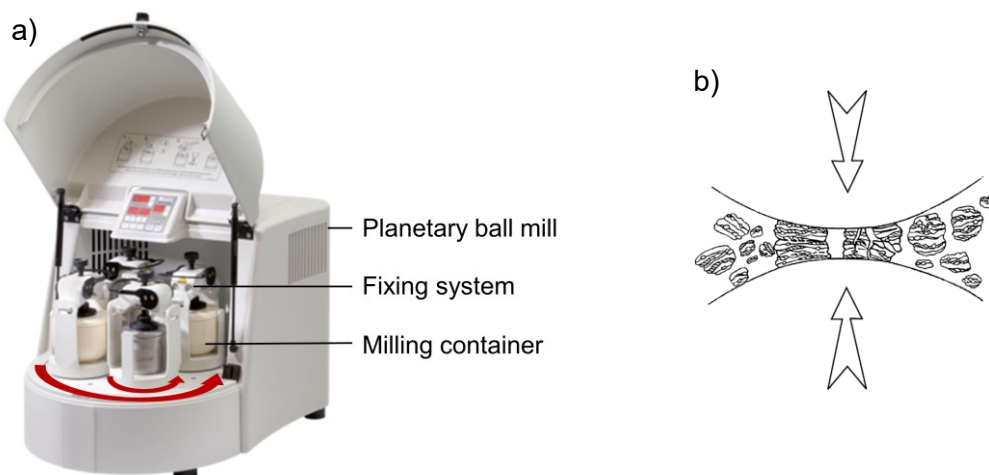


Figure 11. a) Planetary ball mill, red arrows describe the direction of rotation. The milling containers fulfil two superimposed-movements: the self-rotation and the rotation around the centre (adapted from [80]); and b) schematic illustration of a ball-powder-ball collision of a powder mixture. Reproduced from [57].

Mechanical milling also allows various materials to be welded together. This offers the possibility of producing metal-matrix composites by integrating ceramic particles into the metal matrix, as is the case of Mg-SiC nanocomposites. Since nanoparticles tend to

cluster, the high shear stress during mechanical milling helps to distribute the nanoparticles homogeneously in the matrix [76]. During the process, the Mg and SiC powder particles undergo different stages, as shown in Figure 12. Initially, the Mg powder particles are flattened and the SiC nanoparticles are pressed into the matrix, whereby composite powder particles are formed, which contain shear bands with a high dislocation density. This is due to generated friction stress around the nanoparticles, leading to a more heavily deformed Mg matrix than pure metal. Such a friction stress additionally favours recrystallization during the milling process leading to grain size refinement. Therefore, independently of temperature, milled composite powder has higher strength but lower ductility than non-milled powder [69].

With increasing milling duration, the composite powder particles begin to weld together and form agglomerates. While the powder particle size increases, the nanoparticles are far-flung distributed. Subsequently, the particles undergo repeated breaking and cold welding, which leads to a reduction in composite powder particle size [81]. Breaking and cold welding occur simultaneously, with a large extent of annihilation, recombination and formation of dislocations. Small-angle grain boundaries are formed and subgrains develop, which leads to a random grain orientation [82]. The milled composite powder exhibits a higher number of grain boundaries, and thus particle sizes in the range of a few nanometres with increasing reinforcement content. A steady state of breaking and cold welding is reached when multiplication and annihilation of dislocations are in equilibrium. Consequently, particle size and morphology reach a steady state with no further significant changes. The most homogeneous distribution of nanoparticles is achieved at this stage.

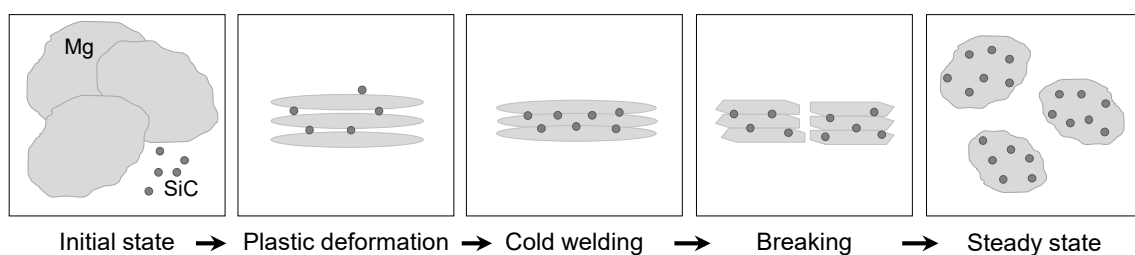


Figure 12. Schematic illustration of the different powder stages during mechanical milling. Adapted from [83].

### 2.3.3. Cold-isostatic pressing (CIP)

During cold-isostatic pressing (CIP), an isostatic pressure is applied onto the material, such that the powder particles are uniformly compressed and, due to mechanical interlocking, form a green body. If mechanical interlocking is insufficient, a polymer binder or wax is added during the mixing or milling process to hold the powder particles together. Figure 13 shows the wet-bag method, which is particularly suitable for small

quantities. For the wet-bag method, the powder is sealed airtight and placed in an elastic mould. The mould is then placed into a pressure chamber, which contains a pressure medium, usually water or oil. The stem pushes the piston towards the pressure medium, which distributes the pressure isostatically to the rubber mould and thus to the powder. In addition to the amount of powder itself, the thickness of the elastic mould has a significant influence on the compaction of the powder [84]. Yang et al. found that the highest density could be achieved using an elastic mould with a wall thickness of 5 mm [85]. In comparison to uniaxial pressing, non-symmetrical and more complicated shapes can be produced in addition to a more homogeneous compaction [84].

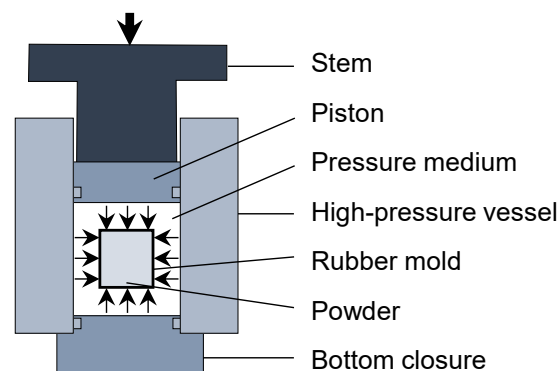


Figure 13. Schematic illustration of cold-isostatic pressing using direct pressurization. Adapted from [86].

The densification during CIP mainly depends on the compressibility of the metal powders, which is strongly influenced by powder particle morphology, size and size distribution as well as plastic deformability. Densification takes place in three stages. In the first stage the powder particles are rearranged and packing density increases [87]. This is followed by elastic-plastic deformation at interparticle contact areas, while the coordination number (number of contacts) continues to increase in the second stage. Thus, as pressure increases, porosity decreases [88,89]. In addition, cold welding and/or mechanical interlocking take place at higher pressures, whereby brittle powder particles fracture and rearrange.

The degree of densification is influenced by powder morphology in such a way that initial flake-like powder morphology can result in larger cavities between the powder particles but also provides a larger contact area during pressing and usually a high potential for plastic deformation [52]. In contrast, equiaxed powder particles exhibit a small contact area between the powder particles, which makes the stress transfer and thus the particle rearrangement and plastic deformation more difficult. Nanoparticles enhance the plastic deformation of composite powder particles with increasing reinforcing content during mechanical milling. The resulting high hardness and low ductility of the nanocomposite

powder particles can hinder additional plastic deformation during the subsequent consolidation [8].

At pressures above 1 GPa and densities above 95 %, massive deformation occurs in the third stage [89], leading to a reduction in pores size so that only small pores remain between the powder particles. Since plastic deformation is the main compaction mechanism of the third stage, high compaction with densities above 95 % is difficult to achieve with highly deformed powder particles. Therefore, powder compacts containing nanoparticles usually show a higher level of porosity and more irregular pores with a broader pore size distribution compared to non-reinforced metal, as shown in lead-free Sn-0.7Cu/Al<sub>2</sub>O<sub>3</sub> nanocomposites by Zhong and Gupta [90]. Furthermore, the larger number of pores can lead to a larger stress in the material, which can significantly decrease the strength of nanocomposites [5,91,92] resulting in faster failure [93].

#### **2.3.4.Sintering**

The process of sintering is a heat treatment process, which compacts powder particles due to physical processes and thereby significantly reduces the porosity. The process is driven by the reduction of free surface energy of the powder particles. This is done by reducing the areas of all free outer and inner surfaces such as grain boundary surfaces and surfaces of open and closed pores, leading to an annihilation of structural defects and the formation of large angle grain boundaries due to interparticle contacts [94].

The green bodies are usually sintered under protective gas, such as H<sub>2</sub>, Ar, and He, or in vacuum. However, Ar and He are expensive, which is why these gases are employed only when reactive powders are sintered. The reason for using protective gases is the high tendency of metal powders to oxidise. Oxide layers on the powder particle surface reduce the material transport between the particles [94]. In addition to material transport, trapped gas, present between the powder particles in closed pores from powder compaction, also influences the sintering. Homogeneous sintering depends on whether gases can diffuse through the metal, are insoluble in the metal, or can form a compound with the metal [95]. In contrast, gas can easily escape from open pores such as those on the sample surface, causing the surface to sinter faster than the centre.

The sintering process itself consists of a heating phase, an isothermal holding time at about 0.7 to 0.9 of the melting temperature and a slow cooling phase to room temperature [94]. In most cases, during the heating phase, a debinding step is carried out at lower temperatures to pyrolyse additives such as polymer binder, wax or lubricants. Several sub-processes take place, which depend, among other factors, on temperature and time. These sinter processes are very often explained using a two-

particle model, as shown in Figure 14a. Typical material transport mechanisms during sintering are volume and surface diffusion, including lattice and grain boundary diffusion, as well as viscous flow, evaporation, and condensation [96]. The pores try to reach their lowest energetic state and deform to minimise surface area, causing the bulk material to shrink as shown in Figure 14b.

Figure 14c shows the different sinter stages. At the initial stage, the density increases slowly with increasing temperature and time and sinter necks are formed between the powder particles leading to grain boundaries. The largest density increase is achieved during the intermediate stage by viscous flow and diffusion processes leading to interconnected pores within a narrow temperature and time range. In the final stage, the pores are isolated and no significant improvement in porosity can be achieved even with a longer holding time. Moreover, recovery of the grains occurs within the material, which can eventually lead to recrystallization, if defect density and thermal activation are sufficient [97].

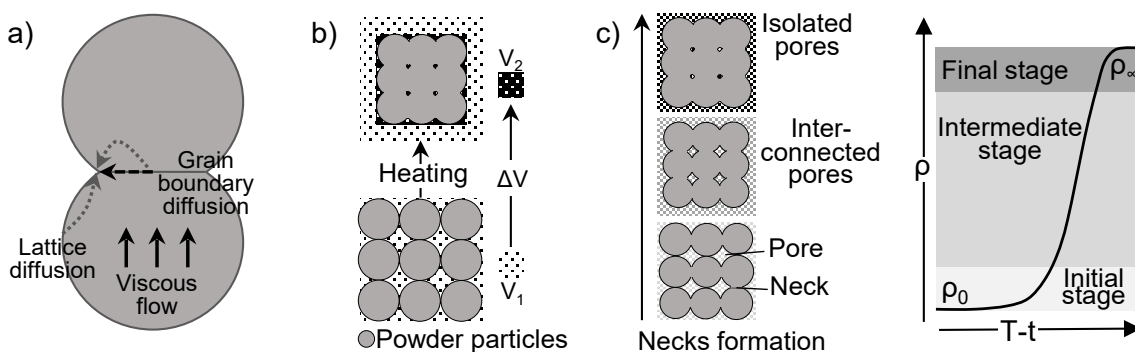


Figure 14. Schematic illustration during sintering of a) material transport mechanisms, b) volume shrinkage and c) sintering stages and specific features during densification. Adapted from [98].

### 2.3.5. Hot isostatic pressing (HIP)

In order to meet higher demands in terms of density, strength, and ultimate strain, hot isostatic pressing (HIP) is employed [94]. During hot isostatic pressing (HIP), the material is simultaneously exposed to high temperature and high gas pressure to obtain completely isotropic material properties. HIP can be employed to compact powder or to further densify pressed and sintered parts. Thereby, temperatures between 100 and 2000°C and pressures between 100 and 200 MPa are usually employed [99]. One concern is to eliminate the porosity. A schematic illustration of the HIP setup is shown in Figure 15. If a simple shape is required, the powder must be sealed in a metal mould, so that the pressure can be transferred to the powder. For complex shapes, it is easier to cold press the powder first with a rubber mould and then sinter it before using HIP.

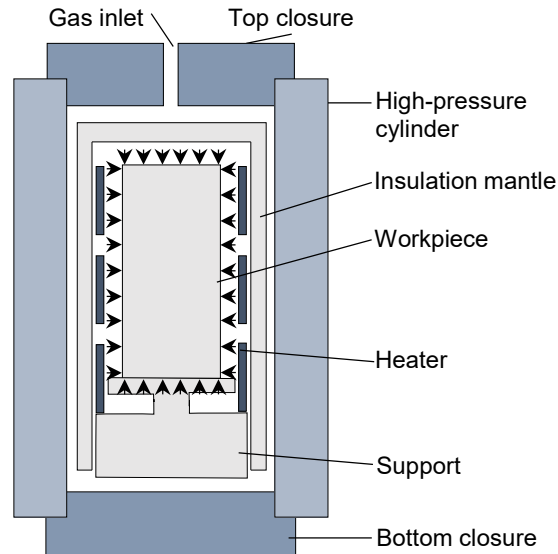


Figure 15. Schematic illustration of hot isostatic pressing setup. Adapted from [100].

In this way, it is possible to produce materials in all shapes and sizes with HIP. Compacts should have closed pores at the sample surface and densities greater than 95 % to minimize the internal pressure of the gases trapped in the pores and to prevent a resulting overpressure [101]. Due to the resulting internal pressure, which depends on the porosity, higher initial densities lead to higher final densities after HIP. Additionally, size and shape of the pores and, thus, the number of initial contact points, just as in the case of CIP, determine whether consolidation is successful [102,103]. With a decreasing number of contact points, densification rate decreases. The elimination of porosity is known to improve fatigue behaviour, creep resistance and ductility, but also achieves an overall reduced scattering of properties [100,104]. As a side note, the sinter-HIP method, which combines sintering and HIP in one process, could be employed to reduce oxygen contamination. However, the method is rather difficult to control due to the complexity of the parameters and the long process time.

### 2.3.6. Indirect hot extrusion

During extrusion, the material, usually encapsulated powder, is forced through a die and thus deformed. Compared to sintering, hot extrusion requires a lower temperature as a higher pressure is applied at the same time, thus reducing the overall process time [84]. Hot extrusion can be performed as direct or indirect process. The advantage of indirect extrusion over direct extrusion is that the billet does not move relative to the container, which means that friction is significantly reduced and therefore less pressure is required and the temperature remains relatively constant [105]. Figure 16 illustrates the indirect hot extrusion process. With indirect hot extrusion, an extruded rod with fewer defects can be produced, since the difference in flow speed between the inner and outer material is

significantly lower [105]. Further, the edge of the die is designed so that the angle of the edge determines the extrusion pressure. A smaller angle increases the homogeneity of the deformation, however lower extrusion pressures must be applied.

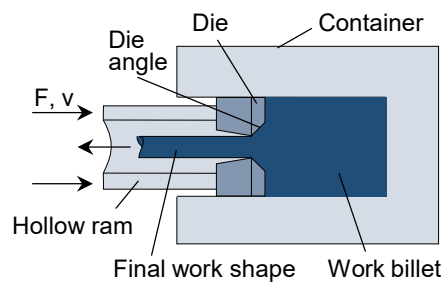


Figure 16. Schematic illustration of the indirect extrusion process. The die is pushed in the work billet, therefore reducing friction on the walls and, thus, keeping the temperature stable. Adapted from [106]

Hot extrusion significantly alters the microstructure, hence the process is employed to further reduce the porosity and, in case of nanocomposites, to distribute the nanoparticles more homogeneously in the matrix [48]. In principle, a homogenous distribution leads to a finer grain size distribution due to the pinning effect of the nanoparticles, as is the case for mechanical milling.

Since the surface of the extruded rod cools faster, a homogeneous microstructure depends on the dimensions of the rod [107]. The high shear stress also leads to a high interfacial strength between matrix and reinforcing particles and thus to a high tensile strength [48]. In addition, the shear stress further breaks up particle clusters that have not yet been broken up by mixing or mechanical milling and ensures a better distribution of the particles within the matrix [18]. However, if the plastic deformation of the work billet is too high, the shear stress can lead to layer formation and detachment of the interface between metal matrix and reinforcing particles.

In the early stages of extrusion, different deformation modes including twinning are activated. However, twins disappear in a later stage, where dynamic recrystallization (DRX) is observed [41]. Studies have shown that pre-twinning, for example by cold pre-forging [108], can improve the ductility of Mg, which is due to twins acting as nucleation sites for DRX during the subsequent process, such as rolling, forging or extruding [109].

Regions with deformed grains are called shear/deformation zones and are ideal sites for the development of DRX nuclei. This effect is relatively weak and becomes stronger with increasing reinforcement content, because nanoparticles additionally act as nuclei [73]. Overall, a microstructure with smaller grain size and a random and therefore weaker texture is created during extrusion [110,111] compared with the sintered state. However, little is known about the influence of SiC nanoparticles on the pure Mg matrix during extrusion process, which were previously produced by powder metallurgy.

Typically a  $\langle 10\bar{1}0 \rangle$  fibre texture parallel to extrusion direction (ED) is prevalent, which weakens with increasing reinforcement content [112]. Besides DRX, this is due to the material flow of Mg around the nanoparticles, which changes the initial orientation [51]. Further, with increasing extrusion temperature, yield strength and tensile strength improve and the recrystallized grains are coarsened [113]. If the temperature is high enough, defect structures such as dislocations can be healed, due to recrystallization of heavily deformed grains [91].

## **2.4. Mechanical properties of Mg-SiC nanocomposites**

This chapter provides an overview of the mechanical properties including quasistatic behaviour, nanoindentation, and fatigue behaviour of Mg-SiC nanocomposites processed by different liquid and solid phase processes. During quasistatic loading, the load is applied slowly, without impact and steadily increasing until specimen failure. A differentiation is made between the behaviour under tensile and compressive loads. Cyclic loading is defined by an alternating load, independent of the frequency and the algebraic sign, since the applied load can only be in the tensile or compression range. The selected stress ratio depends on the prospective application.

### **2.4.1. Quasistatic loading**

#### **2.4.1.1. Compressive behaviour**

Compression tests are mainly employed to determine the flow curve of brittle metals. Compared to pure Mg, Mg-SiC nanocomposites are characterised by a strong relationship between damage and reinforcement content. If SiC particle clusters are present, the dominant damage mechanism changes from particle fracture at low local volume fraction to void formation at clustered regions [93]. In comparison to tensile loading, however, finite element simulations suggest that the higher number of voids generated during compressive loading do not grow significantly. This means that the influence of particle clusters on the fracture behaviour is not as significant as under tensile loading.

Subramanian et al. investigated the compressive behaviour of a Mg-5 wt% Nb metal-metal composite reinforced by 0.13 vol% up to 1.1 vol% SiC nanoparticles. The ultimate compressive strength (UCS) increased from 287 MPa to 315 MPa, while the 0.2% compressive yield strength (CYS) increased from 62 MPa to 106 MPa. Compared to pure Mg with a UCS of 273 MPa and CYS of 74 MPa, the UCS was improved, while the CYS decreased with low reinforcing contents but increased significantly with the addition

of nanoparticles. A reinforcement content of 0.55 vol% already showed an improved CYS. The fracture strain was almost similar for pure Mg and the nanocomposites up to a reinforcement content of 0.27 vol% and decreased from ca. 23 % to 21 % with increasing content; the standard deviation increased [58]. Till now, however, mainly tensile tests have been carried out on Mg-SiC nanocomposites.

#### **2.4.1.2. Tensile behaviour**

Tensile tests are a standardised methods in which materials are subjected to controlled tensile stress until failure. They are employed, amongst other parameters, to determine Young's modulus, yield strength and fracture strain. Especially under tensile loading, nanocomposites require good interfacial bonding of nanoparticles to the metal matrix compared to pure Mg. This is because stress can only be transferred from the matrix to the nanoparticles if there is good interfacial bonding, so that the nanoparticles can also bear the load [114]. The stress concentrated around the nanoparticles can lead to defects at the interface between the Mg matrix and SiC nanoparticles. Both, existing defects at the matrix-nanoparticle interface and newly formed defects lead to reduced tensile strength [115]. With increasing volume fraction of SiC nanoparticles, yield strength (YS) and ultimate tensile strength (UTS) increase. However, fracture strain slightly decreases [7].

So far only a few investigations have been carried out on Mg-SiC nanocomposites. The results are limited to nanocomposites of the most common die casting alloys AZ31 and AZ91, with alloying contents of 1 wt% Zn and 3 wt% or 9 wt% Al (MgAlZn), respectively, and an alloy of Mg and 5 vol% Nb. In order to classify the results, UTS versus fracture strain is compared with pure Mg and the pure alloys. In addition, the tensile behaviour is compared with Mg composites that have been reinforced with SiC micron-sized particles. Only a few of the composites were produced using solid phase processes, such as hot pressing (HP) and microwave sintering (MW). Composites produced using liquid phase processes, such as disintegrated melt deposition (DMD) and semisolid stirring assisted ultrasonic vibration (SAUV), were also displayed in Figure 17. However, all composites have in common that they were extruded in the final manufacturing step.

While non-reinforced Mg and AZ31 achieve a high fracture strain, the large difference between different AZ91 samples illustrates the influence of the production route on the mechanical properties. In case of AZ91 (DMD), a final heat treatment was carried out. The hot-pressed Mg-SiC composites (Mg-SiC<sub>p</sub>) achieve a high UTS, but low fracture strain. The Mg-SiC nanocomposites (Mg-SiC<sub>n</sub>), on the other hand, have a wide fracture strain range, which could be due to their different volume fraction and the alloying

elements of the Mg matrix. These differences can also be observed in the fracture surfaces. While pure Mg has a dominant cleavage fracture, the Mg-5Nb-SiC nanocomposite show also dimple-like features [58].

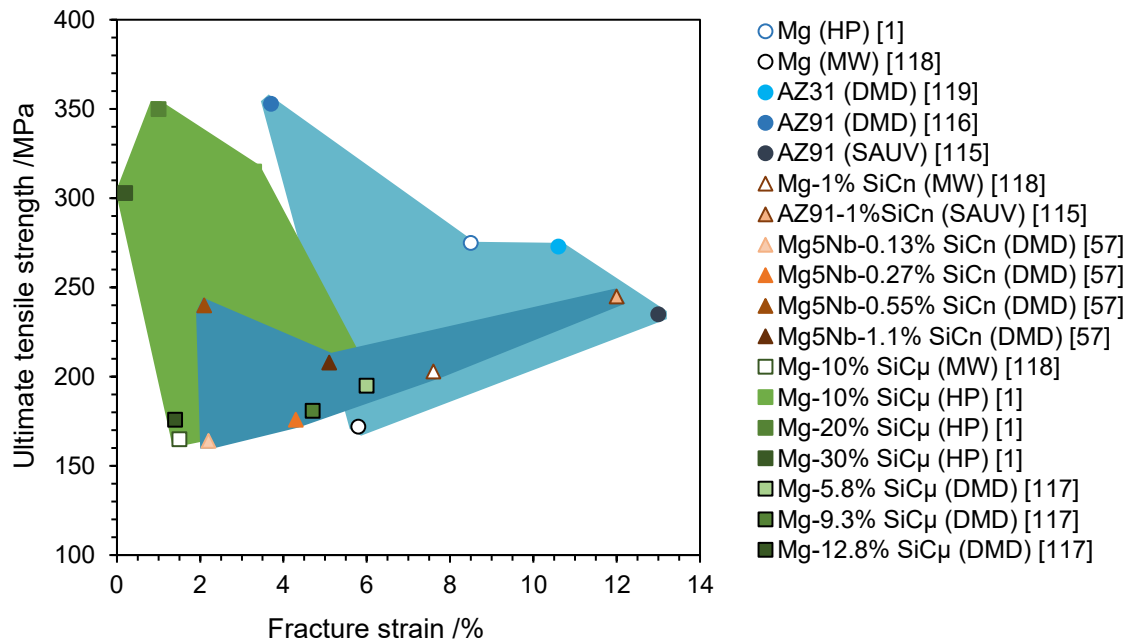


Figure 17. Ultimate tensile strength (UTS) vs. fracture strain of pure Mg, Mg alloys, and their Mg-SiC nanocomposites produced by different processes (HP – Hot pressing; MW – Micro wave sintering; DMD – Disintegrated melt deposition; SAUV - Semisolid stirring assisted ultrasonic vibration) prior to extrusion [1,13,58,116–119]. The legend shows the respective composition, followed by the manufacturing process in parantheses and the reference in square brackets.

### 2.4.1.3. Nanoindentation

Nanoindentation can be successfully employed to locally measure nanohardness  $H$  and elastic modulus  $E$  at micro scale, e.g. [120–122]. An advantage is that, in contrast to the microhardness testing, very small volumes can be sensed and the local deformation behaviour can be investigated [123]. Nanoindentation is therefore particularly suitable for powder particles or small structures, since other tests are not applicable. Usually, a Berkovich indenter is employed to record the load-displacement curves. The effective elastic modulus  $E_{eff}$  follows the relationship between the contact area and the measured unloading stiffness and can be calculated as follows:

$$S = \beta \frac{2}{\sqrt{\pi}} E_{ff} \sqrt{A} , \quad (\text{Eq. 1})$$

where  $\beta$  is a dimensionless parameter accounting for deviation in stiffness and  $A$  is the contact area [124]. To calculate the Young's modulus of the material, elastic displacements of both the specimen and the indenter, has to be taken into account:

$$\frac{1}{E_{eff}} = \frac{1-\nu^2}{E} + \frac{1-\nu_i^2}{E_i}, \quad (\text{Eq. 2})$$

where  $E$  and  $\nu$  are Young's modulus and Poisson's ratio for the specimen and indenter ( $E_i$ ,  $\nu_i$ ), respectively [120].  $E_{eff}$  can thus be used to calculate the Young's modulus of the material.  $E_{eff}$  is also referred to as reduced elastic modulus ( $E_r$ ) in some studies. A typical load-displacement curve is shown in Figure 18a. From the initial portion of the unloading curve, the stiffness  $S$  is experimentally determined using the equation  $S = dP/dh$ , where  $P$  is the load and  $h$  is the displacement [125]. The hardness  $H$  is then calculated using  $H = P_{max}/A$ .

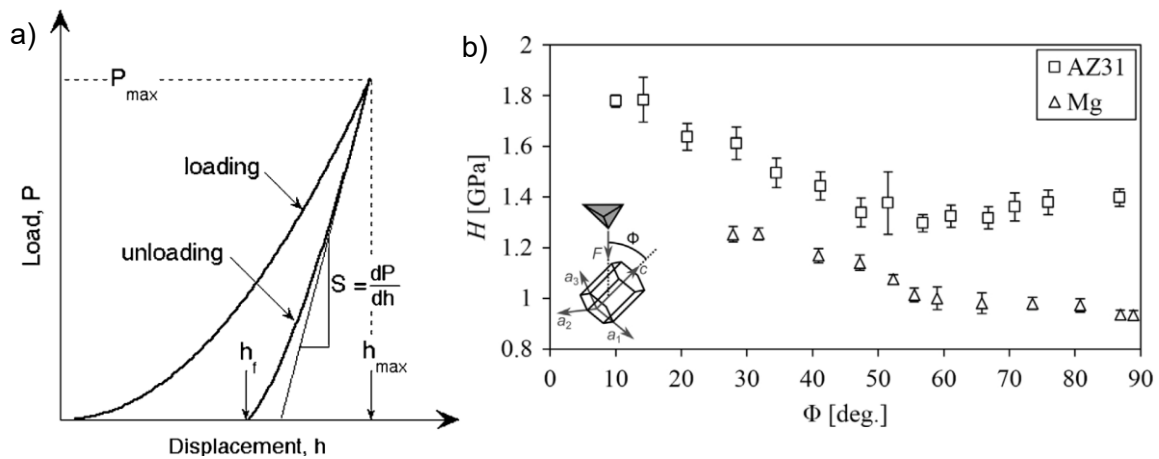


Figure 18. a) Schematic illustration of an indentation load-displacement curve (reproduced from [125] and b) nanohardness of pure Mg and AZ31 as a function of the declination angle  $\Phi$ . Reproduced from [126].

Bočan et al. observed that the nanohardness of coarse grained cast 99.9 % Mg is a function of the declination angle  $\Phi$ , which is the angle between the direction of indentation and the c-axis of the grains [127]. As shown in Figure 18b, nanohardness of pure Mg decreases with increasing angle and almost reaches a plateau at 60 degree. AZ31 exhibits a different behaviour, namely a minimum at ca. 1.3 GPa, and an overall higher hardness.

Besides the grain orientation-dependent hardness, the measurement of the contact area is also affected by material pile-up or sink-in, which is caused by the plastic deformation of the material due to the indenter tip [128]. In case of a pile-up, this leads to an increase in contact area resulting in an overestimation of hardness and elastic modulus [129]. In scanning probe microscopy (SPM) images, this pile-up can either be seen as roughness around the indent or as smoothing of the indent edges.

Another phenomenon is the pop-in effect, which results in a sudden increase in displacement. The load remains the same, resulting in a horizontal line in the loading curve, which is typical for twin formation in coarse-grained Mg [130]. In ultrafine-grained AZ31, Hu et al. reported that no deformation twinning was involved in the plastic

deformation, which is the reason why the pop-in effect gradually disappeared as the grain size decreased [131]. Instead, the movement of dislocations in the basal and non-basal planes and grain boundaries is effectively activated.

## **2.4.2. Cyclic loading**

### **2.4.2.1. Macro fatigue behaviour**

Fatigue properties are among the most important properties of a material, which is to be used in moving structures. Various methods have been developed to analyse the fatigue behaviour, which essentially describes the cyclic plasticity of a polycrystalline material and depends on several parameters such as unit cell, stacking fault energy, grain size, precipitate/reinforcement geometry, and distribution as well as the coherence of the matrix to the reinforcements [129]. Metal fatigue is a random process that leads to scattering properties even in carefully controlled experiments, thus complicating data analysis and the subsequent application [132]. During fatigue loading of Mg alloys, complex mechanisms are active resulting in cyclic hardening or softening. Cyclic hardening is mainly a result of twinning and detwinning occurring during the reversal of compression and tensile loading [133]. Due to the presence of non-reversible twin boundaries, non-basal slip of  $\langle a \rangle$  dislocations is activated as well as twin-twin and slip-twin interactions [32,134]. Furthermore, Wolf et al. [135] observed cyclic hardening in AZ91D at stress amplitudes only above the fatigue strength. Softening can be caused by the coalescence of twin boundaries and/or the formation and growth of fatigue microcracks [136,137]. In addition, Mg is known for asymmetrical deformation behaviour during tension and compression due to the limited independent slip systems. However, as the number of cycles increases, hysteresis loops gradually become more symmetric, which indicates a change of the dominant deformation mechanism from twinning to dislocation slip [133]. This is due to the increased defect density resulting in the activation of prismatic and pyramidal slip. While the hardening contribution via dislocations dominates over cyclic softening processes in monolithic materials [138], the high cyclic strain-hardening often observed in composites is probably due to the higher density of pre-existing dislocations, the interaction of mobile dislocations with the reinforcing SiC particles, and more dislocation–dislocation interactions. [139].

The deformation behaviour of a material can be determined using stress-strain hysteresis loops obtained for each cycle during the test. The evolution of the hysteresis loops, which includes the change of the strain direction and of the stress or strain amplitude depending on whether a stress or strain-controlled test was carried out, is crucial. Figure 19a shows a schematic hysteresis loop and the derived parameters,

which may allow conclusions to be drawn about possible deformation mechanisms. Thereby, the plastic strain amplitude ( $\epsilon_{a,p}$ ) is an important parameter that indicates the ability of a material to deform plastically. This means that, if the width of the hysteresis loop and thus  $\epsilon_{a,p}$  decreases with increasing number of cycles, cyclic hardening occurs. However, SEM and TEM investigations are required to determine the deformation mechanisms.

The most common method to investigate fatigue behaviour is the constant amplitude test (CAT), which is employed to determine the relationship between the stress amplitude and the number of cycles to failure (S-N-curve), thus allowing the determination of the endurance limit. For this purpose, different stress amplitudes are selected and several CATs, each at a certain stress amplitude, are carried out to statistically verify the results. In contrast, the load increase test (LIT) is mostly employed for a fast characterisation, when only few samples are available [140]. LIT starts at a low stress amplitude, whereby the stress amplitude is either continuously or stepwise increased by a certain value after a defined number of cycles ( $N$ ) until sample failure. By plotting the plastic strain amplitude versus the number of cycles, the stress amplitude at which the sample will fail under constant load amplitude can be estimated. However, with localised plastic deformation during cyclic loading, rather low values of plastic strain make the determination of the cyclic yield strength in LIT particularly difficult [135]. The deviation of the plastic strain amplitude thereby helps to identify the critical value where the slope of  $\epsilon_{a,p}$  versus  $N$  changes significantly. For illustration, Figure 19b shows  $\epsilon_{a,p}$  versus  $N$  of casted AZ91D as an example, whereby the stress amplitude is stepwise increased until sample failure. The dotted lines show the range of linear behaviour of  $\epsilon_{a,p}$ . The point, at which the curve deviates from its linear behaviour, is estimated to be the fatigue strength. As has been shown by Wolf et al., the estimated fatigue strength of LIT correlates well with that of CAT [135].

The characterization of the fracture surface to determine the fracture mechanisms and the associated fracture mode is as important as the analysis of the deformation behaviour from the hysteresis loops. Based on the analysis of the origin and mode of crack growth depending on grain size and shape of the micro-constituents, materials can be further improved in order to increase the fatigue strength or other properties such as ductility [141]. Magnesium and its alloys are known to show an early crack initiation if stresses occur above the endurance limit [129]. Further, due to the passing of the slip lines through the grain, the initiation of a transgranular surface crack followed by a transgranular propagation mode is expected, resulting in a cleavage behaviour [132,142]. For Mg-SiC nanocomposites, Shen et al. also observed a small

amount of dimples and cleavage steps at the fracture surface, which they attributed to the inability of Mg to deform uniformly due to the few independent slip systems [49].

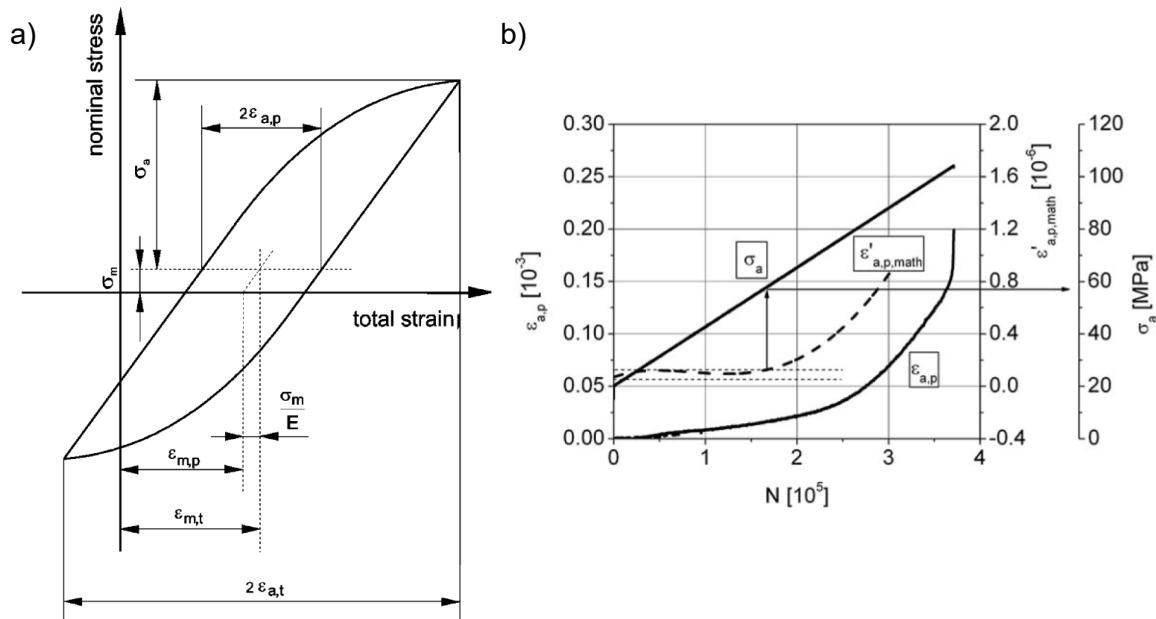


Figure 19. a) Schematic stress-strain hysteresis loop and derived parameters describing the non-linear deformation behaviour of a material ( $\sigma_a$  is the stress amplitude,  $\sigma_m$  the mean stress,  $\varepsilon_{a,p}$  the plastic strain amplitude at the half width of the hysteresis loop at mean stress,  $\varepsilon_{m,t}$  the total mean strain, and  $\varepsilon_{m,p}$  the non-elastic mean strain calculated using  $\varepsilon_{m,t} - \sigma_m/E$ , with  $\varepsilon_{m,t}$  being the total mean strain and  $E$  the elastic modulus; reproduced from [143]); b) plastic strain amplitude versus the number of cycles in a load increase test. Reproduced from [135].

Although microstructural features indicating fatigue plasticity are difficult to recognize, they are a clear sign of fatigue failure. One of these features are striations, which are distinct line markings, parallel to each other, and normal to the local direction of crack propagation. Each striation is the result of one stress cycle, which is the reason why the movement of the crack front can be calculated from the distance between the striations. However, their absence does not necessarily mean that fatigue failure has not occurred [132]. In addition, intrusions and extrusion may indicate fatigue reversal slip that occurs at nearby planes [132].

#### 2.4.2.2. Cyclic nanoindentation

Nanoindentation also offers the possibility of multiple high frequency indentations, thereby performing localised fatigue tests that accumulate mechanical damage. The indenter tip remains in constant contact with the sample surface, which is ensured by a low applied force. Figure 20 shows a load-time curve during cyclic nanoindentation.

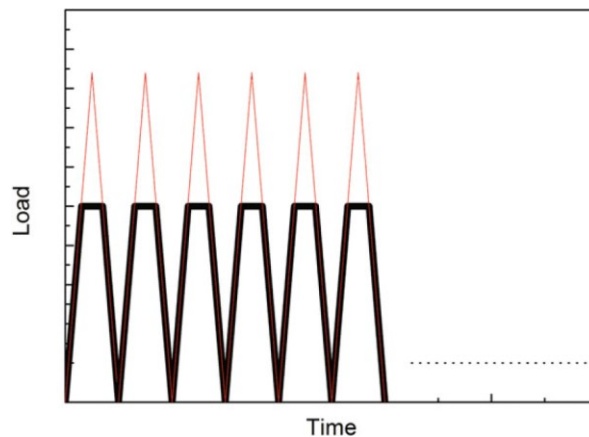


Figure 20. Load-time curve during cyclic nanoindentation. Reproduced from [144].

With the help of nano-fatigue tests, elastic-plastic behaviour as well as crack initiation and propagation behaviour in local areas can be analysed [145]. Cyclic nanoindentation is therefore an effective non-destructive method for studying the intrinsic and extrinsic fatigue mechanisms, especially in nanostructured materials [146,147]. In nanocrystalline metals, deformation mechanisms differ from typical coarse grained metals and alloys: interface-mediated mechanisms such as grain boundary sliding/migration, dislocation nucleation and twinning tend to dominate [144].

Over the past 10 years, there have been a few studies focussing on cyclic nanoindentation of metals within 10 to 1000 cycles, regarding indentation depth propagation and stress intensity assuming fatigue crack growth [145–151], and on films [152–154]. However, only one study investigated solution-treated AZ31 Mg alloy using low cycle nanoindentation up to 300 cycles [155].

In 2009, Xu et al. [146] proposed a simple law of indentation fatigue for a flat cylindrical indenter and found that the process of indentation fatigue is similar to steady-state fatigue crack growth. The researchers concluded that the indentation fatigue depth propagation law has the potential to extract the fatigue properties of materials with small volumes and clarify the fatigue crack mechanisms. This observation is confirmed by Jain et al. [155], who investigated solution treated and aged AZ61 Mg alloy. They found in the solution treated alloy that the indentation depth rate decreases with number of cycles during the primary stage, which is followed by a steady state in the secondary stage, where cyclic hardening and softening are in balance. In the aged case, however, no definite trend was observed, which was attributed to cyclic hardening as dominant mechanism due to the presence of precipitates resulting in restricted plastic flow. Already in 2006, Saraswati et al. [148] attributed the disparity between the loading and unloading paths in doped gold of 5N purity to the interactions between Ca and defects such as

dislocations and grain boundaries during cycling. Thus, they have already shown that defect–solute interactions can be detected by cyclic nanoindentation.

Cavaliere [145] explained the steady-state propagation of indentation fatigue depth with the balance between the dislocations generation and annihilation. The steady state can thus be directly related to the increase in internal stresses and dislocation generation and movement and is comparable to the processes at the crack tip in conventional crack propagation tests. Cavaliere further observed that the development of the plastic zone is directly related to the indentation depth propagation due to the nucleation and growth of cracks by increasing the number of cycles. This is in agreement with Gale et al. [151], who found in copper that with increasing work-hardening, the plastic zone became more local, due to resistance to dislocation motion in the bulk material. Furthermore, this resulted in larger pile-up height and smaller indentation depth, which showed a power law relationship with the distance from the surface.

With a new method, which was first employed by Schmahl et al. [123], investigating AlSiMg foam, the cyclic deformation behaviour can be investigated locally on the nanoscale. Their study has shown that precipitates, grain orientation and grain boundaries significantly influence the cyclic deformation behaviour. However, no cyclic nanoindentation tests have been performed on Mg nanocomposites so far.

### **3. Outline of the thesis and overview of the publications**

In order to be able to produce Mg-SiC nanocomposites with excellent properties, a homogeneous distribution of nanoparticles as well as a high material density are very important. In addition to the nanoparticles and the high density, a small grain size leads to a higher strength and should therefore be aimed for. Pure Mg was used instead of Mg alloy to investigate the densification and strengthening mechanisms without the influence of alloying elements. The present thesis deals with a new manufacturing process that takes the aforementioned factors into account when producing Mg-SiC nanocomposites comprising mechanical milling, uniaxial pressing, cold-isostatic pressing, sintering and hot extrusion. In order to assess the influence of the texture produced by hot extrusion, a texture-free nanocomposite was also produced through HIP as last consolidation step. The manufacturing process route was described, and the results were compared and discussed in terms of density, grain size and SiC distribution. These are the most important parameters for improving the mechanical properties with regard to increased strength and ductility. After a successful production of the Mg-SiC nanocomposites and the performing and analysis of compression and tensile tests, the fatigue behaviour was tested at the macro and nanoscale. The relationship of fracture mechanisms and mechanical properties was discussed as well as the question whether cyclic nanoindentation can predict macro fatigue behaviour.

Following questions are discussed with this thesis:

- Which processes and parameters can meet the requirements concerning full density, nano to sub-microcrystalline grain size, and homogeneous SiC nanoparticle distribution?
- How does the microstructure influence mechanical properties such as hardness, elastic modulus, tensile, compressive, and fatigue behaviour?
- Which adjustments of the process parameters can lead to an altered microstructure that engenders the required mechanical properties?

Some results have not been published but contain essential information on the manufacturing process of the Mg-SiC nanocomposites and their mechanical properties. Therefore, two additional chapters, dealing with these results were added between the manuscripts.

Please note that I changed my last name from Penther to Hübler during my doctorate.

Manuscript I, “Development and characterization of Mg-SiC nanocomposite powders synthesized by mechanical milling”, describes the production of the nanocomposite powder. Reinforcement contents of 1, 3, and 10 vol% SiC nanoparticles were used. The main focus was on the homogenous distribution of SiC nanoparticles within the Mg matrix and a submicron-crystalline microstructure.

Manuscript II, “Microstructure and nanoindentation analysis of Mg-SiC nanocomposite powders synthesized by mechanical milling”, was included mainly to provide information on the mechanical properties such as nanohardness and elastic modulus of the nanocomposite powder particles, which were determined through nanoindentation.

Manuscript III, “Effect of SiC nanoparticles on manufacturing process, microstructure and hardness of Mg-SiC nanocomposites produced by mechanical milling and hot extrusion”, deals with the compressibility of the as-milled nanocomposite powder particles with a reinforcement content of 1 and 10 vol% SiC nanoparticles and their densification into bulk materials. The manufacturing process comprising uniaxial pressing, cold isostatic pressing, sintering, and hot extrusion, as well as the used parameters to produce dense nanocomposites are presented. Grain size and SiC distribution are analysed by TEM and the development of the microstructure is discussed.

The first intermediate chapter shows additional results on the influence of the sintering temperature on the microstructure and discusses the extrusion of sintered Mg-SiC nanocomposites in comparison to the extrusion of nanocomposite powder.

Manuscript IV, “Effect of hot isostatic pressing on densification, microstructure and nanoindentation behaviour of Mg-SiC nanocomposites”, examines the effect of HIP as last process step that achieves isotropic properties due to its isostatic pressure, as opposed to hot extrusion. The microstructure and hardness of the sintered and HIPed nanocomposite with 1 vol% reinforcement content are then compared and discussed with the sintered state and also with regard to hot extrusion.

The results of the compression and tensile tests of extruded Mg nanocomposites are presented and discussed in the second intermediate chapter considering the influence of the manufacturing process and thus the microstructure.

Manuscript V, “Cyclic deformation behaviour of Mg-SiC nanocomposites on the macro and nano scale”, deals with the fatigue properties of the Mg-SiC nanocomposites and focuses on the microstructural characterisation. Fracture mechanisms and fracture behaviour are discussed, as well as the results of the macro and nano fatigue tests regarding plastic deformation.

## 4. Manuscript I

### Development and characterization of Mg-SiC nanocomposite powders synthesized by mechanical milling

#### Publication notification

##### *Keywords:*

Magnesium, SiC nanoparticle, powder, nanocomposite, MMC, ball milling

##### *Authors:*

D. Penther<sup>1</sup>, C. Fleck<sup>1</sup>, A. Ghasemi<sup>1</sup>, R. Riedel<sup>2</sup>, S. Kamrani<sup>1</sup>

<sup>1</sup>Department of Materials Science and Engineering, TU Berlin, 10623 Berlin, Germany

<sup>2</sup>Department of Materials and Earth Sciences, TU Darmstadt, 64287 Darmstadt, Germany

*Journal:* Key Engineering Materials, vol. 742, pp. 165-172, July 2017

*ISSN:* 1662-9795

*DOI:* 10.4028/www.scientific.net/KEM.742.165

##### *Author contributions:*

Due to my late entry in the project, Dr. Alireza Ghasemi took on the production of the first batch of nanocomposite powder. I prepared powders using different parameters at TU Darmstadt, while Dr. Sepideh Kamrani did SEM studies and arranged further investigations at the TU Berlin. She is also responsible for project funding and supervision of the project. Prof. Dr. Claudia Fleck provided a workplace and facilities at TU Berlin and supported me as thesis supervisor. Prof. Dr. Dr. h.c. Ralf Riedel provided a workplace and the equipment at TU Darmstadt. Together with Dr. Sepideh Kamrani, we decided on manufacturing parameters that I used to produce the rest of the powders. The manuscript was written by me and reviewed by all co-authors.

## Abstract

Magnesium powder in micron scale and various volume fractions of SiC particles with an average diameter of 50 nm were co-milled by a high energy planetary ball mill for up to 25 h to produce Mg-SiC nanocomposite powders. The milled Mg-SiC nanocomposite powders were characterized by scanning electron microscopy (SEM) and laser particle size analysis (PSA) to study morphological evolutions. Furthermore, XRD, TEM, EDAX and SEM analyses were performed to investigate the microstructure of the magnesium matrix and distribution of SiC-reinforcement. It was shown that with addition of and increase in SiC nanoparticle content, finer particles with narrower size distribution are obtained after mechanical milling. The morphology of these particles also became more equiaxed at shorter milling times. The microstructural observation revealed that the milling process ensured uniform distribution of SiC nanoparticles in the magnesium matrix even with a high volume fraction, up to 10 vol%.

## 4.1. Introduction

Magnesium is the lightest engineering metal with a density of 1.74 g/cm<sup>3</sup>. Further advantages are its high dimensional stability and superior damping characteristics why it is widely used in the automobile and aviation industries [1, 2]. Nevertheless, magnesium has some limitations such as low strength and poor ductility [3]. This is due to its hexagonal closed packed (hcp) structure, which provides a limited number of independent slip systems. A way to improve the mechanical properties is to reinforce the magnesium matrix with stronger and stiffer particles like ceramics to create a metal matrix composite (MMC) [4]. Thus, the characteristic properties of metals and ceramics are combined and lead to superior specific properties of the MMCs such as strength, elastic modulus and creep resistance at a low density [5–7]. However, the reinforcement with micron sized ceramic particles usually deteriorates the ductility [8]. Recently, it has been demonstrated that the addition of nanosized reinforcements such as ceramic oxides, SiC or carbon nanotubes can lead to a simultaneous increase in strength and ductility of magnesium [9–11]. Nanosized reinforcements can withstand deformation without fracturing, which overall results in a significant increase in strength and ductility of the composite [6, 12–15]. However, the function of nanoparticles in a metallic matrix is related to their distribution in the matrix, which can strongly affect the mechanical properties of the composite. Nevertheless, fabrication of nanocomposites is difficult because the uniform dispersion of nanoparticles throughout the metal matrix is still a challenging task. One of the common procedures to fabricate nanocomposites is mechanical milling. This method results in an acceptable distribution of the reinforcing

particles without the typical segregation of casted composites [12]. In addition, milling is one of the most effective methods for mechanically reducing grain size and producing nanocrystalline powders. In the present study, high-energy mechanical milling was used to incorporate 1 vol%, 3 vol% and 10 vol% SiC nanoparticles homogeneously in a pure magnesium matrix. The effect of the nanoparticle reinforcement on the morphology and microstructure of milled nanocomposite powders was investigated, as a function of the volume fraction of the reinforcement.

## 4.2. Experimental Procedures

Magnesium powder with an average particle size of -325 mesh and two SiC powders, one with an average particle size of 50 nm (SiC<sub>n</sub>) and the other with an average particle size of 1 μm (SiC<sub>μ</sub>) were used. All powders have a purity of 99.8 % and were supplied by Alfa Aesar (Ward Hill, MA, USA). Fig. 1 shows the morphology of the as-received magnesium and SiC nanoparticles.

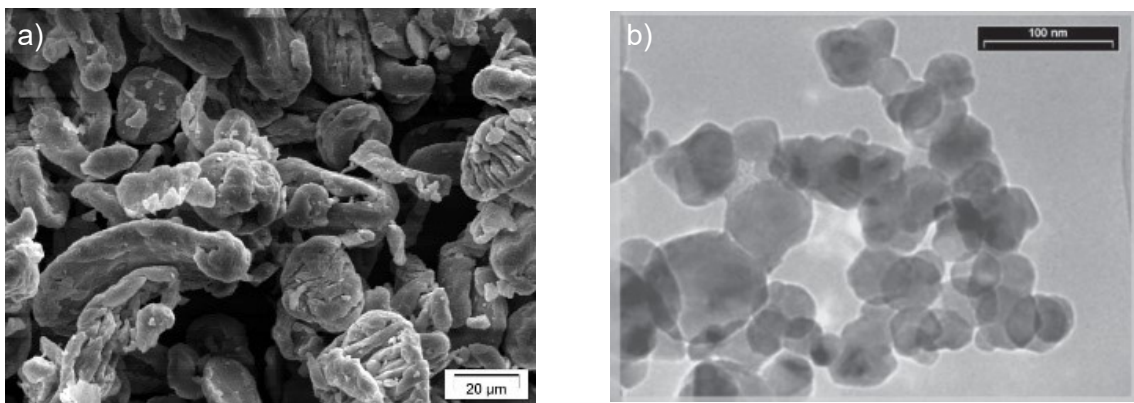


Fig. 1 – Morphology of as-received powders a) SEM micrograph of magnesium and b) TEM micrograph of SiC nanoparticles.

The magnesium powder was mixed with 1 vol%, 3 vol% or 10 vol% of SiC nanoparticles by high-energy mechanical milling. Another powder mixture with 10 vol% SiC microparticles was prepared for comparison. An overview of the powder mixtures and their naming is given in Table 1. To minimize the cold welding effect, 2 wt% stearic acid was added to the mixtures as milling process control agent (PCA) [16]. All powder mixtures were blended for 20 min on a rolling bank. The high-energy mechanical milling was performed in a planetary ball mill (Pulverisette 5, Fritsch, Germany) using zirconia balls in a hard PE vessel for different milling times up to 25 h. The ball-to-powder weight ratio (BPR) was 10:1 and a rotational speed of 250 rpm was used. All the handling, mixing, and milling steps were performed under a high purity argon atmosphere in a glove box.

Table 1 – Mechanically milled powder mixtures of magnesium with volume fractions of 0 vol%, 1 vol%, 3 vol% and 10 vol% SiC particles and corresponding naming.

	MM	M1Sn	M3Sn	M10Sn	M10S $\mu$
Mg [vol%]	100	99	97	90	90
SiC <sub>n</sub> [vol%]	-	1	3	10	-
SiC <sub><math>\mu</math></sub> [vol%]	-	-	-	-	10

After 25 h of mechanical milling, the milled powders were analyzed by SEM (CamScan Series 2, Obducat, Sweden) in order to study their morphology. Additionally, milled powder particles were embedded in epoxy resin. The microstructure and the distribution of the SiC nanoparticles was investigated on ground and polished sections by high resolution SEM (S-2700, Hitachi Ltd., Japan). Further, transmission electron microscopy (TEM; Tecnai G<sup>2</sup> 20 S-TWIN, FEI, USA) was used to investigate the microstructure and distribution of the SiC particles. For this purpose, a lamella was cut out from a powder agglomeration and was thinned to about 100 nm using the focused ion beam technique.

A high performance laser particle size analyzer (LA-950, Horiba, Japan) with a measuring range from 10 nm to 3 mm was used to characterize the particle size and size distribution of the powders after milling. The particles were dispersed in absolute ethanol and ultrasound was applied for 2 min in order to eliminate particle agglomerates. Measurements were made to determine the D50 (median particle size), D90 (the particle size where 90 % of the particles are below that size) and D10 (the particle size where 10 % of the particles are below that size) values of the particles size distribution.

X-ray diffraction patterns were recorded with the X'Pert Pro from PANalytical (Netherlands) to obtain information about the number and nature of the phases. The width of the diffraction peaks was utilized to determine grain (crystallite) size and the amount of microstrain of the magnesium matrix in the mechanically milled nanocomposite powders.

### 4.3. Results and Discussion

The morphology of Mg–10% SiC nanocomposite powders, M10Sn, at different milling times is shown in Fig. 2. At the early stages, the magnesium particles are deformed to a flattened shape with an increase in average size (Fig. 2a, b). Micro-welding between the particles and the onset of fracture were observed at prolonged milling times (Fig. 2c). Due to the welding of the flattened magnesium particles a particle growth started. The powder particles start to break when a sufficient level of defects was generated (Fig. 2d).

The fractured particles repeatedly weld together and break again. A steady state condition and formation of equiaxed particles are attained when a balance between welding and fracturing is reached. For a milling time of 25 h, a change in the morphology is found where the particles acquire a more regular and equiaxed shape (Fig. 2e, f). Further, the average size of the particles decreased and a more uniform distribution was reached. The development of the M10Sn powder represents all stages described previously [12, 14, 17] such as flattening, welding, fracture and steady state.

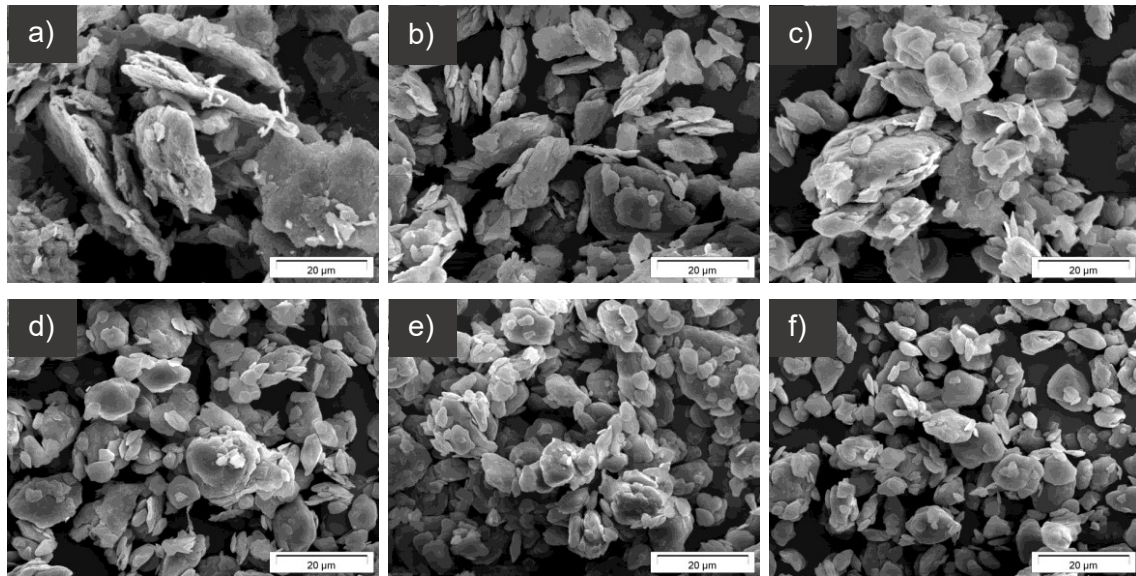


Fig. 2 – Morphology of Mg-10% SiC composite powder after mechanical milling for a) 1 h, b) 3 h, c) 5 h, d) 15 h, e) 20 h and f) 25 h.

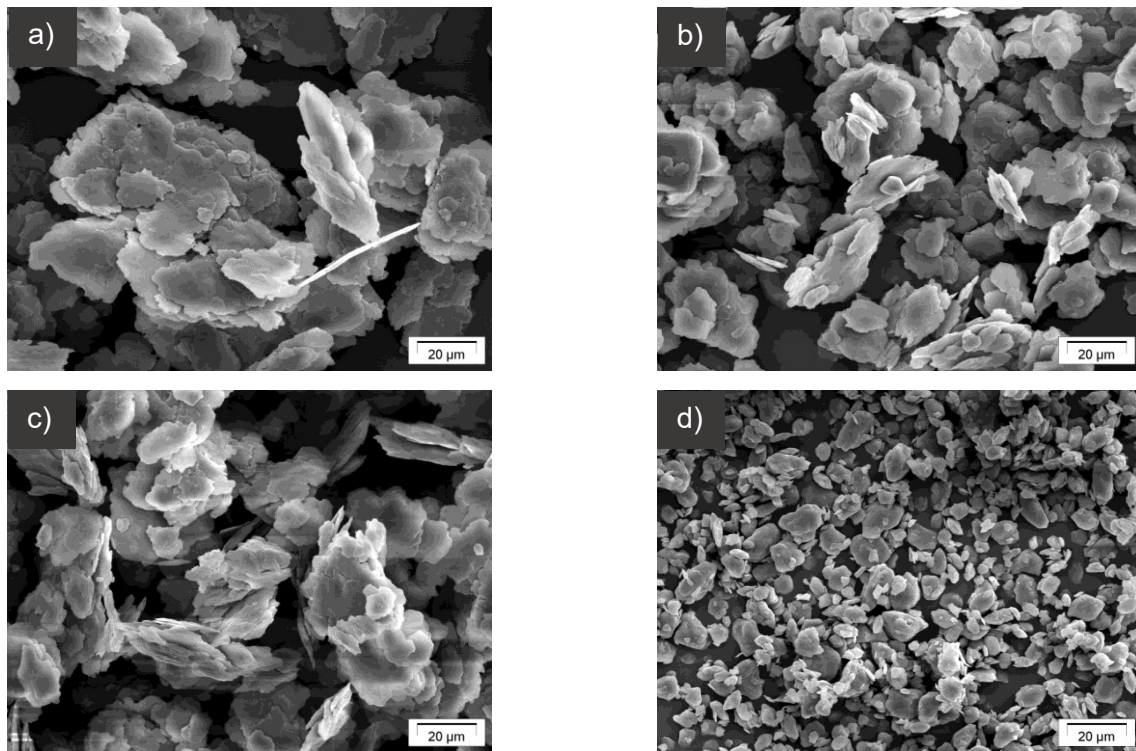


Fig. 3 – Morphology of the milled powders a) MM, b) M1Sn, c) M3Sn and d) M10Sn after 25 h mechanical milling, showing the decrease in particle size with increasing SiC content.

Besides milling time, the volume fraction of the reinforcing particles shows a significant influence on the powder particle morphology during mechanical milling. Fig. 3 shows the morphology of the MM, M1Sn, M3Sn and M10Sn milled powders after 25 h of milling. By increasing the SiC content, the particle sizes become finer and more equiaxed after the same milling time. It appears that SiC nanoparticles promote the fracture of the magnesium matrix during mechanical milling. In case of nanoparticles, the high surface to volume ratio increases the local deformation and the rate of work hardening while the fracture toughness decreases. Consequently, the fracture process is enhanced in the presence of nanoparticles, which in fact results in the formation of finer particles with a narrow size distribution. Fig. 4 shows the morphology of the M10Sn milled powder in comparison to M10S $\mu$  after 25 h of milling. The more equiaxed and finer particles after the same milling time confirms the prominent effect of the SiC nanoparticles to accelerate the mechanical milling process.

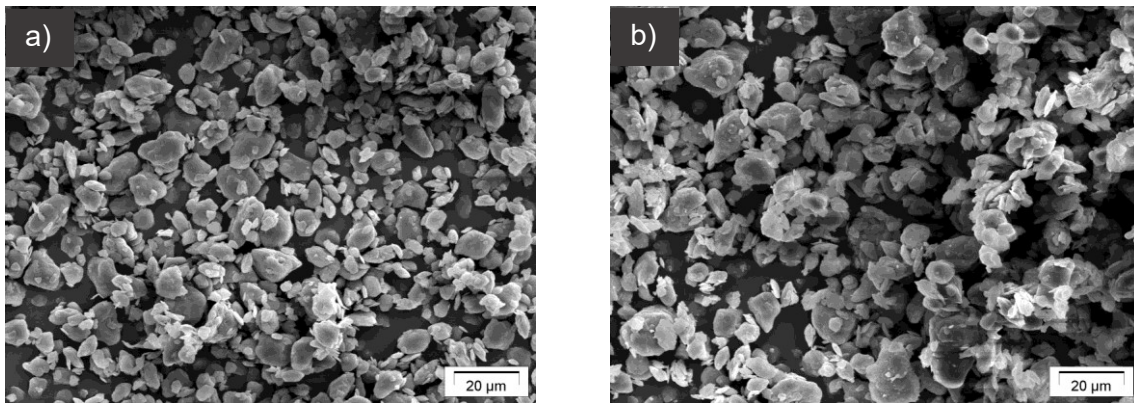


Fig. 4 – Morphology of milled powders a) M10Sn and b) M10S $\mu$  after 25 hours of mechanical milling.

Fig. 5 illustrates the particle size distributions of the MM, M1Sn, M3Sn, M10Sn and M10S $\mu$  milled powders after 25 h of mechanical milling. All the milled powders exhibit a symmetric log-normal size distribution. The symmetrical gaussian bell-shape indicates also the equilibrium between fracture and welding, typical of the final stage of mechanical milling [18]. Furthermore, the results show a reduction in particle size with increasing volume fractions of SiC nanoparticles, which is in consistency with the SEM observations of the powder morphologies.

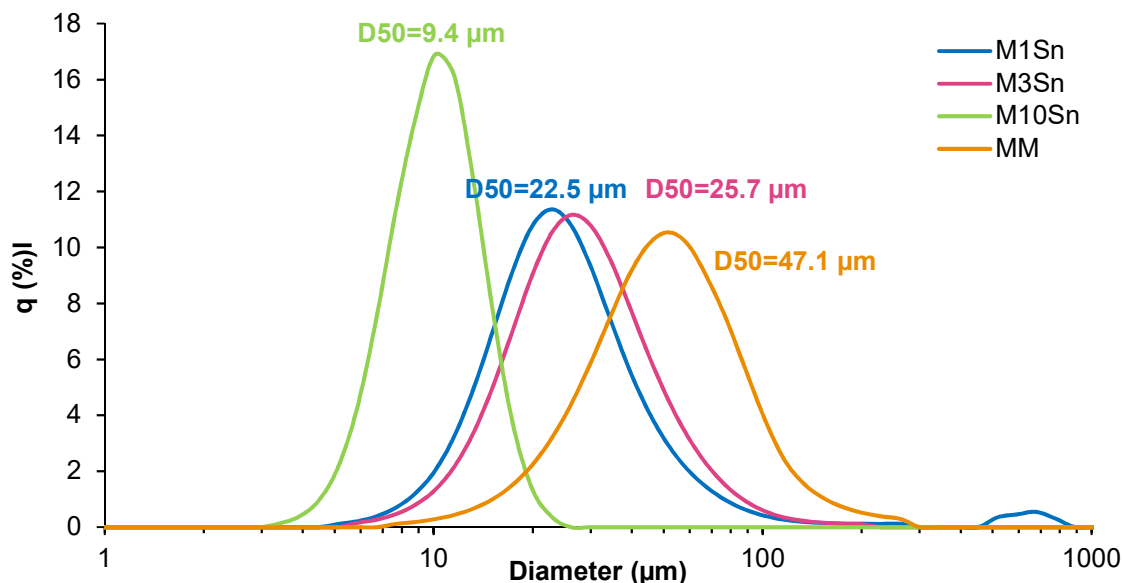


Fig. 5 – Particle size distribution of the milled powders MM, M1Sn, M3Sn and M10Sn.

XRD patterns of the MM, M1Sn, M3Sn and M10Sn powders are shown in Fig. 6a. Besides Mg and SiC, no other phases were detected. Fig. 6b shows a magnified view of the (002) reflex of magnesium. With increasing SiC content, peak broadening is observed while the maximum intensity decreases. As peak broadening represents finer grain sizes and lattice distortion [19], the increase in peak width of magnesium indicates the formation of i) fine crystallite sizes and ii) high density of defects in the magnesium powder with increasing volume fraction of the SiC nanoparticles.

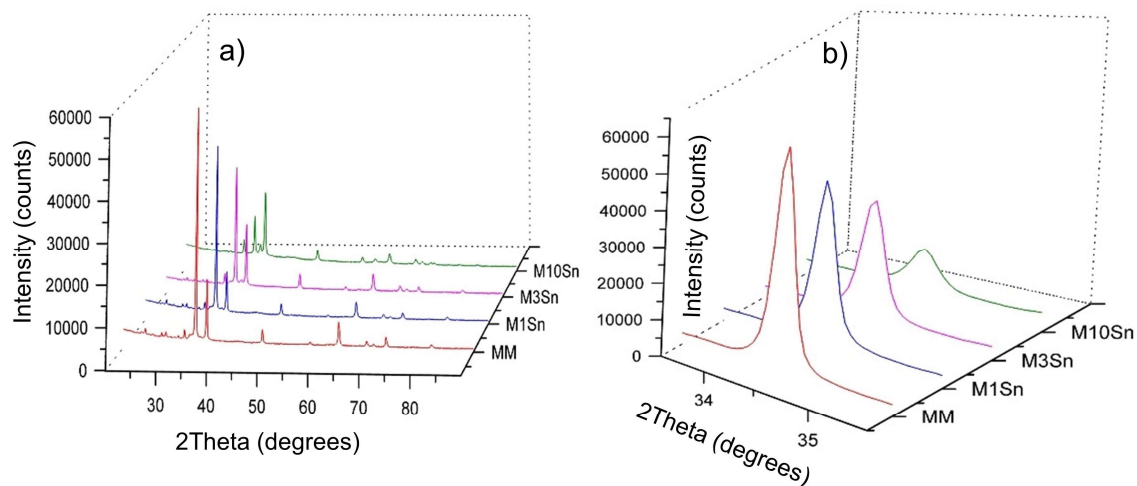


Fig. 6 – XRD patterns of milled powders MM, M1Sn, M3Sn and M10Sn: a) whole pattern, b) magnified view of the (002) Mg peak.

In order to illustrate the distribution of the SiC nanoparticles in the magnesium nanocomposite powders, cross-sections of M10Sn and M10S $\mu$  milled powders are shown in Fig. 7 where the magnesium matrix appears in light grey and the SiC particles appear as white dots. Although it is known that with higher volume fraction of

in comparison to macroparticles, the used mechanical milling setup results in a homogeneous distribution of even 10 vol% of SiC nanoparticles in the magnesium matrix [20]. The EDS elemental mapping regarding Mg and Si elements in Fig. 8 highlights the uniform distribution of SiC nanoparticles as seen by SEM.

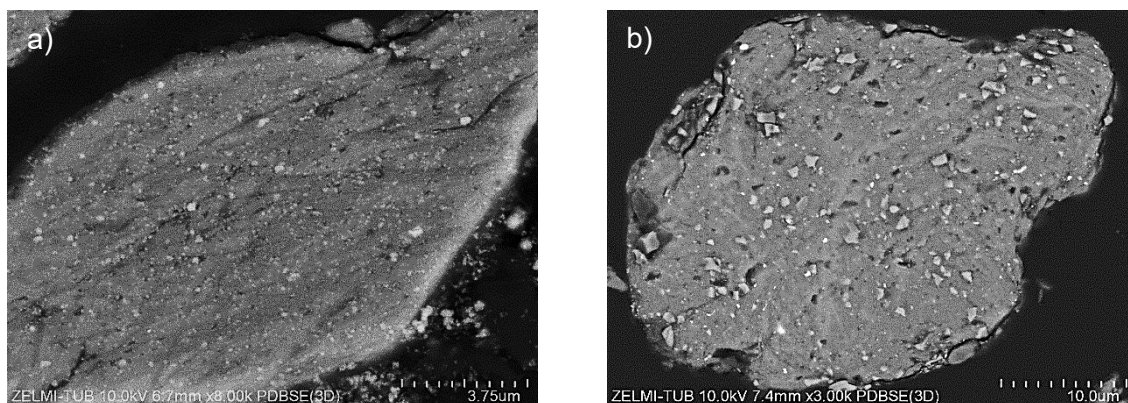


Fig. 7 – Backscattered electron image of a) M10Sn and b) M10S $\mu$  shows a homogeneous distribution of SiC particles (white) in the magnesium matrix (light grey).

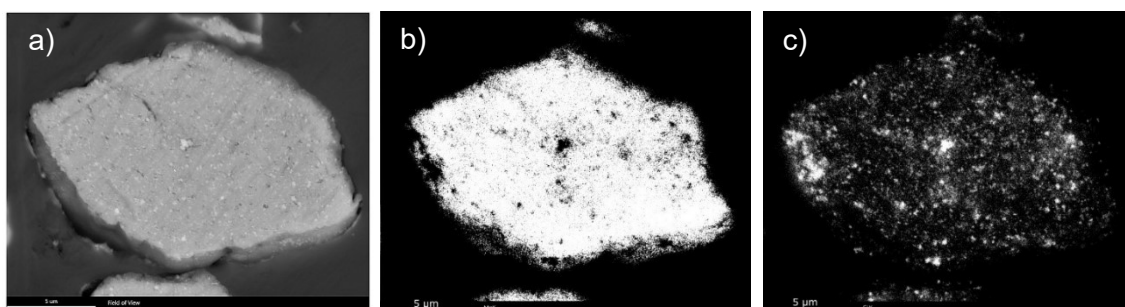


Fig. 8 – Elemental mapping of M10Sn nanocomposite powder: a) SEM micrograph, b) magnesium and c) silicon.

Brightfield TEM micrographs of M10Sn milled powder are shown in Fig. 9. The micrographs not only show the uniform distribution of the SiC nanoparticles, but they furthermore attest to the development of a nanocrystalline magnesium matrix during the mechanical milling process. The TEM results are thus in good agreement with the XRD peak broadening. Figure 9b shows a magnified view of one SiC particle together with the surrounding magnesium matrix. No evidence of the presence of an interfacial product between the SiC nanoparticle and the magnesium matrix was found, indicating the formation of well-bonded interfaces. A strong interfacial bonding between the SiC nanoparticles and the nanocrystalline magnesium matrix is promising in terms of superior mechanical properties of the magnesium nanocomposites.

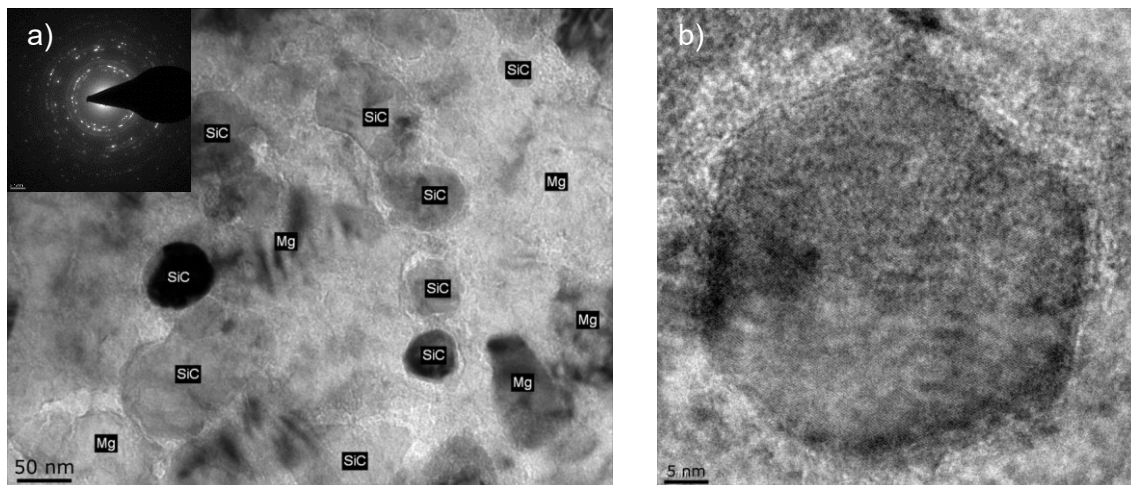


Fig. 9 – Brightfield TEM micrographs of M10Sn nanocomposite powder: a) survey, showing the distribution of SiC particles within the nanocrystalline Mg matrix: the compositions of the marked grains were verified by EDS (results not shown); the inset shows the accompanying SAD pattern; b) magnified view of SiC particle in Mg matrix showing a well-bonded interface.

#### 4.4. Summarising conclusions

Magnesium powder and SiC nanoparticles were co-milled to produce Mg-SiC nanocomposite powders. The morphology as well as the microstructure of the milled powders were studied. With higher milling time the particle size of the Mg-SiC powder decreases. In the same duration of milling process, the higher contents of SiC result in finer particle sizes with more equiaxed morphology. The particle size distribution was in good agreement with the SEM pictures. SEM and TEM analyses verified a homogeneous distribution of SiC nanoparticles in the magnesium matrix, even with a high volume fraction of 10 vol% SiC.

#### 4.5. Acknowledgement

The authors gratefully acknowledge the financial support by the DFG (Deutsche Forschungsgemeinschaft) and the members of the group Non-Metallic Inorganic Materials, Institute of Materials Science at TU Darmstadt for providing the ball mill equipment. The authors would also like to thank the Department of Food Technology and Food Material Science for the particle size distribution measurements as well as Ulrich Gernert and Sören Selve at ZELMI for the support during SEM and TEM analyses.

#### 4.6. References

- [1] T. M. Pollock, Weight loss with magnesium alloys, *Science* 328 (2010) 986–7.
- [2] A. Luo, J. Renaud, I. Nakatsugawa, J. Plourde, Magnesium castings for automotive applications, *JOM* 47 (1995) 28–31.

- [3] M. K. Habibi, K. S. Tun, M. Gupta, An investigation into the effect of ball milling of reinforcement on the enhanced mechanical response of magnesium, *J. Compos. Mater.* 45 (2011) 2483–93.
- [4] J. Llorca, C. González, Microstructural factors controlling the strength and ductility of particle-reinforced metal-matrix composites, *J. Mech. Phys. Solids* 46 (1998) 1–28.
- [5] I. A. Ibrahim, F. A. Mohamed, E. J. Lavernia, Particulate reinforced metal matrix composites - A review, *J. Mater. Sci.* 26 (1991) 1137–56.
- [6] S. C. Tjong, Novel nanoparticle-reinforced metal matrix composites with enhanced mechanical properties, *Adv. Eng. Mater.* 9 (2007) 639–52.
- [7] M. Manoharan, S. Lim, M. Gupta, Application of a model for the work hardening behavior to Mg/SiC composites synthesized using a fluxless casting process, *Mater. Sci. Eng., A* 333 (2002) 243–9.
- [8] H. Z. Ye, X. Y. Liu, Review of recent studies in magnesium matrix composites, *J. Mater. Sci.* 39 (2004) 6153–71. [9] C. S. Goh, J. Wei, L. C. Lee, M. Gupta, Development of novel carbon nanotube reinforced magnesium nanocomposites using the powder metallurgy technique, *Nanotechnology* 17 (2006) 7–12.
- [10] C. S. Goh, M. Gupta, J. Wei, L. C. Lee, Characterization of high performance Mg/MgO nanocomposites, *J. Compos. Mater.* 41 (2007) 2325–35.
- [11] M. J. Shen, W. F. Ying, X. J. Wang, M. F. Zhang, K. Wu, Development of high performance magnesium matrix nanocomposites using nano-SiC particulates as reinforcement, *J. Mater. Eng. Perform.* 24 (2015) 3798–807.
- [12] C. Suryanarayana, N. Al-Aqeeli, Mechanically alloyed nanocomposites, *Prog. Mater. Sci.* 58 (2013) 383–502.
- [13] N. Ramakrishnan, An analytical study on strengthening of particulate reinforced metal matrix composites, *Acta Mater.* 44 (1996) 69–77.
- [14] J. S. Benjamin, Mechanical alloying, *Sci. Am.* 234 (1976) 40–9.
- [15] M. J. Shen, X. J. Wang, T. Ying, K. Wu, W. J. Song, Characteristics and mechanical properties of magnesium matrix composites reinforced with micron/submicron/nano SiC particles, *J. Alloys Compd.* 686 (2016) 831–40.
- [16] C. Machio, H. K. Chikwanda, S. Chikosha, Effect of process control agent (PCA) on the characteristics of mechanically alloyed Ti-Mg powders, *SAIMM* 111 (2011) 149–53.
- [17] C. Suryanarayana, Mechanical alloying and milling, *Prog. Mater. Sci.* 46 (2001) 1–184.
- [18] J. Fogagnolo, F. Velasco, M. Robert, J. Torralba, Effect of mechanical alloying on the morphology, microstructure and properties of aluminium matrix composite powders, *Mater. Sci. Eng., A* 342 (2003) 131–43.
- [19] H.-S. Kim, D.-S. Suhr, G.-H. Kim, D.-W. Kum, Analysis of X-ray diffraction patterns from mechanically alloyed Al-Ti powders, *Metals and Materials* 2 (1996) 15–21.
- [20] K. K. Deng, X. J. Wang, Y. W. Wu, X. S. Hu, K. Wu, W. M. Gan, Effect of particle size on microstructure and mechanical properties of SiCp/AZ91 magnesium matrix composite, *Mater. Sci. Eng., A* 543 (2012) 158–63.

## 5. Manuscript II

### Microstructure and nanoindentation analysis of Mg-SiC nanocomposite powders synthesized by mechanical milling

#### Publication notification

##### *Keywords:*

Mg-SiC nanocomposite, mechanical milling, nanocrystalline structure, nanoindentation

##### *Authors:*

A. Ghasemi, D. Penther, S. Kamrani

Department of Materials Science and Engineering, Technische Universität Berlin, 10623 Berlin, Germany

*Journal:* Materials Characterization 142, pp. 137–143, May 2018

*DOI:* 10.1016/j.matchar.2018.05.023

##### *Author contributions:*

Due to my late entry in the project, Dr. Alireza Ghasemi took on the production of the first batch of nanocomposite powder. I produced rest of the required powders at TU Darmstadt. Dr. Sepideh Kamrani did SEM studies as well as the analysis of XRD results and arranged further investigations at the TU Berlin. She is also responsible for project funding and supervision of the project. I conducted the nanoindentation tests and the evaluation. The manuscript was written by Dr. Alireza Ghasemi and Dr. Sepideh Kamrani and reviewed by me.

This manuscript was included mainly to provide information concerning nanohardness and elastic modulus of the nanocomposite powders determined by nanoindentation tests.

## 5.1. Abstract

Mixtures of magnesium powder and SiC nanoparticles at various volume fractions were mechanically milled to produce nanocrystalline Mg-SiC nanocomposites. X-ray diffraction (XRD), scanning electron microscopy (SEM) and transmission electron microscopy (TEM) were utilized to characterize the microstructure of the milled powders. The microstructural evidences revealed that mechanical milling is a proper method to achieve a uniform distribution of the SiC nanoparticles, even up to 10% in the Mg matrix. Based on the results, higher volume fraction of the SiC nanoparticles raise the value of measured microstrain and reduce the crystallite size of the Mg matrix. The TEM results pointed to the fact that no deformation twinning takes place in the nanostructured Mg matrix even after severe plastic deformation through mechanical milling and the presence of hard SiC nanoparticles up to 10 vol%. The effects of nanoparticle volume fraction on mechanical properties of the milled Mg-SiC nanocomposites were evaluated using nanoindentation tests. The results clearly showed a significant enhancement of nanohardness and reduced elastic modulus in the milled powders compared to that of the reference material namely as-received pure magnesium. It was found that the SiC nanoparticles (even up to 10 vol%), well distributed in the magnesium matrix, remarkably improve the reduced elastic modulus and nanohardness of the nanocomposite powders.

## 5.2. Introduction

An increasing demand for lightweight structural materials in recent decades has met with simultaneous surge in the development of magnesium (Mg) based materials. Aerospace, automobile, electronic, bioimplant and consumer product related industries has been seeking for Mg based structural materials for performance-critical application. However, their low strength and limited ductility compared to other structural materials (e.g. Al and steels) has limited their widespread applications. In order to improve the mechanical properties of Mg, significant efforts have been undertaken to develop Mg matrix composites. These combine low density and superior specific mechanical properties, including strength, stiffness and creep resistance [1–6]. While the reinforcements improve the strength characteristics of Mg, the addition of micron-sized ceramic particles usually deteriorates further the ductility. Many attempts have been made to optimize the drawbacks of the materials with composite structure [7–9]. Recent studies revealed that simultaneous enhancement in strength and ductility of Mg-composites can be achieved by addition of nano-sized reinforcements [10–14]. This effect was explained by a more effective particle hardening mechanism of nano-sized as compared to micron-sized

particles [15,16]. In addition, the nano-sized reinforcements have been shown to activate non-basal slip systems in the Mg matrix at room temperature, an effect, which increases the ductility [17,18]. Despite these promising results, the desired enhancement in the mechanical properties has still not been reached. This is mainly due to difficulties in obtaining a uniform distribution of nanoparticles in the Mg matrix, especially for higher volume fractions. In different studies the regions of agglomerated nanoparticles have been observed, which subsequently decreases the mechanical properties of the composite specially for the samples containing higher than 2 vol% of nanoparticles [19–22].

Mechanical milling is a promising method to overcome the agglomeration observed typically in composites [23–26]. Here, a mixture of brittle reinforcement and ductile matrix powders is milled in a vial containing balls. The collision of the balls causes plastic deformation, repeated cold welding and fracture of the deformed metal particles, as well fragmentation of the brittle powder particles. The fragments of the brittle particles are placed in the interfacial boundaries of the welded metal particles. Then, after a sufficient milling time, the welding and fracturing events reach an equilibrium. Eventually a composite particle forms with a uniform distribution of the reinforcements in the ductile metal matrix with randomly orientated interfaces. Hence, the technique of mechanical milling can be effectively used to synthesize nanocomposites as (a) it results in a fine and uniform dispersion of the nanoparticles; (b) it allows a homogeneous incorporation of high volume fraction of reinforcement components; (c) it reduces the grain size of the metal matrix to the nano-scale, and (d) it is a process taking place near room temperature. Primary aim of this study was to prepare nanocrystalline Mg-composites with a homogeneous distribution of SiC nanoparticles by mechanical milling. In the next steps the microstructure was characterized by XRD, SEM and TEM methods. The Mg grain structure, accumulation of microstrain and distribution of SiC nanoparticles was analyzed to study the effect of SiC nanoparticles and mechanical milling on the microstructure. The effect of the both features has been investigated using nanoindentation measurements to study the contribution of the microstructural characterization on the mechanical properties of the Mg-SiC nanocomposite powders. The focus was primarily on the hardness and modulus of elasticity.

### **5.3. Experimental**

Mg powder with an average particle size of  $-325$  mesh and  $\beta$ -SiC powder with an average particle size of 50 nm (named SiCn in the following) were used. All powders have a purity of 99.8% and were supplied by Alfa Aesar (Ward Hill, MA, USA). Pure Mg powders and Mg-SiCn-composite mixtures containing 1 and 10 vol% SiCn (named MM,

M1Sn and M10Sn, respectively) were prepared by blending in a Turbula T2C mixer (Basel, Switzerland) for 20 min. To prevent excessive cold welding during milling, 2 wt% stearic acid was added to the mixtures as a process control agent (PCA). The mixture was then mechanically milled in a planetary ball mill (Pulverisette 5, Fritsch, Germany) using zirconia balls in a hard polyethylene vessel for different milling times up to 25 h. The rotational speed was 250 rpm, at a ball-to-powder weight ratio (BPR) of 10:1. All the handling, mixing, and milling steps were performed under a high purity argon atmosphere in a glove box.

The morphology of the milled powders was analyzed by scanning electron microscopy (SEM, CamScan Series 2, Obducat, Sweden). A high performance laser particle size analyzer (LA-950, Horiba) with a measuring range from 10 nm to 3 mm was used to characterize the particle size and size distribution of the milled powders. The microstructure, especially the presence and distribution of the reinforcing phase, was investigated on polished milled-powder sections by high resolution SEM (Hitachi S-2700). The images were acquired in the backscattered electron (BSE) mode. For elemental analyses, the SEM was equipped with an energy dispersion spectrometer (EDS).

In order to verify the reinforcement distribution and grain structure of the milled powders, transmission electron microscopy (TEM) was employed. The TEM observations were performed on a Tecnai G2 20 S-TWIN TEM with a LaB6 cathode operating at 200 kV. In the TEM analysis, both bright- and dark-field image techniques, coupled with selected area diffraction (SAD) and EDS were used to characterize specimens prepared by the focused ion beam (FIB) technique. The statistical grain size distribution was estimated from several dark-field micrographs in which around 100 grains were evaluated.

X-ray diffraction (XRD) analysis was carried out in a Panalytical X'Pert Pro diffractometer with Cu-K $\alpha$  radiation between 20° and 80° to determine the crystallite size and the induced lattice strain (micro-strain) in the Mg matrix of the milled nanocomposite powders. The average crystallite size and lattice strain of the Mg matrix were obtained from the XRD peak broadening after refinement and analysis of the diffractograms by an adopted Rietveld's software (FullProf suite-2016). Instrumental resolution parameters for the Rietveld analysis were obtained from a standard silicon specimen. The analysis of the crystallite size and microstrain was conducted by Williamson-Hall approach for deconvoluting size and strain contribution to the X-ray line broadening. According to this approach, the X-ray line broadening is a sum of the contribution from small crystallite size and lattice strain present in the material [27]. The Williamson-Hall approach is described as follows:

$$\beta_{hkl} \cos \theta = \frac{0.9\lambda}{D} + 4\varepsilon \sin \theta$$

where  $\beta_{hkl}$  is the diffraction peak width at half maximum intensity (FWHM),  $\theta$  is the Bragg diffraction angle,  $\lambda$  is the wavelength of the radiation used,  $D$  is the average crystallite size, and  $\varepsilon$  is the average lattice strain.

To evaluate mechanical properties of the milled powders, they were mounted and carefully polished. The mechanical properties of the powders were explored by nanoindentation measurements at room temperature performed using a Nanoindenter (Hysitron TI950 TriboIndenter) system equipped with standard Berkovich diamond indenter tip and a scanning probe microscope (SPM). The indentation was made at a maximum load of about 1 mN and under a loading and unloading rate of 200  $\mu\text{N s}^{-1}$ . The dwell time at maximum load was kept for 10 s. For each sample, at least twenty independent indentations were made of different polished powders. Oliver and Pharr method was used for analyzing nanoindentation load-displacement data to determine nanohardness ( $H_n$ ) and reduced elastic modulus ( $E_r$ ) of the mounted milled powders [28]. By this method, nanohardness and reduced elastic modulus are determined by the data of one complete cycle of loading and unloading. The indentation nanohardness ( $H_n$ ) is expressed as:

$$H_n = \frac{P_{max}}{A_c}$$

where  $A_c$  is the contact area at the maximum load and  $P_{max}$  is the maximum normal load.

The reduced elastic modulus ( $E_r$ ), which represents the elastic deformation that occurs in both sample and indenter tip is estimated from the initial slope of the unloading curve using the following correlation:

$$E_r = \frac{\sqrt{\pi} S}{2 A_c}$$

where  $E_r$ ,  $A_c$  and  $S$  are the reduced elastic modulus, the contact area and the stiffness, respectively.

## 5.4. Results

### 5.4.1 Morphological characterization

The morphology of the MM, M1S<sub>n</sub> and M10S<sub>n</sub> milled powders after a milling time of 25 h is shown in Fig. 1. As can be seen the nanocomposite powders reinforced with 10 vol% SiC<sub>n</sub> are finer and they exhibit a more equiaxed morphology than that of the Mg-1 vol% SiC<sub>n</sub>, M1S<sub>n</sub>, nanocomposite powders and pure Mg milled powders without SiC<sub>n</sub>, MM. The results show that addition of the SiC<sub>n</sub> nanoparticles changes the behavior of the powders during the mechanical milling process leading to reduction of the particle size, as described in our previous work [29]. The change in the particle size was confirmed by measurements of the particle size distribution of the milled powders. The average median diameter, D50, of the milled particles decreases significantly from 47.1 μm for MM powders to 22.5 μm for M1Sn and 9.4 μm for M10Sn nanocomposite powders.

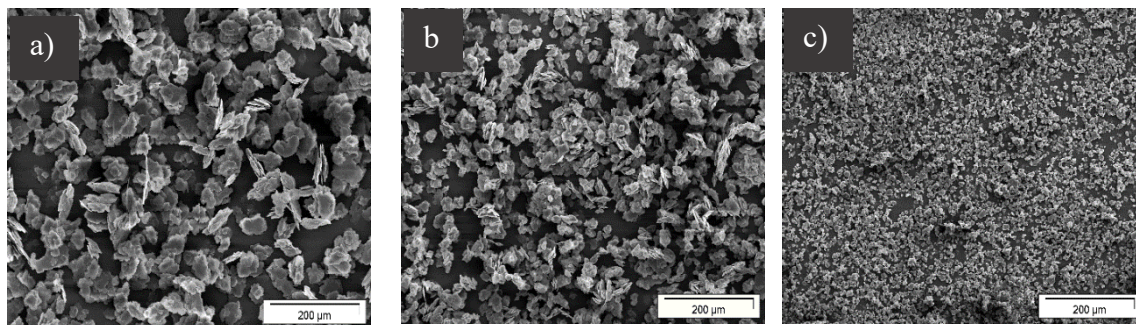


**Fig. 1.** Morphology of the milled powders a) MM, b) M1S<sub>n</sub> and c) M10S<sub>n</sub> after 25h mechanical milling

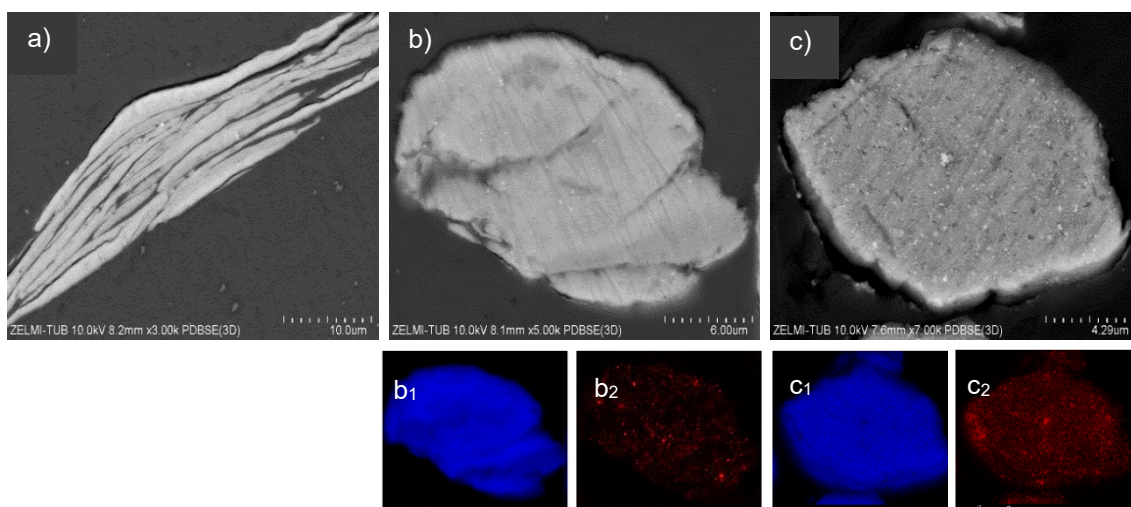
### 5.4.2 Microstructural characterization

Fig. 2 shows the back scattered electron images and the corresponding EDS maps of Mg and silicon taken from cross section of a particle of the MM, M1S<sub>n</sub> and M10S<sub>n</sub> milled powders after 25 h of milling process. The composite milled powders, M1S<sub>n</sub> and M10S<sub>n</sub>, indicate equiaxial shaped particles with a uniform distribution of SiC<sub>n</sub> nanoparticles (Fig. 2 b, c). This suggests that the cyclic welding/fracture processes have already reached a steady state after 25 h milling.

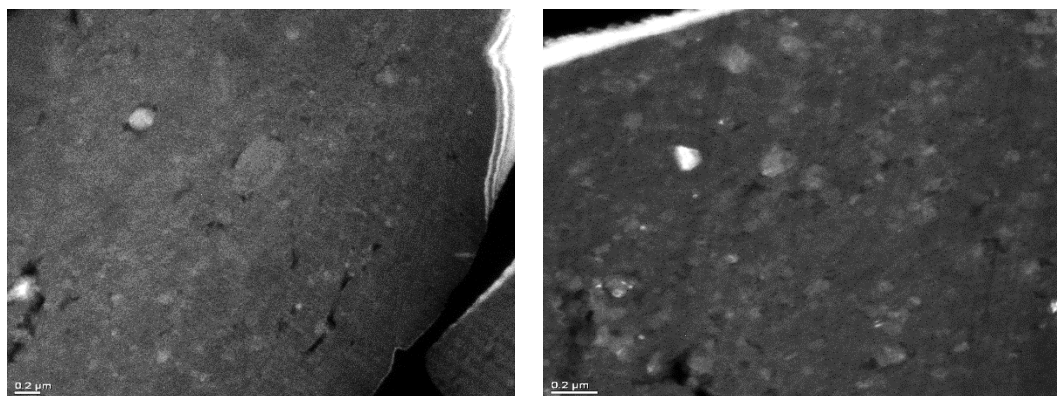
The interfacial boundaries are no longer visible in the M10S<sub>n</sub> milled powder, while a few continuous boundaries between the joined particles in the M1S<sub>n</sub> milled powder are still visible. Comparing with the composite milled powders, it must be noted that the cross section of the MM milled powder shows a layered structure after 25 h milling and the interfacial boundaries between several deformed and welded particles can be clearly observed. The elemental maps of Mg and silicon, as the main elements in the matrix and the reinforcing phase, of the M1S<sub>n</sub> and M10S<sub>n</sub> nanocomposite powders are shown in Fig.

2. It is seen that both elements are uniformly distributed throughout the nanocomposite particles. This emphasize the homogeneous distribution of the SiC<sub>n</sub> nanoparticles within the Mg matrix after 25 h of mechanical milling for reinforcement contents up to 10 vol%.

Fig. 3 shows dispersion of the SiC<sub>n</sub> nanoparticles through elemental contrast characterization by Z-contrast TEM imaging. In this method the more brighter particles in the image corresponding to much heavier elements (here SiC) and the dark area showing lighter elements (here Mg). The Z-contrast images once more reveal that the SiC<sub>n</sub> nanoparticles are uniformly embedded within the Mg matrix and no sign of remarkable clustering or agglomeration of the nanoparticles can be found in both M1S<sub>n</sub> and M10Sn milled powders.



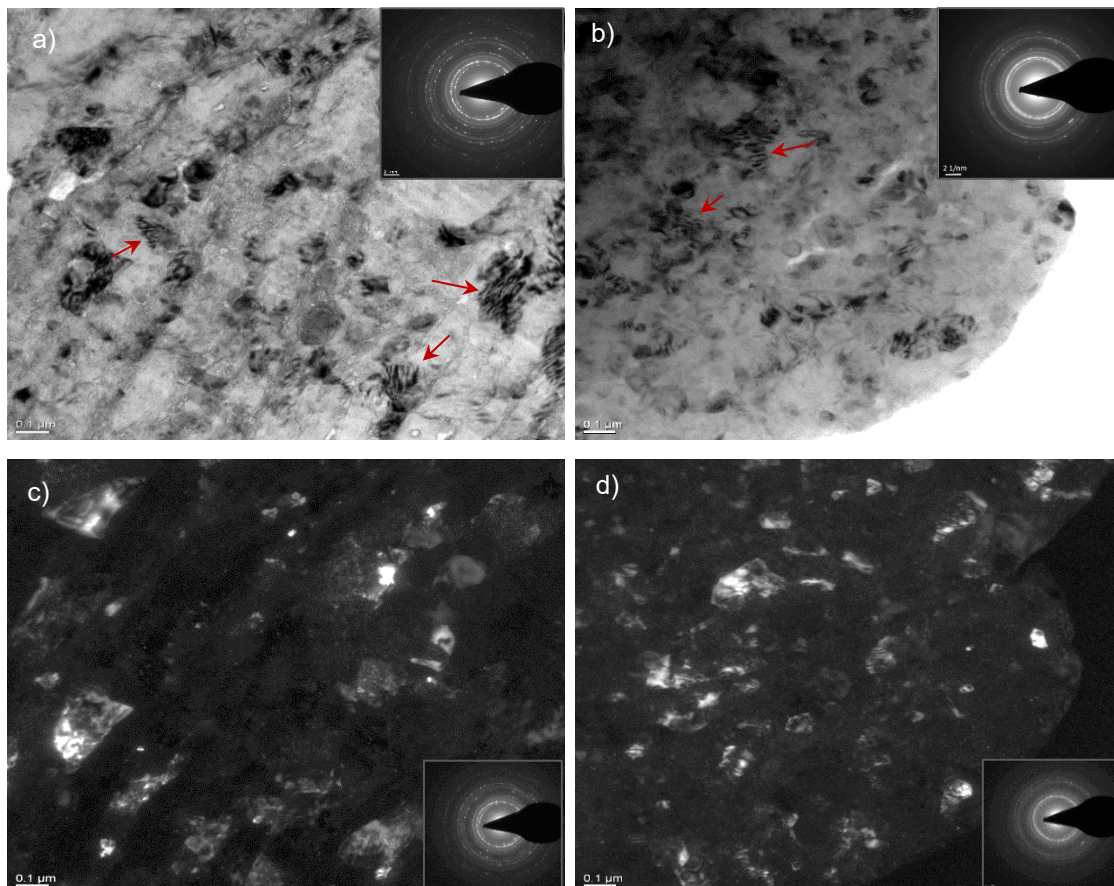
**Fig. 2.** Back scattered electron images of cross section of a) MM, b) M1S<sub>n</sub> and c) M10S<sub>n</sub> milled powder with the corresponding elemental mapping of Mg (b<sub>1</sub>, c<sub>1</sub>; blue) and silicon (b<sub>2</sub>, c<sub>2</sub>; red) of M1S<sub>n</sub> and M10S<sub>n</sub>, respectively



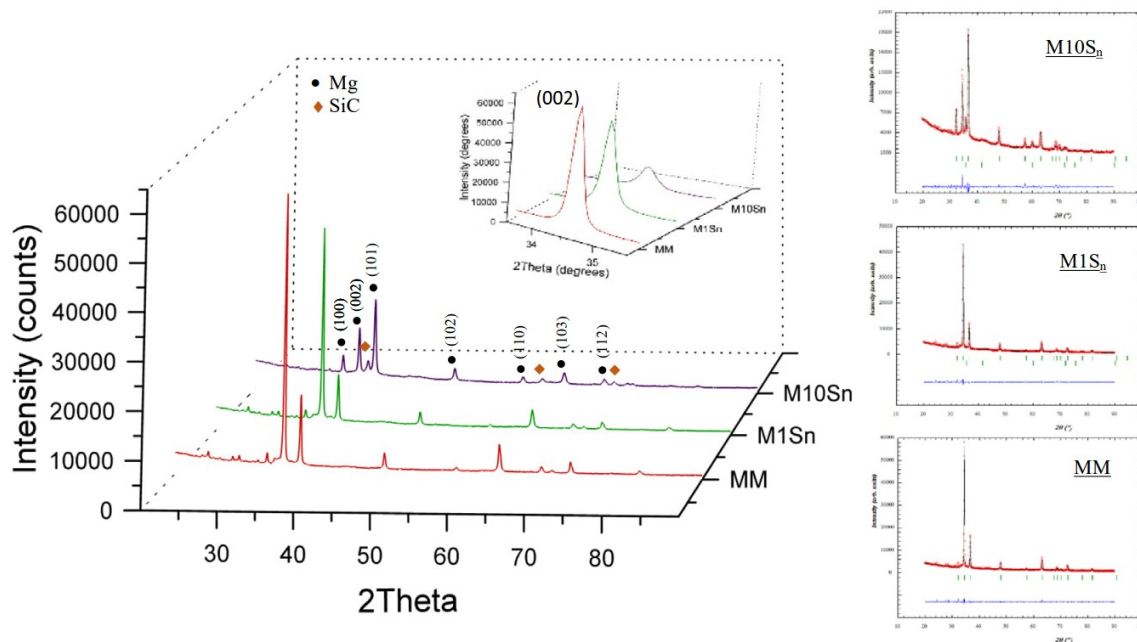
**Fig. 3.** TEM micrographs with Z-contrast of the a) M1S<sub>n</sub> and b) M10S<sub>n</sub> milled powder

Fig. 4(a, b) and (c, d) show the bright field and the dark-field TEM micrographs with corresponding SAD pattern of the milled M1S<sub>n</sub> and M10S<sub>n</sub> powder obtained by selecting the strongest reflection of Mg, namely the (002) Bragg reflection. The TEM micrographs

show near-equiaxed grain morphology with separated well-defined grain boundaries in both milled powders. However, a small number of elongated grains were found in the M1S<sub>n</sub> powder. The feature can be clearly seen also in the dark-field images. Moreover, from the microstructure, we can find that, interior of the most grains of Mg matrix is practically dislocation free, suggesting the occurrence of a dynamic reorganization process. Although, some regime still contained heavily disoriented grains with high density of dislocations (marked in Fig. 4(a, b)). Based on the TEM micrographs no sign of twins was observed in the nanostructured Mg matrix. The SAD patterns show continuous rings and can be indexed according to cubic  $\beta$ -SiC phase and hexagonal close-packed (hcp) Mg matrix. The continuous rings confirm that the Mg grains of the milled powders have been refined remarkably to nano-scale with random crystallographic orientation and high angle grain boundaries. The corresponding SAD pattern of the M10S<sub>n</sub> milled powder shows diffused spots, which implies an increase in the misorientations of grain boundaries and finer microstructure compared to those of the M1S<sub>n</sub> milled powder. The average crystallite size of Mg estimated from statistical crystallite size distribution of several dark-field micrographs was found to be 115.35 and 58.24 nm for M1Sn and M10Sn, respectively.



**Fig. 4.** a, b) TEM bright field micrographs and c, d) TEM dark field micrographs of M1S<sub>n</sub> and M10S<sub>n</sub> nanocomposite powder with the corresponding SAD pattern, respectively.



**Fig. 5.** XRD patterns of MM, M1Sn and M10Sn milled powders with an inserted magnified view of the (002) Mg peak and graphical output of Rietveld refinement analysis for MM, M1Sn and M10Sn respectively (lobs (black): experimental intensity; lcal (red): calculated intensity). (For interpretation of the references to color in this figure legend, the reader is referred to the web version of this article.)

Fig. 5 shows the XRD spectra of the MM, M1Sn and M10Sn milled powders and magnified views of the (002) reflex of Mg. In addition to the Mg peaks, the peaks corresponding to the  $\beta$ -SiC<sub>n</sub> phase are also observed in the nanocomposite powders. Based on the results the intensity of the  $\beta$ -SiC peaks increase with increasing nanoparticle content. In addition, with increasing the SiC<sub>n</sub> content, broadening in the Mg peaks is observed while their maximum intensity decreases. The XRD patterns of the milled powders were refined to determine the crystallite size and the lattice microstrain of the Mg matrix. The measured profile was fitted by a pseudo-Voigt function, which allows in most cases a better modeling of the measured XRD patterns than pure Gauss or Cauchy functions [30]. The results of the Rietveld refinement of the XRD patterns of the MM, M1Sn and M10Sn milled powders are inserted in Fig. 5. It is seen that the experimental and refined results are in very good agreement together. The values of the mean crystallite size and accumulation of lattice strain evaluated by the Williamson-Hall approach are presented in Table 1. Based on the results, the crystallite size of Mg in the composites is smaller than that in the MM, which is remarkably smaller in higher volume fractions of SiC<sub>n</sub> nanoparticles up to a content of 10%. The increasing trend of microstrain values parallel to higher volume fraction of the SiC<sub>n</sub> nanoparticles are in good agreement with higher degree of deformation and our expectations.

### 5.4.3 Nanoindentation

The load-displacement curves obtained from nanoindentation test of the MM, M1S<sub>n</sub> and M10S<sub>n</sub> powders after 25 h milling are represented in Fig. 6. The results of as-received pure Mg powder was also analyzed as a reference for comparison. The typical shape of the load-displacement curves indicates that the milled powders follow an elastic-plastic behavior. It is observed that the loading-unloading curves are to be smooth for all tests. However, the pop-in effect appears in the loading curves of the as-received pure Mg powder. The curves shifted to the left and maximum depth is reduced through the mechanical milling and addition of SiC<sub>n</sub> nanoparticles. The data obtained from analysis of the load-displacement curves are given in Table 2. It is seen that the values of the nanohardness ( $H_n$ ) and reduced elastic modulus ( $E_r$ ) of the milled powders are considerably higher than those of the as-received pure Mg powder. For example, the results showed nearly 62% and 37% enhancement in the nanohardness and reduced elastic modulus of the MM milled powder as compared to those of the as-received pure Mg powder, respectively.

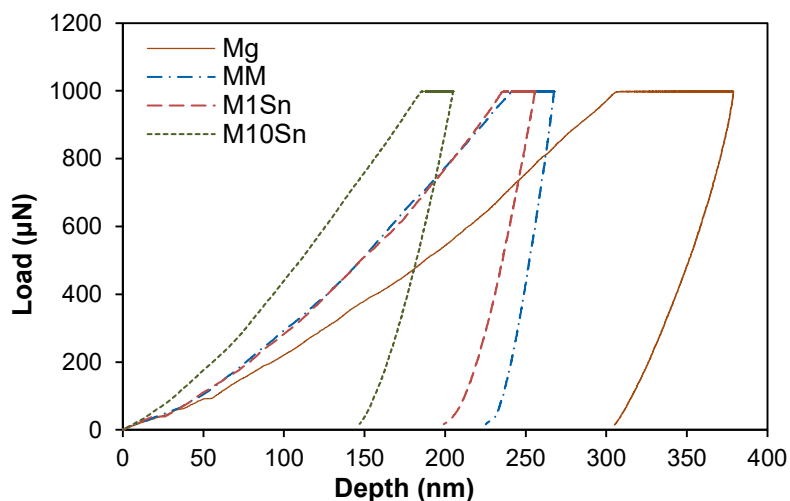


**Fig. 6.** Load- displacement curves obtained from nanoindentation with a maximum load of 1 mN.

Table 2- Nanoindentation values of Mg, MM, M1S<sub>n</sub> and M10S<sub>n</sub> powders

Powder	Max depth (nm)	Reduced elastic modulus, $E_r$ (GPa)	Nanohardness, $H_n$ (GPa)	Ratio of $H_n/E_r \times 10^2$
As-received Mg	356.12	10.51	0.32	3.43
MM	293.86	14.47	0.52	4.04
M1S <sub>n</sub>	274.27	16.29	0.59	4.11
M10S <sub>n</sub>	205.33	22.17	1.11	5.56

As can be seen also in Fig. 7, addition of  $\text{SiC}_n$  nanoparticles significantly enhance the reduced elastic modulus and nanohardness of the milled powders. For instance, the reduced elastic modulus values are 14.47 GPa and 16.29 GPa for MM and  $\text{M1S}_n$ , respectively, which means nearly 12.5% enhancement of elasticity with the addition of such very small amount of nanoparticle. More surprisingly, adding 10 vol% of  $\text{SiC}_n$  nanoparticles into the Mg greatly increased the reduced elastic modulus to 22.17 GPa, a nearly 53% increment. It is seen that the nanohardness of the powders follow a similar trend. The nanohardness of the  $\text{M1S}_n$  and  $\text{M10S}_n$  show 13.4% and 113.1% enhancement compared to that of the MM milled powder. In order to compare the work hardening behavior of the milled powders, the ratio of nanohardness and reduced elastic modulus ( $H_n/E_r$ ) values was estimated. Increase in the  $H_n/E_r$  value is an indicator of the elevated work hardening due to the mechanical milling and  $\text{SiC}_n$  nanoparticles.

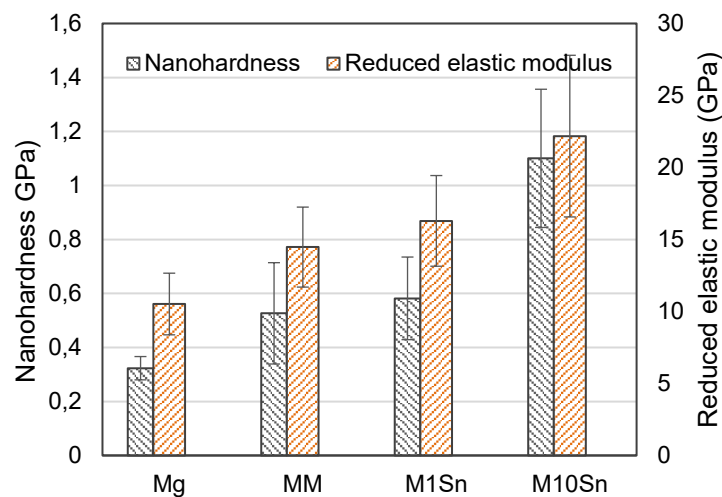


**Fig. 7.** Effect of mechanical milling and volume fraction of  $\text{SiC}_n$  nanoparticle on nanohardness and reduced elastic modulus.

The scanning probe microscopy (SPM) images of one typical indent at maximum load as well as the penetration profile of the MM,  $\text{M1S}_n$  and  $\text{M10S}_n$  milled powders are shown in Fig. 8. Based on the results the triangular impressions of the indents seem smooth with no signs of crack initiation. Observing no apparent pile-ups or sink-ins around the indent edges point to the fact that the similar rate of plastic material flow occurs under application of the indentation load. It can be observed that the  $\text{M10S}_n$  exhibit the smallest indent and the least penetration depth compared to the rest samples, which can be attributed to high content of the hard nanoparticles.

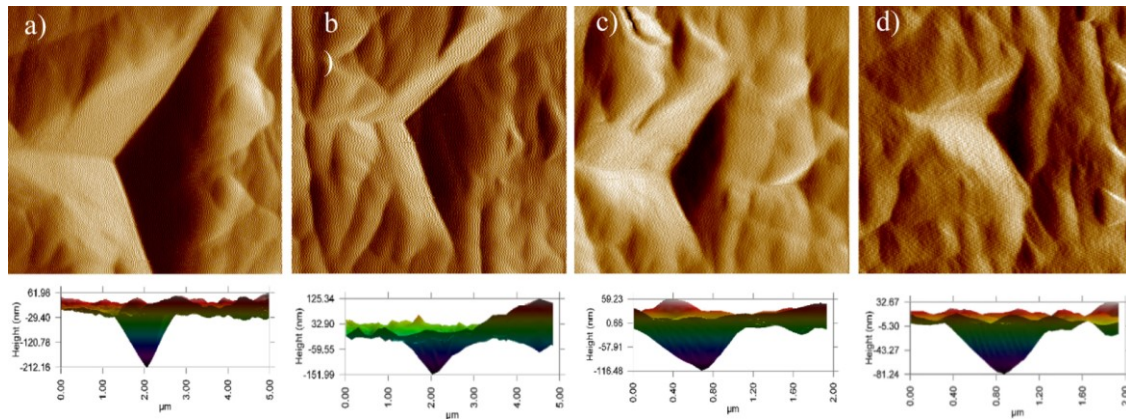


**Fig. 8.** The SPM images of the residual imprints for (a) Mg (b) MM, (c) M1S<sub>n</sub> and (d) M10S<sub>n</sub> milled powder and the corresponding profile for depth of penetration (scan area = 2 × 2 μm).

## 5.5. Discussion

The results of the microstructure characterization approve homogenous distribution of even high volume fraction (10 vol%) of nanoparticles in Mg matrix through mechanical milling process. The method can be used to get an acceptable distribution of nanoparticles which is still a key challenge in manufacturing process of the nanocomposites. The milling process also reduce the size of Mg matrix grain to nano-scale which can improve mechanical properties of the nanocomposite alone. The grain refinement and lattice strain in the milled powders is processed by severe local plastic deformation due to the mechanical milling. Furthermore, existence of the hard SiCn nanoparticles can promote the local plastic deformation and work hardening rate of the Mg matrix which accelerate the grain refinement. The fine nanoparticles are acting as a barrier against free movement of the dislocations leading to accumulation of dislocations which results in dislocation tangles and networks. This can explain the high value of lattice strain and crystal defects in the M10S<sub>n</sub> compared to those of the M1S<sub>n</sub> and MM milled powders. However, the amount of internal lattice strain in the Mg matrix after 25 h milling are not enormous which can be attributed to annihilation of dislocations and conversion of subgrains/cells into nanograins.

The grains of the Mg matrix show a mostly dislocation-free structure after 25 h milling process which implies reaching to a steady-state grain size due to elimination of dislocations. During the milling process the dislocations rearrange into cell structures and deformation shear bands and finally evolve into nano-sized crystallites with high-angle grain boundaries. Hence, rearrangement and elimination of the existing dislocations in addition to the difficulty of dislocation generation at the Mg matrix with nanocrystalline size can explain the remarkable fraction of dislocation-free grains in the

Mg structure even though still a few number of dislocations are remained inside some grains structure.

Based on the TEM observation no evidence of twins has found in the nanostructured Mg matrix even after severe plastic deformation due to the mechanical milling and hard  $\text{SiC}_n$  nanoparticles up to 10 vol%. The later results suggest that deformation twinning is not the dominant plastic deformation mechanism in the milled Mg powders in this study. Here, twinning is expected to become significantly suppressed in the nanocrystalline Mg composites due to a remarkably shorter dislocation glide path and an easy release of stress concentration through cross slip, grain boundary sliding and non-basal slip in the fine Mg grains. The unfavorable twinning in hexagonal close-packed alloys has been also reported, where grain size is reduced below a couple of microns [31,32].

Recent studies [33,34] have reported that the pop-in behavior in the load-displacement curves of coarse-grained pure Mg and AZ31 was associated with the appearance of  $\{1012\}$  twins on the surface. The occurrence of pop-in event in the load-displacement curve of the as-received Mg implies that deformation twinning can be regarded as one of the deformation models in the Mg with coarse grain size. While, the pop-in effect disappears in the nanoindentation tests of milled Mg powders. It can represent that deformation twinning can hardly be observed in Mg with nano grain size (in  $\text{M10S}_n$ ) and even with ultrafine grain size (in MM and  $\text{M1S}_n$ ).

The nanoindentation results clearly revealed that the mechanical milling contributes to increase in both reduced elastic modulus and nanohardness of the Mg powders. Although it may be difficult to correlate the values determined from mounted powders with bulk counterparts, it is valuable to compare the results of different powders measured under the same conditions. The enhanced nanohardness in the MM milled can be attributed to the work hardening and grain refining occurring during the ball milling process. While, the elevated nanohardness of the milled nanocomposite powders,  $\text{M1S}_n$  and  $\text{M10S}_n$ , is believed to be due to possible strengthening mechanisms including Orowan strengthening based on bowing of dislocation by reinforcing particles, Hall-Petch strengthening based on grain refinement and enhanced dislocation density strengthening [35]. Indeed, the enhancement of the mechanical properties of the nanocomposite is attributed to the pinning effect of grain boundaries occurring on the Mg matrix in presence of the reinforcing  $\text{SiC}_n$  nanoparticles. The nanoparticles simultaneously hinder the movement of the dislocations which additionally increase the harness of the metal. The high rate of work hardening ( $H_n/E$ ) in the nanocomposite milled powders is a result of restricted dislocation movement which is happening within the Mg nanocrystalline matrix reinforced by  $\text{SiC}_n$  nanoparticles. The significant achieved enhancement of nanohardness in the  $\text{M10S}_n$  nanocomposite powder can be owed to

the uniform distribution of the SiC<sub>n</sub> nanoparticles in the Mg matrix. In fact, a uniform distribution of nanoparticles is imperative to reach the effective strengthening capacity of the reinforcement in the matrix.

The obtained increments in the reduced elastic modulus of the nanocomposite milled powders could be attributed to the fact that the SiC<sub>n</sub> nanoparticles have higher elastic modulus (~250 GPa) than Mg matrix which lead to increase overall elastic modulus of the nanocomposites as the SiC<sub>n</sub> volume  $f$  increases. The remarkable difference in reduced elastic modulus of the milled pure Mg (14.47 GPa) when compared to that of as-received pure Mg (10.51 GPa) reveal this fact that the mechanical milling cause to enhance elastic modulus of the Mg powders. The main possible contributions to the increase of reduced elastic modulus in MM are: (i) the grain size reduction down to the ultrafine-grained regime since the modulus/rigidity of the grain boundary phase could be higher than the modulus of the grain interior/crystallite [36], (ii) the presence of MgO nanoparticles in Mg matrix originating from the stable oxide layer (3-5 nm) on the as-received Mg powders and reformation of a new layer on the Mg particles during milling which can be fragmented and introduced into the Mg powders by mechanical milling [37]. However, the presence of any oxide or carbide was not observed both during the X-ray analysis (Fig. 5) as well as TEM (SAD pattern) analysis (Fig. 4 inset).

## 5.6. Conclusion

The microstructure characterization and mechanical properties of the ball milled Mg powders were studied to evaluate role of the SiC<sub>n</sub> nanoparticles and mechanical milling process. The following conclusions can be drawn based on the results obtained:

- The mechanical milling for 25 h developed a homogeneous distribution of the SiC<sub>n</sub> nanoparticles up to 10 vol% within the Mg matrix. It seems it could be an effective solution to get a homogeneous incorporation of high volume fraction of reinforcement components which has been a key challenge in processing of nanocomposites so far.
- The TEM micrographs revealed a large number of dislocation-free nanocrystalline Mg grains after 25 h milling. No sign of twins was detected and observed which suggests that twinning deformation in the nanocrystalline Mg is suppressed even after the severe plastic deformation. The finer crystallite sizes of the Mg-phase were obtained with increasing volume fractions of the SiC<sub>n</sub> nanoparticles.
- The milled Mg matrix incorporated with the hard SiC<sub>n</sub> nanoparticles showed a lower load-displacement which is attributed to higher resistance to the indenter. The results indicated that the nanohardness and reduced elastic modulus of the Mg powder have been improved significantly through the mechanical milling and addition of the SiC<sub>n</sub>

nanoparticles which could confirm the achievement of the effective strengthening capacity of the materials.

## 5.7. Acknowledgements

The authors gratefully acknowledge the financial support by the Deutsche Forschungsgemeinschaft (DFG) (Grant number KA 4325/1-1). We also acknowledge Prof. Dr. Ralf Riedel, Non-Metallic Inorganic Materials group (Institute of Materials Science at TU Darmstadt), for providing support and cooperation to produce the materials. The authors further thank Prof. Dr. Stephan Drusch, Department of Food Technology and Food Material Science (TU Berlin), for the particle size distribution measurements, Ulrich Gernert and Sören Selve at the central electron microscopy unit of TU Berlin (ZELMI) for their support during SEM and TEM analyses, and Dr. Stefan Berendts, Institute of Chemistry (TU Berlin) for assistance with the X-ray diffraction measurements.

## 5.8. References

- [1] Q.C. Jiang, H.Y. Wang, B.X. Ma, Y. Wang, F. Zhao, Fabrication of B<sub>4</sub>C particulate reinforced magnesium matrix composite by powder metallurgy, *J. Alloys Compd.* 386 (2005) 177–181.
- [2] Y. Cai, M.J. Tan, G.J. Shen, H.Q. Su, Microstructure and heterogeneous nucleation phenomena in cast SiC particles reinforced magnesium composite, *Mater. Sci. Eng. A* 282 (2000) 232–239.
- [3] Z. Xiuqing, W. Haowei, L. Lihua, T. Xinying, M. Naiheng, The mechanical properties of magnesium matrix composites reinforced with (TiB<sub>2</sub> + TiC) ceramic particulates, *Mater. Lett.* 59 (2005) 2105–2109.
- [4] X.J. Wang, K. Wu, W.X. Huang, H.F. Zhang, M.Y. Zheng, D.L. Peng, Study on fracture behavior of particulate reinforced magnesium matrix composite using in situ SEM, *Compos. Sci. Technol.* 67 (2007) 2253–2260.
- [5] P. Poddar, V.C. Srivastava, P.K. De, K.L. Sahoo, Processing and mechanical properties of SiC reinforced cast magnesium matrix composites by stir casting process, *Mater. Sci. Eng. A* 460-461 (2007) 357–364.
- [6] A. Bochenek, K.N. Braszczyńska, Structural analysis of the MgAl<sub>5</sub> matrix cast composites containing SiC particles, *Mater. Sci. Eng. A* 290 (2000) 122–127.
- [7] B.L. Mordike, T. Ebert, Magnesium: properties - applications - potential, *Mater. Sci. Eng. A* 302 (2001) 37–45.
- [8] H. Zou, X. Zeng, C. Zhai, W. Ding, The effects of yttrium element on microstructure and mechanical properties of Mg–5 wt.% Zn–2 wt.% Al alloy, *Mater. Sci. Eng. A* 402 (2005) 142–148.
- [9] T. Al-Samman, X. Li, Sheet texture modification in magnesium-based alloys by selective rare earth alloying, *Mater. Sci. Eng. A* 528 (2011) 3809–3822.

- [10] Q.B. Nguyen, M. Gupta, Increasing significantly the failure strain and work of fracture of solidification processed AZ31B using nano- $\text{Al}_2\text{O}_3$  particulates, *J. Alloys Compd.* 459 (2008) 244–250.
- [11] C.S. Goh, J. Wei, L.C. Lee, M. Gupta, Simultaneous enhancement in strength and ductility by reinforcing magnesium with carbon nanotubes, *Mater. Sci. Eng. A* 423 (2006) 153–156.
- [12] S.F. Hassan, M. Gupta, Effect of length scale of  $\text{Al}_2\text{O}_3$  particulates on microstructural and tensile properties of elemental mg, *Mater. Sci. Eng. A* 425 (2006) 22–27.
- [13] H. Dieringa, Properties of magnesium alloys reinforced with nanoparticles and carbon nanotubes: a review, *J. Mater. Sci.* 46 (2011) 289–306.
- [14] S. Sankaranarayanan, U.P. Nayak, R.K. Sabat, S. Suwas, A. Almajid, M. Gupta, Nano-ZnO particle addition to monolithic magnesium for enhanced tensile and compressive response, *J. Alloys Compd.* 615 (2014) 211–219.
- [15] S.C. Tjong, Novel nanoparticle-reinforced metal matrix composites with enhanced mechanical properties, *Adv. Eng. Mater.* 9 (8) (2007) 639–652.
- [16] C.S. Goh, J. Wei, L.C. Lee, M. Gupta, Development of novel carbon nanotube reinforced magnesium nanocomposites using the powder metallurgy technique, *Nanotechnology* 17 (2006) 7–12.
- [17] Q.B. Nguyen, M. Gupta, Increasing significantly the failure strain and work of fracture of solidification processed AZ31B using nano- $\text{Al}_2\text{O}_3$  particulates, *J. Alloys Compd.* 459 (2008) 244–250.
- [18] S.F. Hassan, M. Gupta, Development of nano- $\text{Y}_2\text{O}_3$  containing magnesium nanocomposites using solidification processing, *J. Alloys Compd.* 429 (2007) 176–183.
- [19] K.B. Nie, X.J. Wang, K. Wu, X.S. Hu, M.Y. Zheng, Development of SiCp/AZ91 magnesium matrix nanocomposites using ultrasonic vibration, *Mater. Sci. Eng. A* 540 (2012) 123–129.
- [20] Q.B. Nguyen, K.S. Tun, C.Y.H. Lim, W.L.E. Wong, M. Gupta, Influence of nano-alumina and sub-micron copper on mechanical properties of magnesium alloy AZ31, *Compos. Part B* 55 (2013) 486–491.
- [21] A. Das, S.P. Harimkar, Effect of graphene nanoplate and silicon carbide nanoparticle reinforcement on mechanical and tribological properties of spark plasma sintered magnesium matrix composites, *J. Mater. Sci. Technol.* 30 (2014) 1059–1070.
- [22] K.K. Deng, K. Wu, Y.W. Wu, K.B. Nie, M.Y. Zheng, Effect of submicron size SiC particulates on microstructure and mechanical properties of AZ91 magnesium matrix composites, *J. Alloys Compd.* 504 (2010) 542–547.
- [23] N. Zhao, P. Nash, X. Yang, The effect of mechanical alloying on SiC distribution and the properties of 6061 aluminum composite, *J. Mater. Process. Technol.* 170 (2005) 586–592.
- [24] J.B. Fogagnolo, E.M. Ruiz-Navas, M.H. Robert, J.M. Torralba, 6061 Al reinforced with silicon nitride particles processed by mechanical milling, *Scr. Mater.* 47 (2002) 243–248.
- [25] D.L. Zhang, Processing of advanced materials using high-energy mechanical milling, *Prog. Mater. Sci.* 49 (2004) 537–560.

- [26] L. Lu, M.O. Lai, C.W. Ng, Enhanced mechanical properties of an Al based metal matrix composite prepared using mechanical alloying, *Mater. Sci. Eng. A* 252 (1998) 203–211.
- [27] G.K. Williamson, W.H. Hall, X-ray line broadening from filed aluminum and wolfram, *Acta Metall.* 1 (1953) 22–31.
- [28] W.C. Oliver, G.M. Pharr, An improved technique for determining hardness and elastic modulus using load and displacement sensing indentation experiments, *J. Mater. Res.* 7 (1992) 1564–1583.
- [29] D. Penther, C. Fleck, A. Ghasemi, R. Riedel, S. Kamrani, Development and characterization of Mg-SiC nanocomposite powders synthesized by mechanical milling, *Key Eng. Mater.* 742 (2017) 165–172.
- [30] G.K. Wertheim, M.A. Butler, K.W. West, D.N.E. Buchanan, Determination of the Gaussian and Lorentzian content of experimental line shapes, *Rev. Sci. Instrum.* (11) (1974) 1369–1371.
- [31] Q. Yang, A.K. Ghosh, Deformation behavior of ultrafine-grain (UFG) AZ31B mg alloy at room temperature, *Acta Mater.* 54 (2006) 5159–5170.
- [32] M.R. Barnett, A rationale for the strong dependence of mechanical twinning on grain size, *Scr. Mater.* 59 (2008) 696–698.
- [33] J. Bočan, J. Maňák, A. Jäger, Nanomechanical analysis of AZ31 magnesium alloy and pure magnesium correlated with crystallographic orientation, *Mater. Sci. Eng. A* 644 (2015) 121–128.
- [34] T. Guo, F. Siska, M.R. Barnett, Distinguishing between slip and twinning events during nanoindentation of magnesium alloy AZ31, *Scr. Mater.* 110 (2016) 10–13.
- [35] J.B. Ferguson, F.S. Jaber, C.S. Kim, P. Rohatgi, K. Cho, On the strength and strain to failure in particle-reinforced magnesium metal-matrix nanocomposites (Mg MMNCs), *Mater. Sci. Eng. A* 558 (2012) 193–204.
- [36] H. Gleiter, Nanocrystalline materials, *Prog. Mater. Sci.* 33 (1989) 223–315.
- [37] M. Wolff, T. Ebel, M. Dahms, Sintering of magnesium, *Adv. Eng. Mater.* 12 (2010) 829–836.

---

## 6. Manuscript III

Effect of SiC nanoparticles on manufacturing process, microstructure and hardness of Mg-SiC nanocomposites produced by mechanical milling and hot extrusion

### Publication notification

#### *Keywords:*

Magnesium, SiC nanoparticle, powder, nanocomposite, MMC, ball milling

#### *Authors:*

D. Penther<sup>1</sup>, A. Ghasemi<sup>1</sup>, R. Riedel<sup>2</sup>, C. Fleck<sup>1</sup>, S. Kamrani<sup>1</sup>

<sup>1</sup>Department of Materials Science and Engineering, Technische Universität Berlin, 10623 Berlin, Germany

<sup>2</sup>Department of Materials and Earth Sciences, Technische Universität Darmstadt, 64287 Darmstadt, Germany

*Journal:* Materials Science & Engineering A, 738, pp. 264–272, October 2018

*DOI:* 10.1016/j.msea.2018.09.106

#### *Author contributions:*

I produced the powders and performed parameter studies at TU Darmstadt regarding the manufacturing processes comprising uniaxial and cold-isostatic pressing and sintering, and produced the bulk materials. Prof. Dr. Dr. h.c. Ralf Riedel provided a workplace and the equipment at TU Darmstadt. Together with Dr. Sepideh Kamrani, I planned the investigations. I analysed the compressibility behaviour, characterised the microstructure by SEM and performed the Vickers hardness tests. Dr. Sepideh Kamrani is also responsible for project funding and supervision of the project. Prof. Dr. Claudia Fleck provided a workplace and facilities at TU Berlin and supported me as thesis supervisor. I wrote the manuscript, which was reviewed by all co-authors.

## 6.1. Abstract

The production of fully dense Mg-SiC nanocomposites with a homogeneous distribution of SiC nanoparticles through powder metallurgy techniques is still a challenging issue. We propose to combine sintering and hot extrusion of mechanically milled composite powders to encompass the known difficulties of conventional processing. Here, we report on the effect of SiC nanoparticle content on the compressibility, microstructure and hardness of SiC-Mg nanocomposites during the different consolidation steps. Cold-isostatic pressing, sintering and indirect hot extrusion were used for compaction and consolidation. Near dense Mg-SiC nanocomposites with 1 and 10 vol% SiC nanoparticles were successfully produced with a homogeneous distribution of the nanoparticles. Scanning electron microscopy, X-ray diffraction and transmission electron microscopy were used to characterise the microstructure of the powders and of the sintered and extruded Mg-SiC nanocomposites. Vickers microhardness tests were done to reveal the hardening effect after sintering and extrusion. The nanoparticles pin the grain boundaries and foster dynamic recrystallisation, so that a nanograined Mg matrix develops and is preserved even after the final consolidation step. The results further show a very good interface adherence between nanoparticles and matrix contributing to the high hardness of the nanocomposites.

## 6.2. Introduction

Magnesium (Mg) is the lightest structural metal with a density of  $1.74 \text{ g/cm}^3$ . In addition, Mg exhibits a good stiffness-to-weight ratio [1], high dimensional stability and superior damping characteristics compared to aluminium [2, 3]. These attributes make Mg and its alloys a popular choice for different applications as for example in the automobile, aerospace and electronics industries. Mg has a hexagonal close-packed crystal structure with nearly ideal  $c/a$  ratio. Thus, it acts more brittle and possesses a low ductility, low elastic modulus and limited strength compared to other metals like aluminium. In order to better exploit the light weight construction potential of Mg, significant efforts have been made to develop Mg matrix composites. These combine the favourable properties of pure magnesium and of the reinforcing phase and lead to a material with low density and yet superior specific mechanical properties, such as strength, stiffness and creep resistance [4–6]. Although strength can be increased by particulate reinforcements, in some cases their addition deteriorates the ductility of the obtained composites, especially in case of micron sized reinforcing particles [7]. Recent work showed the potential of nano particulates as reinforcements enhancing both strength and ductility of Mg composites [8]. In comparison to micron-sized particles nano-sized reinforcements

possess a higher ultimate strength and they can therefore much better withstand deformation without fracturing [5, 9–12]. In addition, nanoparticles have been shown to effectively pin grain boundaries in composites. Consequently, they hinder grain growth during powder metallurgical processing leading to an increase in ductility [13].

The functionality of nanoparticles, and, therefore, their impact on the mechanical properties of the composite, is, however, strongly dependent on their uniform distribution in the matrix. Because of their small size and large specific surface area, it is extremely difficult to incorporate, distribute and disperse them uniformly in the Mg matrix. Mechanical milling is a promising method for dispersion of small reinforcing particles into metal powders. We previously successfully achieved a homogeneous distribution of SiC nanoparticles in Mg powders for reinforcement contents of up to 10 vol% by mechanical milling. The composite powders further exhibited a nanocrystalline structure [14, 15].

The compressibility of the powder is one of the most important characteristics of metallic powders as it determines the potential in decreasing the volume, thus allowing a formation of a dense green body under appropriate pressure [16]. Consolidation of the powders is the following step, usually done by a typical powder metallurgical process, comprising pressing and sintering [17], or by extrusion [18]. However, effective consolidation of milled nanocomposite powders into bulk samples that possess both full density and a nanocrystalline structure, is challenging. The compressibility of metallic powders is strongly influenced by particle morphology and plastic deformability. During mechanical milling the powders experience a high degree of plastic deformation and strain hardening which is accelerated by the hard reinforcing particles [16, 19, 20]. The resulting high hardness and low ductility impede additional plastic deformation of the composite powder particles during the following compaction stages [9]. Therefore, after consolidation, powders containing nanoparticles usually reveal a higher level of porosity and more irregular pores with a broad pore size distribution [21]. These microstructural phenomena significantly decrease the mechanical properties of nanocomposites [5, 22, 23].

We therefore chose to combine powder processing by mechanical milling to produce Mg-SiC nanocomposite powders, with a three-step consolidation process comprising cold-isostatic pressing, sintering and, additionally, hot extrusion, to produce fully dense Mg-SiC nanocomposites with a homogeneous distribution of SiC nanoparticles in the Mg matrix, for reinforcement contents of up to 10 vol%. Here, we present and discuss our findings regarding the evolution of the microstructure of the nanocomposites during the different powder compaction steps. The focus is on the effect of mechanical milling and of different volume fractions of nanoparticles on compaction and densification behaviour of Mg-SiC nanocomposites as well as on the microhardness.

### 6.3. Materials and methods

Mg powder with an average particle size of -325 mesh and SiC powder with an average particle size of 50 nm (SiC<sub>n</sub>) were used. All powders had a purity of 99.8 % and were supplied by Alfa Aesar. To produce Mg-SiC composite powders, the Mg powder was mixed with 1 or 10 vol% of SiC nanoparticles by high-energy mechanical milling up to 10 hours (10 vol% SiC) or 25 hours (1 vol% SiC) according to the procedure described previously [14]. Because no strong mechanical interlocking was achieved for the M10S<sub>n</sub> powder after a milling time of 25 h, milling time was reduced to reduce work hardening of the powders, among other phenomena, and consequently raising the compressibility. The composite powders will be referred to as M1S<sub>n</sub> and M10S<sub>n</sub>, respectively. For comparison, pure Mg without any reinforcement, named MM, was also milled. A high performance laser particle size analyser was used to characterize the particle size of the milled powders. Morphological changes and microstructural features of the milled powders during the different processing steps were analysed by scanning electron microscopy (SEM). Further, transmission electron microscopy was used to investigate the reinforcement distribution. Quasistatic nanoindentation was performed on embedded and polished powder particles using a Hysitron TI 950 TriboIndenter. At least 15 indents were executed on different powder particles. To compare the work hardening of the milled powders, the ratio of nanohardness and reduced elastic modulus ( $H/E_r$ ) was calculated. For further details regarding the analysing routines see our previous work [14, 15, 24].

To better understand the interactions between the different powder properties and the pressures used during pressing, compressibility tests were performed. For precompaction, the composite powders were uniaxially pressed with a pressure of 90 MPa and silicone oil as lubricant in a steel cylindrical die (10 mm inner diameter) with a hydraulic press (Paul-Otto (P/O) Weber GmbH). The green bodies were subsequently cold-isostatically pressed for further compaction, with pressures varying between 100 and 700 MPa. Based on the results of the compressibility tests, the milled powder composites were also precompacted by uniaxial pressing using silicone oil, however in a bigger steel die with a diameter of 20 mm with a pressure of 140 MPa and a holding time of 15 min. The green bodies were further compacted by cold-isostatic pressing (CIP) in a latex protective cover with a holding time of 10 min and the most favourable pressure of 700 MPa. The green bodies were subsequently sintered at 600 °C for 2 h in argon atmosphere. The sintered samples were ground to remove a potential oxide layer and indirect hot extruded at 400 °C with a press ratio of 22:1.

The relative density of each, the isostatically pressed, the sintered and the extruded samples was determined in ethanol by the Archimedes method. Theoretical maximum densities of the composites were calculated using the rule of mixtures considering the densities of Mg and SiC, 1.738 and 3.16 g/cm<sup>3</sup>, respectively.

The evolution of the microstructure and the SiC nanoparticle distribution of the samples after each processing step was investigated on ground and polished sections by light microscopy (DMR, Leica Microsystems) and by high resolution SEM (HRSEM, Hitachi S-2700). The reinforcement distribution and the grain structure of the Mg matrix were further evaluated qualitatively by transmission electron microscopy (TEM, Tecnai G<sup>2</sup> 20 S-TWIN, FEI), on specimens prepared by the focused ion beam (FIB) technique. Additionally, crystallite sizes of around 100 Mg grains were measured in dark field TEM micrographs to obtain a statistical crystallite size distribution. Further, scanning transmission electron microscopy (STEM) setup was used to perform energy-dispersive X-ray spectroscopy (EDS) mappings. X-ray diffraction patterns were recorded with the X'Pert Pro (PANalytical) to obtain information about the number and nature of the phases after extrusion. The width of the diffraction peaks was evaluated to determine the crystallite size of the Mg matrix by the Williamson-Hall method. For micro-Vickers hardness cross sections of the sintered and extruded samples were polished with 250 nm diamond spray (Struers) and tested on a Zwick 3212 hardness tester with a force of 1.961 N (HV 0.2) and a dwell time of 10 s.

## 6.4. Results

### 6.4.1 Powder characteristics

Figure 1 shows SEM micrographs of mechanically milled powders of MM and M1S<sub>n</sub> after 25 hours and of M10S<sub>n</sub> after 10 hours of milling. Milling times and average particle sizes of the different milled powders are summarized in Table 1. The addition of the SiC nanoparticles strongly influences the morphology of the milled powder particles. The MM milled powder particles are slightly deformed as compared to the original Mg powder and they show a flattened shape. Compared to the MM powders, the M1S<sub>n</sub> powder particles exhibit a more irregular shape and a smaller particle size which suggests enhanced welding and fracturing due to presence of only 1 vol% of SiC nanoparticles. The M10S<sub>n</sub> milled powders exhibit an even more equiaxed morphology and the particle size is significantly smaller, although only milled for 10 hours. All differences are statistically significant.

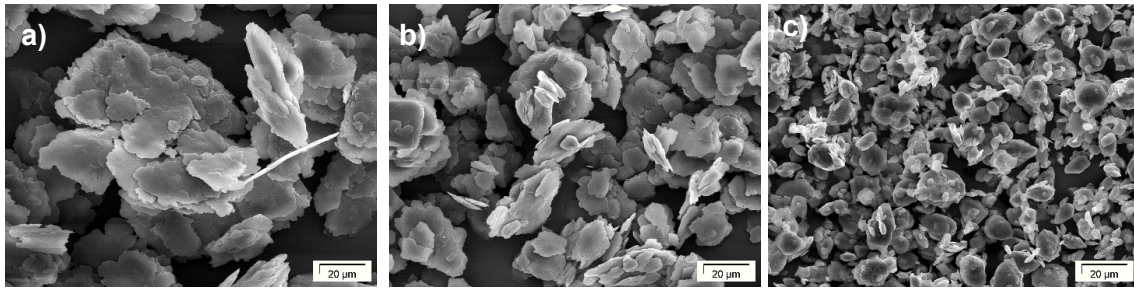


Figure 1. SEM images of the morphology of milled powders a) MM, b) M1S<sub>n</sub> after 25 h and c) M10S<sub>n</sub> after 10 h mechanical milling.

The change in morphology and the decrease in particle size with adding and increasing reinforcement contents emphasize the significant influence of the nanoparticles on the powder behaviour during mechanical milling.

Milling of the pure Mg-powder increases the nanohardness by about 62 % compared to the as-received pure Mg powder (table 1). With increasing volume fraction of SiC nanoparticles the nanohardness increases even more, to a value more than twice the nanohardness of MM and M1S<sub>n</sub> powders in case of M10S<sub>n</sub>. Mechanical milling alone and addition of SiC nanoparticles have a significant influence on the nanohardness of the powders. TEM analysis and SEM elemental mapping showed a homogeneous distribution of the SiC nanoparticles throughout the milled powders. Further details regarding the morphological and microstructural characteristics of the milled powders have been published previously [15, 24].

Table 1. Powder characteristics like reinforcement content, milling time, average particle size and nanohardness of Mg, MM, M1S<sub>n</sub> and M10S<sub>n</sub>. Values marked with \* are statistically highly significant (t-test).

	SiC content (vol%)	Milling time (h)	Average particle size ( $\mu\text{m}$ )	Nanohardness (GPa)
Mg	0	0	29.7	0.32
MM	0	25	47.1	0.52
M1S <sub>n</sub>	1	25	22.5	0.59
M10S <sub>n</sub>	10	10	10.1	1.41

## 6.4.2 Compressibility of powders

The milled Mg and composite powders show the typical compressibility behaviour expected for metal powders (fig. 2, table 2). The relative green density increases with increasing compaction pressure, however with a decreasing rate so that an increase in the pressure becomes less and less effective for achieving higher densities. The relative green density (RGD), that is density of the green bodies related to theoretical density of the composite, reached during cold isostatic pressing, decreases with increasing volume fraction of the nanoparticles. However, compared to the non-reinforced, MM, powder,

compressibility is only slightly affected by addition of 1 vol% of nanoparticles. For a pressure of 700 MPa, even the same RGD is reached for this nanocomposite and the milled Mg powders. In contrast, the addition of 10 vol% of nanoparticles has a much stronger effect on the compressibility.

The microstructure and shape of the pores indicate the differences in powder compressibility due to the presence of SiC nanoparticles (fig. 3). Two types of pores are observed within the green bodies: elongated pores, that appear crack-like, and ellipsoid pores. Both MM and M1S<sub>n</sub> green bodies exhibit mainly elongated pores with a uniform distribution. The elongated pores of the M1S<sub>n</sub> compact are shorter which may be due to the smaller particle size of the milled M1S<sub>n</sub> powder. In the compact with 10 vol% SiC nanoparticles ellipsoid pores are the dominant pore morphology which form a higher porosity level of the M10S<sub>n</sub> compact.

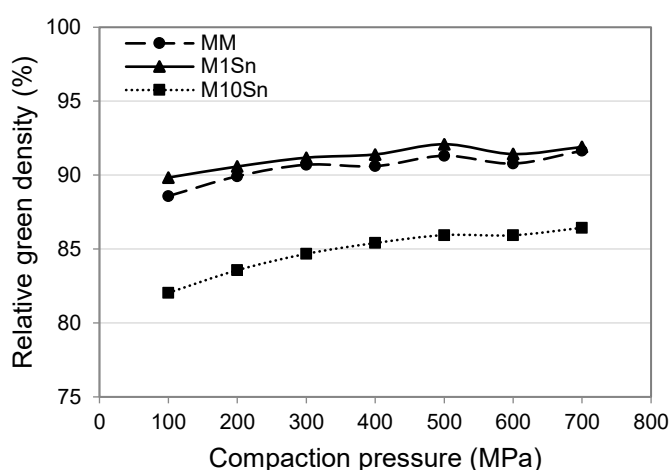


Figure 2. Compressibility curves - relative green density (%) over compaction pressure (MPa) - of mechanically milled pure Mg powder, MM, and composite powders, M1S<sub>n</sub> and M10S<sub>n</sub> determined for cold-isostatic pressing with different pressures.

Table 2. Relative densities of MM, M1S<sub>n</sub> and M10S<sub>n</sub> after cold isostatic pressing with different pressures.

Pressure (MPa)	Relative density (%)						
	100	200	300	400	500	600	700
MM	88.6	89.9	90.7	90.6	91.3	90.8	91.6
M1S <sub>n</sub>	89.4	90.2	90.8	91.0	91.7	91.0	91.5
M10S <sub>n</sub>	82.0	83.6	84.7	85.4	86.0	85.9	86.7

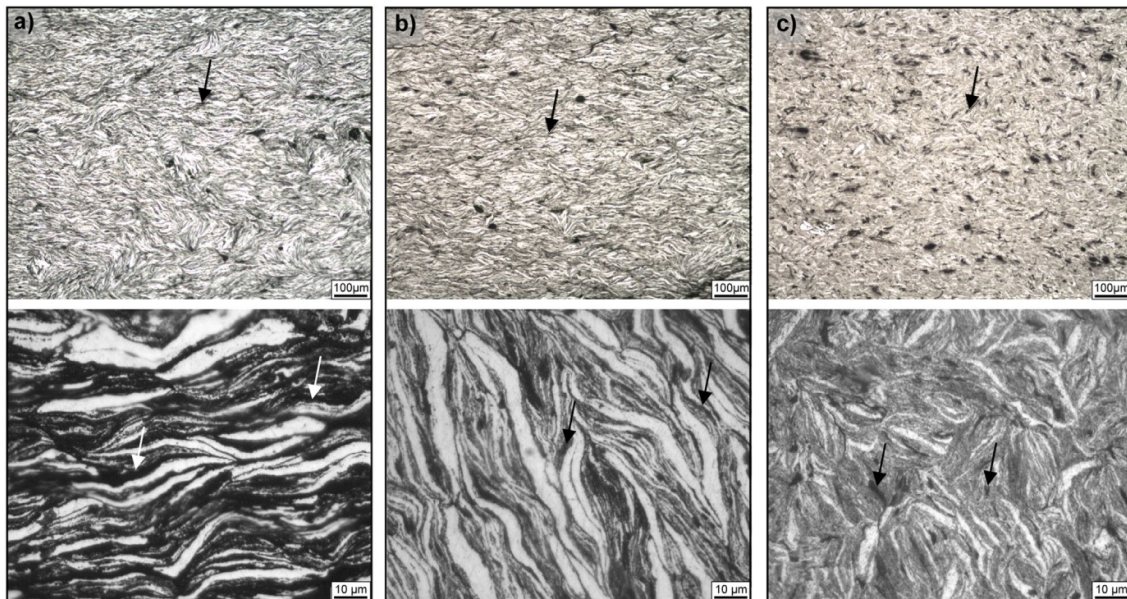


Figure 3. Light micrographs of cross-sections of cold-isostatically pressed green bodies: a) MM, b) M1S<sub>n</sub> and c) M10S<sub>n</sub> (compaction pressure 700 MPa).

### 6.4.3 Consolidation to nearly dense materials

Consolidation comprises all processing steps to produce (nearly) dense materials, from powder compaction, that is pre-pressing and cold isostatic pressing, over sintering to hot extrusion. The effect of the different consolidation steps on the relative density is illustrated in fig. 4, values in table 3. As to be expected, the density of the samples increases due to sintering and hot extrusion as compared to the isostatically pressed green bodies. Sintering alone has a moderate effect on the densification, seen in the only slight increase in density of all compositions. Light micrographs of the sintered samples demonstrate, however, a clearly visible effect of sintering on the microstructure and the pore shape. After sintering, MM exhibits a uniform distribution of equiaxed pores, in contrast to the elongated shape after cold isostatic pressing. M1S<sub>n</sub> contains a mixture of equiaxed and elongated pores. The latter are shorter, however than after cold isostatic pressing. This change in pore shape may be attributed to the formation of sinter necks. The composition with 10 vol% nanoparticles, M10S<sub>n</sub>, still shows a uniform distribution of slightly elongated pores in micron size, thus smaller than after cold-isostatic pressing.

Table 3. Relative density (%) of sintered and hot extruded MM, M1S<sub>n</sub> and M10S<sub>n</sub>.

Relative density (%)	MM	M1S <sub>n</sub>	M10S <sub>n</sub>
Sintered	93.8	93.8	87.9
Extruded	99.0	99.9	99.4

Subsequent hot extrusion is a crucial step to achieve nearly 100 % relative density in all samples (fig. 4, 5). Independent of the reinforcement content, hot extrusion closes the

majority of the pores still present in the sintered samples, due to the vigorous plastic deformation and recrystallisation. The extruded samples therefore all reach very high relative densities of more than 98 %. For M10S<sub>n</sub>, the strongest increase in relative density, by 11.6 % versus the sintered state, is achieved. For M1S<sub>n</sub> a relative density of 99.9 % is reached, which is the highest value for all compositions investigated. Secondary electron (SE) SEM observations confirmed the nearly pore-free microstructure after extrusion. The remaining pores are mainly in the sub-micron and nanometre range (fig. 5). The backscattered electron (BSE) micrographs additionally show the uniformly distributed SiC nanoparticles.

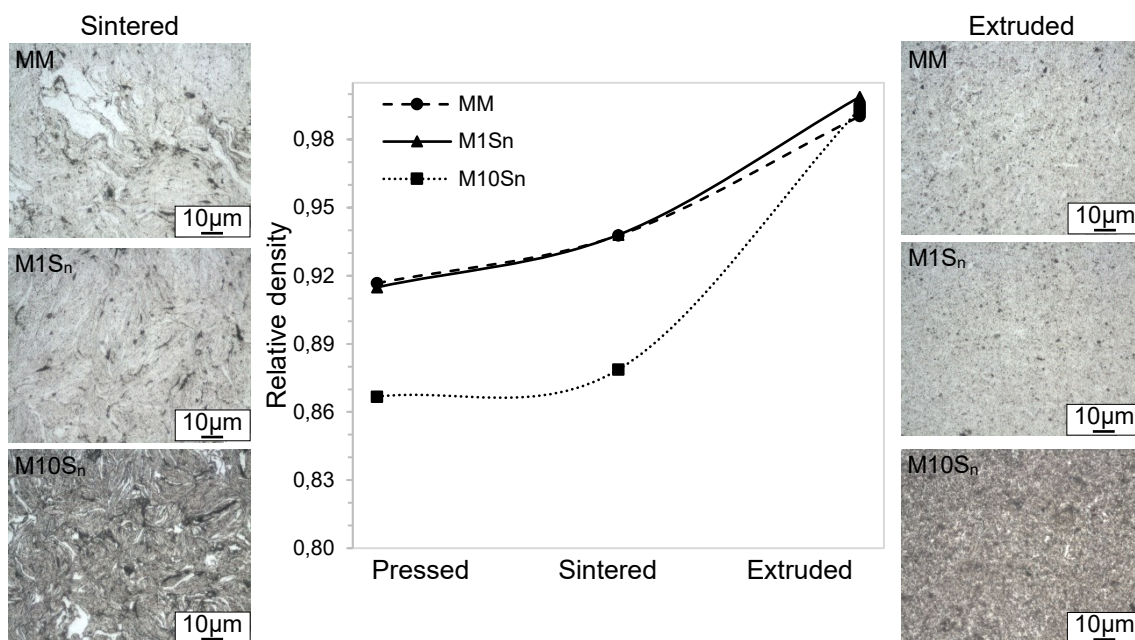


Figure 4. Relative density of pressed, sintered and hot extruded MM, M1S<sub>n</sub> and M10S<sub>n</sub>, together with light micrographs showing the microstructures for the sintered and extruded states.

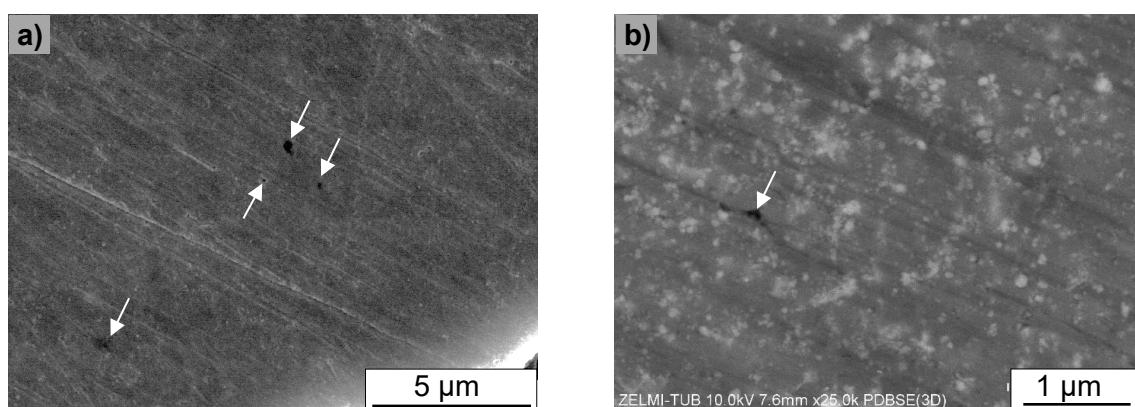


Figure 5. SEM micrographs of cross-sections through a hot extruded M1S<sub>n</sub> nanocomposite sample: a) SE-SEM, showing nanopores, marked with white arrows; b) BSE-HRSEM showing the uniform distribution of SiC nanoparticles (white) and two nanopores (black).

#### 6.4.4 TEM microstructural characterisation

The TEM micrographs and the statistical grain size distributions, derived from these images, of milled composite powders of M1S<sub>n</sub> and M10S<sub>n</sub> illustrated in Fig. 6a and b show a homogeneous distribution of SiC nanoparticles in the nanostructured Mg matrix. Both milled powders show a near-equiaxed grain morphology with well-defined grain boundaries. However, a number of elongated Mg grains were found in the M1S<sub>n</sub> powder, exemplarily marked in fig. 6a with dotted lines. In addition, some areas, marked with arrows, are observed which still contain grains with a high density of dislocations indicating high stress levels. Grain size distributions reveal average Mg grain sizes of 115 and 58 nm for M1S<sub>n</sub> and M10S<sub>n</sub> powder, respectively.

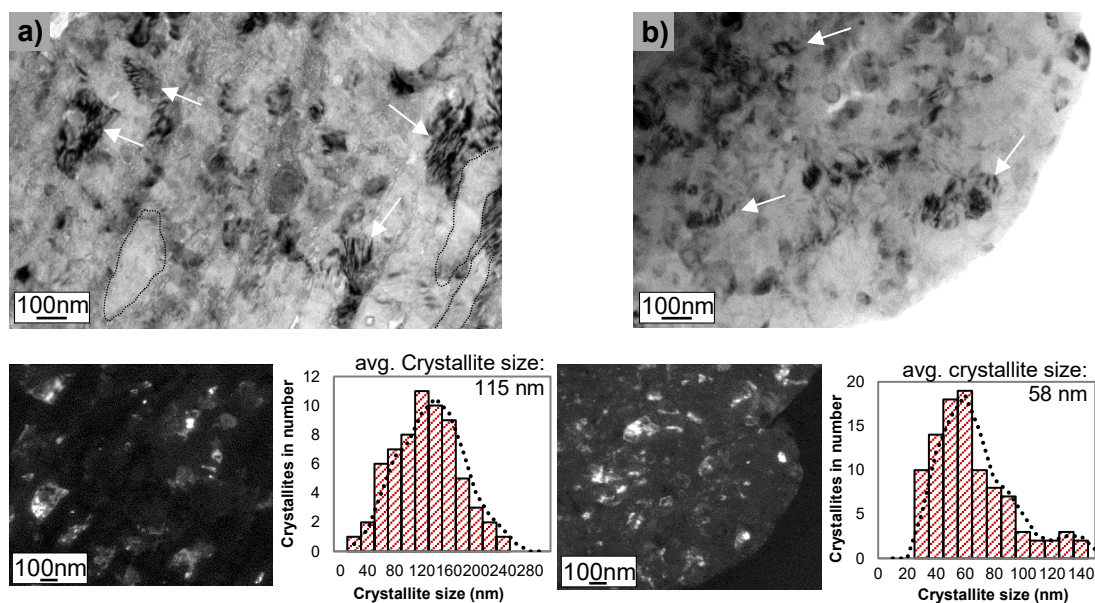


Figure 6. TEM bright field (top row) and dark field (bottom) micrographs and statistical grain size distribution of milled composite particles a) M1S<sub>n</sub>, elongated Mg grains, marked with dotted lines, and b) M10S<sub>n</sub> showing homogeneous distribution of SiC nanoparticles and high dislocation density.

Figure 7 and 8 show typical TEM micrographs and EDS results for the extruded nanocomposites. The bright field image (fig. 7a) highlights the homogeneous distribution of the SiC nanoparticles in the Mg matrix, as also observed by HRSEM (fig. 5b). The microstructure is mainly free of dislocations. In dark field imaging mode (fig. 7b), besides isolated small grains with strong diffraction intensities, there are bigger areas of dozens of small grains, one marked with dotted line, which show no dislocations in bright field mode indicating dynamic recrystallisation (DRX) occurred. The elemental map of silicon (fig. 7c) from the same area as shown in the bright field TEM micrograph in fig. 7a confirms the homogeneous distribution of the SiC nanoparticles. The elemental map of oxygen also reveals the presence of MgO. The statistical grain size distribution of extruded M1S<sub>n</sub>, fig. 7d, represents a moderately bimodal grain size distribution of submicron size grains with two peaks.

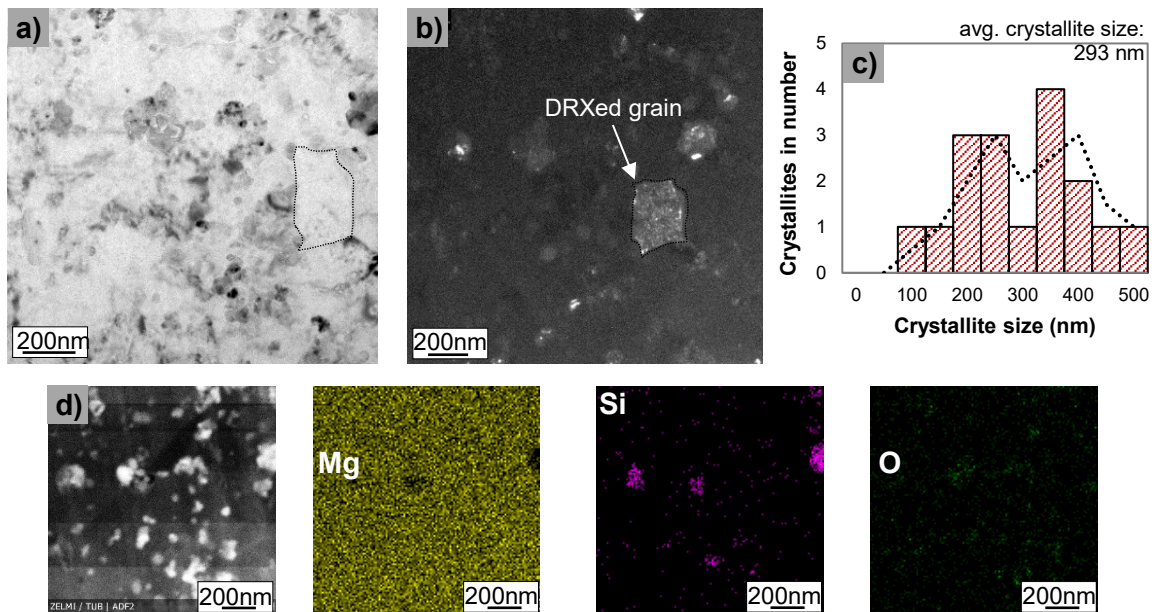


Figure 7. Microstructure of extruded M1Sn: a) TEM bright field; b) TEM dark field showing DRXed grain, marked with dotted line; c) statistical grain size distribution derived from the TEM micrographs; d) STEM image and elemental maps of magnesium, silicon and oxygen (same area as shown in a).

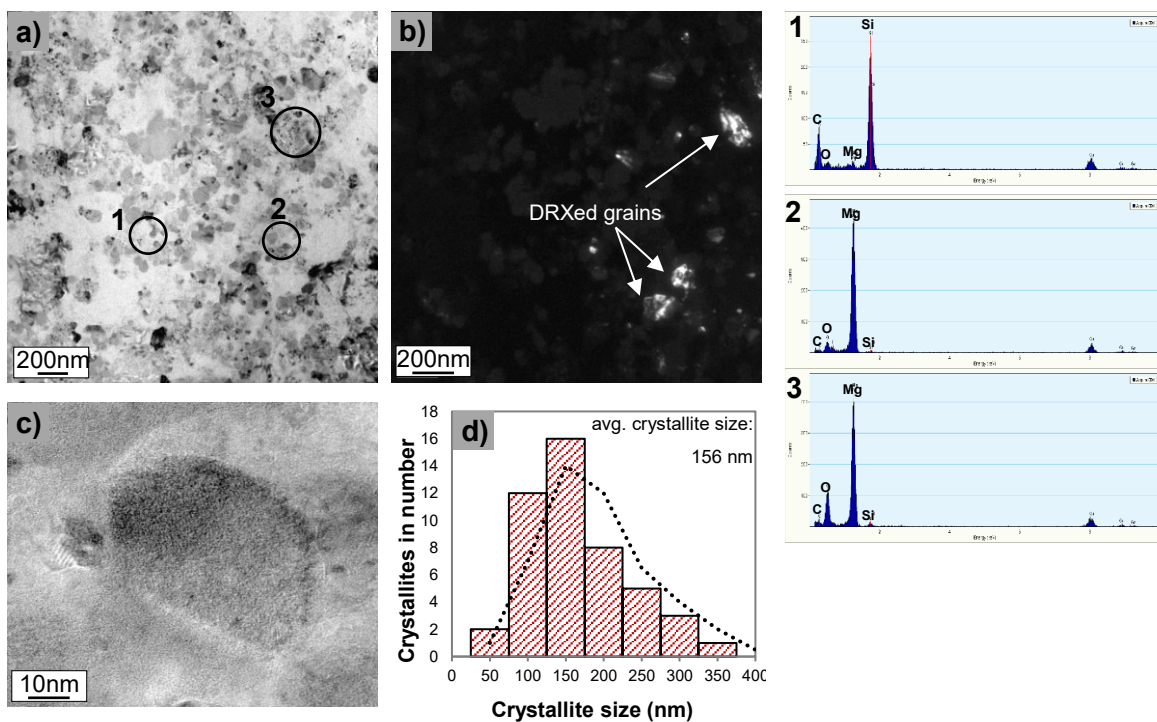


Figure 8. TEM micrographs of extruded M10Sn showing a) homogenous distribution of SiC nanoparticles in Mg matrix, with corresponding EDS spectra of marked circles; b) dark field showing DRXed grains; c) HRTEM of interface between SiC nanoparticle and Mg matrix; and d) statistical grain size distribution.

The bright field TEM micrograph of extruded  $M10S_n$  nanocomposite (fig. 8a), also reveals a homogeneous distribution of the SiC nanoparticles in a nanostructured Mg matrix which appears free of dislocations. With STEM-EDS, three point measurements, marked with 1 to 3 in fig. 8a, were performed. Point 1 was identified as SiC whereas point 2 shows pure magnesium. MgO nanoparticles marked as point 3 were also detected in the nanocomposite. The appearance of MgO was confirmed for all extruded samples by XRD analysis. These MgO particles may be assumed to originate from the native oxide layer on the Mg surface, which is broken down during the milling process, due to their nano-scale. High-resolution TEM images of the interface between a SiC nanoparticle and the surrounding Mg matrix (fig. 8c) show a continuously connected interface, indicating the SiC nanoparticles are very well embedded in Mg matrix without any detachment down to the atomic level. Compared to  $M1S_n$  the statistical grain size distribution of  $M10S_n$  reveals one peak with submicron size grains. It clearly reveals the achievement of an even finer submicron-grain size with increasing volume fractions of the SiC nanoparticles in both milled powder and extruded samples.

#### 6.4.5 Microhardness

Figure 9 shows the microhardness of MM,  $M1S_n$  and  $M10S_n$  samples after sintering and hot extrusion. The average HV 0.2 hardness increases with addition of the nanoparticles, and, for the composites, with increasing  $SiC_n$  content. Compared to the sintered state, the hardness significantly increases by more than 57 % due to hot extrusion. The extruded  $M10S_n$  composite possesses the highest value of 99.5 HV 0.2. This not only highlights the significant effect of the reinforcement content but also the important effect of the final extrusion step for the properties of the nanocomposites. All values are statistically significant.

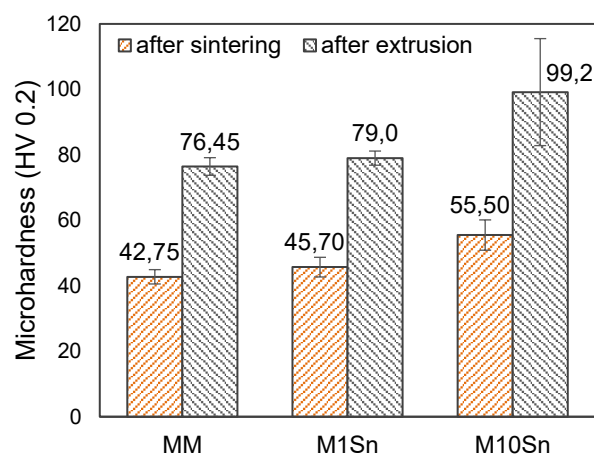


Figure 9. Average HV 0.2 microhardness of MM,  $M1S_n$  and  $M10S_n$  after sintering and hot extrusion. All values are statistically significant (t-test).

## 6.5. Discussion

With our novel processing scheme, comprising cold-isostatic pressing, sintering and hot-extrusion of mechanically milled composite powders we achieved nearly dense SiC-Mg nanocomposites with a high hardness. The microstructural characterisation revealed that the milling process reduces the grain size of the Mg matrix to the nano-scale which by itself is beneficial for the mechanical properties of the nanocomposites. Mechanical milling supports the grain refinement in the milled powders due to severe plastic deformation which is further accelerated by the hard SiC nanoparticles. Because of the high surface-to-volume ratio of the SiC nanoparticles severe plastic deformation occurs locally around the particles, leading to increased plastic deformation and an acceleration of the work hardening of the Mg matrix [25]. However, the high hardness of the composite powder particles prevents additional deformation during the following consolidation steps, resulting in difficulties in processing of the milled powders by the conventional compaction methods, comprising pressing and sintering only, or just hot extrusion. It is well known that rearrangement and plastic deformation of powder particles play an important role in the compressibility of composite powders, particularly for higher amounts of reinforcing particles.

For cold-isostatic pressing, increasing pressures lead to a higher degree of particle movement and plastic deformation, both required to reach higher levels of density and better bonding between the particles [26]. The M10S<sub>n</sub> milled powder particles are much harder than both the MM and the M1S<sub>n</sub> particles. Therefore, they can deform less, which partially explains the noticeably lower compressibility of this powder. An additional component is particle morphology and size. Equiaxed powder particles with a fine and uniform particle size distribution, as in M10S<sub>n</sub> (fig. 1), convey the applied far-field compressive stress to the evenly distributed neighbouring particles through their contact points (fig. 10), leading to a symmetrical local stress field. However, in case of particles with irregular, flake-like morphology, such as M1S<sub>n</sub> or MM, an asymmetrical local stress field develops, with a strong shear component. This leads to cold-welding of the powders [19]. The lower hardness, together with the higher specific surface and their flake-like shape allows a higher packing efficiency and better mechanical bonding of the flat particles. This, in consequence leads to a better compressibility of the powder with no or a lower reinforcement content.

The absolute particle size and the particle size distribution are further key factors that influence the compressibility of the milled powders. The surface area per unit mass increases due to the particle size reduction, which might increase the internal friction between the powder particles and consequently decreasing the flow rate [22].

In comparison to  $M10S_n$ , MM and  $M1S_n$  milled powders have a broader particle size distribution resulting in fine particles filling the interspace between the coarse particles, thus increasing the powder packing and the green density. Additionally, the Mg matrix experiences a stronger work hardening as the SiC nanoparticle content increases explaining the increased hardness of the  $M10S_n$  milled powders. The thus limited plastic deformation as well as the equiaxed, fine and a narrow particle size distribution of  $M10S_n$  significantly affected the lower deformation capability and lower degree of densification. The powder particle morphology also affects the formation of different shaped pores during powder compaction (Fig. 10). In case of spherical particles ( $M10S_n$ ), the pores have a semi-circular and irregular shape, while compaction of flat shaped particles (MM and  $M1S_n$ ) results in pores with elongated morphology.

Generally, during sintering, sinter necks form and pores tend to acquire a rounder shape, with a reduced surface energy. Nevertheless, sintering process is not enough to reach a dense composite. Therefore, subsequent extrusion is critically necessary to achieve nearly 100 % relative density.

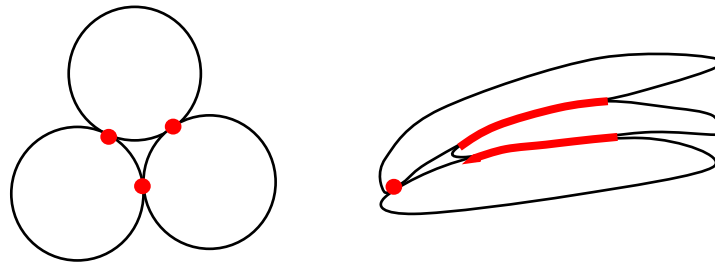


Figure 10. Schematic drawing of pore space and contact points between equiaxed and flat shaped powder particles during compaction.

Grain size refinement is well known to be the only strengthening mechanism which increases both strength and ductility of metals [8]. Thus, our nanocomposite powders with a nano-grained Mg matrix are an excellent starting point to produce nanocomposites with both high strength and high ductility. However, the corresponding large grain boundary energy results in a high tendency to grain growth during high temperature treatments. Grain growth during sintering and hot extrusion might therefore have been a serious complication during further processing of the milled  $M1S_n$  and  $M10S_n$  powders. Both  $M1S_n$  and  $M10S_n$  bulk nanocomposites, however, still exhibit an ultrafine grain structure. The SiC nanoparticles therefore effectively restrict grain growth during the consolidation steps at high temperature due to their pinning effect on grain boundaries, which can inhibit or delay the recrystallisation and grain growth of the matrix [27, 28]. Consequently, the grain size after extrusion decreases with increasing volume fraction of nanoparticles, and  $M1S_n$  with its more distantly spaced nanoparticle arrangement as compared to  $M10S_n$  exhibits a bimodal grain size distribution. Further, with addition of the SiC nanoparticles more defects are introduced into the Mg matrix during mechanical

milling. Thus much more deformation energy is stored. This leads to a larger driving force which in turn promotes dynamic recrystallisation (DRX) of the matrix during the hot deformation process. The dislocation-free ultrafine grains with a near-equiaxed morphology which are observed for both the M1S<sub>n</sub> and the M10S<sub>n</sub> nanocomposites indicate that DRX is indeed a process taking place.

All in all, our process allowed us to produce nearly pore-free SiC-Mg nanocomposites with evenly distributed nanoparticles in a nanograined Mg matrix which is an excellent result, especially for the M10S<sub>n</sub> samples with high content of SiC nanoparticles and the difficulties in densification. The few pores found are also in the nm-scale. The observed increase in hardness of the nanocomposites as compared to the milled pure Mg samples is due to effective interaction of several influencing parameters: (i) uniform distribution of SiC nanoparticles in the Mg matrix achieved by mechanical milling even for very high volume fractions of nanoparticles of up to 10 vol%, (ii) strengthening based on interactions with particles, that restrict or impede dislocation movement, such as the Orowan mechanism, (iii) strengthening by an ultrafine grain size of the matrix, achieved by mechanical milling and stabilised due to the pinning effect of the SiC nanoparticles, and (iv) an effective load transfer from the Mg matrix to the SiC nanoparticles due to a defect-free, intimate interfacial bond.

## 6.6. Conclusions

We studied the effect of different contents of SiC nanoparticles on the compressibility and consolidation of mechanically milled Mg composite powders in a newly developed process, combining pressing, sintering and hot extrusion of the milled powders. The following are our main results:

- The hardness of the composite powders increases due to mechanical milling which prevents additional deformation during the consolidation steps. With increasing pressure during cold-isostatic pressing, higher densities of the green bodies are reached, due to higher degrees of particle movement and plastic deformation. In case of milled powders, the milling process results in equiaxed and fine particles with a narrow particle size distribution, as in M10S<sub>n</sub>, have a lower deformation capability and allow a lower degree of densification, as compared to MM and M1S<sub>n</sub> powders with flat, pan-cake like particles.
- Nearly dense Mg-SiC nanocomposites were successfully produced, which is an excellent result, especially for the M10S<sub>n</sub> samples with their high content of SiC nanoparticles and the corresponding difficulties in densification.
- The nanocomposites exhibit a nanograined matrix, due to the effective pinning of the grain boundaries by the nanoparticles. This pinning restricts grain growth

during the high temperature consolidation steps, and the high degree of deformation energy stored during mechanical milling fosters dynamic recrystallisation, both ensuring the nm grain size of the composites.

The high hardness of the composites produced by this new process can be attributed to the mutually interactive influences of (i) a uniform distribution of SiC nanoparticles in the Mg matrix achieved by mechanical milling up to high particle contents, (ii) strengthening due to particle/dislocation interactions, (iii) strengthening by an ultrafine grain size achieved by mechanical milling and stabilized due to the pinning effect of the SiC nanoparticles, and (iv) effective load transfer from the Mg matrix to the SiC nanoparticles due to a defect-free matrix-reinforcement interface.

## 6.7. Acknowledgement

The authors gratefully acknowledge the financial support by the Deutsche Forschungsgemeinschaft (DFG) (grant number KA 4325/1-1). We also acknowledge the Non-Metallic Inorganic Materials group, Institute of Materials Science at TU Darmstadt, for providing support and cooperation to produce the materials. The authors further thank Ulrich Gernert and Sören Selve, central electron microscopy unit (ZELMI) of TU Berlin for their support during SEM and TEM analyses, Dr. Stefan Berendts, Institute of Chemistry, TU Berlin, for assistance with the X-ray diffraction measurements and Sören Müller and René Nitschke, Extrusion Research and Development Center (FZS), Metallic Materials, TU Berlin for execution and support during hot extrusion process.

## 6.8. References

- [1] M.R. Krishnadev, R. Angers, C.G.K. Nair, C. Huard, The structure and properties of magnesium-matrix composites, *JOM*. 45 (1993) 52–54. <https://doi.org/10.1007/BF03222407>.
- [2] A. Luo, J. Renaud, I. Nakatsugawa, J. Plourde, Magnesium castings for automotive applications, *JOM*. 47 (1995) 28–31. <https://doi.org/10.1007/BF03221226>.
- [3] T.M. Pollock, Weight loss with magnesium alloys, *Science*. 328 (2010) 986–987, doi:10.1126/science.1182848.
- [4] I.A. Ibrahim, F.A. Mohamed, E.J. Lavernia, Particulate reinforced metal matrix composites - A review, *J. Mat. Sci.* 26 (1991) 1137–1156. <https://doi.org/10.1007/BF00544448>.
- [5] S.C. Tjong, Novel Nanoparticle-Reinforced Metal Matrix Composites with Enhanced Mechanical Properties, *Adv. Eng. Mater.* 9 (2007) 639–652. <https://doi.org/10.1002/adem.200700106>.

- [6] M. Manoharan, S.C.V. Lim, M. Gupta, Application of a model for the work hardening behavior to Mg/SiC composites synthesized using a fluxless casting process, *Mater. Sci. Eng. A.* 333 (2002) 243–249. [https://doi.org/10.1016/S0921-5093\(01\)01845-7](https://doi.org/10.1016/S0921-5093(01)01845-7).
- [7] H.Z. Ye, X.Y. Liu, Review of recent studies in magnesium matrix composites, *J. Mater. Sci.* 39 (2004) 6153–6171. <https://doi.org/10.1023/B:JMSC.0000043583.47148.31>.
- [8] M.J. Shen, W.F. Ying, X.J. Wang, M.F. Zhang, K. Wu, Development of High Performance Magnesium Matrix Nanocomposites Using Nano-SiC Particulates as Reinforcement, *J. Mater. Eng. Perform.* 24 (2015) 3798–3807. <https://doi.org/10.1007/s11665-015-1707-7>.
- [9] C. Suryanarayana, N. Al-Aqeeli. Mechanically alloyed nanocomposites, *Prog. Mater. Sci.* 58 (2013) 383–502. <https://doi.org/10.1016/j.pmatsci.2012.10.001>.
- [10] N. Ramakrishnan, An analytical study on strengthening of particulate reinforced metal matrix composites, *Acta Mater.* 44 (1996) 69–77, [https://doi.org/10.1016/1359-6454\(95\)00150-9](https://doi.org/10.1016/1359-6454(95)00150-9).
- [11] J.S. Benjamin, Mechanical Alloying, *Sci. Am.* 234 (1976) 40–49. <https://doi.org/10.1038/scientificamerican0576-40>.
- [12] M.J. Shen, X.J. Wang, T. Ying, K. Wu, W.J. Song, Characteristics and mechanical properties of magnesium matrix composites reinforced with micron/submicron/nano SiC particles, *J. Alloys Compd.* 686 (2016) 831–840. <https://doi.org/10.1016/j.jallcom.2016.06.232>.
- [13] A. Sanaty-Zadeh, Comparison between current models for the strength of particulate-reinforced metal matrix nanocomposites with emphasis on consideration of Hall–Petch effect, *Mater. Sci. Eng. A.* 531 (2012) 112–118. <https://doi.org/10.1016/j.msea.2011.10.043>.
- [14] D. Penther, C. Fleck, A. Ghasemi, R. Riedel, S. Kamrani, Development and Characterization of Mg-SiC Nanocomposite Powders Synthesized by Mechanical Milling, *KEM.* 742 (2017) 165–172. <https://doi.org/10.4028/www.scientific.net/KEM.742.165>.
- [15] S. Kamrani, D. Penther, A. Ghasemi, R. Riedel, C. Fleck, Microstructural characterization of Mg-SiC nanocomposite synthesized by high energy ball milling, *Adv. Powder Technol.* 29 (2018) 1742–1748. <https://doi.org/10.1016/j.apt.2018.04.009>.
- [16] M. Moazami-Goudarzi, F. Akhlaghi, Effect of nanosized SiC particles addition to CP Al and Al–Mg powders on their compaction behaviour, *Powder Technol.* 245 (2013) 126–133. <https://doi.org/10.1016/j.powtec.2013.04.025>.
- [17] H. Ramezanalizadeh, M. Emamy, M. Shokouhimehr, A novel aluminum based nanocomposite with high strength and good ductility, *J. Alloys Compd.* 649 (2015) 461–473. <https://doi.org/10.1016/j.jallcom.2015.07.088>.
- [18] Y.B. Liu, S.C. Lim, L. Lu, M.O. Lai, Recent development in the fabrication of metal matrix-particulate composites using powder metallurgy techniques, *J. Mater. Sci.* 29 (1994) 1999–2007. <https://doi.org/10.1007/BF01154673>.
- [19] J.B. Fogagnolo, E.M. Ruiz-Navas, M.H. Robert, J.M. Torralba, The effects of mechanical alloying on the compressibility of aluminium matrix composite powder, *Mater. Sci. Eng. A.* 355 (2003) 50–55. [https://doi.org/10.1016/S0921-5093\(03\)00057-1](https://doi.org/10.1016/S0921-5093(03)00057-1).

- [20] K.A. Nazari, A. Nouri, T. Hilditch, Compressibility of a Ti-based alloy with varying amounts of surfactant prepared by high-energy ball milling, *Powder Technol.* 279 (2015) 33–41. <https://doi.org/10.1016/j.powtec.2015.03.044>.
- [21] X.L. Zhong, M. Gupta, Development of lead-free Sn–0.7Cu/Al<sub>2</sub>O<sub>3</sub> nanocomposite solders with superior strength, *J. Phys. D: Appl. Phys.* 41 (2008) 1–7. <https://doi.org/10.1088/0022-3727/41/9/095403>.
- [22] S.F. Hassan, M. Gupta, Creation of High Performance Mg Based Composite Containing Nano-Size Al<sub>2</sub>O<sub>3</sub> Particulates as Reinforcement, *JMNM.* 23 (2005) 151–154. <https://doi.org/10.4028/www.scientific.net/JMNM.23.151>.
- [23] S.F. Hassan, M. Gupta, Development of high performance magnesium nanocomposites using nano-Al<sub>2</sub>O<sub>3</sub> as reinforcement, *Mater. Sci. Eng. A.* 392 (2005) 163–168. <https://doi.org/10.1016/j.msea.2004.09.047>.
- [24] A. Ghasemi, D. Penther, S. Kamrani, Microstructure and nanoindentation analysis of Mg-SiC nanocomposite powders synthesized by mechanical milling, *Mater. Charact.* 142 (2018) 137–143. <https://doi.org/10.1016/j.matchar.2018.05.023>.
- [25] J.B. Fogagnolo, F. Velasco, M.H. Robert, J.M. Torralba, Effect of mechanical alloying on the morphology, microstructure and properties of aluminium matrix composite powders, *Mater. Sci. Eng. A.* 342 (2003) 131–143. [https://doi.org/10.1016/S0921-5093\(02\)00246-0](https://doi.org/10.1016/S0921-5093(02)00246-0).
- [26] A. Salvadori, S. Lee, A. Gillman, K. Matouš, C. Shuck, A. Mukasyan, M.T. Beason, I.E. Gunduz, S.F. Son, Numerical and experimental analysis of the Young's modulus of cold compacted powder materials, *Mech. of Mater.* 112 (2017) 56–70, <https://doi.org/10.1016/j.mechmat.2017.05.010>.
- [27] T. Sakai, A. Belyakov, R. Kaibyshev, H. Miura, J.J. Jonas, Dynamic and post-dynamic recrystallization under hot, cold and severe plastic deformation conditions, *Prog. Mater. Sci.* 60 (2014) 130–207. <https://doi.org/10.1016/j.pmatsci.2013.09.002>.
- [28] A. Belyakov, F.G. Wei, K. Tsuzaki, Y. Kimura, Y. Mishima, Incomplete recrystallization in cold worked steel containing TiC, *Mater. Sci. Eng. A.* 471 (2007) 50–56. <https://doi.org/10.1016/j.msea.2007.04.022>.

## 7. Additional results on manufacturing processes

In addition to the publications, additional parameter studies are presented in this chapter to discuss the sinterability of Mg at different sintering temperatures and holding times. Furthermore, the mechanisms and factors that influence the extrusion process are discussed, since in this thesis sintered material was used for hot extrusion, which is usually carried out with powder.

### 7.1. Sintering behaviour

SEM images in Figure 21a-b show the influence of the sintering temperatures of 550 °C and 600 °C on the microstructure and emphasize that pure Mg had the lowest porosity at 600 °C. An increase in the holding time at a temperature of 600 °C showed no reduction in porosity and no significant change in pore shape towards rounder pores (Figure 21c-e), which would indicate a successful sintering process.

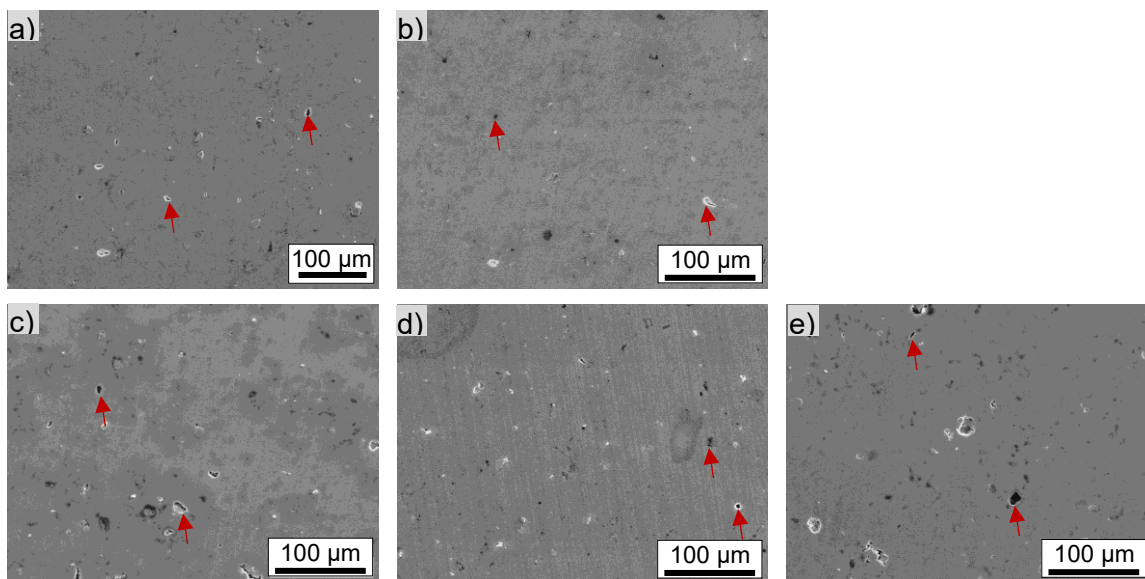


Figure 21. SEM images of sintered pure Mg: a) 2 h at 550 °C, b) 2 h at 600 °C, c) 4 h at 600 °C, d) 6 h at 600 °C, e) 10 h at 600 °C. Some pores are exemplarily marked with arrows.

One explanation could be the presence of a native oxide layer on the powder particle surface or rather the presence of MgO particles at the grain boundaries after mechanical milling. A holding time of 2 hours was therefore chosen in order to minimize the time for possible grain growth, since a higher density could not be achieved after a longer holding time. However, it can be assumed that recovery and recrystallization, and thus grain growth, could not be completely suppressed during sintering at 600 °C but was additionally hindered to a certain extent by the nanoparticles.

## 7.2. Extrusion behaviour

As known, hot extrusion at around 400 °C is suitable for Mg [135–137]. A further investigation comparing CIPed and sintered nanocomposites with regard to the extrusion behaviour shows that a higher density is achieved after extrusion with the sintered state. The corresponding SEM images of the cross sections of the extruded M1S<sub>n</sub> are shown in Figure 22. Although it can initially be assumed that the deformability of the powder particles during extrusion is better than the sintered state due to the mechanically interlocking compared to the chemical bond after sintering, the powder particles undergo high plastic deformation due to mechanical milling and the powder compaction processes. Here, recovery during sintering reveals its advantageous effects during extrusion, since the material still has enough capacity to be plastically deformed, which leads to a higher density of the CIPed-sintered and extruded M1S<sub>n</sub> compared to the CIPed and extruded M1S<sub>n</sub>. However, it was not possible to extrude M10S<sub>n</sub> into a flat rod. The limited plastic deformation of M10S<sub>n</sub> during extrusion was the result of an already existing high defect density, which was increased by the large volume fraction of nanoparticles during extrusion. Since the nanoparticles hindered the necessary recovery during sintering and defects as well as nanoparticles act as nuclei for dynamic recrystallization during hot extrusion, this massive grain refinement leads to increasing strength. Thus, the force limit of the press is reached due to the small sample volume and dimensions, which is the reason why no further deformation is achieved and the extrusion process cannot be continued.

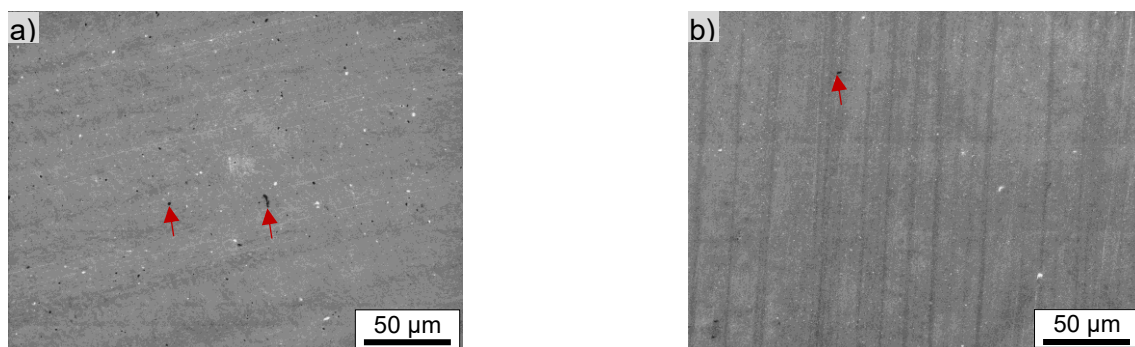


Figure 22. SEM images after hot extrusion of a) CIPed and b) CIPed and sintered pure Mg. Some pores are exemplarily marked with arrows.

---

## 8. Manuscript IV

### Effect of hot isostatic pressing on densification, microstructure and nanoindentation behaviour of Mg-SiC nanocomposites

#### Publication notification

##### *Keywords:*

Mg-SiC nanocomposite, hot isostatic pressing (HIP), Vickers hardness, nanoindentation

##### *Authors:*

D. Hübler<sup>1</sup>, A. Ghasemi<sup>1</sup>, R. Riedel<sup>2</sup>, C. Fleck<sup>1</sup>, S. Kamrani<sup>1</sup>

<sup>1</sup>Technische Universität Berlin, Faculty III – Process Sciences, Institute of Material Science and Technology, Chair of Materials Science and Engineering, Straße des 17. Juni 135, 10623 Berlin, Germany

<sup>2</sup>Technische Universität Darmstadt, Department of Materials and Earth Sciences, Group Dispersive Solids, Otto-Berndt-Straße 3, 64287 Darmstadt, Germany

*Journal:* Journal of Materials Science, 55, pp. 10582-10592, May 2020

*DOI:* 10.1007/s10853-020-04758-5

Licensed under a CC Attribution 4.0: <http://creativecommons.org/licenses/by/4.0/>

##### *Author contributions:*

I produced the the bulk materials up to the sintering process at TU Darmstadt and arranged the hot isostatic pressing at Fraunhofer IKTS Dresden. Prof. Dr. Dr. h.c. Ralf Riedel provided a workplace and the equipment at TU Darmstadt. Together with Dr. Sepideh Kamrani, I planned the investigations at TU Berlin. Dr. Sepideh Kamrani is also responsible for project funding and supervision of the project. Prof. Dr. Claudia Fleck provided a workplace and facilities at TU Berlin and supported me as thesis supervisor. I characterised the microstructure by SEM, performed Vickers hardness and nanoindentation tests and did the evaluation of the results. I wrote the manuscript, which was reviewed by all co-authors.

## 8.1. Abstract

The production of fully dense nanocomposites with a homogeneous distribution of nanoparticles through powder metallurgy (PM) techniques is challenging. Additionally to mechanical milling, pressing and sintering, a final consolidation process is needed to fully densify the nanocomposite. Hot isostatic pressing (HIP) is a promising alternative method to other hot forming processes to eliminate porosity in these PM parts. In contrast to hot extrusion, for instance, isotropic properties are achieved, and textures, as they are usually observed in Mg after uniaxial deformation, are avoided. Here, we evaluate the effect of HIP on the densification, microstructure and (nano)hardness of Mg-SiC nanocomposites. Even though density increased indeed, we observed no increase in the mechanical properties, due to significant heterogeneity in the microstructure. SiC-free regions with a higher grain size developed. Local nanohardness measurements of the HIPed Mg nanocomposite revealed that these regions had a significantly lower nanohardness than the SiC containing regions. Under consideration of mechanisms reported to be active in Mg in the pressure and temperature regime we used, we conclude that grain growth is the most likely mechanism leading to the microstructure observed after HIP. This is driven by the thermodynamic pressure to decrease the grain boundary energy and facilitated by a slightly inhomogeneous distribution of SiC nanoparticles in the sintered nanocomposite

## 8.2. Introduction

Strength and stiffness of metallic materials can be significantly improved compared to the pure metal by adding nanoscale particles, thus designing metal matrix nanocomposites (MMNC) [1–3]. Such nanocomposites are usually processed through a powder metallurgical (PM) route, comprising mechanical powder compaction and sintering steps. However, achieving full density while keeping the ultrafine microstructure during the consolidation process, is still a challenge. This is why an additional consolidation process is needed to fully densify the material. HIP is a promising method to eliminate porosity in these PM parts. Thus, components can be designed, which meet the specifications for use in highly stressed applications [4]. In comparison with hot extrusion as additional consolidation step, HIP avoids texture formation and, therefore, anisotropic properties due to the uniformly applied pressure. The pressure can additionally help to overcome restraining effects in composites due to nanoparticles compared to sintering [5]. Further advantages of the HIP process in general are the production of near-net shaped structures, and the greater design freedom in comparison with hot extrusion [6].

Powder is often directly HIPed in a vacuum-sealed flexible capsule. However, the capsule has to be removed after HIP by machining, pickling or sandblasting [7]. Another alternative is the sinter-HIP process which combines two steps and consolidates precompacted powder, while preventing oxidation due to a better control of atmosphere and reducing the risk of grain growth due to the eliminated re-heating in the second step [5, 7]. However, in our case, we separated the process in two steps sintering and HIP in order to characterise the mechanisms occurring during the individual process steps.

While for pure metal powders plastic deformation and creep are possible dominant mechanisms for improving the compaction during HIP [8], creep plays, however, only a minor role in the compaction of metal composite powders due to the nanoparticles [9].

Thus, HIPping composites seems to involve different mechanisms than HIPping pure metals. Until now, only a few studies on HIP of metal-matrix composites exist. But HIP has a high potential of achieving full theoretical density and of reaching a uniform compaction, while reducing the overall property scatter, as Xu et al. showed for a cast Al-SiC composite [10]. They further showed that yield stress decreased drastically as ductility increased mainly due to the reduction of porosity. Lange et al. investigated the influence of microinclusions on densification during HIP: inclusion volume fractions above 20% lead to inclusion networks which substantially reduced the densification rate [9]. Thus, even though the reinforcing phase constrains the deformation, strength and creep resistance of the products are nevertheless increased compared to the pure metal. For nanocomposites, this means that the amount of reinforcement has to be as small as possible, while still retaining the positive effects of nanoparticles such as Orowan strengthening and hindering of grain growth.

To the best of our knowledge there are no reports regarding HIP of magnesium nanocomposites. We investigated the effect of HIP on the densification, the microstructure and the mechanical properties of a Mg-SiC nanocomposite with a reinforcement content of 1 vol % SiC nanoparticles compared to non-reinforced Mg. Besides microhardness, we discuss our findings regarding nanohardness and effective elastic modulus of non-reinforced Mg and Mg-SiC nanocomposite locally at the micron to the submicron scale. We then compare our findings on the densification during HIP and the resulting mechanical properties with those achieved by extrusion of Mg-SiC nanocomposites which we reported previously [11].

## 8.3. Experimental procedure

### 8.3.1 Processing

Nanocomposite powders with a reinforcement content of 1 vol % SiC nanoparticles were prepared by high-energy mechanical milling, precompacted by uniaxial pressing and further compacted by cold-isostatic pressing (CIP) before sintering (see Table 1). Further details are given in our previous works [11, 12]. To achieve fully dense bodies and isotropic properties, HIP was applied as additional consolidation step. The surface of the sintered samples was first ground to remove the oxide layer. Then, HIP was performed under argon atmosphere. The HIP unit was preheated to 200 °C for 1 h followed by pressure build-up to 100 MPa over 2 h. After a pressure of 100 MPa was reached the unit was heated up to 500 °C with a heating rate of 5 K min<sup>-1</sup>. After a holding time of 1 h, the unit was cooled down to room temperature with a cooling rate of 3 K min<sup>-1</sup> before the pressure was released. As a reference, non-reinforced Mg samples were produced in the same way as the Mg nanocomposite. Henceforth, the samples will be referred to as “non-reinforced Mg”, “Mg” and “Mg nanocomposite”, “Mg-SiC”.

Table 1. Overview of the process parameters.

	Temperature (°C)	Time (h)	Pressure (MPa)	Atmosphere
Mechanical milling	-	25	-	Argon
Cold-isostatic pressing	-	10 min	700	Oil
Sintering	600	2	-	Argon

### 8.3.2 Microstructural analysis

The microstructure and the porosity of the samples following sintering and HIP were investigated on ground and polished sections. After grinding with sandpaper up to 4000-grit with ethanol as lubricant, the sections were stepwise polished, using diamond spray down to ¼ µm particle size (Struers), cleaned with ethanol and blow-dried. The pore shape and distribution and the characteristics of the nanoindenters were investigated by scanning electron microscopy (SEM), using a Gemini SEM 500 (Zeiss, Germany) in secondary electron (SE) mode at an accelerating voltage of 8 kV. The grain structure of the Mg matrix and the reinforcement distribution were evaluated qualitatively by transmission electron microscopy (TEM, Tecnai G<sup>2</sup> 20 S-TWIN, FEI, USA), on a specimen prepared parallel to the uniaxial pressing direction by the focused ion beam (FIB) technique. For quantification of the grain size and to obtain a statistical grain size distribution, the diameters of at least 200 Mg grains were measured in dark field TEM

micrographs using the measuring tool of the ImageJ software (National Institute of Health, USA). Further, scanning transmission electron microscopy (STEM) was used to analyse the elemental composition of the Mg grains and the grain boundaries by an energy-dispersive X-ray spectroscopy (EDS) line scan.

The relative density of the materials was determined by 2D pore analysis on SEM images by ImageJ. At least 5 SEM images of different regions of the cross-section of each sample were analysed with the help of the tool “Analyze Particles” at a magnification of 500 after digital enhancement of the contrast and segmentation. The percentage amount of pores was determined within a region of interest sized  $113\ \mu\text{m} \times 78\ \mu\text{m}$  in each of the five micrographs.

### 8.3.3 Mechanical properties

The mechanical properties were investigated by micro- and nanoindentation for the sintered and sintered/HIPed states. Sections were prepared and polished as described above for the microstructural analysis. For the microhardness measurements, a Zwick 3212 (Germany) microhardness tester was used with a maximum force of 1.961 N (HV 0.2) and a dwell time of 10 s. To quantify the local hardness, nanoindentation was performed with a Hysitron TI 950 TriboIndenter (Bruker Corporation, Massachusetts, USA) equipped with a standard Berkovich diamond indenter tip. A maximum load of 1 mN with a dwell time of 10 s and a loading and unloading rate of  $200\ \mu\text{N s}^{-1}$  were used. At least 100 indents were made in several areas of each sample in grid-wise arrangements of  $5 \times 5$  indents with a distance of  $15\ \mu\text{m}$  between the single indents to obtain a statistically significant average of nanohardness ( $H_n$ ) and effective elastic modulus ( $E_{\text{eff}}$ ). As Si free and Si containing regions were identified in the HIP Mg nanocomposites (see below, ch. 3.1, Fig. 2), additionally at least 50 indents were made for local nanohardness measurements in each of the two different regions using grids of  $3 \times 1$  indents with a distance between single indents of  $10\ \mu\text{m}$ . Nanohardness and  $E_{\text{eff}}$  were determined by the method described by Oliver and Pharr [13, 14]. The statistical significance was determined homoscedastic using a t-test and a two-tailed distribution at a significance level of  $\alpha = 0.05$  [15].

## 8.4. Results

### 8.4.1 Microstructural characterisation

Figure 1 shows SEM micrographs of typical metallographic sections of a non-reinforced Mg and a Mg nanocomposite specimen both after sintering (Fig. 1 a,b) and after HIP (Fig. 1 c,d). The Mg matrix appears light grey, while the former powder particle

boundaries are dark grey and the pores black. The sintered samples have an almost uniform distribution of the pores. Mg exhibits more equiaxed pores (arrows), while the Mg-SiC contains elongated as well as equiaxed pores. The elongated pores appear along the contact points of former powder particles. They are thus arranged along lines, resembling a string of pearls surrounding the grains. These pores seem to be separated by thin struts of material. After HIP, the samples still show pores; in some areas, these are homogeneously distributed, in others, however, they are clustered in string-like lines, just as in the sintered nanocomposite. While the Mg does not show a significantly different pore shape compared to the sintered state, the Mg-SiC exhibits more ellipsoidal and equiaxed pores with micron and submicron sizes. Although both sintered samples exhibit different pore morphologies, the relative densities of the non-reinforced Mg and the Mg nanocomposite are similar (Table 2). In contrary, after HIP, the Mg-SiC nanocomposite exhibits the highest density, compared to the sintered state as well as compared to the pure Mg sample.

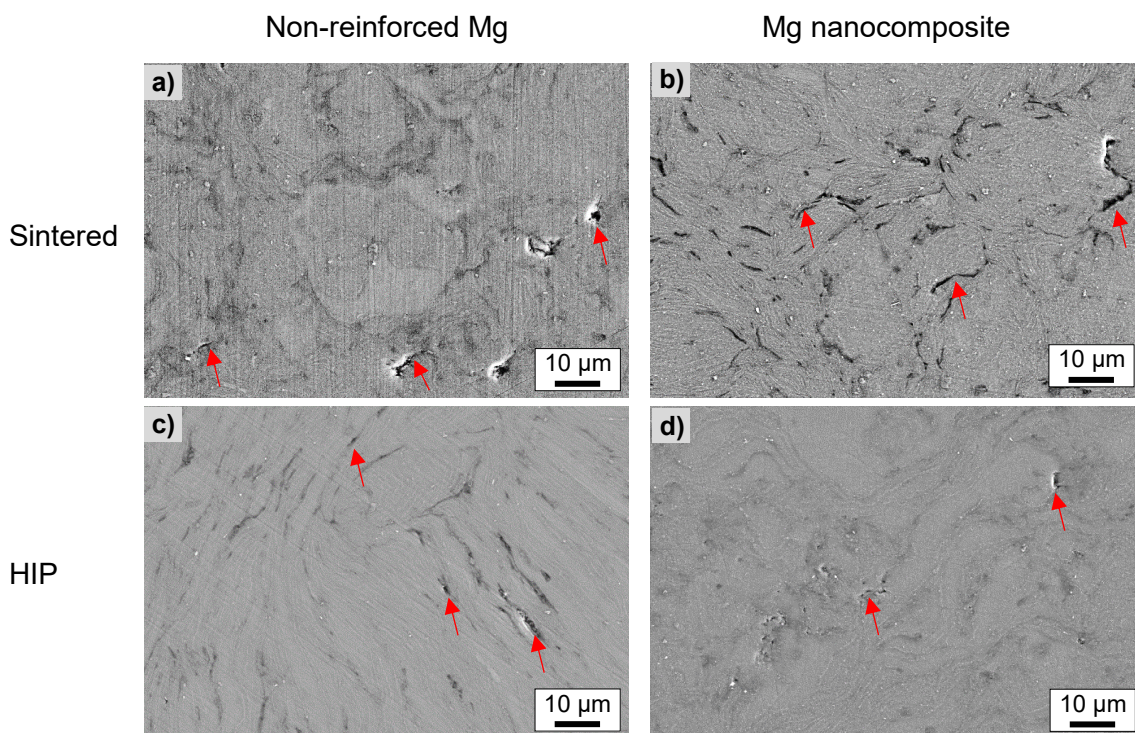


**Fig. 1** SEM micrographs of (a,b) sintered and (c,d) HIPed non-reinforced Mg and Mg nanocomposite: the magnesium matrix appears in light grey and the boundaries between former powder particles in dark grey. The arrows denote elongated pores which appear in black

Table 2. Relative density of sintered and HIPed samples determined by 2D pore analysis.

	Relative density (%)	
	Sintered	HIP
Non-reinforced Mg	97.9	98.1
Mg nanocomposite	97.5	99.1

A more detailed characterisation of the microstructure of the HIPed Mg-SiC is possible by SEM investigations. At a low magnification (Fig. 2a) we observe two different areas: one appearing in dark grey and the other one in light grey. The latter is much more abundant, comprising approximately 70 to 80% of the area, thus representing the major part of the sample. The maximum extension of the dark grey regions seems to be on the range of 40  $\mu\text{m}$ . Figure 2b shows the microstructure in more detail. The areas appearing in dark grey at the lower magnification show less contrast at this magnification and have been marked with dashed lines for clarity. Figure 2c shows elemental maps of Si and Mg in the light and dark grey areas which prove that the dark and light grey areas are regions free of Si and regions containing Si, respectively. Accordingly, the dark grey areas will be referred to as “SiC-free regions” in the following.

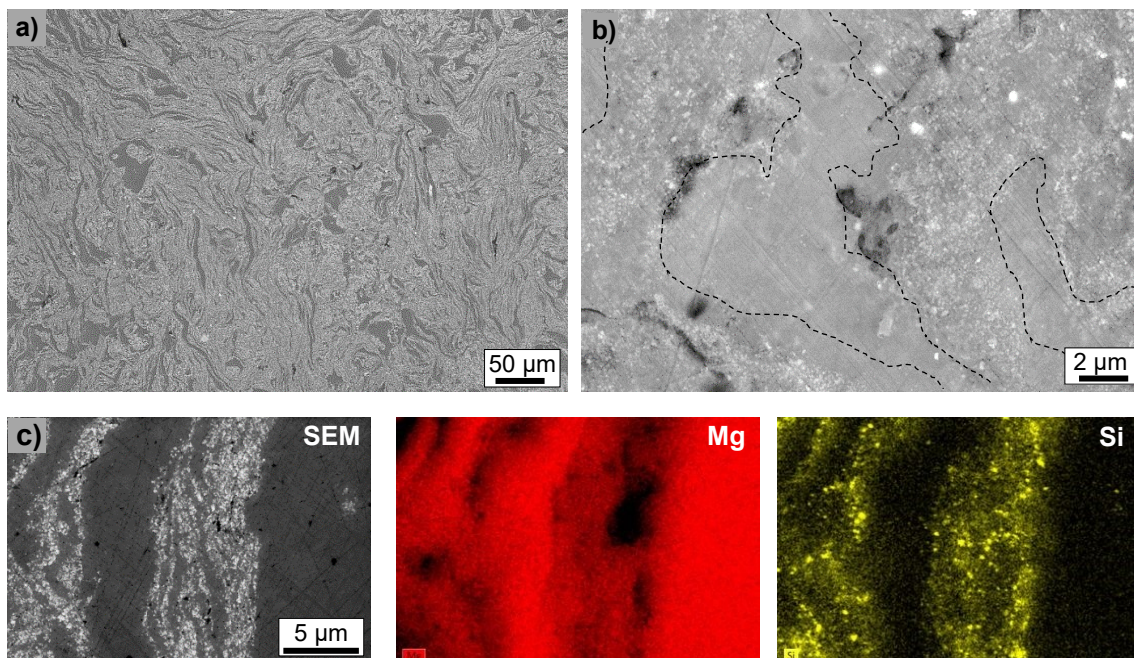


**Fig. 2** SEM micrographs of a cross section of a HIPed Mg nanocomposite specimen: a) enhanced material contrast imaging reveals differences in the microstructure where some areas appear in darker grey and others in light grey; b) detailed view at higher magnification (areas that appear in dark grey at lower magnification are surrounded by dashed lines): these areas appear smoother and more homogeneous, while the areas that appear brighter at lower magnification look more heterogeneous; c) micrograph and corresponding elemental maps of magnesium and silicon showing that Si only appears in the light grey areas.

To further analyse the microstructure of the two different regions of the HIPed Mg-SiC in terms of grain size and SiC distribution, TEM analyses were performed. The two regions can be clearly distinguished in the dark-field TEM micrograph in Fig. 3a. At the top and the bottom of this figure the SiC-free regions are visible, while the SiC containing region is located in between. Figure 3b shows the SiC-free region in higher magnification illustrating large Mg grains, which are surrounded by white particles. These are  $\text{MgO}_x$ , located at the grain boundaries of the Mg matrix in the SiC-free regions, as shown by

EDX (Fig. 3c). The EDX analysis also affirms that no SiC nanoparticles exist within the Mg grains. The bright field TEM micrograph in Fig. 3d shows that the SiC containing region has small equiaxed Mg grains, with a homogeneous distribution of SiC nanoparticles throughout the grains. The grain size distribution was evaluated separately in the different areas and is displayed together in Fig. 3e. The grain size distribution is bimodal. The large amount of small grains belongs to the SiC containing region, and the smaller number of larger grains with sizes greater than 1  $\mu\text{m}$  belongs to the SiC-free region. Averaging over both regions, we determined a grain size of 270 nm.

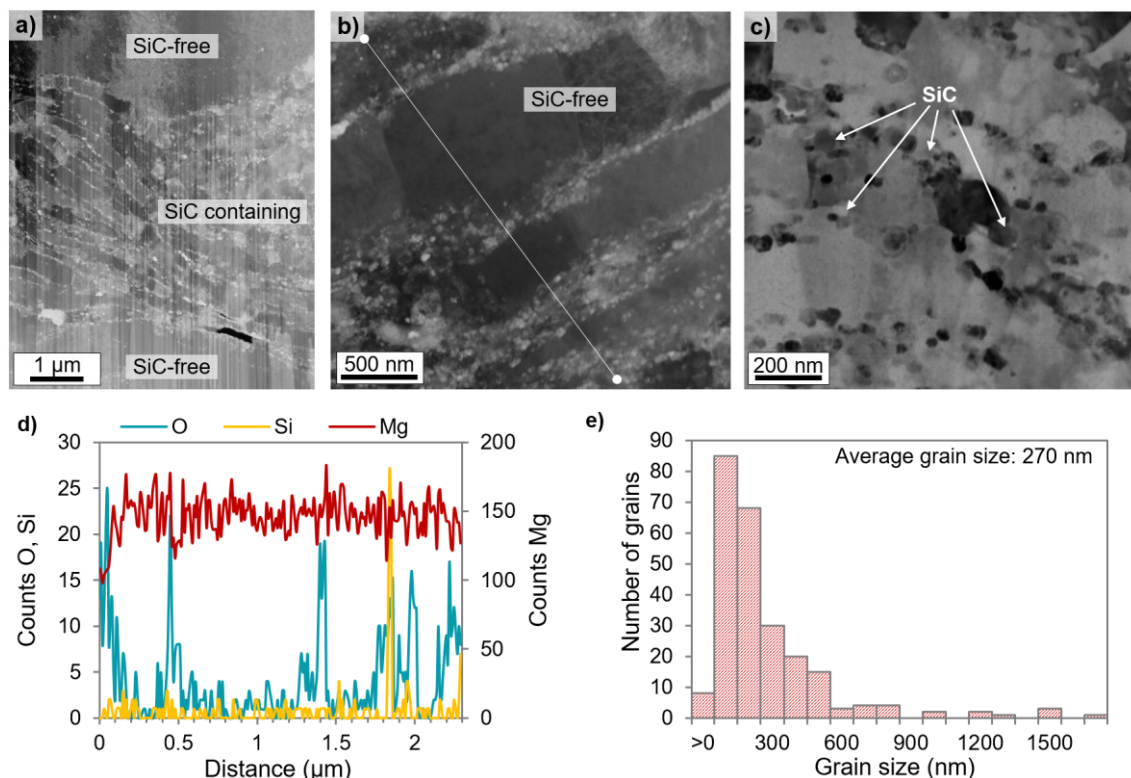


**Fig 3** TEM micrographs of a HIPed Mg nanocomposite specimen: a) dark field (DF) micrograph showing the overall microstructure parallel to the uniaxial pressing direction: SiC-free regions (top and bottom, appear light grey in SEM) and SiC containing region in between (appears dark grey in SEM), vertical lines are artefacts from sample preparation; b) DF image showing the SiC-free region, line scan in d is denoted by the white line; c) bright field micrograph showing SiC nanoparticles in the SiC containing region which are marked with arrows; d) line scan along the direction; e) statistical grain size distribution shows large amount of small grains belonging to the SiC containing regions and a low amount of large grains belonging to the SiC free region.

### 8.4.2 Mechanical properties

The average Vickers microhardness of all four material compositions and states is shown in Fig. 4. Considering the determined grain sizes, the Vickers indent, exhibiting a size of 40- 50  $\mu\text{m}$ , includes a high number of grains, thus leading to an average hardness value. On the microscale, for both materials a slight increase in hardness is observed after HIP compared to the sintered state. The HIPed Mg-SiC has the highest Vickers

hardness with an increase to 49.3 HV 0.2. All states except the sintered Mg-SiC and the HIPed Mg differ statistically significantly.

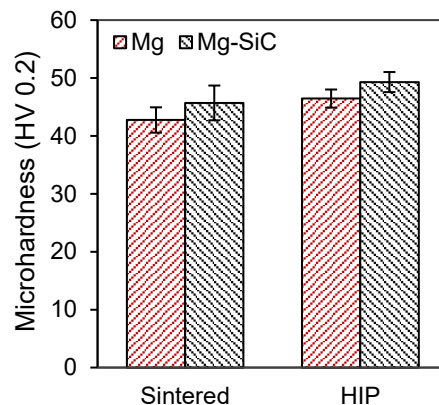


**Fig 4** Average Vickers microhardness values (HV 0.2): the differences between all states are significantly different with the exemption of the difference between the sintered Mg nanocomposite and the HIPed non-reinforced Mg. The black vertical lines denote the standard deviation.

The mechanical properties on the nanoscale, and, specifically, the local property variations due to the two different, SiC-free and SiC-containing regions, in the HIPed nanocomposite were assessed by nanoindentation. Typical load-displacement curves are shown in Fig. 5. The shape of the curves is typical for an elastic-plastic behaviour. For the sintered states, the load-displacement curves are smooth, while both HIPed samples show small pop-in effects. The curves of the Mg nanocomposite are shifted slightly towards lower displacements (“to the left”) compared to the non-reinforced Mg, reflecting a higher resistance to deformation. The nanoindents of the sintered and HIPed samples (Fig. 5), have a size of approximately 1 to 2  $\mu\text{m}$  and show no signs of crack initiation. Brighter areas, visible at the edges of the imprints, suggest minor pile-up.

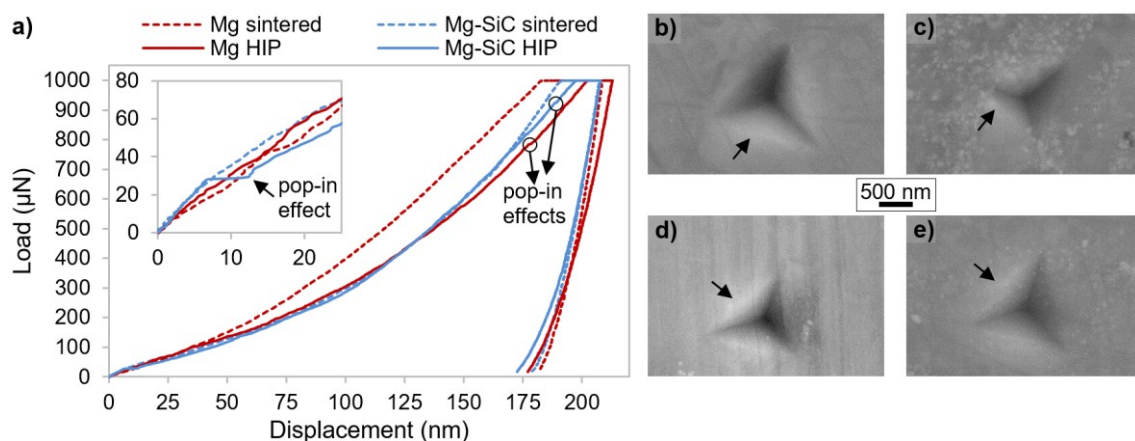


**Fig. 5** a) Load-displacement curves obtained by nanoindentation with a maximum load of 1 mN. Only the HIPed samples show a pop-in effect for low loads (inset). b-e) SEM images of typical indents on **b,c** sintered and **d,e** HIPed cross sections of non-reinforced Mg (left: **b,d**) and Mg nanocomposite (right: **c,e**): minor pile-up is observed at the indent edges, visible as rims in lighter grey at the edges of the triangular indents, marked with arrows.

Figure 6 summarises the nanoindentation results. Compared to the sintered samples, only the nanohardness of Mg increased significantly through HIP. The HIPed Mg and the HIPed Mg-SiC show the highest average nanohardness values, with 0.83 and 0.86 GPa, respectively, but these values are not statistically significantly different from each other.

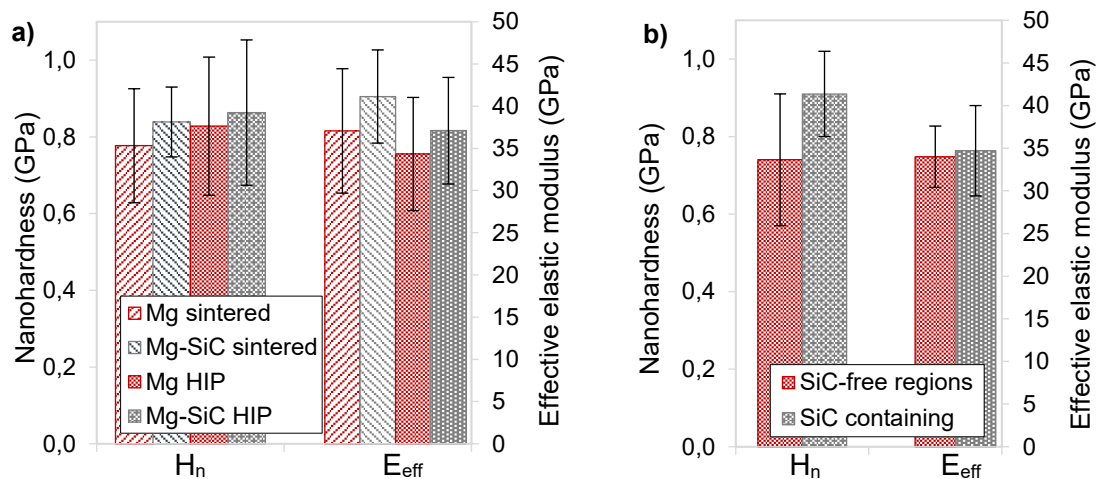


**Fig. 6** a) Average nanohardness and effective elastic modulus ( $E_{eff}$ ) values of non-reinforced Mg and Mg nanocomposite in the sintered and HIPed states; b) Influence of the local microstructure on the nanohardnesses and the  $E_{eff}$  of Mg nanocomposite: SiC-free regions possess significantly lower nanohardness than the SiC containing regions, while  $E_{eff}$  is comparable. The vertical black lines denote the standard deviation.

The average  $E_{eff}$  of the HIPed materials, both in the non-reinforced Mg and in the reinforced state, statistically significantly decreased by 7.5 and 9.7%, respectively, compared to the sintered samples. However, in all cases, the addition of the hard SiC nanoparticles increased the effective elastic modulus of the Mg nanocomposite as compared to the non-reinforced state.

The local nanohardness and effective elastic modulus values of the SiC-free and the SiC-containing regions in the HIPed Mg-SiC are shown in Fig. 6b. While  $E_{eff}$  shows no difference, the nanohardness of the SiC-free regions (0.74 GPa) is lower than nanohardness of the SiC containing regions (0.91 GPa).

## 8.5. Discussion

Hot isostatic pressing has been routinely used for the production of standard sintered materials to achieve isotropic densification of metal and ceramic powders before sintering. Here, we investigated an alternative use of HIP as an additional processing step to densify Mg-SiC nanocomposites following pressing and sintering of nanostructured composite powders. We compared the outcome with hot extrusion, another uniaxial hot forming process. Due to the combined application of high pressure and high temperature, HIP is expected to profoundly modify the microstructure of the

nanocomposites. Indeed, we observed significant changes in the size and shape of the pores, the grain size and the distribution of the nanoparticles. Furthermore, and importantly, the density increased. All in all, however, the mechanical properties stayed below the expected values: the high temperature allowed significant grain growth, leading to a coarsening of the microstructure and to the formation of SiC-free regions. These negative effects were not sufficiently counteracted by the positive effect of the higher density. We therefore conclude that either the isostatically applied pressure was not high enough to induce sufficient plastic deformation, or the temperature was too high, so that the coarsening of the microstructure happened too fast. Dynamic recrystallisation therefore either was totally hindered by the effect of Zener pinning by the nanoparticles, or it did not take place to an extent sufficient to counterbalance the coarsening.

In principle, at the pressure and temperature applied, a variety of deformation mechanisms are possible during HIP. Due to the ultrafine microstructure of our Mg nanocomposite, grain boundary sliding (GBS) and Coble creep may be expected to take place. Based on the densification map of Frost and Ashby for pure Mg [16], we may safely assume that dislocation creep and volume diffusion are the most likely mechanisms, besides Coble creep. In contrast, Dieringa expects that, at temperatures between 200 and 300 °C, dislocation creep and grain boundary sliding are the mechanisms preferred to Coble creep and volume diffusion [17]. Dynamic recrystallisation and Nabarro-Herring creep, on the other hand, are less likely because these mechanisms are known to occur only at higher temperatures than those we used. Furthermore, SiC nanoparticles and other fine oxide particles are well known to extensively increase the creep resistance by pinning dislocations and hindering grain boundary diffusion [18, 19].

Based on our findings, we propose the model shown in Fig. 7 that schematically describes which deformation mechanisms we assume to be active, and the sequence of events during the microstructure evolution of our materials. Ideally, the SiC nanoparticles should be homogeneously distributed in the Mg-SiC nanocomposites. The real microstructure, however, is inhomogeneous with some Mg grains lacking SiC nanoparticles along their grain boundaries. Thus, some grain boundaries are not pinned. Consequently, due to the relatively long exposure time to elevated temperatures during the HIP process, and due to the high thermodynamic pressure because of the very fine grains, grain growth is likely to occur in these areas. Concomitantly, in areas with less nanoparticles, these move together with the grain boundaries [20] and a region devoid of SiC nanoparticles and with a coarser grain size develops. Eventually, the migrating grain boundaries meet more and more nanoparticles until they are stopped. In areas where SiC nanoparticles are homogeneously distributed, grain growth is hindered

through Zener pinning, and so are grain boundary sliding, dynamic recrystallisation, Coble creep and the overall diffusion. Additionally, we assume that MgO can act as a barrier and suppress volume diffusion to the grain interior. This corroborates the findings of Dadbakhsh and Hao in Al-Fe<sub>2</sub>O<sub>3</sub> composites [21]. The existence of large Mg grains in a former ultrafine microstructure was also reported by Yao et al. for an Al6063-SiC nanocomposite after extrusion [20]. The authors explained this finding with the higher internal driving force for grain growth compared to the dragging force of few individual nanoparticles, that is, Zener pinning. In pure Mg, the fine MgO particles prevent the grain growth; however, the dragging force is not as great as that of the larger nanoparticles, which is the reason why the grains can grow larger.

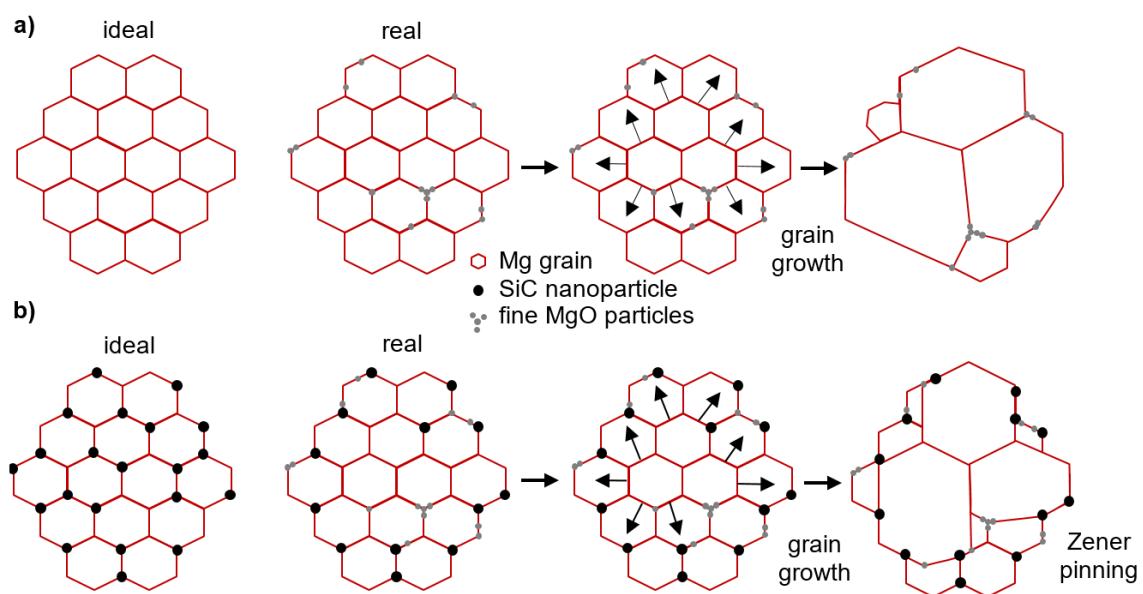


**Fig. 7** Schematic illustrations of ideal and real microstructures including a model of the possible mechanisms involved for a) pure Mg and b) Mg-SiC nanocomposite. Mg grains keep their shape due to the applied isostatic pressure. The internal driving force for grain growth is higher than the dragging force of the few individual SiC nanoparticles or MgO particles. When a certain amount of particles has accumulated, the grain boundary movement is stopped by Zener pinning, which also hinders recrystallization.

Interestingly, the Mg nanocomposite showed a higher densification during HIP than the non-reinforced Mg. This may be explained by the finer grain size and, thus, the higher number of grain boundaries present in the Mg nanocomposite which allows more grain boundary diffusion and sliding, despite the nanoparticles. TEM investigations could help clarify the mechanisms. However, visualising dislocations in the hcp crystal structure is very complex and challenging, especially if the grain orientations of the nano-sized Mg grains in the TEM foil are not known. In principle, EBSD analysis is a possibility to characterise the grain orientations in a TEM foil; however, this is not feasible in the Mg nanocomposites due to their extremely small grain size.

Densification of the Mg nanocomposites during HIP was lower than what we observed during hot extrusion [11]. Possible reasons are the very low strain rates and the uniform pressure during HIP. The latter leads to a uniform stress distribution within the specimen, and shear stresses are negligible. As a consequence, the overall amount of plastic deformation is lower and, thus, pore removal is less effective because the driving force for dynamic recrystallisation is lower. Additionally, due to the longer process time of HIP (>1 h compared to a few minutes for hot extrusion), there is more time for diffusion. We may safely assume that the longer time supports some diffusion driven processes, which assist in increasing the density, and lead to a rounding of the formerly elongated pores of the Mg nanocomposite during HIP. However, the increase in density is small and other mechanisms seem more likely to contribute to densification than diffusion driven processes, as discussed above.

The microstructural features, such as grain size and SiC distribution, strongly influence the mechanical properties, according to the Hall-Petch relationship and the Orowan mechanism, respectively. The development of few SiC-free regions with their relatively large Mg grains appears to be sufficient to reduce the microhardness, so that no significant improvement can be observed compared to the sintered state despite the increase in density. Nanoindentation showed that the SiC-free regions indeed exhibit a lower local nanohardness; this may be due to deformation twinning, which is an additional deformation mechanism besides sliding of dislocations and which has been observed to take place in coarse-grained Mg to a greater extent [22]. The pop-in observed in the loading curve of the nanoindentation loading cycle corroborates twinning, as also described by Hu et al. [23]. Thus, in addition to the lower effective elastic modulus, the SiC-free regions are expected to allow a higher amount of plastic deformation. Note that the increase in  $E_{\text{eff}}$  in the Mg nanocomposite compared to Mg is mainly due to the higher elastic modulus of the SiC nanoparticles. The indents have edge lengths in the range of 1 to 2  $\mu\text{m}$  and depths in the range of 200 nm. They are therefore much larger than the nanoparticles which exhibit sizes of up to 50 nm at maximum. We may therefore safely assume that nearly always both phases, the Mg matrix and the SiC nanoparticles are present in the indented volume, however, with locally varying relative contents. This explains the high scatter of the results, and the higher  $E_{\text{eff}}$  of the nanocomposites as compared to the pure Mg. Furthermore, high standard deviations of  $E_{\text{eff}}$  and of the nanohardness are expected, because there may be grain boundaries below the surface in the region of the indented volume which will surely influence the plastic deformation and thus the nanoindentation results.

After HIP, the result is a material with pronounced stress and strain inhomogeneity during mechanical loading. On the one hand, this heterogeneity may be disadvantageous; on

the other hand, the more ductile SiC free regions might also be beneficial in slowing cracks down. Further tests on macroscopic specimens are needed to evaluate the full potential of the nanocomposites after different processing steps.

## **8.6. Conclusions**

Here, we report on the effect of hot isostatic pressing on the densification, the microstructure evolution and the mechanical properties measured by micro and nanoindentation of a Mg-SiC nanocomposite. As compared to uniaxial hot forming processes, HIP is a promising alternative because the isostatic pressure may help preventing the development of a texture as it usually develops in the hcp Mg materials during hot extrusion, for instance. Even though we achieved an increase in density no increase in the mechanical properties was achieved, mainly due to grain growth and the development of SiC-free, non-reinforced regions. Since the isostatic pressure causes too little shear and, therefore, deformation energy is low, dynamic recrystallisation is not induced and the increase in density is limited. Technologically, pressures up to 200 MPa are possible. However, based on our observations and the discussion of possible deformation mechanisms, we may safely assume that doubling the pressure will not have a major influence on the densification. This is mainly due to the hindering of deformation mechanisms by nanoparticles. Further studies need to be carried out in order to validate the assumed mechanisms.

## **8.7. Acknowledgement**

The authors gratefully acknowledge the financial support by the DFG (Deutsche Forschungsgemeinschaft). We also acknowledge Claudia Fasel from the group Dispersive Solids, Institute of Materials and Earth Sciences at TU Darmstadt, for her support during material production and the Non-Metallic Inorganic Materials group for providing technical cooperation. We further thank Jan Räthel from the Fraunhofer Institute for Ceramic Technologies and Systems (IKTS, Dresden) for performing the sinter and HIP process. The SEM and TEM analyses were performed at the Central Electron Microscopy Unit (ZELMI) of TU Berlin. The authors thank Christoph Fahrenson and Sören Selve for their valuable support during these measurements.

## **Conflicts of interest**

The authors declare that they have no conflict of interest.

## 8.8. References

- [1] Ibrahim IA, Mohamed FA, Lavernia EJ (1991) Particulate reinforced metal matrix composites - A review, *J. Mat. Sci.* 26(5):1137–1156
- [2] Tjong SC (2007) Novel nanoparticle-reinforced metal matrix composites with enhanced mechanical properties, *Adv. Eng. Mater.* 9(8):639–652
- [3] Shen MJ, Ying WF, Wang XJ, Zhang MF, Wu K (2015) Development of high performance magnesium matrix nanocomposites using nano-SiC particulates as reinforcement, *J. Mater. Eng. Perform.* 24(10):3798–3807
- [4] Bocanegra-Bernal MH (2004) Hot Isostatic Pressing (HIP) technology and its applications to metals and ceramics, *J. Mater. Sci.* 39(21):6399–6420
- [5] Atkinson HV, Davies S (2000) Fundamental aspects of hot isostatic pressing: An overview, *Metall and Mat Trans A* 31(12):2981–3000
- [6] Viswanathan V, Laha T, Balani K, Agarwal A, Seal S (2006) Challenges and advances in nanocomposite processing techniques, *Mater. Sci. Eng. R Rep.* 54(5-6):121–285
- [7] Loh NL, Sia KY (1992) An overview of hot isostatic pressing, *J. Mater. Process. Technol.* 30(1):45–65
- [8] Swinkels FB, Wilkinson DS, Arzt E, Ashby MF (1983) Mechanisms of hot-isostatic pressing, *Acta Mater.* 31(11):1829–1840
- [9] Lange FF, Atteraa L, Zok F, Porter JR (1991) Deformation consolidation of metal powders containing steel inclusions, *Acta Mater.* 39(2):209–219
- [10] Xu ZM, Loh NL, Zhou W (1997) Hot isostatic pressing of cast SiCp-reinforced aluminium-based composites, 7th International Scientific Conference: Achievements in Mechanical & Materials Engineering 67(1):131–136
- [11] Penther D, Ghasemi A, Riedel R, Fleck C, Kamrani S (2018) Effect of SiC nanoparticles on manufacturing process, microstructure and hardness of Mg-SiC nanocomposites produced by mechanical milling and hot extrusion, *Mater. Sci. Eng., A* 738:264–272
- [12] Kamrani S, Penther D, Ghasemi A, Riedel R, Fleck C (2018) Microstructural characterization of Mg-SiC nanocomposite synthesized by high energy ball milling, *Adv. Powder Technol.* 29:1742–1748
- [13] Oliver WC, Pharr GM (1992) An improved technique for determining hardness and elastic modulus using load and displacement sensing indentation experiments, *J. Mater. Res.* 7(06):1564–1583
- [14] Oliver WC, Pharr GM (2004) Measurement of hardness and elastic modulus by instrumented indentation: Advances in understanding and refinements to methodology, *J. Mater. Res.* 19(01):3–20
- [15] Kim TK (2015) T test as a parametric statistic, *Korean J. Anesthesiol.* 68(6):540–546
- [16] Frost HJ, Ashby MF (1982) Deformation-mechanism maps the plasticity and creep of metals and ceramics, 1st edn. Pergamon Press, Oxford
- [17] Dieringa H (2011) Properties of magnesium alloys reinforced with nanoparticles and carbon nanotubes: A review, *J. Mat. Sci.* 46(2):289–306

- [18] Basak AK, Pramanik A, Islam MN, Anandakrishnan V (2015) In: Lau AKT, Umer R, Dong Y (eds) *Fillers and reinforcements for advanced nanocomposites*. Woodhead Publishing is an imprint of Elsevier, Cambridge, pp 349–367
- [19] Park K-T, Lavernia EJ, Mohamed FA (1990) High temperature creep of silicon carbide particulate reinforced aluminum, *Acta Mater.* 38(11):2149–2159
- [20] Yao X, Zheng YF, Quadir MZ, Kong C, Liang JM, Chen YH, Munroe P, Zhang DL (2018) Grain growth and recrystallization behaviors of an ultrafine grained Al-0.6 wt%Mg-0.4 wt%Si-5vol.%SiC nanocomposite during heat treatment and extrusion, *J. Alloys Compd.* 745:519–524
- [21] Dadbakhsh S, Hao L (2012) Effect of hot isostatic pressing (HIP) on Al composite parts made from laser consolidated Al/Fe<sub>2</sub>O<sub>3</sub> powder mixtures, 7th International Scientific Conference: Achievements in Mechanical & Materials Engineering 212(11):2474–2483
- [22] Bočan J, Maňák J, Jäger A (2015) Nanomechanical analysis of AZ31 magnesium alloy and pure magnesium correlated with crystallographic orientation, International Symposium on Physics of Materials, 2005 644:121–128
- [23] Hu J, Zhang W, Bi G, Lu J, Huo W, Zhang Y (2017) Nanoindentation creep behavior of coarse-grained and ultrafine-grained pure magnesium and AZ31 alloy, *Mater. Sci. Eng., A.* 698:348–355

## 9. Additional results on mechanical properties

### 9.1. Compression test

For compression tests, rods with a diameter of 6.4 mm were extruded and cylindrical specimens with a diameter of 5 mm and a height of 10 mm were cut in the extrusion direction using wire electronic discharge machining (EDM, AGIECUT AC Vertex 1 F, GF Machining Solutions GmbH). After grinding and polishing the sample surface down to  $\frac{1}{4}$   $\mu\text{m}$  using diamond spray (Struers), the compressive behaviour of at least 3 samples of Mg, MM, M1Sn, M3Sn, and M10Sn was tested parallel to the extrusion direction at room temperature in ambient air with a strain rate of  $10^{-4}$   $\text{s}^{-1}$  using a compression-tension module (Kammrath & Weiss GmbH). The stress-strain curves in Figure 23 represent a typical curve for each composition. Mg shows a typical brittle behaviour with a shear of 45 degree, as can also be seen in Figure 23b. MM shows the largest fracture strain of all samples, but also the lowest ultimate compressive strength (UCS), while M3Sn exhibits almost the same fracture strain but a higher strength. A significant increase in yield strength (YS) can be seen from M1Sn to M10Sn, while the UCS decreases with increasing reinforcement content. Except for Mg, all samples in Figure 23c-e show a typical bulge, which indicates plastic deformation. The average compression yield strength (0.2 % CYS), ultimate compression strength (UCS), and fracture strain are summarised in Table 2.

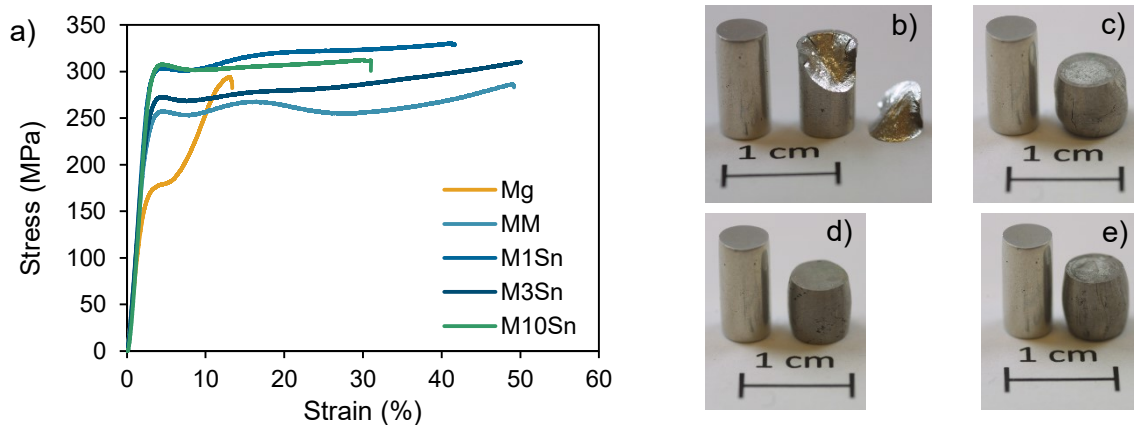


Figure 23. a) Engineering stress vs. strain curves showing the compressive behaviour and photos of initial and compressed samples of b) Mg, c) MM, d) M1Sn and e) M10Sn.

Table 2. Average compression yield strength (0.2 % CYS), ultimate compression strength (UCS) and fracture strain of Mg, MM, M1S<sub>n</sub> and M3S<sub>n</sub> and M10S<sub>n</sub>.

	0.2 % CYS (MPa)	UCS (MPa)	Fracture strain (%)
Mg	190±2	326±26	12±2
MM	254±3	310±4	48±3
M1S <sub>n</sub>	274±3	327±3	36±6
M3S <sub>n</sub>	271±8	310±1	46±4
M10S <sub>n</sub>	293±5	306±6	32±2

As shown in the Manuscripts I and III, the grain size of MM significantly decreased by mechanical milling and could be kept in submicron range during densification. Since all other compaction steps are the same, the significantly increased fracture strain and CYS compared to Mg can be attributed to the submicron-crystalline structure of MM, which is confirmed by Tun and Gupta [156]. Due to the grain refinement, slip is the dominant mechanism, while less twinning occurs. The slight upward concave compression curve of Mg might be due to twinning as the main mechanism [157]. Instead, the increased fracture strain of MM is associated with a lower UCS and vice versa in the case of M1S<sub>n</sub>. Further, the increased fracture strain of M3S<sub>n</sub> suggests that the nanoparticles increased the resistance to crack propagation resulting in an increased crack deflection. In case of M10S<sub>n</sub>, the nanoparticles and the high amount of grain boundaries further restrict the activation of non-basal slip systems [158], which is reflected in the decreasing fracture strain. However, UCS remains the same compared to M3S<sub>n</sub>, which indicates that no further improvement in UCS can be achieved by increasing the reinforcement content and suggests that the optimal reinforcement content lays between 1 and 3 vol% SiC nanoparticles.

## 9.2. Tensile test

For tensile tests, flat rods with a dimensions of 15 mm x 2 mm were extruded and specimens with the dimensions shown in Figure 24 were cut out using wire EDM. After grinding and polishing the sample surface down to ¼ µm using diamond spray (Struers), the compressive behaviour of at least 3 samples of Mg, MM, M1S<sub>n</sub>, and M3S<sub>n</sub> was tested parallel to the extrusion direction at room temperature in ambient air with a strain rate of 10<sup>-4</sup> s<sup>-1</sup> using an electrodynamic testing machine (E3000 tension-torsion, Instron).

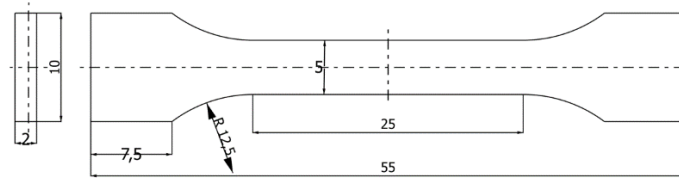


Figure 24. Technical drawing with dimensions (mm) of the tensile sample.

The stress-strain curves in Figure 25a represent a typical curve for each composition, while Figure 25b shows an image of a tensile sample. The average values of UTS and fracture strain are summarized in Figure 25c. Mg shows the lowest UTS and the highest fracture strain. The kink in the curve indicates that the sample slightly slipped out of the fixture, which is the reason why a higher strain was recorded. MM, M1S<sub>n</sub>, and M3S<sub>n</sub> show a higher tensile yield strength (0.2 % TYS and UTS compared to Mg indicating less plastic deformability; M1S<sub>n</sub> has the highest values overall. The fracture strain of MM, M1S<sub>n</sub>, and M3S<sub>n</sub> is not significantly different and is in all cases smaller than that of Mg.

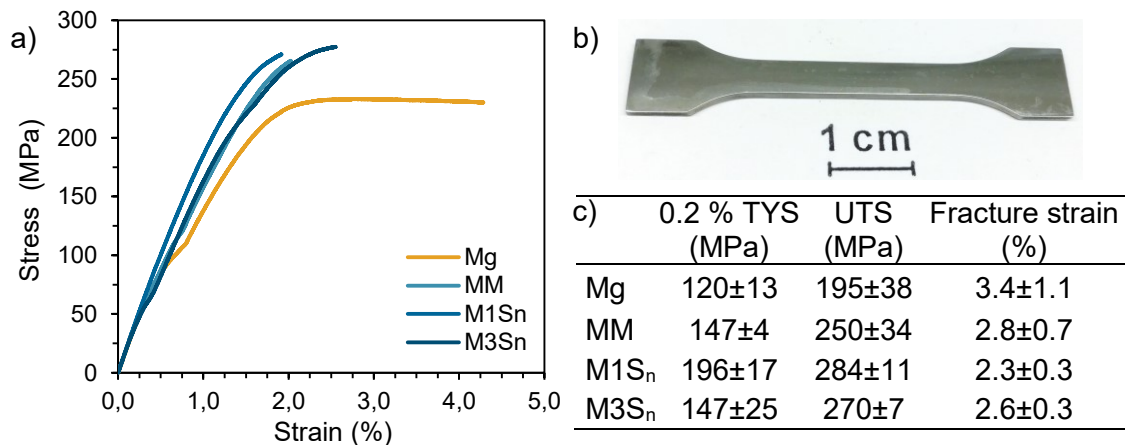


Figure 25. a) Engineering stress vs. strain curves showing the tensile behaviour, b) an image of a tensile sample, and average c) tensile yield strength (0.2 % TYS), ultimate tensile strength (UTS), and fracture strain of Mg, MM, M1S<sub>n</sub>, and M3S<sub>n</sub>.

The increase in the yield strength of MM, M1S<sub>n</sub>, and M3S<sub>n</sub> can be attributed to the grain refinement and the homogeneous SiC distribution as well as to the absence of intermediate phases, which leads to an excellent interfacial bond between reinforcements and Mg matrix in case of the nanocomposites. Non-basal slip is the main reason for improved ductility since basal slip and twinning under tensile loading are usually inhibited, in case of Mg [159]. However, no significant increase in fracture strain was observed with increasing volume fraction, although grain refinement and texture weakening occurred during extrusion; additionally, nanoparticles are likely to pin grain boundaries, sinking the barrier of the activation of non-basal slip systems.

## 10. Manuscript V

# Cyclic deformation behaviour of Mg-SiC nanocomposites on the macro and nano scale

### Publication notification

#### *Keywords:*

Mg-SiC nanocomposite, fatigue behaviour, load increase test, cyclic nanoindentation, cyclic deformation behaviour

#### *Authors:*

D. Hübler<sup>1,2</sup>, K. Winkler<sup>3</sup>, R. Riedel<sup>4</sup>, S. Kamrani<sup>1</sup>, C. Fleck<sup>1</sup>

<sup>1</sup> Chair of Materials Science and Engineering, Institute of Technology Berlin, Berlin, Germany

<sup>2</sup> Division Tribology and Wear Protection, Bundesanstalt für Materialforschung und -prüfung, Berlin, Germany

<sup>3</sup> Theoretical Biophysics, Institute for Biology, Humboldt University Berlin, Berlin, Germany

<sup>4</sup> Fachgebiet Disperse Feststoffe, Fachbereich Material- und Geowissenschaften, Technische Universität Darmstadt, Darmstadt, Germany

#### *Journal:*

Fatigue & Fracture of Engineering Materials & Structures, pp. 1-14, Oktober 2021

DOI: 10.1111/ffe.13600

Licensed under a CC Attribution 4.0: <http://creativecommons.org/licenses/by/4.0/>

#### *Author contributions:*

I produced the bulk materials up to the sintering process at TU Darmstadt. Prof. Dr. Dr. h. c. Ralf Riedel provided a workplace and the equipment at TU Darmstadt. Together with Dr. Sepideh Kamrani, I arranged the cutting of the samples at Fraunhofer IPK Berlin. Dr. Sepideh Kamrani is also responsible for project funding and supervision of the project. Together with Prof. Dr. Claudia Fleck, I planned the investigations. Further, she provided the facilities at TU Berlin and supported me as thesis supervisor. I performed the cyclic nanoindentation and macro fatigue tests and did the evaluation of the results. Kai Winkler has written most of a program for data evaluation, which I have adapted further. I wrote the manuscript in close discussion with Prof. Dr. Claudia Fleck, which was reviewed by all co-authors.

**Nomenclature:** 3D, Three dimensional; CAT, Constant amplitude test; CRSS, Critical resolved shear stress;  $D_{\min}$ , Minimum displacement at minimum load;  $\Delta D_{\min\text{-norm}}$ , Normalised by the number of cycles between measurement cycles and minimum load; E, Young's modulus; ED, Extrusion direction; EDM, Electrical discharge machining; LIT, Load increase test; M1S<sub>n</sub>, Mg-SiC nanocomposite (1 vol% SiC nanoparticles); M3S<sub>n</sub>, Mg-SiC nanocomposite (3 vol% SiC nanoparticles); MM, Mechanically milled pure Mg; MMC, Metal-matrix composite; N, Number of cycles;  $N_x$  and  $N_{x+1}$ , consecutive measurement cycles; ODF, Orientation density distribution function;  $P_{\max/\min}$ , Load in the nanoindentation tests; R, Stress ratio; SEM, Scanning electron microscopy; SDE, Strength difference effect; SPM, Scanning probe microscopy; vol%, Volume percent; XRD, X-ray diffraction;  $\varepsilon_{a,p}$ , Plastic strain amplitude;  $\varepsilon_{m,p}$ , Plastic mean strain;  $\varepsilon_{m,t}$ , total mean strain;  $\sigma_a$ , Stress amplitude;  $\sigma_m$ , mean stress;  $\sigma_{\max}$ , Maximum stress;  $\sigma_{\min}$ , Minimum stress.

## 10.1. Abstract

Metal-ceramic nanocomposites are promising candidates for applications necessitating light weight and excellent fatigue resistance. We produced Mg-SiC nanocomposites from mechanically milled powders, yielding a homogeneous nanocrystalline structure and excellent quasistatic strength values. Little is known, however, about the fatigue behaviour of such composites. Here we used load increase tests on the macro-scale to yield estimation values of the fatigue endurance limit. Fatigue strength increased significantly for the materials processed by the powder metallurgical route. We further investigated the cyclic deformation behaviour under stress-controlled conditions on the macro and nano scale. Cyclic nanoindentation showed that indentation depth and cyclic plastic deformation decreased with increasing reinforcement content, hinting to a higher cyclic strength and corroborating the results from the macroscopic load increase tests. Our results therefore show that cyclic nanoindentation reliably determines the plastic deformation behaviour of Mg nanocomposites offering the possibility of fast material analysis.

## 10.2. Introduction

There is increasing need for lightweight materials capable of sustaining cyclic loading over a long lifetime, specifically in the vehicle or aviation industry. Designing such materials requires thorough understanding of the fatigue behaviour and cyclic deformation behaviour<sup>1</sup>. Metal-matrix composites (MMCs) offer a promising way to combine low weight with high strength and ductility, also for cyclic loading conditions. In

MMCs reinforced with micron-sized SiC particles, interface debonding and/or particle cracking are the predominant failure mechanisms, both under quasistatic and fatigue loading<sup>2, 3</sup>. Fatigue resistance of MMCs depends on many parameters, comprising grain size, reinforcement geometry and distribution as well as coherence between reinforcements and matrix. The use of nanoparticles in MMCs has high potential to promote excellent interfacial bonding, and thus excellent load-bearing capability<sup>4-7</sup>. Importantly, regarding fatigue resistance, nanoparticles promote strain hardening within nanocomposites as well during processing as during service loading. This leads to a higher density of pre-existing dislocations with beneficial dislocation-nanoparticle as well as dislocation-dislocation interactions<sup>8</sup>. One consequence is the activation of non-basal slip systems in the Mg matrix, which can lead to improved fracture strains<sup>2, 9</sup>.

To provide local information on cyclic plastic zone, cyclic hardening, and crack propagation, nanoindentation has been suggested<sup>10</sup>. The method gives insights into dynamic processes within a material that lead to both, dislocation generation and annihilation due to the effective applied stress, and distribution of internal stresses. So far only one study reports on the nano fatigue behaviour of a Mg alloy using nanoindentation. Loading was, however, limited to 300 cycles<sup>11</sup>. Schmahl et al.<sup>12</sup> presented nanofatigue experiments on an Al-Si-Mg alloy with loading up to a much higher cycle number of  $10^5$ .

In contrast to cyclic nanoindentation, a large number of macro fatigue tests has been published for Mg alloy composites, e.g.<sup>8</sup>, including Mg alloy-SiC composites<sup>13, 14</sup>, and pure Mg nanocomposites<sup>3, 15-19</sup>. On the macro level, constant amplitude (CAT) and load increase tests (LIT) are often used to investigate the complex processes during fatigue loading. Specifically, LIT are useful for estimating the fatigue endurance limit and cyclic stress strain curves, when only a small number of samples is available as previously shown for a variety of materials, also for Mg alloys<sup>20, 21</sup>. While endurance limits of about 60 MPa (CAT,  $2 \times 10^6$  cycles)<sup>10</sup> and 71 MPa (CAT,  $1.2 \times 10^6$  cycles) have been reported for pure Mg and AZ31, respectively, reinforcement of AZ31 by  $\text{Al}_2\text{O}_3$  nanoparticles improved the fatigue endurance limit to 91 MPa<sup>18</sup>. Therefore, an increase in endurance limit can also be assumed for pure-Mg-nanocomposites. To the best of our knowledge, there are no studies on the macro-fatigue behaviour of Mg-SiC nanocomposites.

Here we report on high-cycle nano and macro fatigue tests on a Mg-SiC MMC made from mechanically milled composite powders with nanoscale reinforcements. Nanofatigue tests were performed up to cycle numbers of  $10^5$  and analysed using the method proposed previously for Al alloys<sup>12</sup>. Fatigue mechanisms were investigated by observations of fracture surfaces of macro fatigued samples, and texture analysis was deployed to support our conclusions on the active deformation mechanisms.

Comparisons of the plastic deformation behaviour on the nano and macro scale helped us to evaluate to what extent cyclic nanoindentation tests can be used to predict the macro fatigue behaviour.

## 10.3. Materials and Methods

### 10.3.1 Sample preparation

Mg-SiC nanocomposites with SiC nanoparticles with volume fractions of 1 vol% and 3 vol% were produced by high-energy mechanical milling, cold-isostatic pressing, sintering and hot extrusion. Mg powder with an average particle size of -325 mesh and  $\beta$ -SiC powder with an average particle size of 50 nm were used. Further details of the processing are given in Penther et al.<sup>22</sup>. We previously showed<sup>22, 23</sup> that this processing route leads to a homogeneous distribution of the nanoparticles in the matrix, and to a very fine grain that is retained throughout all processing steps. Henceforth, these nanocomposites are referred to as M1S<sub>n</sub> and M3S<sub>n</sub> for samples with reinforcement contents of 1 or 3 vol% SiC nanoparticles, respectively. Mechanically milled pure Mg (MM) and non-milled pure Mg (Mg) were used as reference materials. One nanoindentation specimen was cut off from each extruded flat rod with dimensions of 15 x 2 mm. The cross-sections were then ground stepwise with SiC paper down to 4000-grit using ethanol as lubricant, and subsequently polished, using ethanol and diamond spray down to a particle size of  $\frac{1}{4}$   $\mu\text{m}$ . Three fatigue specimens of each composition were extracted from as-extruded flat rods, cut parallel to the extrusion direction (ED) by wire electrical discharge machining (EDM; AGIECUT AC Vertex 1 F, GF Machining Solutions GmbH, Geneva, Switzerland). The geometry and size of the specimens is shown in Figure 1. In order to remove the oxide layer and the EDM induced damage, thus preventing stress raising effects during testing, the sample surfaces were stepwise polished using diamond spray down to 1  $\mu\text{m}$  particle size (Struers, Ballerup, Denmark). We may safely assume a surface roughness in the range of about 1  $\mu\text{m}$  as bigger scratches were excluded by light microscopic inspection.

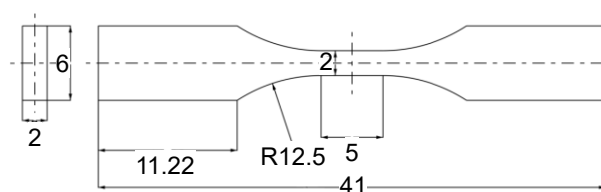


**Figure 1** Geometry of the fatigue specimens

## 10.3.2 Mechanical testing

### 10.3.2.1 Nanofatigue behaviour

For local fatigue analysis, cyclic nanoindentation was performed with a Hysitron TI 950 TriboIndenter (Bruker Corporation, Billerica, Massachusetts, USA) equipped with a standard Berkovich diamond indenter tip. High frequency “loading” cycles ( $f = 201$  Hz) were combined with interspersed low frequency “measurement” cycles ( $f = 0.05$  Hz) as described in detail elsewhere<sup>12</sup> at maximum and minimum loads of 968  $\mu\text{N}$  and 72  $\mu\text{N}$ , respectively. Note that, in compliance with the usual notation in nanoindentation, the loads are given as positive values even though they are compressive loads. The maximum number of cycles was  $10^5$ . Several areas of each sample were cyclically indented with a grid arrangement of 4 x 5 indents, with all indents in a grid 10  $\mu\text{m}$  apart from each other.

The hysteresis data of at least 20 indents per sample were evaluated by custom-made code, and the evaluated parameters were averaged over all indents, resulting in average-value-curves. To analyse the plastic deformation behaviour, we evaluated the changes in  $D_{min}$  during cyclic loading. Because slight differences in the applied force could not be avoided ( $\sim 9\%$  in  $P_{min}$ ),  $D_{min}$  were normalised by the corresponding  $P_{min}$ :

$$\Delta(D_{min}/P_{min}) = (D_{min}/P_{min})(N_{x+1}) - (D_{min}/P_{min})(N_x) \quad (\text{eq. 1})$$

with  $D_{min}$ , minimum displacement at minimum load,  $N_x$  and  $N_{x+1}$ , number of cycles in consecutive measurement cycles, indicated by subscripts “x” and “x+1”. Because the number of cycles between measurement cycles was not constant,  $\Delta(D_{min}/P_{min})$  was normalised by the number of cycles between consecutive measurement cycles:

$$\Delta D_{min-norm} = \Delta(D_{min}/P_{min}) / (N_{x+1} - N_x) \quad (\text{eq. 2})$$

To evaluate cyclic plasticity further, the ratio of minimum to maximum displacement within a loading cycle,  $D_{min}/D_{max}$  was analysed. The value correlates with the amount of irreversible and reversible deformation in a single loading/unloading cycle: higher values indicate relatively more plastic (irreversible) deformation, while lower values indicate the opposite. Changes in this ratio with  $N$  indicate softening for increasing ratios and hardening for decreasing ratios.

The cyclic indents were imaged by the scanning probe microscopy (SPM) mode of the nanoindenter. The topography images of two indents were analysed for each material regarding size and volume of the indent and pile-up using the open-source program Gwyddion<sup>24</sup>.

### 10.3.2.2 Macro-fatigue behaviour

Stress-controlled stepwise load increase (LIT) tests were performed in ambient air at room temperature on an ElectroPuls E3000 (Instron, Buckinghamshire, UK). The long axis of the samples was aligned exactly with the loading axis to avoid bending stresses. Force was measured using the inbuilt 5 kN load cell (accuracy  $\pm 0.005\%$  for  $F \leq 50$  N and  $\pm 0.5\%$  for  $F > 50$  N). Strain was measured using an inductive displacement sensor (multi NCDT Serie 300, Micro-Epsilon Messtechnik, Ortenburg, Germany) with a resolution of 0.4 % that was attached to the grips. Calibration was carried out using 1 mm long strain gauges with a tolerance of  $\pm 0.85 \mu\text{m/m}$  (FLK-1-23, Tokyo Measuring Instruments Laboratory Co., Ltd., Tokyo, Japan) mounted on the gauge length of a sample.

Three samples of each composition were tested using a sinusoidal waveform with completely reversed loading ( $R = \sigma_{min}/\sigma_{max} = -1$ ) at a frequency of 5 Hz. Loading started with a stress amplitude of 10 MPa; after a number of  $10^4$  cycles the stress amplitude was increased by 5 MPa over  $10^3$  cycles. These steps were repeated until specimen failure. From the hysteresis loops, the plastic strain amplitude, plastic mean strain ( $\epsilon_{m,p} = \epsilon_{m,t} - \sigma_m/E$ , with  $\epsilon_{m,t}$  = total mean strain,  $\sigma_m$  = mean stress,  $E$  = Young's modulus) and minimum and maximum strain were determined by custom-made code. In order to precisely determine the stress amplitude for which the plastic strain amplitude increases significantly, thus estimating the cyclic yield strength and from this the fatigue endurance limit<sup>13</sup>, the plastic strain amplitude, plotted versus the number of cycles, was fitted by a third degree polynomial function, and the first derivation of this curve was used to determine the change in slope. A "significant" change was defined as a deviation of the first derivation from a linear progression over the number of cycles.

Topography of the fracture surfaces was investigated using a Phenom XL (Thermo Fisher Scientific, Waltham, USA) scanning electron microscope at an accelerating voltage of 10 kV. Surface filter with shortest and longest cut-off wavelengths of  $\lambda_s = 223.61$  nm and  $\lambda_c = 282.84 \mu\text{m}$ , respectively, were employed to determine the mean arithmetic height  $S_a$ .

### 10.3.3 Texture analysis

In order to investigate the influence of texture as a function of the reinforcement content, X-ray diffraction (XRD) measurements were performed on longitudinal sections (cut parallel to ED), corresponding to the X-ray direction being orthogonal to ED, using a psi-diffractometer (Huber) with a position sensitive detector (PSD-50M, M. Braun GmbH), monochromatic Co  $K_\alpha$  radiation, an accelerating voltage of 40 kV and a collimated beam diameter of 2 mm. To observe the intensity distribution of the  $\{10\bar{1}0\}$ ,  $\{0002\}$ ,  $\{10\bar{1}1\}$ ,

$\{10\bar{1}2\}$  and  $\{11\bar{2}0\}$  reflections, the samples were tilted ( $\psi$  axis) and rotated ( $\phi$  axis) in 5 deg steps from  $0^\circ$  to  $55^\circ$  and  $0^\circ$  to  $355^\circ$ , respectively. The orientation distribution function was determined from the experimental data after rotation by  $90^\circ$  to analyse the texture in a cross-sectional plane orthogonal to ED using the ODF program system<sup>25</sup> and the Matlab software package MTEX<sup>26</sup>.

## 10.4. Results

### 10.4.1 Cyclic nanoindentation

Figure 2 shows SPM topography images and 3D elevation profiles of cyclic indents in Mg, MM, M1S<sub>n</sub> and M3S<sub>n</sub>. Indent and pile-up volumes of all samples are plotted in Figure 3. The data clearly show decreasing indentation sizes and depths for mechanically milled MM as compared to non-milled Mg, and with increasing reinforcement content for the mechanically milled nanocomposites. Significant pile-up is seen at the edges of all indents, but no cracks were observed in the vicinity of any of the indents.

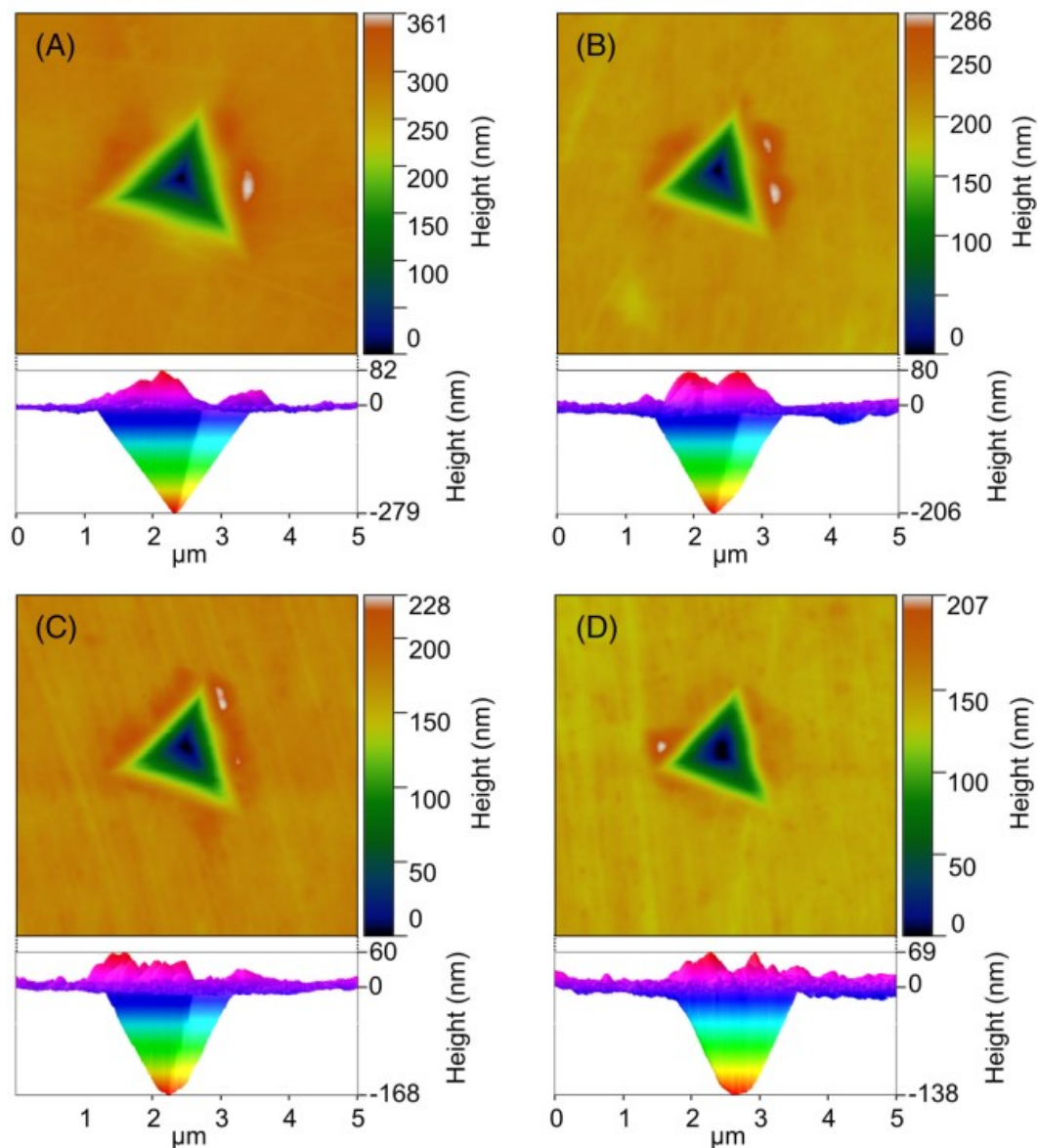


**Figure 2** SPM topography images (top) and 3D elevation profiles (bottom) of nanoindentations, loaded up to  $N = 10^5$  cycles, showing pile-up in all samples: (A) Mg, (B) MM, (C) M1S<sub>n</sub> and (D) M3S<sub>n</sub>

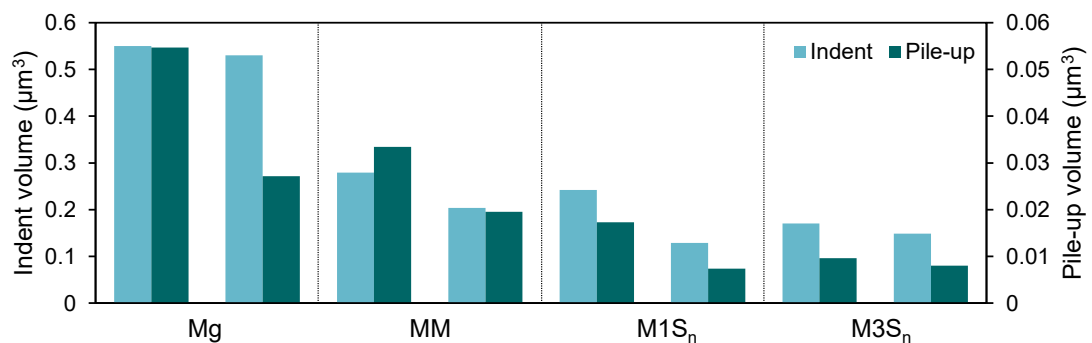


**Figure 3** Indent and pile-up volumes after cyclic nanoindentation up to  $N = 10^5$  cycles for two typical indents per material

Fig. 4A shows the average ratios of  $D_{min}$  to  $D_{max}$  plotted versus  $N$ . All sample types exhibit a steep increase within the first ten cycles, followed by smaller increases with ongoing

cyclic loading. While the Mg curve has a slightly convex shape for higher cycle numbers and a linear slope for  $N \geq 10^4$ , the curves of the nanocomposites have slightly concave progressions with an increasing trend for higher cycle numbers. This is most pronounced for M3S<sub>n</sub>. Over the investigated range of cycle numbers, Mg exhibits the highest values of  $D_{min}/D_{max}$ . Mechanical milling and nanoparticle reinforcement lead to lower values, with similar ratios for MM and M1S<sub>n</sub> and much lower values for M3S<sub>n</sub>.

The average values of  $\Delta D_{min-norm}$  are plotted versus  $N$  in Figure 4B. Two regimes with significantly different behaviour are observed: the “incipient” fatigue regime up to  $N = 10^3$ , and the “advanced” regime from  $N = 10^4$  to  $N = 10^5$ . The incremental plastic deformation per cycle decreases over  $N$ . Within the first 10 cycles,  $\Delta D_{min-norm}$  decreases by more than 60% for all materials, and hardly any differences are observed between the different materials. Subsequently,  $\Delta D_{min-norm}$  continues to decrease, but with a lower rate, and only small changes can be identified with increasing cycle number. Up to  $N = 10^4$ , Mg and M3S<sub>n</sub> exhibit the overall highest and lowest values, respectively, while the values of MM and M1S<sub>n</sub> are very similar and lie between the Mg and M3S<sub>n</sub> curves. The same differences between the materials are observed in the advanced regime. However, while MM exhibits a saturation state with constant values for  $N \geq 2 \cdot 10^4$ , the values of all other samples slightly further decrease to higher cycle numbers, after which they also enter a saturation state. The numbers of cycles, for which saturation is reached, increase with increasing reinforcement content, up to  $N = 7 \cdot 10^4$  for M3S<sub>n</sub>. For M3S<sub>n</sub>, a slightly increasing trend is observed for higher cycle numbers beyond this threshold.

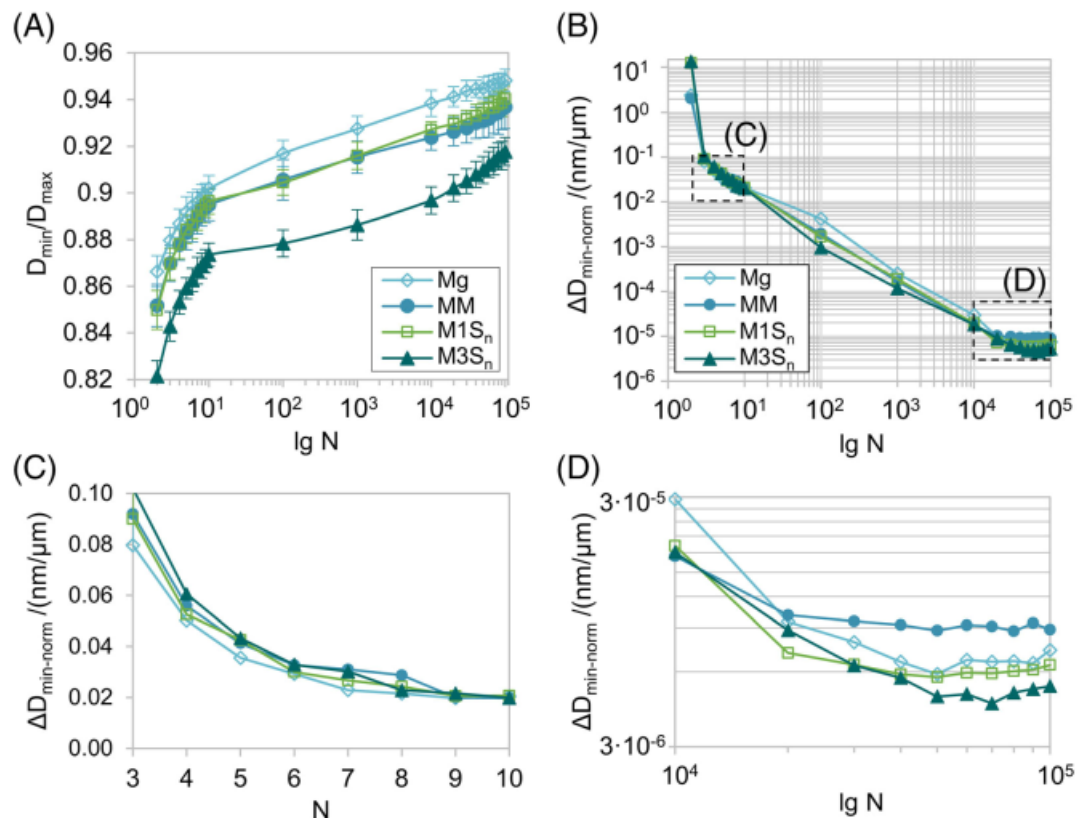


**Figure 4** Cyclic deformation behaviour during nanofatigue loading: (A) average values and standard deviations of  $D_{min}/D_{max}$  plotted versus  $N$ ; (B-D) average  $\Delta D_{min-norm}/N$ -curves (B) for the whole test, (C) in the “incipient” regime ( $N \leq 10^3$  cycles), (D) in the “advanced” regime ( $N \geq 10^4$ ). For standard deviations see supplementary figure S1

### 10.4.2 Estimation of the fatigue endurance limit

Fig. 5A shows typical progressions of plastic strain amplitude ( $\epsilon_{a,p}$ ) versus  $N$  together with fitted polynomial functions from stress-controlled macro-fatigue tests, performed with  $R = -1$ . The small values and the relatively high scatter of  $\epsilon_{a,p}$  make it difficult to extract the cyclic yield strength from the original curves. Fitting polynomials, and evaluating the first derivative, allows clear determination of the critical stress amplitude, where  $\epsilon_{a,p}$  becomes significant<sup>20</sup>. The first derivatives of the fits of the plastic strain amplitude versus the number of cycles highlight the change in  $\epsilon_{a,p}$  with increasing stress amplitude (Fig. 5B). The range where the slope of  $\epsilon_{a,p}$  shows a significant change from the initially extremely low values indicates the estimation value of the cyclic yield strength and, thus, of the endurance limit. This range of significant change in  $\epsilon_{a,p}$  is marked with arrows. From these graphs, we estimate an endurance limit for MM of about 95 MPa. Both nanocomposites, M1S<sub>n</sub> (data not shown) and M3S<sub>n</sub>, exhibit a higher value of about 110 MPa. The value for Mg is much lower than for the mechanically milled materials (60 MPa; data not shown).

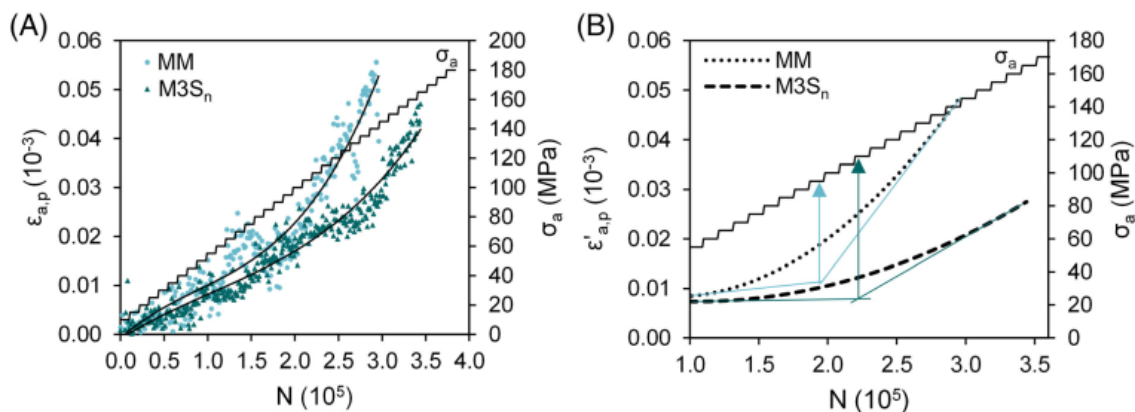
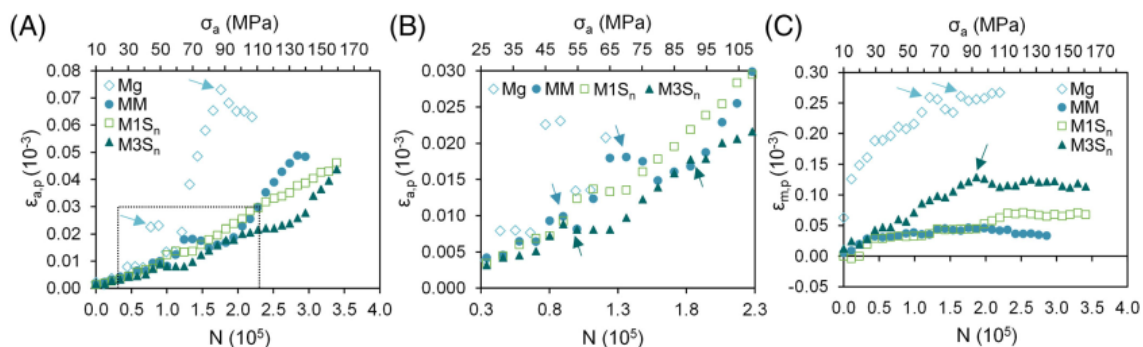


**Figure 5** Progression of plastic strain amplitude versus number of cycles of mechanically milled Mg (MM) and Mg-SiC nanocomposites M3S<sub>n</sub> in LIT: (A) typical examples of  $\epsilon_{a,p}/N$ -curves (dotted graphs) together with their fitted polynomial functions (full lines); (B) plots of the differentiated fit functions for  $\epsilon_{a,p}$  with the estimated fatigue endurance limits, marked by arrows

### 10.4.3 Cyclic deformation behaviour

Figure 6A shows the development of  $\epsilon_{a,p}$ , averaged over each loading step, versus  $N$  and versus  $\sigma_a$  for the same specimens as shown in Figure 5. Averaging over the loading steps highlights some typical aspects of the cyclic deformation behaviour. In the beginning, all materials exhibit a linear increase in  $\epsilon_{a,p}$  with increasing stress amplitude. In the further course, Mg shows two steep increases between 40 and 45 MPa as well as 60 and 90 MPa resulting in the highest overall  $\epsilon_{a,p}$  values.

To better discriminate differences between the mechanically milled materials, a magnified view of the lower loading regime (dotted rectangle in Figure 6A) is shown in Figure 6B. These materials, MM, M1S<sub>n</sub> and M3S<sub>n</sub>, exhibit similar values of the plastic strain amplitude up to a stress amplitude of 50 MPa. MM shows two significant cyclic hardening events (blue arrows in figure 6B) between 50 and 55 MPa as well as 75 and 80 MPa each followed by strong cyclic softening. After the second cyclic hardening event, the plastic strain amplitude for MM steadily increases until it reaches a saturation state at 135 MPa shortly before fracture in the next loading step (140 MPa). Overall, M1S<sub>n</sub> shows cyclic hardening with only two small plateau regions, between 60 and 65 MPa and at 150 MPa right before fracture at 160 MPa. M3S<sub>n</sub> exhibits only one plateau between 55 and 65 MPa. In the further course,  $\epsilon_{a,p}$  shows slight cyclic hardening at 90 MPa and 115 MPa. From 140 MPa onwards,  $\epsilon_{a,p}$  of M3S<sub>n</sub> almost linearly increases until fracture at 160 MPa.



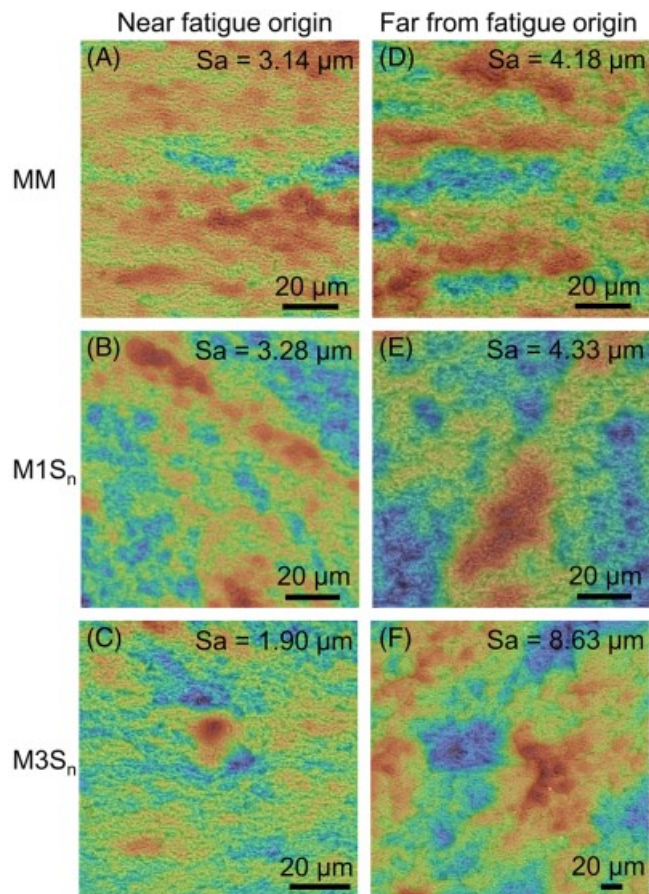
**Figure 6** Cyclic deformation and cyclic creep behaviour of Mg, MM, M1S<sub>n</sub> and M3S<sub>n</sub> averaged over each load step: (A) plastic strain amplitude ( $\epsilon_{a,p}$ ), (B) magnified view of the progression of  $\epsilon_{a,p}$  in the lower loading regime (marked by the dotted rectangle in panel A), and (C) plastic mean strain ( $\epsilon_{m,p}$ ) plotted versus number of cycles ( $N$ ) and stress amplitude ( $\sigma_a$ )

Fig. 6C shows the development of plastic mean strain over the number of cycles and corresponding stress amplitude. Mg exhibits pronounced creep in the positive direction. In some loading steps, namely 55 to 65 MPa and 80 MPa,  $\epsilon_{m,p}$  shows a more pronounced increase, followed by a decrease over several loading steps. From 90 MPa onwards, only a small further increase in  $\epsilon_{m,p}$  is observed. The decrease in  $\epsilon_{m,p}$  correlates with the cyclic hardening phases described above (Fig. 6A). MM and M1S<sub>n</sub> exhibit almost similar  $\epsilon_{m,p}$  values up to a stress amplitude of 95 MPa, and much lower than those observed for Mg. In the further course,  $\epsilon_{m,p}$  decreases slightly for MM, while  $\epsilon_{m,p}$  of M1S<sub>n</sub> increases up to a stress amplitude of 115 MPa and only remains constant until fracture for higher stress amplitudes. M3S<sub>n</sub> increases up to a stress amplitude of 95 MPa showing significantly more pronounced tensile creep than both, MM and M1S<sub>n</sub>. From 95 MPa onwards,  $\epsilon_{m,p}$  first slightly decreases until 110 MPa and then remains more or less constant until fracture.

#### 10.4.5 Fracture surface morphology

Figure 7 shows roughness profiles, plotted as colour maps, of the fracture surfaces near the fatigue origin (left) and far from the fatigue origin (right) of MM (A, D), M1S<sub>n</sub> (B, E) and M3S<sub>n</sub> (C, F). Fatigue failure generally started on the surface, at one of the edges of the rectangular samples. Dark red colour is associated with peaks, whereas blue indicates valleys. The mean arithmetic height  $S_a$  is denoted in each image. As to be expected, all materials show lower roughness near the fatigue origin than further away from it. MM and M1S<sub>n</sub> exhibit very similar roughness values, both at the fatigue origin and further away from it. In contrast, M3S<sub>n</sub> has a very smooth fracture surface near the fatigue origin, but a relatively rough surface further away. With a value of 1.90  $\mu\text{m}$  near the fatigue origin and 8.63  $\mu\text{m}$  further away,  $S_a$  only reaches a little bit more than half

(60 %) the values measured for MM and M1S<sub>n</sub> near the fatigue origin, but double the values of MM and M1S<sub>n</sub> further away.



**Figure 7** Roughness profiles as colour maps near the fatigue origin (A-C) and far from the fatigue origin (bottom D-F) of (A, D) MM, (B, E) M1S<sub>n</sub> and (C, F) M3S<sub>n</sub>. Dark red indicates peaks whereas blue indicates valleys. The mean arithmetic height  $S_a$  is denoted in each profile

### 10.4.6 Textures

Pole figures of Mg, MM, M1S<sub>n</sub> and M3S<sub>n</sub>, illustrating the density distribution of crystallographic grain orientations in the basal (0001), prismatic (10 $\bar{1}$ 0) and pyramidal planes (10 $\bar{1}$ 1), are represented in Figure 8. As to be expected, Mg shows a strong texture. The two maxima of the (0001) plane indicate that the basal planes are parallel to ED (Figure 8A). The three maxima of the (10 $\bar{1}$ 0) pole figure correspond to a preferential orientation of the prism planes of the hexagonal unit cell. Mechanical milling of the powders leads to a much weaker texture, both for the non-reinforced MM and the nanocomposites (Figure 8B-D). Specifically, we observe weakening of the texture by rotation of the basal plane from its parallel orientation to the ED. The (0001) pole figure of the nanocomposites (Figure 8C,D) shows two maxima, whereby the intensity is slightly higher in M3S<sub>n</sub>. All samples also exhibit a strong maximum in the (10 $\bar{1}$ 0) pole figure,

which is associated with the fibre texture. Here, too, the intensity increases in M3S<sub>n</sub> compared to M1S<sub>n</sub>.

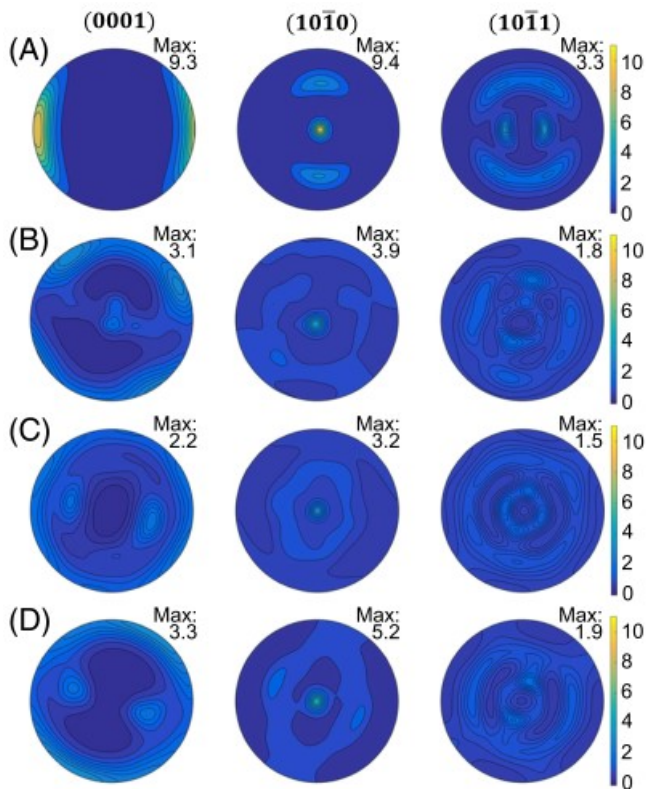


**Figure 8** Pole figures of (A) Mg, (B) MM, (C) M1S<sub>n</sub> and (D) M3S<sub>n</sub> illustrating the density distribution of crystallographic grain orientations in cross-sections (note: ED is orthogonal to the viewing plane) for the basal (0001), prismatic (10 $\bar{1}0$ ), and pyramidal planes (10 $\bar{1}1$ )

## 10.5. Discussion

Cyclic fatigue behaviour is one of the most important properties to be considered when designing parts in motion. The deformation behaviour under fatigue loading is influenced by the manufacturing processes and the resulting microstructure. Here, we investigated the cyclic deformation behaviour of Mg-SiC nanocomposites on the nano scale using cyclic nanoindentation, and on the macro scale using stress-controlled LIT. Due to the small number of samples available, LIT was a helpful method to estimate the fatigue endurance limit and to gain insights into the cyclic deformation behaviour. Interestingly, cyclic nanoindentation and macroscopic, fully reversed cyclic loading lead to similar observations despite the different loading conditions. Grain size, defect density and texture strongly determine the fatigue limit and the cyclic deformation capability by complex interactions.

We propose that the interaction of different microstructural features and the corresponding strengthening mechanisms, including grain boundary strengthening, work hardening and precipitation hardening, together with crack-particle interactions

contribute to different extents to cyclic plastic deformability, leading to different fatigue failure mechanisms in the different materials. Figure 9 summarises the influence of reinforcement content on microstructural features, that is grain size and dislocation density, and on plastic deformability. In the following, we will discuss these connections in detail.

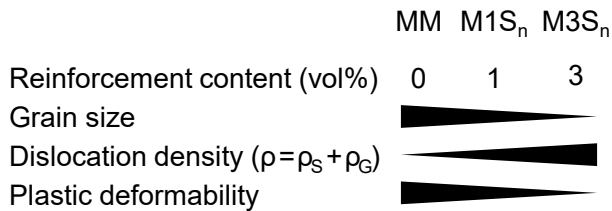


**Figure 9** Microstructural features and plastic deformability dependent on the reinforcement content. Dislocation density  $\rho$  comprises density of statistically stored dislocations ( $\rho_S$ ) and of geometrically necessary dislocations ( $\rho_G$ ).  $\rho_G$  increases with increasing amount of grain boundaries and reinforcement content

### 10.5.1 Specifics of the microstructure

The deformation behaviour under fatigue loading is influenced by the manufacturing processes and the resulting microstructural parameters. We previously showed that mechanical milling leads to nanocrystalline, nano-composite powders<sup>22,23</sup>. Even during the following processing steps, comprising cold-isostatic pressing, sintering and hot extrusion, nano-crystallinity is preserved. Another important microstructural factor influencing the deformation behaviour is texture. Mg wrought alloys usually develop a pronounced basal fiber texture during extrusion<sup>27,28</sup>. In contrast, we unexpectedly observed a weak, tilted basal fiber texture in the mechanically milled materials. The weak texture and the tilting of the c-axis can only be partially explained by the decrease in grain size and the randomisation of grain orientations due to dynamic recrystallization<sup>17,29</sup>. A further possible explanation is a slight torsional stress exerted during extrusion due to the shape of the die. A similar effect of a spiral-shaped basal texture, where the c-axis deviates outwards instead of being oriented orthogonal to the extrusion direction, was described by She et al. for on-line twist extrusion<sup>30</sup>.

Further, the extruded nanocomposites contain a higher amount of dislocations as compared to the non-reinforced but mechanically milled pure magnesium variant MM<sup>22,31</sup>. This is caused by extensive plastic deformation during mechanical milling, leading to a higher dislocation density in the nanoparticle reinforced variants. Defect density is further influenced by the difference in thermal expansion coefficients between SiC particles and Mg matrix. All this results in a build-up of defects around the nanoparticles during the manufacturing process and thus in an increase in defect density in the nanocomposites. Although the higher dislocation density that is reached due to

the nanoparticles triggers dynamic recrystallisation which explains the small retained grain size, not all defects are removed during the process. This observation is in good agreement with results reported by Koneva et al.<sup>32</sup>, where strong barriers such as nanoparticles and grain boundaries lead to the accumulation of geometrically necessary dislocations ( $\rho_G$ ). These retained dislocations significantly influence the mechanical behaviour of the nanocomposites by determining the plastic deformability. Grain size decreases and defect density increases with increasing reinforcement content because interactions between (a lower volume fraction of) nanoparticles and dislocations lead to less plastic deformation and less dynamic recrystallization during extrusion in M1S<sub>n</sub> as compared to M3S<sub>n</sub><sup>22</sup>. As a result, M1S<sub>n</sub> also has a lower quasistatic strength but a higher ductility than M3S<sub>n</sub> and microhardness increases as a function of the decrease in grain size and increase in dislocation density<sup>22</sup>.

### 10.5.2 Microstructural effects on fatigue endurance

Pure Mg showed a fatigue endurance limit of 60 MPa, estimated from macro-LIT. This value is comparable with those commonly reported for pure magnesium<sup>20</sup>. As expected, the estimation values increased by using mechanically milled powders and, further, by addition of nanoparticles. Since the main microstructural difference between Mg and MM is the grain refinement of the latter, the higher endurance limit of MM compared to Mg is therefore likely due to Hall-Petch hardening by grain refinement. Increasing nanoparticle contents in the nanocomposites lead to even smaller grain sizes<sup>22</sup> and a decrease in tension-compression-asymmetry, which explains the increase in endurance limit when nanoparticles are added. Compared to Mg, the materials made from mechanically milled powders, namely MM, M1S<sub>n</sub> and M3S<sub>n</sub>, show a higher plastic deformability due to their extremely small grain size. Concomitantly, grain boundary strengthening triggers the activation of non-basal slip. This finding highlights the very positive effect of mechanical milling as a first process step. Surprisingly, however, increasing reinforcement contents had no additional positive effect, despite the decrease in grain size, and the corresponding higher work hardening capability and quasistatic strength. An explanation is the increased dislocation density with increasing reinforcement content due to the pinning-effect of the nanoparticles, which decreases plastic deformability and facilitates faster crack growth once a fatigue crack has been initiated. Relatively lower energy absorption and faster crack velocities near the fatigue origin, suggesting a more brittle fracture behaviour for small crack lengths, as compared to MM and M1S<sub>n</sub>, are supported by the observation of a very smooth fracture surface of M3S<sub>n</sub> near the fatigue origin. Similarly, Sattari and Atrian<sup>33</sup> describe a reduced dimple size, that is a more brittle fracture mode, with increasing SiC content in fatigued Al-SiC nanocomposites. Further explanation of the very smooth fracture surface near the fatigue origin in M3S<sub>n</sub> is given

by the geometric model for roughness-induced crack closure<sup>34</sup>. The authors stated that the extent of crack closure is a strong function of surface roughness, mode II crack tip displacement and grain size. The model suggests that the plastic zone size exceeds the grain size during fatigue initiation, especially in case of M3S<sub>n</sub> with the smallest grain size of all investigated materials. This leads to a more planar crack path due to activation of more than one slip system.

The effect of increasing brittleness with increasing nanoparticle content is counteracted by a higher propensity to crack deflection and energy absorption due to microcrack formation at particle-matrix interfaces. We see this in regions far from the fatigue origin, where crack deflection leads to a plastic zone that is smaller than the grain size. Consequently, we measure the highest roughness on the fracture surfaces in M3S<sub>n</sub>, together with a serrated fracture path due to slip along one single slip system.

We therefore conclude that the resistance against crack formation and against crack growth both play important but different roles for the deformation behaviour of M1S<sub>n</sub> and M3S<sub>n</sub> thus explaining the similar fatigue endurance limits.

### **10.5.3 Macro-scale cyclic deformation behaviour**

We further evaluated stress-controlled LIT regarding deformation and creep behaviour. Our observation of tensile cyclic creep is in good agreement with our quasistatic results where we observed higher compressive than tensile strength<sup>35,36</sup>. This is surprising in light of the other reports on extruded magnesium materials. Generally, a strong ring-fiber texture is observed which leads to lower strength in compression as compared to tension<sup>37,38</sup>. This asymmetric deformation behaviour, the so-called strength difference effect (SDE), is due to inhibition of basal slip and activation of twinning under compression<sup>39,40</sup>. Reasons for the low and inverse tension-compression asymmetric behaviour that we see in our mechanically milled Mg-SiC nanocomposites may be:

- i) weakening of the texture due to an increase in dynamic recrystallisation with increasing reinforcement content,
- ii) the slightly tilted texture, since the tension-compression yield asymmetry is orientation-dependent<sup>38</sup>, and
- iii) the low strain amplitude of less than 0.2% resulting in an overall decreased asymmetry<sup>40</sup>.

Texture strongly influences the activation of certain slip systems and/or twinning. A weak texture involves a significant number of randomly oriented grains that exhibit a lower Schmid factor for extension twinning. Thus, activation of twinning is hindered, leading to more pronounced work hardening. Hassan and Lewandowski<sup>8</sup> ascribed the work

hardening to a higher density of pre-existing dislocations, dislocation-dislocation interaction and interactions of mobile dislocations with nanoparticles leading to forest dislocations. The small grain sizes ( $<1 \mu\text{m}$ ) and the tilted, weak fiber texture suggest that negligible or no twinning took place<sup>41</sup> and that consequently, secondary deformation modes such as non-basal dislocation slip, are more prominent<sup>42</sup>. This conjecture is confirmed by the observation of Lin et al.<sup>43</sup>, who reported for equal channel angular extrusion of an AZ31 alloy easier slip in tensile testing than in compression testing, resulting in lower yield strength and ultimate tensile strength, due to the preferred orientation of the basal planes.

Maxima in the pole figures can be associated with the activity of different slip systems. Based on observations by Minárik et al.<sup>44</sup> on the influence of texture in the Mg alloy LAE442 on the deformation mechanisms we deduce that prismatic slip, associated with maxima in the (0001) pole figure and additional texture intensities in the (10 $\bar{1}$ 0) pole figure, is the predominant deformation mechanism in our Mg material. Accordingly, basal slip predominates in the nanocomposites, as it is associated with maxima in the (0001) pole figures. We therefore assume that activation of prismatic slip in the nanocomposites can be a reason for the significantly higher endurance limit compared to pure Mg.

Comparison of  $\epsilon_{m,p}$  of Mg with MM, M1S<sub>n</sub> and M3S<sub>n</sub> indicates reduced cyclic creep for the latter (see Figure 6C). These observations well match the findings of Dieringa<sup>45</sup>, who reported improved creep resistance in mechanically milled composites. A reason for higher cyclic creep under tension of M3S<sub>n</sub> compared to MM and M1S<sub>n</sub> may be hindered twinning due to a small grain size and the pinning-effect of the nanoparticles resulting in faster crack initiation.

We further conclude that the relatively high plastic deformation indicated by a steep increase in  $\epsilon_{a,p}$  over several loading steps of M3S<sub>n</sub> (Figure 6A) is due to microcrack formation and growth and less to real plastic deformation<sup>17</sup>. This conclusion is corroborated by the observation of decreasing slopes of the hysteresis loops, with cyclic loading (Figure S2).

#### 10.5.4 Nano-scale cyclic deformation behaviour

High cycle fatigue tests on the nanoscale, performed by cyclic nanoindentation, are still very scarce. For the first time, we characterised the nano-fatigue behaviour of Mg-SiC nanocomposites by repeatedly nanoindenting the same position up to  $10^5$  cycles. The load-indentation curves yield information on the cyclic deformation behaviour, and quantitative evaluation of indent and pile-up volumes reflects the plastic deformation capability of the different nanocomposites.

As to be expected, the largest indents and the highest pile-up were observed for Mg. This is associated with its relatively low strength and its low potential for work hardening<sup>46</sup>. The latter allows relatively high amounts of plastic deformation and easy propagation of the plastic zone. Conversely, in the case of nanoparticle reinforced composites, the regions of higher defect density surrounding the nanoparticles, and the extremely small grain size of the nanocomposites hinder dislocation movement and thus hamper the propagation of the plastic zone developing beneath the indenter tip. This leads to less plastic deformation and, concurrently, to smaller indent and pile-up sizes with increasing reinforcement contents.

The significant change in  $D_{min}/D_{max}$  over the course of loading hints to significant plastic deformation and cyclic hardening in all materials. Interestingly, we see only little local variation in the behaviour between indents performed at different positions in one material, in contrast to what we observed for an Al-Si-Mg alloy<sup>12</sup>. This is due to the much finer, homogeneous microstructure of the materials investigated here. Thus, the nanoindents are much larger than the typical microstructural unit, and we probe volumes of interest that represent the bulk material. In materials with a coarser microstructure, the nano-cyclic deformation behaviour varies to a great extent depending on indent position. This applies when the mean distance between particles or precipitates in the volume beneath the indent is relatively large as compared to indent size or when grain size is so large that single grains are indented and differences in grain orientation become crucial for plastic deformation (e.g. Schmahl et al.<sup>12</sup> and Bočan et al.<sup>47</sup>).

MM showed a steeper incline in  $D_{min}/D_{max}$  in the advanced regime compared to Mg. This can be related to a higher degree of work hardening, due to the smaller grain size and higher defect density. These two parameters lead to an internal reaction stress that lowers the energy gap to the critical resolved shear stress (CRSS). Thus, in the case of MM, non-basal slip is activated more easily. Compared to the other compositions, M3S<sub>n</sub> exhibits the smallest grain size and highest defect density. It further shows the least plastic deformation with increasing number of cycles, which is mainly attributed to the greater restriction of plastic flow by the higher content of nanoparticles and the resulting smaller distances between them.

This observation is also reflected in the progressions of  $\Delta D_{min-norm}$  with the number of cycles: MM shows the highest incremental plastic deformation. Surprisingly, Mg and M1S<sub>n</sub> exhibit very similar curves with almost the same plastic deformation range. Possible reasons are the low number of independent slip systems in the case of Mg and the nanoparticle-dislocation interaction in the case of M1S<sub>n</sub>. As compared to M1S<sub>n</sub>, the higher nanoparticle content in M3S<sub>n</sub> leads to a significant decrease in  $\Delta D_{min-norm}$  with increasing numbers of cycles. In the late advanced regime, however, the incremental

plastic deformation of  $M3S_n$  increases, which may possibly be explained by the activation of non-basal slip.

### 10.5.5 Comparison of nano and macro fatigue behaviour

MM,  $M1S_n$  and  $M3S_n$  show similar plastic deformation behaviour in both nano and macro fatigue tests up to  $2 \cdot 10^4$  and  $10^5$  cycles, respectively. Surprisingly, Mg exhibited lower  $\epsilon_{a,p}$  values than MM in the nano fatigue tests, but higher values in the macro fatigue tests. We attribute this observation to the absence of microcrack formation in the nano fatigue tests. Similar to the macro fatigue tests, we hypothesize that the main plastic deformation mechanism in cyclic nanoindentation is dislocation sliding and that no or only minimal twinning is induced.

## 10.6. Conclusions

This study contributes in several ways to our understanding of the cyclic fatigue behaviour of Mg-SiC nanocomposites on both the nano and macroscale. Macrofatigue tests showed that mechanical milling of the powders leads to a tremendous increase in the fatigue endurance limit. This is due to the higher amount of grain boundaries restricting dislocation movements. Dislocation movements are additionally hindered by nanoparticles in the nanocomposites. The results further indicate that the plastic deformation behaviour determined through cyclic nanoindentation tests is comparable to the behaviour observed in macro fatigue tests. Thus, using cyclic nanoindentation allows fast and easy assessment of material performance with a small number of samples and with minimal material consumption, thus saving time and cost intensive macrofatigue tests.

We conclude that nano fatigue tests directly predict the plastic deformation behaviour on the macro-scale if the interaction volume below the cyclic nanoindent is representative for the bulk microstructure

## 10.7. Acknowledgements

The authors gratefully acknowledge the financial support by the DFG (Deutsche Forschungsgemeinschaft), and we are grateful to Fraunhofer Institute for Ceramic Technologies and Systems (IKTS, Dresden) for performing the hot isostatic pressing. The authors thank Rigerta Tola for sample preparation, Reinhard Meinke for support with macro fatigue testing, and Merle Schmahl for assistance during cyclic nanoindentation testing. The authors further thank Sören Müller and René Nitschke, Extrusion Research and Development Center (FZS), Metallic Materials, TU Berlin for execution and support

during hot extrusion, and Jonas Schmidt, Metallic Materials, TU Berlin for the texture measurements. Thanks go to Fraunhofer Institute for Production Systems and Design Technology (IPK) for cutting the fatigue specimens using EDM. We are further grateful to Christoph Fahrenson, Central Electron Microscopy Unit (ZELMI), TU Berlin for his support during SEM analyses. Open Access funding is provided by Projekt DEAL..

## Conflict of interest

The authors declare that there is no conflict of interest.

## Author contributions

**D. Hübler:** Conceptualization (supporting), Formal analysis, Investigation, Validation, Visualization, Writing – Original Draft Preparation, Writing – Review & Editing; **K. Winkler:** Software, Data curation, Validation, Writing – Review & Editing; **R. Riedel:** Resources, Writing – Review & Editing; **S. Kamrani:** Conceptualization (lead), Project Administration, Funding acquisition, Writing – Review & Editing; **C. Fleck:** Conceptualization (supporting), Methodology, Resources, Supervision, Writing – Review & Editing

## Supplementary

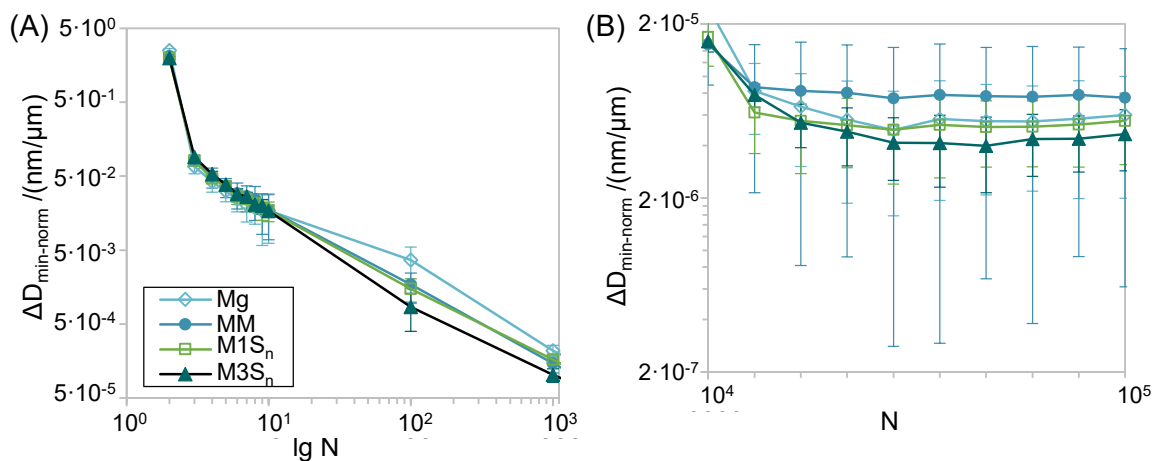


**Figure S1** Standard deviations of  $\Delta D_{min-norm}$ - $N$  curves a) in the "incipient regime" ( $N \leq 10^3$ ) and b) the "advanced" regime ( $N \geq 10^4$ ) presented in the inset of Mg, MM, M1S<sub>n</sub> and M3S<sub>n</sub>

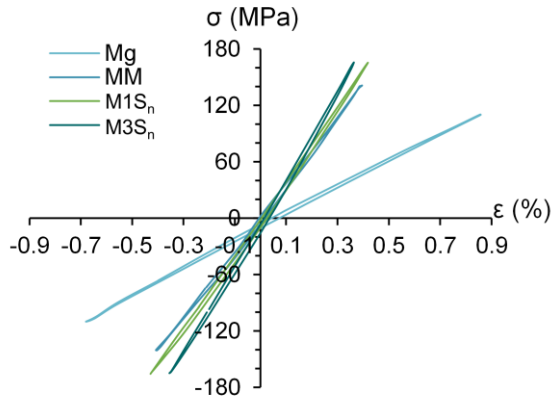


**Figure S2** Hysteresis loops of Mg, MM, M1S<sub>n</sub> and M3S<sub>n</sub> at the cycle before fracture. The slope increases with increasing reinforcement content

## 10.8. References

1. Potzies C, Kainer KU. Fatigue of Magnesium Alloys. *Adv Eng Mater.* 2004;6(5):281–289.
2. Luk MJ, Mirza FA, Chen DL, Ni DR, Xiao BL, Ma ZY. Low cycle fatigue of SiCp reinforced AA2009 composites. *Mater Des (1980-2015).* 2015;66:274–283.
3. Goh CS, Gupta M, Wei J, Lee LC. The Cyclic Deformation Behavior of Mg—Y<sub>2</sub>O<sub>3</sub> Nanocomposites. *J Compos Mater.* 2008;42(19):2039–2050.
4. Chamos AN, Charitidis CA, Skarmoutsou A, Pantelakis SG. An investigation on the high stress sensitivity of fatigue life of rolled AZ31 magnesium alloy under constant amplitude fatigue loading. *Fatigue Fract Eng Mater Struct.* 2010;33(4):252–265.
5. Luo A. Processing, microstructure, and mechanical behavior of cast magnesium metal matrix composites. *Metall Mater Trans A.* 1995;26(9):2445–2455.
6. Lan J, Yang Y, Li X. Microstructure and microhardness of SiC nanoparticles reinforced magnesium composites fabricated by ultrasonic method. *Mater Sci Eng, A.* 2004;386(1–2):284–290.
7. Zhang Z, Chen DL. Contribution of Orowan strengthening effect in particulate-reinforced metal matrix nanocomposites. *Mater Sci Eng, A.* 2008;483–484:148–152.
8. Hassan HA, Lewandowski JJ. Effects of particulate volume fraction on cyclic stress response and fatigue life of AZ91D magnesium alloy metal matrix composites. *Mater Sci Eng, A.* 2014;600:188–194.
9. Koike J, Kobayashi T, Mukai T, Watanabe H, Suzuki M, Maruyama K et al. The activity of non-basal slip systems and dynamic recovery at room temperature in fine-grained AZ31B magnesium alloys. *Acta Mater.* 2003;51(7):2055–2065.
10. Gall K, Biallas G, Maier HJ, Gullett P, Horstemeyer MF, McDowell DL et al. In-situ observations of high cycle fatigue mechanisms in cast AM60B magnesium in vacuum and water vapor environments. *Int J Fatigue.* 2004;26(1):59–70.

11. Jain S, Gokhale A, Jain J, Singh SS, Hariharan K. Fatigue behavior of aged and solution treated AZ61 Mg alloy at small length scale using nanoindentation. *Int Symp Phys Mater*. 2017;684:652–659.
12. Schmahl M, Märten A, Zaslansky P, Fleck C. Nanofatigue behaviour of single struts of cast A356.0 foam: cyclic deformation, nanoindent characteristics and sub-surface microstructure. *Mater Des*. 2020;195:109016.
13. Srivatsan TS, Al-Hajri M, Lam PC. The quasi-static, cyclic fatigue and final fracture behavior of a magnesium alloy metal-matrix composite. *Compos B Eng*. 2005;36(3):209–222.
14. Vaidya AR, Lewandowski JJ. Effects of SiCp size and volume fraction on the high cycle fatigue behavior of AZ91D magnesium alloy composites. *Mater Sci Eng, A*. 1996;220(1-2):85–92.
15. Jabbari AH, Delavar H, Sedighi M. High cycle fatigue behavior of magnesium matrix nanocomposite at elevated temperatures. *Mech Mater*. 2020;142:103278.
16. Jabbari AH, Shafiee Sabet A, Sedighi M, Jahed H, Sommitsch C. Low cycle fatigue behavior of magnesium matrix nanocomposite at ambient and elevated temperatures. *Mater Sci Eng, A*. 2020;793:139890.
17. Tekumalla S, Bibhanshu N, Shabadi R, Suwas S, Ha TMH, Gupta M. Evolution of texture and asymmetry and its impact on the fatigue behaviour of an in-situ magnesium nanocomposite. *Mater Sci Eng, A*. 2018;727:61–69.
18. Srivatsan TS, Godbole C, Quick T, Paramsothy M, Gupta M. Mechanical Behavior of a Magnesium Alloy Nanocomposite Under Conditions of Static Tension and Dynamic Fatigue. *J Mater Eng Perform*. 2013;22(2):439–453.
19. Srivatsan TS, Godbole C, Paramsothy M, Gupta M. The role of aluminum oxide particulate reinforcements on cyclic fatigue and final fracture behavior of a novel magnesium alloy. *Mater Sci Eng, A*. 2009; 532:196–211.
20. Wolf B, Fleck C, Eifler D. Characterization of the fatigue behaviour of the magnesium alloy AZ91D by means of mechanical hysteresis and temperature measurements. *Int J Fatigue*. 2004;26(12):1357–1363.
21. Fleck C, Löhe D. Cyclic deformation behavior of newly developed microalloyed Mg wrought alloys in corrosive environment. In: *Magnesium Technology 2007*, ed. Beals RS, Luo AA, Neelameggham NR, Pekguleryuz MO; 2007:275–279.
22. Penther D, Ghasemi A, Riedel R, Fleck C, Kamrani S. Effect of SiC nanoparticles on manufacturing process, microstructure and hardness of Mg-SiC nanocomposites produced by mechanical milling and hot extrusion. *Mater Sci Eng, A*. 2018;738:264–272.
23. Kamrani S, Penther D, Ghasemi A, Riedel R, Fleck C. Microstructural characterization of Mg-SiC nanocomposite synthesized by high energy ball milling. *Adv Powder Technol*. 2018;29:1742–1748.
24. Nečas D, Klapetek P. Gwyddion: an open-source software for SPM data analysis. *Open Physics* 2012;10(1). <https://doi.org/10.2478/s11534-011-0096-2>.
25. Bunge HJ (ed.). *Program system ODF-analysis for cubic crystal symmetry, orthorhombic sample symmetry*. 2nd ed. Göttingen: Cuvillier; 1999.

26. Bachmann F, Hielscher R, Schaeben H. Texture Analysis with MTEX – Free and Open Source Software Toolbox. *Solid State Phenom.* 2010;160:63–68.
27. Pahlevanpour AH, Behravesb SB, Adibnazari S, Jahed H. Characterization of anisotropic behaviour of ZK60 extrusion under stress-control condition and notes on fatigue modeling. *Int J Fatigue.* 2019;127:101–109.
28. Lou XY, Li M, Boger RK, Agnew SR, Wagoner RH. Hardening evolution of AZ31B Mg sheet. *Int J Plast.* 2007;23(1):44–86.
29. Kavyani M, Ebrahimi GR, Sanjari M, Haghshenas M. Texture evaluation in warm deformation of an extruded Mg–6Al–3Zn alloy. *J Magnes Alloy.* 2016;4(2):89–98.
30. She J, Peng P, Tang AT, Zhang JY, Mao JJ, Liu TT et al. Novel on-line twist extrusion process for bulk magnesium alloys. *Mater Des.* 2019;182:108011.
31. Penther D, Fleck C, Ghasemi A, Riedel R, Kamrani S. Development and Characterization of Mg–SiC Nanocomposite Powders Synthesized by Mechanical Milling. *Key Eng Mater.* 2017;742:165–172.
32. Koneva N, Popova N, Fedorischeva M, Kozlov E. Geometrically Necessary Dislocations in Deformed Martensitic Steel. *Adv Mater Res.* 2014;1013:23–30.
33. Sattari S, Atrian A. Investigation of deep rolling effects on the fatigue life of Al–SiC nanocomposite. *Mater Res Express.* 2018;5(1):15052.
34. Suresh S, Ritchie RO. A geometric model for fatigue crack closure induced by fracture surface roughness. *Metall Mater Trans A.* 1982;13(9):1627–1631.
35. Hübler D. From mechanically milled powders to Mg-SiC nanocomposites: relationships between processing, microstructure and mechanical properties. Doctoral dissertation. Technische Universität Berlin; 2021 (yet unpublished).
36. Kamrani S, Hübler D, Ghasemi A, Fleck C. Enhanced Strength and Ductility in Magnesium Matrix Composites Reinforced by a High Volume Fraction of Nano- and Submicron-Sized SiC Particles Produced by Mechanical Milling and Hot Extrusion. *Materials.* 2019;12(20):3445.
37. Yu M-H, Ma G-W, Qiang H-F, Zhang Y-Q. Generalized Plasticity. Berlin, Heidelberg: Springer-Verlag Berlin Heidelberg; 2006.
38. Yin DL, Wang JT, Liu JQ, Zhao X. On tension–compression yield asymmetry in an extruded Mg–3Al–1Zn alloy. *J Alloys Compd.* 2009;478(1):789–795.
39. Garcés G, Pérez P, Adeva P. Effect of the extrusion texture on the mechanical behaviour of Mg–SiCp composites. *Scripta Mater.* 2005;52(7):615–619.
40. Begum S, Chen D, Xu S, Luo A. Low cycle fatigue properties of an extruded AZ31 magnesium alloy. *Int J Fatigue.* 2009;31(4):726–735.
41. Kaya AA. Physical metallurgy of magnesium. In: Pekguleryuz MO, Kainer KU, Arslan Kaya A, editors. *Fundamentals of Magnesium Alloy Metallurgy* Woodhead Publishing Series in Metals and Surface Engineering. Woodhead Publishing; 2013:33–84.
42. Agnew SR, Yoo MH, Tomé CN. Application of texture simulation to understanding mechanical behavior of Mg and solid solution alloys containing Li or Y. *Acta Mater.* 2001;49(20):4277–4289.

43. Lin HK, Huang JC, Langdon TG. Relationship between texture and low temperature superplasticity in an extruded AZ31 Mg alloy processed by ECAP. *Int Symp on Phys Mater*. 2005. 2005;402(1-2):250–257.
44. Minárik P, Král R, Čížek J, Chmelík F. Effect of different c/a ratio on the microstructure and mechanical properties in magnesium alloys processed by ECAP. *Acta Mater*. 2016;107:83–95.
45. Dieringa H. Properties of magnesium alloys reinforced with nanoparticles and carbon nanotubes: A review. *J Mater Sci*. 2011;46(2):289–306.
46. Broitman E. Indentation Hardness Measurements at Macro-, Micro-, and Nanoscale: A Critical Overview. *Tribol Lett*. 2016;65(1):23.
47. Bočan J, Maňák J, Jäger A. Anisotropic Mechanical Properties of Pure Magnesium Analyzed by In Situ Nanoindentation. *Key Eng Mater*. 2015;662:11–14.

## 11. Overall discussion

### 11.1. Manufacturing process

The production of Mg nanocomposites with enhanced strength and ductility is a key challenge that has been intensively investigated by reinforcing Mg or Mg alloys with different nanoparticles [21, 130–134]. Especially the homogeneous distribution of the nanoparticles has proven to be difficult. It has been shown that the distribution can best be controlled using the powder metallurgical route. Due to the poor sinterability of Mg, an additional consolidation step is necessary after sintering in order to achieve full density. The processes employed to produce the Mg-SiC nanocomposites in this thesis are summarised in Figure 26.

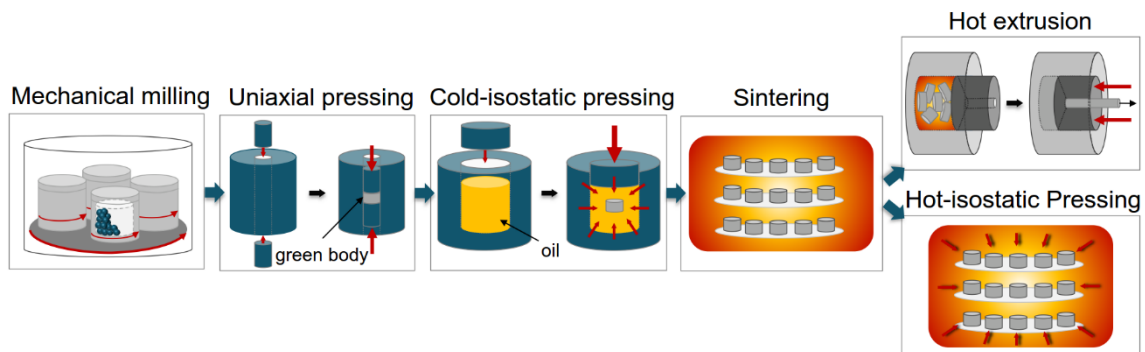


Figure 26. Schematic illustration of the manufacturing processes mechanical milling, uniaxial pressing, cold-isostatic pressing, sintering, and hot extrusion or hot-isostatic pressing.

The microstructure and mechanical properties of the dense Mg-SiC nanocomposites are the result of the interaction of various mechanisms, which are summarized in Figure 27. During mechanical milling many defects were formed due to the plastic deformation of the Mg powder particles, which subsequently formed subgrain boundaries and later grains with extremely reduced size. A steady state was achieved during mechanical milling, when powder particle size and particle morphology did not change significantly. Hence, a homogeneous SiC distribution has been achieved in the Mg matrix, in which only small SiC clusters are present. The cold-isostatic pressing further deformed the composite powder particles and mechanically interlocked them. While the influence of the process parameters on the microstructure and the compaction behaviour of the composite powder particles were already discussed in the first publications, the parameter choice of the sintering process was discussed in the additional chapter 7.

**Mechanical milling** → **Cold-isostatic pressing** → **Sintering** → **Hot extrusion**

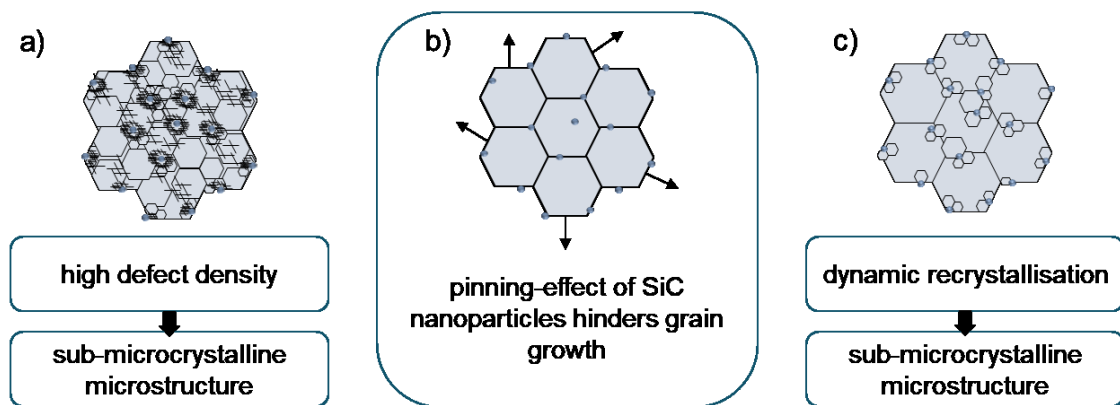


Figure 27. Schematic illustration of the assumed mechanisms during manufacturing of the Mg-SiC nanocomposites. a) During mechanical milling, a high defect density is generated, which leads to a sub-microcrystalline microstructure; b) the pinning-effect of SiC nanoparticles hinders grain growth during sintering; c) nanoparticles act as nuclei for dynamic recrystallization during hot extrusion.

As a texture-free alternative to the hot extrusion process, hot isostatic pressing was chosen as last consolidation step producing Mg-SiC nanocomposites. Although it is common to use HIP after sintering for complete compaction, the process has been employed rarely for nanocomposites [160–162]. HIP is known to reduce grain growth compared to sintering, because a lower temperature can be employed due to the applied pressure. Surprisingly, grain growth occurred during the HIP processing of the Mg-SiC nanocomposite and formed two areas with and without SiC nanoparticles, which were not yet present after sintering. It can therefore be assumed that grain growth already started to a small extent during sintering and continued during HIP even at a lower process temperature. The TEM investigations indicate that discontinuous grain growth (secondary recrystallisation) took place, during which the driving force for grain growth of some grains was greater than the dragging force of the nanoparticles, which is Zener pinning [163]. Yao et al. observed the same phenomena in Al6063-SiC nanocomposites [164]. Certainly, grain growth and migration are influenced by the particle size and their volume fraction in the matrix. The process is driven by the decrease of the surface energy of the grain boundary as is the case when particles pin grain boundaries due to the reduction in grain boundary area [165]. Consequently, an unpinning of particles and thus the migration of grain boundaries occurs first with the largest grain, whereby the energy of the system decreases due to the elimination of grain interfaces. When the particles are pushed together due to the grain growth, the next larger grain can grow in order to further decrease the grain boundary energy, whereby regions with a significantly larger grain size develop, while regions with sub-microcrystalline grain size remain next to it.

Considering the bimodal grain size after HIP and thus a non-uniform distribution of SiC nanoparticles, and since it is not possible to completely prevent grain growth during sintering, hot extrusion is the better option as last consolidation process to achieve a sub-microcrystalline microstructure and a completely dense material. The larger pressure during extrusion and the strong deformation caused a dynamic recrystallization of the grains, which was missing in the HIP process in order to keep the grain size small. In addition to the significant increase in density to over 99% by hot extrusion, small SiC clusters are broken up due to the shear stresses during extrusion, which further improves the SiC distribution. However, hot extrusion can lead to a strong fibre texture and thus asymmetry tension-compression behaviour [166,167]. Since a symmetrical tension-compression behaviour is usually desired, the HIP process offers a great advantage in that respect.

## 11.2. Mechanical properties

### 11.2.1. Compression behaviour

As the Vickers hardness in Manuscript III showed, the hardness increased with increasing reinforcement content. An increase can be observed as well when comparing the nanohardness of powder and bulk materials (Figure 28). Further, the embedding resin around the powder particles has a significant influence on the nanohardness and may lead to lower values. This must be considered, when performing nanoindentation measurements. The small difference of powder and bulk nanohardness of M10S<sub>n</sub> suggests that a high defect density was achieved already during mechanical milling, leading to a higher nanohardness compared to the other samples. The nanohardness significantly increased with the following compaction process steps, which can be attributed to grain refinement and defect accumulation, thus increasing the resistance against further plastic deformation.

In Figure 28, the nanohardness of other composites than M10S<sub>n</sub> with the same reinforcement content, namely M10S<sub>μ</sub> and M10S<sub>n</sub>-mixed, are also shown. While M10S<sub>μ</sub> was reinforced with SiC particles with a particle size of 1 μm, M10S<sub>n</sub>-mixed was reinforced with nanoparticles, which were mixed with the Mg powder but not mechanically milled [168]. The decrease in nanohardness and elastic modulus demonstrates once more the importance of mechanical milling and the use of nanoparticles as reinforcements instead of micron sized particles. The elastic modulus was calculated from the effective elastic modulus using equation 1 and the rule of mixture for the Poisson ratios of the composites ( $\nu_{Mg} = 0.35$ ,  $\nu_{SiC} = 0.14$ ,  $\nu_i = 0.07$ ,  $E_i = 1140$  GPa [169,170]). It is remarkable that the calculated elastic modulus almost matches the determined modulus from the fatigue tests.

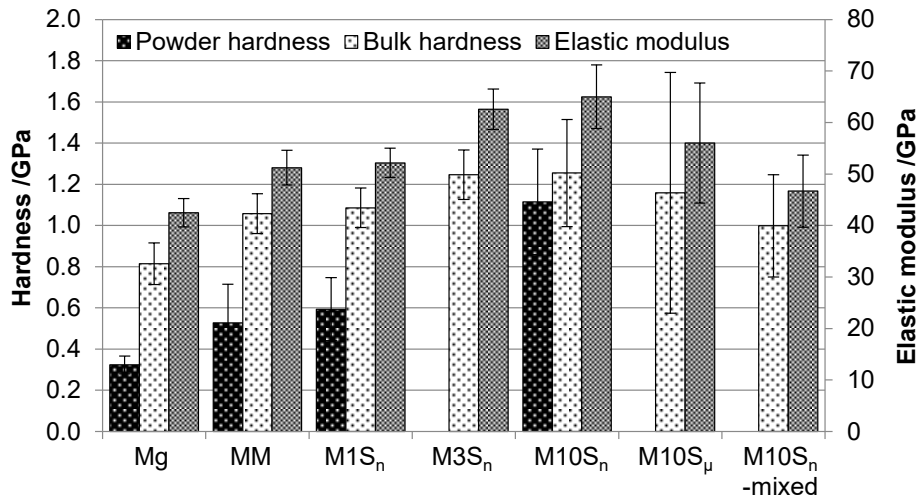


Figure 28. Powder and bulk nanohardness as well as calculated elastic modulus for Mg, MM, M1S<sub>n</sub>, and M10S<sub>n</sub>. Hardness and elastic modulus values of M10S<sub>μ</sub> and M10S<sub>n</sub>-mixed were taken from [168].

Compression tests, whose results are shown in Figure 29, revealed a higher yield strength than observed in other studies on nanocomposites [159,171,172]. Even Mg showed an overall increased CYS and UCS compared to pure Mg, which is most likely due to the different production processes. Although Mg-ZnO nanocomposites were produced using the powder metallurgy technique as the compositions in this thesis, the powder was blended but not mechanically milled using milling balls. The Mg-TiO<sub>2</sub> and Mg-TiB<sub>2</sub> nanocomposites were produced using disintegrated melt deposition followed by hot extrusion and exhibit grain sizes in the micrometre range, like the Mg-ZnO nanocomposites. The higher grain sizes allow dislocations to move easier as well as twinning deformation. The plastic deformation, which was observed in the mechanically milled powder in Manuscript I, and the resulting grain refinement might have affected the compressive behaviour of Mg, MM, M1S<sub>n</sub>, M3S<sub>n</sub>, and M10S<sub>n</sub> in such a way that all samples showed an increased strength compared to the other studies.

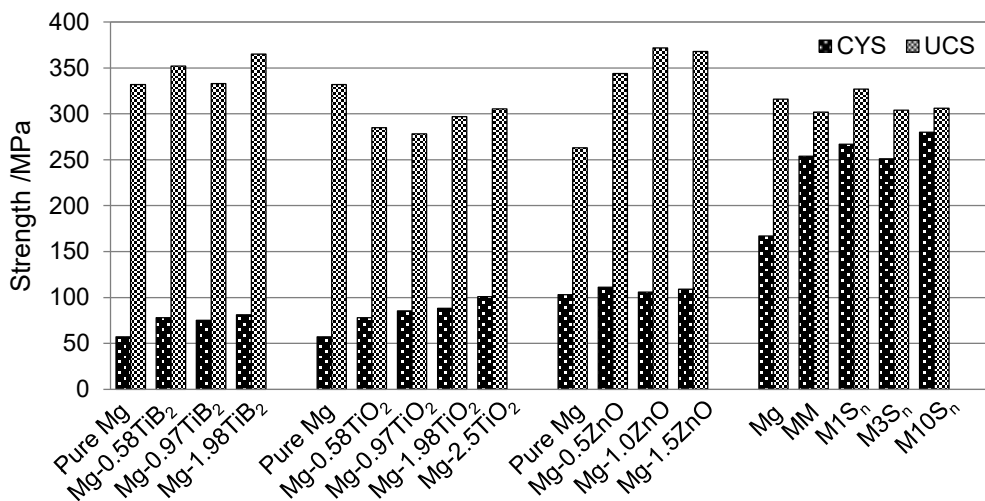


Figure 29. Compressive yield strength (0.2% CYS) and ultimate compression strength (UCS) of Mg, MM, M1S<sub>n</sub>, M3S<sub>n</sub>, and M10S<sub>n</sub> compared to other studies [159,171,172].

### 11.2.2. Tensile behaviour

The measured value in chapter 9.2 of the yield strength of Mg is in agreement with that of Tun et al. [159], while MM, M1S<sub>n</sub>, and M3S<sub>n</sub> have a higher YS than those observed in other studies. The study of Meenashisundaram et al. [171] indicates that a minimum reinforcement content of 2 % is required in order to improve the tensile strength in Mg-TiO<sub>2</sub> nanocomposites. In this thesis, grain refinement is the reason for the higher UTS of MM compared to Mg. A further increase in UTS, which was observed for the Mg-SiC nanocomposites can be attributed to Hall-Petch, dislocation density and Orowan strengthening.

The tensile properties regarding the ultimate tensile strength of the Mg-SiC nanocomposites M1S<sub>n</sub> and M3S<sub>n</sub>, as well as the Mg references produced in this thesis are compared to other studies (see also chapter 2.4.2. Tensile behaviour) and presented in Figure 30. Compared to Mg (MW), the non-milled Mg shows slightly higher UTS, but significantly lower fracture strain. In contrast, MM shows a significantly higher UTS than Mg, which is due to the grain refinement. Overall, the Mg-SiC nanocomposites M1S<sub>n</sub> and M3S<sub>n</sub> were outperformed by Mg alloys in terms of fracture strain to UTS. This is due among others to the alloying elements, which cause an increase in ductility, while Mn-rich precipitates lead to precipitation strengthening [173]. Furthermore, the Mg-SiC nanocomposites showed higher tensile strength compared to Mg-SiC<sub>μ</sub> composites produced through DMD. Further, only the Mg-SiC<sub>μ</sub> composites with less than 10% reinforcement content showed a higher fracture strain compared to the produced Mg-SiC nanocomposites.

In most cases, nanocomposites from other studies showed a lower UTS and a higher fracture strain than the Mg-SiC nanocomposites studied in this thesis. One explanation is their grain size in the micrometre range, which is known to increase the ductility. However, the grain size has been reported only in few studies, which is why the reason for the higher ductility cannot be fully assessed.

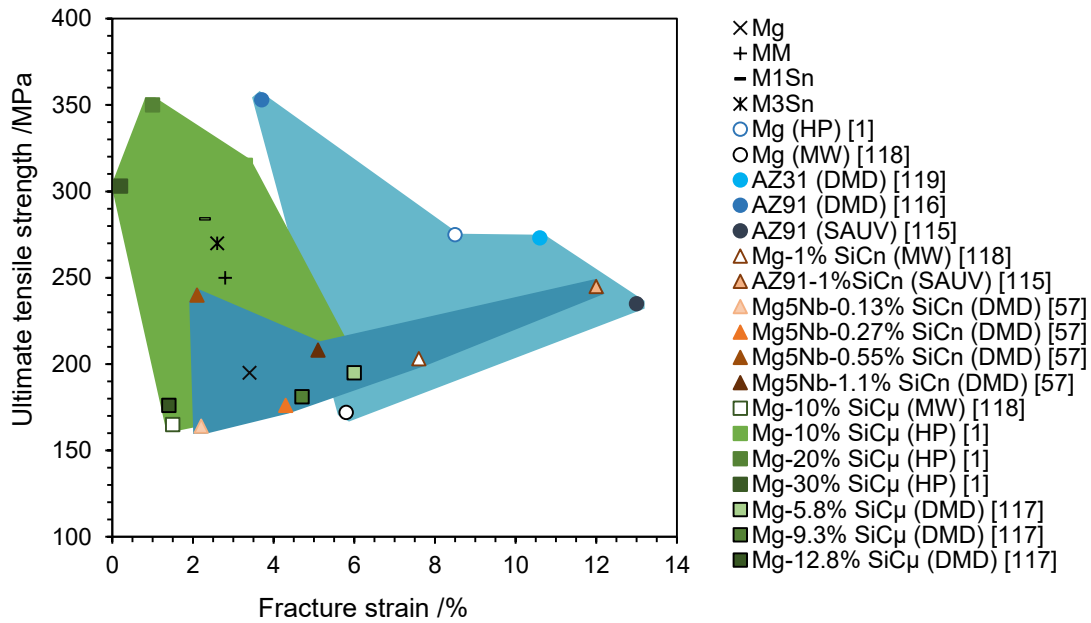


Figure 30. Comparison of the ultimate tensile strength (UTS) vs. fracture strain of the produced Mg, MM, M1Sn, and M3Sn to pure Mg, Mg alloys, and their Mg-SiC nanocomposite of other studies, which were produced by different processes prior to extrusion. (HP – Hot pressing; MW – Micro wave sintering; DMD – Disintegrated melt deposition; SAUV - Semisolid stirring assisted ultrasonic vibration) prior to extrusion [1,13,58,116–119]. The legend shows the respective composition, followed by the manufacturing process in parentheses and the reference in square brackets.

The range of ductility of pure Mg reported in the literature is 5–8% [174], which is in agreement with the fracture strain reported by Krishnadev et al. and Wong and Gupta [1,119]. The value measured in this thesis is hence lower. This might be due to different mechanisms. It is reported that ductility improvement can be attributed to fine particles [92,175], grain size refinement [175], non-basal slip activation [176,177], and changes in texture [110,159,178]. In contrast, Berbenni et al. claimed that a decrease of the ductility can arise from an inhomogeneous grain size distribution [179]. The grain size distribution after extrusion is, however, quite narrow for the nanocomposites (Manuscript III). In addition, since a high homogeneity of the grain size leads to an increased yield strength [159], not the distribution but the grain size itself could be in this case the reason for the reduced ductility. As reported by Tun et al. [180], non-milled powder, which exhibited a larger grain size and a lower defect density, achieved a higher fracture strain than Mg nanocomposites, which were produced by mechanical milling. Moreover, the dislocation density further increases with increasing strain during loading [181,182].

As a matter of fact, nanoparticles increase the dislocation density due to Frank-Read source [183], Orowan pinning [55–57], and thermal expansion differences between matrix and reinforcements [60,64]. Along with the increase in dislocation density, the grain size is reduced due to nanoparticles, which limits the amount of stress that can be

build up. Therefore, it can be assumed that non-basal planes could not be activated and/or were pinned by grain boundaries and nanoparticles and that the resolved shear stress was locally insufficient high to reach the critical value for non-basal slip. Small MgO inclusions, observed in all compositions, might have further enhanced strain hardening. However, till now no defects have been found to confirm predicted mechanisms, since TEM investigations are hampered by the complexity of the hcp structure, the small grain size, and the high reactivity to oxygen.

Comparing compression and tensile properties, an asymmetry was observed. Since both compression and tensile tests were carried out under the same strain rate, the strain rate dependence of the tensile yield strength [184] is not the reason for the different behaviour. The TYS of Mg materials with a strong basal texture is typically higher than the CYS [110,178]. Although Mg showed a strong texture compared to the other compositions, the CYS was higher than the TYS, resulting in TYS to CYS ratios of 0.6 to 0.7, which is significantly lower than the values above 1.0 reported in other studies [167]. For compression and tensile tests, rods with different cross sections, round and rectangular, with almost similar press ratios of 22 and 23.6, respectively, were produced. This small difference in press ratio and the different shape have influenced the extrusion process. It is assumed that the higher press ratio in case of the flat rectangular rods and their reduced thickness lead to an increased shear stress and thus plastic deformation during extrusion [111]. The resulting lower elastic and plastic deformability explains the lower yield strength and the significant lower fracture strain under tension compared to compression.

### 11.2.3. Fatigue behaviour

Extruded Mg usually shows a strong tension-compression asymmetry and cyclic creep under compression [185]. The reason is the higher tensile yield strength (TYS) compared to the compression yield strength (CYS) due to the activation of twinning under tension in strongly textured materials.

During fatigue testing, cyclic creep under tension occurred, which is in contrast to the tension-compression-asymmetry generally observed for extruded magnesium. Quasistatic compression and tensile tests revealed a higher CYS than TYS (see 9. Additional results on mechanical properties). Since the deployed stress amplitude is lower than the determined yield strength from the compression and tensile tests, it is highly unlikely that twinning is dominant during fatigue testing [166]. Another reason might be the submicron-crystalline grain size achieved during extrusion, which restricts twinning and promotes the activation of non-basal slip.

Micro- and nanoindentation, with a high local resolution, can help to further understand the cyclic deformation behaviour at the macro level. An excellent correlation of the cyclic behaviour of metallic materials, more precisely the cyclic hardening exponent and the plastic indentation depth amplitude, was shown for the determination by cyclic Vickers indentation tests in comparison to CAT [186]. In addition, the cyclic behaviour could be determined with a higher local resolution, when the force was reduced from 1000 mN to 100 mN, which resulted in a decreased pile-up volume [187]. However, due to the submicron-crystalline grain sizes of the Mg-SiC nanocomposites, Vickers indents with diagonal sizes larger than 5  $\mu\text{m}$  would result in an average over many grains. Therefore, cyclic nanoindentation is more suitable to investigate the cyclic deformation behaviour.

Although Mg-SiC nanocomposites possess nanoparticles and hence a small grain size, which significantly influence dislocation movement, plastic deformation behaviour during fatigue testing is comparable on the nano and macro scale [188]. TEM investigations can further help to analyse the dislocation-nanoparticle and dislocation-grain boundary interaction.

## 12. Conclusion and outlook

### *Conclusion*

Reinforcing Mg with SiC nanoparticles is a suitable method to produce Mg parts with high strength without decreasing ductility, while the density can be kept smaller than  $2 \text{ g/cm}^3$ . Their high fracture toughness and specific surface area makes SiC nanoparticles a good choice for Mg nanocomposites. A new processing route comprising uniaxial pressing, cold-isostatic pressing, sintering, and hot extrusion was established, with which a homogeneous distribution of nanoparticles up to a volume fraction of 10 % and an almost completely dense bulk material with a sub-microcrystalline microstructure were achieved. It has been shown that mechanical milling achieved a sub-microcrystalline structure and a homogeneous distribution of SiC nanoparticles up to a reinforcement content of 10 vol%, where only a few agglomerations were visible. A homogeneous distribution of the SiC nanoparticles could be maintained through hot extrusion and dynamic recrystallization occurred, which was promoted by the nanoparticles. In this way, significant grain growth was inhibited. In contrast to extrusion, areas without SiC nanoparticles and grain growth were observed through HIP, resulting in a decrease in hardness compared to the sintered state. Therefore, mechanical properties were investigated on the extruded compositions. The higher compressive yield strength compared to the tensile yield strength is assumed to be due to the small grain size, which hindered twinning under tension and favoured slip under compression. Overall, mechanical milling is important to decrease the grain size and thus increase hardness and fatigue strength of the bulk material. By increasing the volume fraction of SiC nanoparticles, the hardness further increased, while the fatigue strength remained constant. This is the reason why various mechanisms are assumed to be active, including Hall-Petch, dislocation density, and Orowan strengthening.

### *Outlook*

Regarding the manufacturing process, a detailed parameter study of the influence of the HIP process on the microstructure of Mg nanocomposites can help to further understand the underlying mechanisms of the grain coarsening. It can also be assumed that the HIP process produces nanocomposites with higher ductility compared to the extruded nanocomposites. In addition, at least tensile and compression tests of the HIP nanocomposite should be carried out to investigate the influence of the microstructure with bimodal grain size on the properties, since He et al. [189] found that hierarchical Mg-SiC nanocomposites offer better tensile properties and higher ductility than homogeneous Mg-SiC nanocomposites.

Some changes in the manufacturing process route might improve the ductility of the extruded nanocomposites. Heat treatment before extrusion or a longer sintering time can lead to recovery, which increases the ductility of the material and causes less plastic deformation during extrusion. Furthermore, a post-extrusion heat treatment at a recrystallization temperature of 150°C for 5h could also be effective to enhance 0.2% YS, UTS and ductility, as reported by Ugandhar et al. for Mg-SiC composites [190]. In this case, the grain size of the Mg-SiC composites was in micrometre range and did not change during the heat treatment. The grain size of the nanocomposites produced in this thesis are in sub-micrometre range and may therefore grow to micrometre size during heat treatment. A fully recovered and recrystallized microstructure of a Mg-SiC nanocomposite might lead to both high strength and ductility.

Since this thesis is based on basic research on pure Mg, improving the ductility of Mg using alloying elements has not been investigated, but should be considered in the future works. In Mg-Zn-Mn alloys, the addition of Ca results in improved mechanical properties due to the weakening of the basal texture [191], which is known to increase the ductility [177]. AM alloys, containing Mn and high concentrations of Al, generally possess superior extrudability compared to AZ alloys, due to the absence of Zn-containing eutectic ternary phases [192]. In addition, rare earth Mg alloys, such as Mg-8.0Gd-3.0Y-0.5%Zr, showed a weakened texture and near tension-compression symmetry during cyclic loading [193].

Although microstructural investigations regarding the structure-property relationship have already answered many questions, detailed TEM investigations of the tested samples aimed to fully understand the deformation mechanisms and dislocation movements within the complex crystal structure are missing. A pre-characterization through EBSD, which would have supported the TEM investigations, was not possible due to the sub-micro to nanocrystalline microstructure and the high oxygen affinity of the nanocomposites. Recently, a preliminary investigation using precession electron diffraction (PED) found that grain orientation can be ascertained to align the grains in such a way that defects are visible.

Finally, finite element method (FEM) has gained great importance to simulate material behaviour during manufacturing processes and mechanical testing. The use of this method is particularly advantageous when, as in this thesis, only a small number of samples is available. FEM should therefore be employed to predict manufacturing parameters and material properties based on experimental data and assumptions.

### 13. List of symbols and abbreviations

---

Latin symbol

---

$A$	Contact area
$b$	Burgers vector
$d$	Grain size
$d^*$	Critical particle size
$E$	Elastic modulus
$E_{eff}$	Effective elastic modulus
$E_i$	Elastic modulus of the indenter
$E_r$	Reduced elastic modulus
$f$	Volume fraction
$F$	Force
$G$	Shear modulus
$h$	Displacement
$h_f$	Final depth
$h_{max}$	Maximum displacement
$H$	Nanohardness
$K_y$	Strengthening coefficient
$P$	Load
$P_{max}$	Maximum load
$r$	Particle radius
$S$	Stiffness
$t$	Time
$T$	Temperature
$v$	Velocity
$V$	Volume

---

Greek symbol

---

$\Delta\alpha$	Difference of linear expansion coefficient
$\Delta T$	Difference in temperature
$\varepsilon_{a,p}$	Plastic strain amplitude
$\varepsilon_{m,p}$	Non-elastic mean strain
$\varepsilon_{m,t}$	Total mean strain
$\rho_0$	Initial density
$\rho_\infty$	Final density
$\sigma_0$	Starting stress for dislocation movement
$\sigma_a$	Stress amplitude
$\sigma_m$	Mean stress
$\sigma_y$	Yield stress
$\tau_{OR}$	Orowan shear stress
$\Phi$	Declination angle
$\nu$	Poisson's ratio of the specimen
$\nu_i$	Poisson's ratio of the indenter
$\nu_{Mg}$	Poisson's ratio of magnesium
$\nu_{SiC}$	Poisson's ratio of silicon carbide

---

Abbreviation	
BPR	Ball-to-powder ratio
CAT	Constant amplitude test
CIP	Cold isostatic pressing
CRSS	Critical resolved shear stress
CTE	Coefficient of thermal expansion
CYS	Compression yield strength
DMD	Disintegrated melt deposition
DRX	Dynamic recrystallization
ED	Extrusion direction
EDM	Electronic discharge machining
fcc	Face-centered cubic
hcp	Hexagonal closed packed
HIP	Hot isostatic pressing
HP	Hot pressing
LIT	Load increase test
Mg	Magnesium
MM	Milled magnesium
MMC	Metal matrix composites
M1S <sub>n</sub>	Mg + 1 vol% SiC nanoparticles
M3S <sub>n</sub>	Mg + 3 vol% SiC nanoparticles
M10S <sub>n</sub>	Mg + 10 vol% SiC nanoparticles
MW	Microwave sintering
ND	Normal direction
PED	Precession electron diffraction
PM	Powder metallurgy
RD	Rolling direction
RSS	Resolved shear stress
RT	Room temperature
SAUV	Semisolid stirring assisted ultrasonic vibration
SEM	Scanning electron microscopy
SPM	Scanning probe microscopy
TD	Transverse direction
TEM	Transmission electron microscopy
TYS	Tensile yield strength
UCS	Ultimate compression strength
UTS	Ultimate tensile strength
YS	Yield strength

## 14. References

- [1] Krishnadev MR, Angers R, Nair CGK, Huard C. The structure and properties of magnesium-matrix composites. *The Journal of The Minerals, Metals & Materials Society (TMS)* 1993;45(8):52–54. <https://doi.org/10.1007/BF03222407>.
- [2] Luo A, Renaud J, Nakatsugawa I, Plourde J. Magnesium castings for automotive applications. *The Journal of The Minerals, Metals & Materials Society (TMS)* 1995;47(7):28–31. <https://doi.org/10.1007/BF03221226>.
- [3] Pollock TM. Weight loss with magnesium alloys. *Science* 2010;328(5981):986–987. <https://doi.org/10.1126/science.1182848>.
- [4] Ibrahim IA, Mohamed FA, Lavernia EJ. Particulate reinforced metal matrix composites - A review. *Journal of Materials Science* 1991;26(5):1137–1156. <https://doi.org/10.1007/BF00544448>.
- [5] Tjong SC. Novel Nanoparticle-Reinforced Metal Matrix Composites with Enhanced Mechanical Properties. *Advanced Engineering Materials* 2007;9(8):639–652. <https://doi.org/10.1002/adem.200700106>.
- [6] Manoharan M, Lim SCV, Gupta M. Application of a model for the work hardening behavior to Mg/SiC composites synthesized using a fluxless casting process. *Materials Science and Engineering: A* 2002;333(1–2):243–249. [https://doi.org/10.1016/S0921-5093\(01\)01845-7](https://doi.org/10.1016/S0921-5093(01)01845-7).
- [7] Shen MJ, Ying WF, Wang XJ, Zhang MF, Wu K. Development of High Performance Magnesium Matrix Nanocomposites Using Nano-SiC Particulates as Reinforcement. *Journal of Materials Engineering and Performance* 2015;24(10):3798–3807. <https://doi.org/10.1007/s11665-015-1707-7>.
- [8] Suryanarayana C, Al-Aqeeli N. Mechanically alloyed nanocomposites. *Progress in Materials Science* 2013;58(4):383–502. <https://doi.org/10.1016/j.pmatsci.2012.10.001>.
- [9] Ramakrishnan N. An analytical study on strengthening of particulate reinforced metal matrix composites. *Acta Materialia* 1996;44(1):69–77. [https://doi.org/10.1016/1359-6454\(95\)00150-9](https://doi.org/10.1016/1359-6454(95)00150-9).
- [10] Benjamin JS. Mechanical Alloying. *Scientific American* 1976;234(5):40–49. <https://doi.org/10.1038/scientificamerican0576-40>.
- [11] Shen MJ, Wang XJ, Ying T, Wu K, Song WJ. Characteristics and mechanical properties of magnesium matrix composites reinforced with micron/submicron/nano SiC particles. *Journal of Alloys and Compounds* 2016;686:831–840. <https://doi.org/10.1016/j.jallcom.2016.06.232>.

- [12] Goh CS, Wei J, Lee LC, Gupta M. Development of novel carbon nanotube reinforced magnesium nanocomposites using the powder metallurgy technique. *Nanotechnology* 2006;17(1):7–12. <https://doi.org/10.1088/0957-4484/17/1/002>.
- [13] Alam ME, Han S, Nguyen QB, Salem Hamouda AM, Gupta M. Development of new magnesium based alloys and their nanocomposites. *Journal of Alloys and Compounds* 2011;509(34):8522–8529. <https://doi.org/10.1016/j.jallcom.2011.06.020>.
- [14] Gupta M, Wong WLE. Magnesium-based nanocomposites: Lightweight materials of the future. *Materials Characterization* 2015;105:30–46. <https://doi.org/10.1016/j.matchar.2015.04.015>.
- [15] Moazami-Goudarzi M, Akhlaghi F. Effect of nanosized SiC particles addition to CP Al and Al–Mg powders on their compaction behavior. *Powder Technology* 2013;245:126–133. <https://doi.org/10.1016/j.powtec.2013.04.025>.
- [16] Fogagnolo JB, Ruiz-Navas EM, Robert MH, Torralba JM. The effects of mechanical alloying on the compressibility of aluminium matrix composite powder. *Materials Science and Engineering: A* 2003;355(1):50–55. [https://doi.org/10.1016/S0921-5093\(03\)00057-1](https://doi.org/10.1016/S0921-5093(03)00057-1).
- [17] Nazari KA, Nouri A, Hilditch T. Compressibility of a Ti-based alloy with varying amounts of surfactant prepared by high-energy ball milling. *Powder Technology* 2015;279:33–41. <https://doi.org/10.1016/j.powtec.2015.03.044>.
- [18] Ramezanalizadeh H, Emamy M, Shokouhimehr M. A novel aluminum based nanocomposite with high strength and good ductility. *Journal of Alloys and Compounds* 2015;649:461–473. <https://doi.org/10.1016/j.jallcom.2015.07.088>.
- [19] Liu YB, Lim SC, Lu L, Lai MO. Recent development in the fabrication of metal matrix-particulate composites using powder metallurgy techniques. *Journal of Materials Science* 1994;29(8):1999–2007. <https://doi.org/10.1007/BF01154673>.
- [20] Hull AW. The Crystal Structure of Magnesium. *Proceedings of the National Academy of Sciences of the United States of America* 1917;3(7):470–473.
- [21] Staroselsky A, Anand L. A constitutive model for hcp materials deforming by slip and twinning. *International Journal of Plasticity* 2003;19(10):1843–1864. [https://doi.org/10.1016/S0749-6419\(03\)00039-1](https://doi.org/10.1016/S0749-6419(03)00039-1).
- [22] Jiang S, Jiang Z, Chen Q. Deformation twinning mechanism in hexagonal-close-packed crystals. *Scientific Reports* 2019;9(1):618. <https://doi.org/10.1038/s41598-018-37067-8>.

- [23] Mises R von. Mechanik der festen Körper in plastisch-deformablen Zustand. Nachrichten von der königlichen Gesellschaft der Wissenschaften zu Göttingen 1913;Math.-phys. Klasse 4:582–592.
- [24] Krauß M. Zur thermischen Ermüdung der Magnesiumbasislegierungen AZ31 und AZ91. Zugl.: Kassel, Univ., Diss., 2006. Kassel: Kassel Univ. Press; 2007.
- [25] Wang W, Liu J, Soh AK. Crystal plasticity modeling of strain rate and temperature sensitivities in magnesium. *Acta Mechanica* 2019;230(6):2071–2086. <https://doi.org/10.1007/s00707-019-2374-9>.
- [26] Schmid E, Boas W. Kristallplastizität: Mit Besonderer Berücksichtigung der Metalle. Berlin, Heidelberg, s.l.: Springer Berlin Heidelberg; 1935.
- [27] Pyzalla A, Brodmann M, Lee PL, Haeffner D. Microstructure, Texture and Residual Microstrains in MgAl8Zn Deformed at Very High Strain Rates. In: *Magnesium Alloys and their Applications*. John Wiley & Sons, Ltd, p. 125–130.
- [28] Ion SE, Humphreys FJ, White SH. Dynamic recrystallisation and the development of microstructure during the high temperature deformation of magnesium. *Acta Metallurgica* 1982;30(10):1909–1919. [https://doi.org/10.1016/0001-6160\(82\)90031-1](https://doi.org/10.1016/0001-6160(82)90031-1).
- [29] Biswas S, Suwas S, Sikand R, Gupta AK. Analysis of texture evolution in pure magnesium and the magnesium alloy AM30 during rod and tube extrusion. *Materials Science and Engineering: A* 2011;528(10–11):3722–3729. <https://doi.org/10.1016/j.msea.2011.01.021>.
- [30] Agnew SR, Yoo MH, Tomé CN. Application of texture simulation to understanding mechanical behavior of Mg and solid solution alloys containing Li or Y. *Acta Materialia* 2001;49(20):4277–4289. [https://doi.org/10.1016/S1359-6454\(01\)00297-X](https://doi.org/10.1016/S1359-6454(01)00297-X).
- [31] Kammer C. *Magnesium-Taschenbuch*. 1st ed. Düsseldorf Aluminium-Verlag.; 2000.
- [32] Agnew SR, Duygulu Ö. Plastic anisotropy and the role of non-basal slip in magnesium alloy AZ31B. *International Journal of Plasticity* 2005;21(6):1161–1193. <https://doi.org/10.1016/j.ijplas.2004.05.018>.
- [33] Goh CS, Gupta M, Wei J, Lee LC. The Cyclic Deformation Behavior of Mg—Y<sub>2</sub>O<sub>3</sub> Nanocomposites. *Journal of Composite Materials* 2008;42(19):2039–2050. <https://doi.org/10.1177/0021998308094544>.

- [34] Hauser, F.E., Starr, C.D., Tietz, L., Dorn, J.E. Deformation mechanisms in polycrystalline aggregates of magnesium. *Transactions of American Society for Metals* 1955;47:102–134.
- [35] Deng K-K, Wang X-J, Wang C-J, Shi J-Y, Hu X-S, Wu K. Effects of bimodal size SiC particles on the microstructure evolution and fracture mechanism of AZ91 matrix at room temperature. *Materials Science and Engineering: A* 2012;553:74–79. <https://doi.org/10.1016/j.msea.2012.05.094>.
- [36] Barnett MR. Twinning and the ductility of magnesium alloys: Part I. “Tension” twins. *Materials Science and Engineering: A* 2007;464(1-2):1–7. <https://doi.org/10.1016/j.msea.2006.12.037>.
- [37] Barnett MR. Twinning and the ductility of magnesium alloys: Part II. “Contraction” twins. *Materials Science and Engineering: A* 2007;464(1–2):8–16. <https://doi.org/10.1016/j.msea.2007.02.109>.
- [38] Jiang J, Godfrey A, Liu W, Liu Q. Microtexture evolution via deformation twinning and slip during compression of magnesium alloy AZ31. *Materials Science and Engineering: A* 2008;483-484:576–579. <https://doi.org/10.1016/j.msea.2006.07.175>.
- [39] Hu H. *Texture of Metals*. *Texture* 1974;1(4):233–258. <https://doi.org/10.1155/TSM.1.233>.
- [40] Wang YN, Huang JC. Texture analysis in hexagonal materials. *Materials Chemistry and Physics* 2003;81(1):11–26. [https://doi.org/10.1016/S0254-0584\(03\)00168-8](https://doi.org/10.1016/S0254-0584(03)00168-8).
- [41] Bohlen J, Yi SB, Swiostek J, Letzig D, Brokmeier HG, Kainer KU. Microstructure and texture development during hydrostatic extrusion of magnesium alloy AZ31. *Scripta Materialia* 2005;53(2):259–264. <https://doi.org/10.1016/j.scriptamat.2005.03.036>.
- [42] Chaudry UM, Hamad K, Kim J-G. On the ductility of magnesium based materials: A mini review. *Journal of Alloys and Compounds* 2019;792:652–664. <https://doi.org/10.1016/j.jallcom.2019.04.031>.
- [43] Ye HZ, Liu XY. Review of recent studies in magnesium matrix composites. *Journal of Materials Science* 2004;39(20):6153–6171. <https://doi.org/10.1023/B:JMSC.0000043583.47148.31>.
- [44] Chawla N, Shen Y-L. Mechanical Behavior of Particle Reinforced Metal Matrix Composites. *Advanced Engineering Materials* 2001;3(6):357–370. [https://doi.org/10.1002/1527-2648\(200106\)3:6<357:AID-ADEM357>3.0.CO;2-I](https://doi.org/10.1002/1527-2648(200106)3:6<357:AID-ADEM357>3.0.CO;2-I).
- [45] Lee SM. *Handbook of Composite Reinforcements*. Wiley; 1992.

- [46] Llorca J, González C. Microstructural factors controlling the strength and ductility of particle-reinforced metal-matrix composites. *Journal of the Mechanics and Physics of Solids* 1998;46(1):1–28. [https://doi.org/10.1016/S0022-5096\(97\)00038-0](https://doi.org/10.1016/S0022-5096(97)00038-0).
- [47] Nan C-W, Clarke DR. The influence of particle size and particle fracture on the elastic/plastic deformation of metal matrix composites. *Acta Materialia* 1996;44(9):3801–3811. [https://doi.org/10.1016/1359-6454\(96\)00008-0](https://doi.org/10.1016/1359-6454(96)00008-0).
- [48] Seo YH, Kang CG. Effects of hot extrusion through a curved die on the mechanical properties of SiCp/Al composites fabricated by melt-stirring. *Composites Science and Technology* 1999;59(5):643–654. [https://doi.org/10.1016/S0266-3538\(98\)00123-7](https://doi.org/10.1016/S0266-3538(98)00123-7).
- [49] Shen M-J, Ying T, Chen F-Y, Hou J-M. Effect of Micro- and Nano-SiC Particulate Reinforcements in Magnesium-Based Metal Matrix Composites. *Journal of Materials Engineering and Performance* 2016;25(6):2222–2229. <https://doi.org/10.1007/s11665-016-2068-6>.
- [50] Gu W-I. Bulk Al/SiC nanocomposite prepared by ball milling and hot pressing method. *Transactions of Nonferrous Metals Society of China* 2006;16:S398-S401. [https://doi.org/10.1016/S1003-6326\(06\)60219-7](https://doi.org/10.1016/S1003-6326(06)60219-7).
- [51] Deng KK, Wu K, Wu YW, Nie KB, Zheng MY. Effect of submicron size SiC particulates on microstructure and mechanical properties of AZ91 magnesium matrix composites. *Journal of Alloys and Compounds* 2010;504(2):542–547. <https://doi.org/10.1016/j.jallcom.2010.05.159>.
- [52] Canakci A, Varol T, Erdemir F. The Effect of Flake Powder Metallurgy on the Microstructure and Densification Behavior of B4C Nanoparticle-Reinforced Al–Cu–Mg Alloy Matrix Nanocomposites. *Arabian Journal for Science and Engineering* 2016;41(5):1781–1796. <https://doi.org/10.1007/s13369-015-1969-2>.
- [53] Luo A. Processing, microstructure, and mechanical behavior of cast magnesium metal matrix composites. *Metallurgical and Materials Transactions A* 1995;26(9):2445–2455. <https://doi.org/10.1007/BF02671259>.
- [54] Lan J, Yang Y, Li X. Microstructure and microhardness of SiC nanoparticles reinforced magnesium composites fabricated by ultrasonic method. *Materials Science and Engineering: A* 2004;386(1–2):284–290. <https://doi.org/10.1016/j.msea.2004.07.024>.
- [55] Zhang Z, Chen DL. Contribution of Orowan strengthening effect in particulate-reinforced metal matrix nanocomposites. *Materials Science and Engineering: A* 2008;483-484:148–152. <https://doi.org/10.1016/j.msea.2006.10.184>.

- [56] Queyreau S, Monnet G, Devincré B. Orowan strengthening and forest hardening superposition examined by dislocation dynamics simulations. *Acta Materialia* 2010;58(17):5586–5595. <https://doi.org/10.1016/j.actamat.2010.06.028>.
- [57] Zhang Z, Chen D. Consideration of Orowan strengthening effect in particulate-reinforced metal matrix nanocomposites: A model for predicting their yield strength. *Scripta Materialia* 2006;54(7):1321–1326. <https://doi.org/10.1016/j.scriptamat.2005.12.017>.
- [58] Subramanian J, Loh Z, Seetharaman S, Hamouda AS, Gupta M. Microstructure and Mechanical Properties of Mg-5Nb Metal-Metal Composite Reinforced with Nano SiC Ceramic Particles. *Metals* 2012;2(2):178-194. <https://doi.org/10.3390/met2020178>
- [59] Hall E. The Deformation and Ageing of Mild Steel: III Discussion of Results. *Proceedings of the Physical Society. Section B* 1951;64(9):747.
- [60] Cáceres CH, Blake AH. On the strain hardening behaviour of magnesium at room temperature. *International Symposium on Physics of Materials*, 2007;462(1–2):193–196. <https://doi.org/10.1016/j.msea.2005.12.113>.
- [61] Ferguson JB, Sheykh-Jaberi F, Kim C-S, Rohatgi PK, Cho K. On the strength and strain to failure in particle-reinforced magnesium metal-matrix nanocomposites (Mg MMNCs). *Materials Science and Engineering: A* 2012;558:193–204. <https://doi.org/10.1016/j.msea.2012.07.111>.
- [62] Lukáč P, Trojanová Z. Influence of grain size on ductility of magnesium alloys. *Materials Engineering* 2011;18.
- [63] Sanaty-Zadeh A. Comparison between current models for the strength of particulate-reinforced metal matrix nanocomposites with emphasis on consideration of Hall–Petch effect. *Materials Science and Engineering: A* 2012;531:112–118. <https://doi.org/10.1016/j.msea.2011.10.043>.
- [64] Redsten AM, Klier EM, Brown AM, Dunand DC. Mechanical properties and microstructure of cast oxide-dispersion-strengthened aluminum. *Materials Science and Engineering: A* 1995;201(1):88–102. [https://doi.org/10.1016/0921-5093\(94\)09741-0](https://doi.org/10.1016/0921-5093(94)09741-0).
- [65] Balogh L, Figueiredo RB, Ungár T, Langdon TG. The contributions of grain size, dislocation density and twinning to the strength of a magnesium alloy processed by ECAP. *Special Topic Section: Local and Near Surface Structure from Diffraction* 2010;528(1):533–538. <https://doi.org/10.1016/j.msea.2010.09.048>.
- [66] Czerwinski F. *Magnesium Injection Molding*. Springer US; 2007.

- [67] Spitzer WG, Kleinman D, Walsh D. Infrared Properties of Hexagonal Silicon Carbide. *Physical Review Journals* 1959;113(1):127–132. <https://doi.org/10.1103/PhysRev.113.127>.
- [68] Spitzer WG, Kleinman DA, Frosch CJ. Infrared Properties of Cubic Silicon Carbide Films. *Physical Review Journals* 1959;113(1):133–136. <https://doi.org/10.1103/PhysRev.113.133>.
- [69] Ferkel H, Mordike BL. Magnesium strengthened by SiC nanoparticles. *Materials Science and Engineering: A* 2001;298(1-2):193–199. [https://doi.org/10.1016/S0921-5093\(00\)01283-1](https://doi.org/10.1016/S0921-5093(00)01283-1).
- [70] Li Z, Bradt RC. Thermal expansion of the cubic (3C) polytype of SiC. *Journal of Materials Science* 1986;21(12):4366–4368. <https://doi.org/10.1007/BF01106557>.
- [71] Friend CM. The effect of temperature on the tensile strength of short  $\alpha$ -alumina fibre/aluminium alloy metal matrix composites. *Scripta Metallurgica* 1989;23(1):33–37. [https://doi.org/10.1016/0036-9748\(89\)90088-4](https://doi.org/10.1016/0036-9748(89)90088-4).
- [72] Saravanan RA, Surappa MK. Fabrication and characterisation of pure magnesium-30 vol.% SiCp particle composite. *Materials Science and Engineering: A* 2000;276(1–2):108–116. [https://doi.org/10.1016/S0921-5093\(99\)00498-0](https://doi.org/10.1016/S0921-5093(99)00498-0).
- [73] Deng KK, Wang XJ, Wu YW, Hu XS, Wu K, Gan WM. Effect of particle size on microstructure and mechanical properties of SiCp/AZ91 magnesium matrix composite. *Materials Science and Engineering: A* 2012;543:158–163. <https://doi.org/10.1016/j.msea.2012.02.064>.
- [74] Hu H. Squeeze casting of magnesium alloys and their composites. *Journal of Materials Science* 1998;33(6):1579–1589. <https://doi.org/10.1023/A:1017567821209>.
- [75] Esmaily M, Mortazavi N, Svensson JE, Halvarsson M, Wessén M, Johansson LG et al. A new semi-solid casting technique for fabricating SiC-reinforced Mg alloys matrix composites. *Composites Part B* 2016;94:176–189. <https://doi.org/10.1016/j.compositesb.2016.02.019>.
- [76] Chen L-Y, Peng J-Y, Xu J-Q, Choi H, Li X-C. Achieving uniform distribution and dispersion of a high percentage of nanoparticles in metal matrix nanocomposites by solidification processing. *Scripta Materialia* 2013;69(8):634–637. <https://doi.org/10.1016/j.scriptamat.2013.07.016>.
- [77] Rauber C, Lohmüller A, Opel S, Singer RF. Microstructure and mechanical properties of SiC particle reinforced magnesium composites processed by injection molding. *Materials Science and Engineering: A* 2011;528(19-20):6313–6323. <https://doi.org/10.1016/j.msea.2011.04.088>.

- [78] Kuziora P, Wyszyńska M, Polanski M, Bystrzycki J. Why the ball to powder ratio (BPR) is insufficient for describing the mechanical ball milling process. *International Journal of Hydrogen Energy* 2014;39(18):9883–9887. <https://doi.org/10.1016/j.ijhydene.2014.03.009>.
- [79] Abdellahi M, Bahmanpour H, Bahmanpour M. The best conditions for minimizing the synthesis time of nanocomposites during high energy ball milling: Modeling and optimizing. *Ceramics International* 2014;40(7, Part A):9675–9692. <https://doi.org/10.1016/j.ceramint.2014.02.049>.
- [80] Fritsch GmbH. Planetary Mill: Pulverisette 5/4. [June 09, 2021]; Available from: [https://www.fritsch-international.com/fileadmin/\\_processed\\_/csm\\_P-5\\_4-classic-line\\_96e80277bf.png](https://www.fritsch-international.com/fileadmin/_processed_/csm_P-5_4-classic-line_96e80277bf.png).
- [81] Arik H. Production and characterization of in situ  $Al_4C_3$  reinforced aluminum-based composite produced by mechanical alloying technique. *Materials & Design* 2004;25(1):31–40. [https://doi.org/10.1016/S0261-3069\(03\)00163-8](https://doi.org/10.1016/S0261-3069(03)00163-8).
- [82] Fecht H-J. Nanostructure formation by mechanical attrition. *Nanostructured Materials* 1995;6(1-4):33–42. [https://doi.org/10.1016/0965-9773\(95\)00027-5](https://doi.org/10.1016/0965-9773(95)00027-5).
- [83] Fogagnolo JB, Velasco F, Robert MH, Torralba JM. Effect of mechanical alloying on the morphology, microstructure and properties of aluminium matrix composite powders. *Materials Science and Engineering: A* 2003;342(1-2):131–143. [https://doi.org/10.1016/S0921-5093\(02\)00246-0](https://doi.org/10.1016/S0921-5093(02)00246-0).
- [84] Viswanathan V, Laha T, Balani K, Agarwal A, Seal S. Challenges and advances in nanocomposite processing techniques. *Materials Science and Engineering: R: Reports* 2006;54(5-6):121–285. <https://doi.org/10.1016/j.mser.2006.11.002>.
- [85] Yang HC, Kim JK, Kim KT. Rubber isostatic pressing and cold isostatic pressing of metal powder. *Materials Science and Engineering: A* 2004;382(1-2):41–49. <https://doi.org/10.1016/j.msea.2004.04.056>.
- [86] Kobe Steel, Ltd. What is Cold Isostatic Pressing (CIP)? [June 09, 2021]; Available from: <https://www.kobelco.co.jp/english/products/ip/technology/cip.html>.
- [87] Jones W. *Fundamental principles of powder metallurgy*. London: Edward Arnold Publisher Ltd; 1960.
- [88] Fischmeister HF, Arzt E, Olsson LR. Particle Deformation and Sliding During Compaction of Spherical Powders: A Study by Quantitative Metallography. *Powder Metallurgy* 1978;21(4):179–187. <https://doi.org/10.1179/pom.1978.21.4.179>.

- [89] German RM. Particle packing characteristics. Princeton, NJ: Metal Powder Industries Federation; 1989.
- [90] Zhong XL, Gupta M. Development of lead-free Sn–0.7Cu/Al<sub>2</sub>O<sub>3</sub> nanocomposite solders with superior strength. *Journal of Physics D: Applied Physics* 2008;41(9):1–7. <https://doi.org/10.1088/0022-3727/41/9/095403>.
- [91] Hassan SF, Gupta M. Creation of High Performance Mg Based Composite Containing Nano-Size Al<sub>2</sub>O<sub>3</sub> Particulates as Reinforcement. *Journal of Metastable and Nanocrystalline Materials* 2005;23:151–154. <https://doi.org/10.4028/www.scientific.net/JMNM.23.151>.
- [92] Hassan SF, Gupta M. Development of high performance magnesium nano-composites using nano-Al<sub>2</sub>O<sub>3</sub> as reinforcement. *Materials Science and Engineering: A* 2005;392(1-2):163–168. <https://doi.org/10.1016/j.msea.2004.09.047>.
- [93] Prangnell PB, Barnes SJ, Roberts SM, Withers PJ. The effect of particle distribution on damage formation in particulate reinforced metal matrix composites deformed in compression. *Materials Science and Engineering: A* 1996;220(1):41–56. [https://doi.org/10.1016/S0921-5093\(96\)10461-5](https://doi.org/10.1016/S0921-5093(96)10461-5).
- [94] Schatt W. *Pulvermetallurgie: Technologien und Werkstoffe*. 2nd ed. Berlin, Heidelberg: Springer-Verlag Berlin Heidelberg; 2007.
- [95] Shaler AJ, Wulff J. Mechanism of Sintering. *Industrial & Engineering Chemistry Research*. 1948;40(5):838–842. <https://doi.org/10.1021/ie50461a014>.
- [96] Wilder DR, Fitzsimmons ES. Further Study of Sintering Phenomena. *Journal of the American Ceramic Society* 1955;38(2):66–71. <https://doi.org/10.1111/j.1151-2916.1955.tb14578.x>.
- [97] Hornbogen E, Warlimont H. *Metalle: Struktur und Eigenschaften der Metalle und Legierungen*. 5<sup>th</sup> ed. Berlin, Heidelberg: Springer; 2006.
- [98] Gómez SY, Hotza D. Predicting powder densification during sintering. *Journal of the European Ceramic Society* 2018;38(4):1736–1741. <https://doi.org/10.1016/j.jeurceramsoc.2017.10.020>.
- [99] Atkinson HV, Davies S. Fundamental aspects of hot isostatic pressing: An overview. *Metallurgical and Materials Transactions A* 2000;31(12):2981–3000. <https://doi.org/10.1007/s11661-000-0078-2>.
- [100] Bocanegra-Bernal MH. Hot Isostatic Pressing (HIP) technology and its applications to metals and ceramics. *Journal of Materials Science* 2004;39(21):6399–6420. <https://doi.org/10.1023/B:JMSC.0000044878.11441.90>.

- [101] German RM. Sintering With External Pressure. In: German R, editor. Sintering: From Empirical Observations to Scientific Principles, 1<sup>st</sup> ed. s.l.: Elsevier Reference Monographs; 2014, p. 305–354.
- [102] Li EKH, Funkenbusch PD. Hot isostatic pressing (HIP) of powder mixtures and composites: Packing, densification, and microstructural effects. Metallurgical and Materials Transactions A 1993;24(6):1345–1354. <https://doi.org/10.1007/BF02668202>.
- [103] Nair SV, Tien JK. Densification mechanism maps for hot isostatic pressing (HIP) of unequal sized particles. Metallurgical and Materials Transactions A 1987;18(1):97–107. <https://doi.org/10.1007/BF02646226>.
- [104] Xu ZM, Loh NL, Zhou W. Hot isostatic pressing of cast SiCp-reinforced aluminium-based composites. 7<sup>th</sup> International Scientific Conference: Achievements in Mechanical & Materials Engineering 1997;67(1):131–136. [https://doi.org/10.1016/S0924-0136\(96\)02832-4](https://doi.org/10.1016/S0924-0136(96)02832-4).
- [105] Reginald Genders. Direct and indirect extrusion of metals (US2675125A); 1954.
- [106] Groover MP. Fundamentals of modern manufacturing: Materials, processes, and systems. Hoboken, NJ: John Wiley & Sons, Inc; 2020.
- [107] Roy S, Kannan G, Suwas S, Surappa MK. Effect of extrusion ratio on the microstructure, texture and mechanical properties of (Mg/AZ91)<sub>m</sub>–SiCp composite. Materials Science and Engineering: A 2015;624:279–290. <https://doi.org/10.1016/j.msea.2014.10.063>.
- [108] Park SH, Kim HS, Bae JH, Yim CD, You BS. Improving the mechanical properties of extruded Mg–3Al–1Zn alloy by cold pre-forging. Scripta Materialia 2013;69(3):250–253. <https://doi.org/10.1016/j.scriptamat.2013.04.011>.
- [109] Chen Y, Jin L, Dong J, Zhang Z, Wang F. Twinning effects on the hot deformation behavior of AZ31 Mg alloy. Materials Characterization 2016;118:363–369. <https://doi.org/10.1016/j.matchar.2016.06.014>.
- [110] Garcés G, Pérez P, Adeva P. Effect of the extrusion texture on the mechanical behaviour of Mg–SiCp composites. Scripta Materialia 2005;52(7):615–619. <https://doi.org/10.1016/j.scriptamat.2004.11.024>.
- [111] Li N, Huang G, Xin R, Liu Q. Influence of extrusion ratio on microstructure and texture developments of high-temperature extruded AZ31 Mg alloy. Science China Technological Sciences 2012;55(2):490–495. <https://doi.org/10.1007/s11431-011-4671-y>.

- [112] Roy TK, Subramanian C, Suri AK. Pressureless sintering of boron carbide. *Ceramics International* 2006;32(3):227–233. <https://doi.org/10.1016/j.ceramint.2005.02.008>.
- [113] Wang XJ, Xu L, Hu XS, Nie KB, Deng KK, Wu K et al. Influences of extrusion parameters on microstructure and mechanical properties of particulate reinforced magnesium matrix composites. *Materials Science and Engineering: A* 2011;528(21):6387–6392. <https://doi.org/10.1016/j.msea.2011.04.064>.
- [114] Garcés G, Oñorbe E, Pérez P, Klaus M, Genzel C, Adeva P. Influence of SiC particles on compressive deformation of magnesium matrix composites. *Materials Science and Engineering: A* 2012;533:119–123. <https://doi.org/10.1016/j.msea.2011.10.103>.
- [115] Habibi MK, Tun KS, Gupta M. An investigation into the effect of ball milling of reinforcement on the enhanced mechanical response of magnesium. *Journal of Composite Materials* 2011;45(24):2483–2493. <https://doi.org/10.1177/0021998311401098>.
- [116] Nie KB, Wang XJ, Xu L, Wu K, Hu XS, Zheng MY. Effect of hot extrusion on microstructures and mechanical properties of SiC nanoparticles reinforced magnesium matrix composite. *Journal of Alloys and Compounds* 2012;512(1):355–360. <https://doi.org/10.1016/j.jallcom.2011.09.099>.
- [117] Hassan SF, Ho KF, Gupta M. Increasing elastic modulus, strength and CTE of AZ91 by reinforcing pure magnesium with elemental copper. *Materials Letters* 2004;58(16):2143–2146. <https://doi.org/10.1016/j.matlet.2004.01.011>.
- [118] Gupta M, Lai MO, Saravananathan D. Synthesis, microstructure and properties characterization of disintegrated melt deposited Mg/SiC composites. *Journal of Materials Science* 2000;35(9):2155–2165. <https://doi.org/10.1023/A:1004706321731>.
- [119] Wong WLE, Gupta M. Effect of Hybrid Length Scales (Micro + Nano) of SiC Reinforcement on the Properties of Magnesium. *Solid State Phenomena* 2006;111:91–94. <https://doi.org/10.4028/www.scientific.net/SSP.111.91>.
- [120] Oliver WC, Pharr GM. An improved technique for determining hardness and elastic modulus using load and displacement sensing indentation experiments. *Journal of Materials Research* 1992;7(06):1564–1583. <https://doi.org/10.1557/JMR.1992.1564>.
- [121] Mussert KM, Vellinga WP, Bakker A, van der Zwaag S. A nano-indentation study on the mechanical behaviour of the matrix material in an AA6061 - Al<sub>2</sub>O<sub>3</sub> MMC. *Journal of Materials Science* 2002;37(4):789–794. <https://doi.org/10.1023/A:1013896032331>.

- [122] Wang HF, Nelson JC, Gerberich WW, Deve HE. Evaluation of in situ mechanical properties of composites by using nanoindentation techniques. *Acta Metallurgica et Materialia* 1994;42(3):695–700. [https://doi.org/10.1016/0956-7151\(94\)90267-4](https://doi.org/10.1016/0956-7151(94)90267-4).
- [123] Schmahl M, Märten A, Zaslansky P, Fleck C. Nanofatigue behaviour of single struts of cast A356.0 foam: cyclic deformation, nanoindent characteristics and sub-surface microstructure. *Materials & Design* 2020;195:109016. <https://doi.org/10.1016/j.matdes.2020.109016>.
- [124] Lame O, Bellet D, Di Michiel M, Bouvard D. In situ microtomography investigation of metal powder compacts during sintering. *Nuclear Instruments and Methods in Physics Research Section B: Beam Interactions with Materials and Atoms* 2003;200:287–294. [https://doi.org/10.1016/S0168-583X\(02\)01690-7](https://doi.org/10.1016/S0168-583X(02)01690-7).
- [125] Oliver WC, Pharr GM. Measurement of hardness and elastic modulus by instrumented indentation: Advances in understanding and refinements to methodology. *Journal of Materials Research* 2004;19(01):3–20. <https://doi.org/10.1557/jmr.2004.19.1.3>.
- [126] Bočan J, Maňák J, Jäger A. Nanomechanical analysis of AZ31 magnesium alloy and pure magnesium correlated with crystallographic orientation. *International Symposium on Physics of Materials*, 2005 2015;644:121–128. <https://doi.org/10.1016/j.msea.2015.07.055>.
- [127] Bočan J, Maňák J, Jäger A. Anisotropic Mechanical Properties of Pure Magnesium Analyzed by *In Situ* Nanoindentation. *Key Engineering Materials* 2015;662:11–14. <https://doi.org/10.4028/www.scientific.net/KEM.662.11>.
- [128] McElhanev KW, Vlassak JJ, Nix WD. Determination of indenter tip geometry and indentation contact area for depth-sensing indentation experiments. *Journal of Materials Research* 1998;13(5):1300–1306. <https://doi.org/10.1557/JMR.1998.0185>.
- [129] Chamos AN, Charitidis CA, Skarmoutsou A, Pantelakis SG. An investigation on the high stress sensitivity of fatigue life of rolled AZ31 magnesium alloy under constant amplitude fatigue loading. *Fatigue & Fracture of Engineering Materials & Structures* 2010;33(4):252–265. <https://doi.org/10.1111/j.1460-2695.2009.01434.x>.
- [130] Guo T, Siska F, Cheng J, Barnett M. Initiation of basal slip and tensile twinning in magnesium alloys during nanoindentation. *Journal of Alloys and Compounds* 2018;731:620–630. <https://doi.org/10.1016/j.jallcom.2017.10.088>.
- [131] Hu J, Zhang W, Peng G, Zhang T, Zhang Y. Nanoindentation deformation of refine-grained AZ31 magnesium alloy: Indentation size effect, pop-in effect

- and creep behavior. *International Symposium on Physics of Materials*, 2018;725:522–529. <https://doi.org/10.1016/j.msea.2018.03.104>.
- [132] Pook LP. *Metal fatigue: What it is, why it matters*. Dordrecht: Springer; 2007.
- [133] Castro F, Jiang Y. Fatigue of extruded AZ31B magnesium alloy under stress- and strain-controlled conditions including step loading. *Mechanics of Materials* 2017;108:77–86. <https://doi.org/10.1016/j.mechmat.2017.03.002>.
- [134] Xiong Y, Yu Q, Jiang Y. An experimental study of cyclic plastic deformation of extruded ZK60 magnesium alloy under uniaxial loading at room temperature. *International Journal of Plasticity* 2014;53:107–124. <https://doi.org/10.1016/j.ijplas.2013.07.008>.
- [135] Wolf B, Fleck C, Eifler D. Characterization of the fatigue behaviour of the magnesium alloy AZ91D by means of mechanical hysteresis and temperature measurements. *International Journal of Fatigue* 2004;26(12):1357–1363. <https://doi.org/10.1016/j.ijfatigue.2004.04.005>.
- [136] Jiang L, Jonas JJ, Luo AA, Sachdev AK, Godet S. Influence of {10-12} extension twinning on the flow behavior of AZ31 Mg alloy. *Materials Science and Engineering: A* 2007;445-446:302–309. <https://doi.org/10.1016/j.msea.2006.09.069>.
- [137] Yu Q, Zhang J, Jiang Y. Fatigue damage development in pure polycrystalline magnesium under cyclic tension–compression loading. *International Symposium on Physics of Materials*, 2011;528(25-26):7816–7826. <https://doi.org/10.1016/j.msea.2011.06.064>.
- [138] Chen P-C, Lin S-J, Jahn M-T. A study on the low-cycle fatigue properties of SiCp/6061 Al composites. *Journal of Materials Science* 1997;32(15):4153–4158. <https://doi.org/10.1023/A:1018670328085>.
- [139] Hassan HA, Lewandowski JJ. Effects of particulate volume fraction on cyclic stress response and fatigue life of AZ91D magnesium alloy metal matrix composites. *Materials Science and Engineering: A* 2014;600:188–194. <https://doi.org/10.1016/j.msea.2014.02.021>.
- [140] Deryagin GA, Shtovba YK, Shneeroba EI. Accelerated methods of determining the endurance limit of aluminum alloys. *Strength of Materials* 1970;2(4):308–314. <https://doi.org/10.1007/BF01527744>.
- [141] Sih GC, Chao CK. Failure initiation in unnotched specimens subjected to monotonic and cyclic loading. *Theoretical and Applied Fracture Mechanics* 1984;2(1):67–73. [https://doi.org/10.1016/0167-8442\(84\)90041-7](https://doi.org/10.1016/0167-8442(84)90041-7).

- [142] Liu WC, Dong J, Zhang P, Yao ZY, Zhai CQ, Ding WJ. High cycle fatigue behavior of as-extruded ZK60 magnesium alloy. *Journal of Materials Science* 2009;44(11):2916–2924. <https://doi.org/10.1007/s10853-009-3385-z>.
- [143] Fleck C, Eifler D. Deformation behaviour and damage accumulation of cortical bone specimens from the equine tibia under cyclic loading. *Journal of Biomechanics* 2003;36(2):179–189. [https://doi.org/10.1016/S0021-9290\(02\)00364-0](https://doi.org/10.1016/S0021-9290(02)00364-0).
- [144] Cavaliere P (ed.). *Fatigue and Fracture of Nanostructured Materials*. Cham: Springer International Publishing; 2021.
- [145] Cavaliere P. Cyclic deformation of ultra-fine and nanocrystalline metals through nanoindentation: Similarities with crack propagation. *Procedia Engineering* 2010;2(1):213–222. <https://doi.org/10.1016/j.proeng.2010.03.023>.
- [146] Xu B, Yue Z, Chen X. An indentation fatigue depth propagation law. *Scripta Materialia* 2009;60(10):854–857. <https://doi.org/10.1016/j.scriptamat.2009.01.027>.
- [147] Carmine M, Fabrizio N, Emanuele S, Franco F. Analysis of fatigue damage in shape memory alloys by nanoindentation. *International Symposium on Physics of Materials, 2005* 2017;684:335–343. <https://doi.org/10.1016/j.msea.2016.12.003>.
- [148] Saraswati T, Sritharan T, Mhaisalkar S, Breach CD, Wulff F. Cyclic loading as an extended nanoindentation technique. *International Symposium on Physics of Materials, 2005* 2006;423(1):14–18. <https://doi.org/10.1016/j.msea.2005.10.080>.
- [149] Shen Y-L, Blada CB, Williams JJ, Chawla N. Cyclic indentation behavior of metal–ceramic nanolayered composites. *International Symposium on Physics of Materials, 2005* 2012;557:119–125. <https://doi.org/10.1016/j.msea.2012.05.103>.
- [150] Zehnder C, Peltzer J-N, Gibson JSK-L, Korte-Kerzel S. High strain rate testing at the nano-scale: A proposed methodology for impact nanoindentation. *Materials & Design* 2018;151:17–28. <https://doi.org/10.1016/j.matdes.2018.04.045>.
- [151] Gale JD, Achuthan A. The effect of work-hardening and pile-up on nanoindentation measurements. *Journal of Materials Science* 2014;49(14):5066–5075. <https://doi.org/10.1007/s10853-014-8213-4>.
- [152] Liu J-N, Xu B-S, Wang H-D, Cui X-F, Zhu L-N, Jin G. Measurement for mechanical behavior and fatigue property of Cu films by nanoscale dynamic

- load method. *Materials and Design* 2015;65:1136–1142.  
<https://doi.org/10.1016/j.matdes.2014.08.043>.
- [153] Faisal NH, Prathuru AK, Goel S, Ahmed R, Droubi MG, Beake BD et al. Cyclic Nanoindentation and Nano-Impact Fatigue Mechanisms of Functionally Graded TiN/TiNi Film. *Shape Memory and Superelasticity* 2017;3(2):149–167.  
<https://doi.org/10.1007/s40830-017-0099-y>.
- [154] Steck JG, Fleming RA, Goss JA, Zou M. Deformation and fatigue resistance of Al/a-Si core-shell nanostructures subjected to cyclic nanoindentation. *Applied Surface Science* 2018;433:617–626.  
<https://doi.org/10.1016/j.apsusc.2017.09.255>.
- [155] Jain S, Gokhale A, Jain J, Singh SS, Hariharan K. Fatigue behavior of aged and solution treated AZ61 Mg alloy at small length scale using nanoindentation. *International Symposium on Physics of Materials, 2005* 2017;684:652–659. <https://doi.org/10.1016/j.msea.2016.12.111>.
- [156] Tun KS, Gupta M. Enhanced mechanical properties and near unity yield asymmetry in equiatomic high entropy alloy particles reinforced magnesium composites. *Journal of Alloys and Compounds* 2019;810:151909.  
<https://doi.org/10.1016/j.jallcom.2019.151909>.
- [157] Barnett MR, Keshavarz Z, Beer AG, Atwell D. Influence of grain size on the compressive deformation of wrought Mg–3Al–1Zn. *Acta Materialia* 2004;52(17):5093–5103. <https://doi.org/10.1016/j.actamat.2004.07.015>.
- [158] Tun KS, Gupta M. Compressive deformation behavior of Mg and Mg/(Y<sub>2</sub>O<sub>3</sub>+Ni) nanocomposites. *Materials Science and Engineering: A* 2010;527(21-22):5550–5556. <https://doi.org/10.1016/j.msea.2010.05.025>.
- [159] Tun KS, Jayaramanavar P, Nguyen QB, Chan J, Kwok R, Gupta M. Investigation into tensile and compressive responses of Mg–ZnO composites. *Materials Science and Technology* 2012;28(5):582–588.  
<https://doi.org/10.1179/1743284711Y.0000000108>.
- [160] Suryanarayana C. Synthesis of nanocomposites by mechanical alloying. *Journal of Alloys and Compounds* 2011;509:S229-S234.  
<https://doi.org/10.1016/j.jallcom.2010.09.063>.
- [161] Jiang X, Liu W, Li Y, Shao Z, Luo Z, Zhu D et al. Microstructures and mechanical properties of Cu/Ti<sub>3</sub>SiC<sub>2</sub>/C/graphene nanocomposites prepared by vacuum hot-pressing sintering and hot isostatic pressing. *Composites Part B* 2018;141:203–213. <https://doi.org/10.1016/j.compositesb.2017.12.050>.
- [162] Knowles AJ, Jiang X, Galano M, Audebert F. Microstructure and mechanical properties of 6061 Al alloy based composites with SiC

- nanoparticles. *Journal of Alloys and Compounds* 2014;615:S401-S405.  
<https://doi.org/10.1016/j.jallcom.2014.01.134>.
- [163] Nes E, Ryum N, Hunderi O. On the Zener drag. *Acta Metallurgica* 1985;33(1):11–22. [https://doi.org/10.1016/0001-6160\(85\)90214-7](https://doi.org/10.1016/0001-6160(85)90214-7).
- [164] Yao X, Zheng YF, Quadir MZ, Kong C, Liang JM, Chen YH et al. Grain growth and recrystallization behaviors of an ultrafine grained Al-0.6 wt%Mg-0.4 wt%Si-5vol.%SiC nanocomposite during heat treatment and extrusion. *Journal of Alloys and Compounds* 2018;745:519–524.  
<https://doi.org/10.1016/j.jallcom.2018.02.145>.
- [165] Gladman T. On the theory of the effect of precipitate particles on grain growth in metals. *Proceedings of the Royal Society of London A* 1966;294(1438):298–309. <https://doi.org/10.1098/rspa.1966.0208>.
- [166] Tekumalla S, Bibhanshu N, Shabadi R, Suwas S, Ha TMH, Gupta M. Evolution of texture and asymmetry and its impact on the fatigue behaviour of an in-situ magnesium nanocomposite. *Materials Science and Engineering: A* 2018;727:61–69. <https://doi.org/10.1016/j.msea.2018.04.101>.
- [167] Yin DL, Wang JT, Liu JQ, Zhao X. On tension–compression yield asymmetry in an extruded Mg–3Al–1Zn alloy. *Journal of Alloys and Compounds* 2009;478(1-2):789–795.  
<https://doi.org/10.1016/j.jallcom.2008.12.033>.
- [168] Kamrani, Hübler, Ghasemi, Fleck. Enhanced Strength and Ductility in Magnesium Matrix Composites Reinforced by a High Volume Fraction of Nano- and Submicron-Sized SiC Particles Produced by Mechanical Milling and Hot Extrusion. *Materials* 2019;12(20):3445.  
<https://doi.org/10.3390/ma12203445>.
- [169] Hysitron Incorporated 2014. TI 950 TriboIndenter User Manual: Revision 9.3.0314.
- [170] Friedrich HE, Mordike BL. *Magnesium Technology: Metallurgy, Design Data, Applications*. Springer Berlin Heidelberg; 2006.
- [171] Meenashisundaram GK, Nai MH, Almajid A, Gupta M. Development of high performance Mg–TiO<sub>2</sub> nanocomposites targeting for biomedical/structural applications. *Materials & Design (1980-2015)* 2015;65:104–114.  
<https://doi.org/10.1016/j.matdes.2014.08.041>.
- [172] Meenashisundaram GK, Seetharaman S, Gupta M. Enhancing overall tensile and compressive response of pure Mg using nano-TiB<sub>2</sub> particulates. *Materials Characterization* 2014;94:178–188.  
<https://doi.org/10.1016/j.matchar.2014.05.021>.

- [173] Stanford N, Atwell D. The Effect of Mn-rich Precipitates on the Strength of AZ31 Extrudates. *Metallurgical and Materials Transactions A* 2013;44(10):4830–4843. <https://doi.org/10.1007/s11661-013-1817-5>.
- [174] Buch A. *Pure metals properties: a scientific-technical handbook*. ASM International; 1999.
- [175] Nguyen QB, Gupta M. Increasing significantly the failure strain and work of fracture of solidification processed AZ31B using nano- $\text{Al}_2\text{O}_3$  particulates. *Journal of Alloys and Compounds* 2008;459(1-2):244–250. <https://doi.org/10.1016/j.jallcom.2007.05.038>.
- [176] Koike J, Kobayashi T, Mukai T, Watanabe H, Suzuki M, Maruyama K et al. The activity of non-basal slip systems and dynamic recovery at room temperature in fine-grained AZ31B magnesium alloys. *Acta Materialia* 2003;51(7):2055–2065. [https://doi.org/10.1016/S1359-6454\(03\)00005-3](https://doi.org/10.1016/S1359-6454(03)00005-3).
- [177] Goh CS, Wei J, Lee LC, Gupta M. Ductility improvement and fatigue studies in Mg-CNT nanocomposites. *Composites Science and Technology* 2008;68(6):1432–1439. <https://doi.org/10.1016/j.compscitech.2007.10.057>.
- [178] Garcés G, Rodríguez M, Pérez P, Adeva P. Effect of volume fraction and particle size on the microstructure and plastic deformation of Mg– $\text{Y}_2\text{O}_3$  composites. *International Symposium on Physics of Materials, 2005* 2006;419(1-2):357–364. <https://doi.org/10.1016/j.msea.2006.01.026>.
- [179] Berbenni S, Favier V, Berveiller M. Impact of the grain size distribution on the yield stress of heterogeneous materials. *International Journal of Plasticity* 2007;23(1):114–142. <https://doi.org/10.1016/j.ijplas.2006.03.004>.
- [180] Tun KS, Wong WLE, Nguyen QB, Gupta M. Tensile and Compressive Responses of Ceramic and Metallic Nanoparticle Reinforced Mg Composites. *Materials* 2013;6(5):1826-1839. <https://doi.org/10.3390/ma6051826>
- [181] van den Beukel A. Grain size dependence of the dislocation density in cold worked metals. *Scripta Metallurgica* 1978;12(9):809–813. [https://doi.org/10.1016/0036-9748\(78\)90041-8](https://doi.org/10.1016/0036-9748(78)90041-8).
- [182] Hansen N. The effect of grain size and strain on the tensile flow stress of aluminium at room temperature. *Acta Metallurgica* 1977;25(8):863–869. [https://doi.org/10.1016/0001-6160\(77\)90171-7](https://doi.org/10.1016/0001-6160(77)90171-7).
- [183] Campbell JD, Simmons JA, Dorn JE. On the Dynamic Behavior of a Frank-Read Source. *Journal of Applied Mechanics* 1961;28(3):447–453. <https://doi.org/10.1115/1.3641726>.

- [184] Sukedai E, Yokoyama T. Investigation of tensile–compressive yield asymmetry and the role of deformation twin in extruded pure magnesium. *International Journal of Materials Research* 2010;101(6):736–740. <https://doi.org/10.3139/146.110332>.
- [185] Begum S, Chen D, Xu S, Luo A. Low cycle fatigue properties of an extruded AZ31 magnesium alloy. *International Journal of Fatigue* 2009;31(4):726–735. <https://doi.org/10.1016/j.ijfatigue.2008.03.009>.
- [186] Kramer HS, Starke P, Klein M, Eifler D. Cyclic hardness test PHYBAL<sub>CHT</sub> – Short-time procedure to evaluate fatigue properties of metallic materials. *International Journal of Fatigue* 2014;63:78–84. <https://doi.org/10.1016/j.ijfatigue.2014.01.009>.
- [187] Blinn B, Görzen D, Klein M, Eifler D, Beck T. PhyBaLCHT – Influence of indentation force on the results of cyclic hardness tests and investigations of comparability to uniaxial fatigue loading. *International Journal of Fatigue* 2019;119:78–88. <https://doi.org/10.1016/j.ijfatigue.2018.09.025>.
- [188] Hübler D, Winkler K, Riedel R, Kamrani S, Fleck C. Cyclic deformation behaviour of Mg-SiC nanocomposites on the macro and nano scale, *Fatigue & Fracture of Engineering Materials & Structure* 2021; 1-14. <https://doi.org/10.1111/ffe.13600>
- [189] He X, Liu J, An L. The mechanical behavior of hierarchical Mg matrix nanocomposite with high volume fraction reinforcement. *International Symposium on Physics of Materials, 2005* 2017;699:114–117. <https://doi.org/10.1016/j.msea.2017.05.067>.
- [190] Ugandhar S, Gupta M, Sinha SK. Enhancing strength and ductility of Mg/SiC composites using recrystallization heat treatment. *Composite Structures* 2006;72(2):266–272. <https://doi.org/10.1016/j.compstruct.2004.11.010>.
- [191] Suh B-C, Sasaki T, Nakata T, Kamado S, Hono K. Effect of Ca on the Microstructure, Texture and Mechanical Properties in Mg–Zn–Mn Based Alloy. In: Solanki KN, Orlov D, Singh A, Neelameggham NR, editors. *Magnesium Technology 2017*. Cham, s.l.: Springer International Publishing; 2017, p. 525–531.
- [192] Alaneme KK, Okotete EA. Enhancing plastic deformability of Mg and its alloys—A review of traditional and nascent developments. *Journal of Magnesium and Alloys* 2017;5(4):460–475. <https://doi.org/10.1016/j.jma.2017.11.001>.

- [193] Wang F, Dong J, Jiang Y, Ding W. Cyclic deformation and fatigue of extruded Mg–Gd–Y magnesium alloy. *Materials Science and Engineering: A* 2013;561:403–410. <https://doi.org/10.1016/j.msea.2012.10.048>.